ASPECTS OF THE GEOLOGY, GEOCHEMISTRY AND METAMORPHISM OF THE LOWER OREBODY, BROKEN HILL DEPOSIT, AGGENEYS.

Dennis Hoffmann

A thesis submitted in fulfilment for the degree of Master of Science in the Department of Geological Sciences at the University of Cape Town.

March 1993

CONTENTS

LIST OF FIGURES

and garnet quartzite, respectively (modified after Smith, 1986; used with permission).

Figure 4.5. Interpreted N-S drill section (Y+20665) through the LOB and UOB successions. See text for annotation of "P". HS - Hangingwall Schist, IS - Intermediate Schist, US - Upper Footwall Schist.

Figure 4.6. Interpreted N-S drill section (Y+20405) through the LOB and UOB successions. Compare with Figure 4.5.

Figure 4.7. Garnet quartzite with breccia texture. Location: borehole BHU2659.

Figure 4.8. Ternary diagram showing QMIF, AMIF, GMIF and MMIF iron formation-types as a function of their silicate mineral contents. MMIF- massive magnetite iron formation, QMIF- quartz magnetite iron formation, GMIF- garnet magnetite iron formation and AMIF- amphibole magnetite iron formation.

Figure 4.9. Isopach map showing the total thickness of the LOB iron formation. The iron formation along the NW margin of the deposit was excluded due the effects of folding. Compare with Figure 4.2.

Figure 4.10. Photograph of amphibole magnetite iron formation showing alternating amphibole- and garnet-rich mesobands.

Figure 4.11. Banded garnet magnetite iron formation at the NW margin of the LOB. Location: stope 11/0700 lift 7. Scale: Magnet-pen has 14 cm length.

Figure 4.12. Massive magnetite iron formation with coarse-grained porphyroblasts of garnet and tourmaline. Location: stope 8/1100 lift 8.

Figure 4.13. Photographs showing the nature, textures and features in the LOB massive sulphide: (a) massive sulphide rock with banding of pyrrhotite and quartz and disseminated galena within bands (b) massive sulphide rock with massive texture and galena-rich mylonite developed along the contact with garnet quartzite. Location: stope 13/0700 lift 10.

Figure 4.14. Down-plunge projection showing the variation of CuX100/(Cu+Pb+Zn) within LOB massive sulphide rock. Cu decreases from west to east (modified after Smith, 1989; used with permission). Compare with Figure 4.2.

Figure 4.15. Position of faults on down plunge projection. Compare with Figure 4.2.

Figure 5.1. Foliated garnet-biotite-sillimanite-muscovite-quartz schist of the US. Note overgrowth of muscovite (Musc) on biotite (Bio). Fine-grained mica, sericite (Ser), cross-cuts coarser grained euhedral muscovite and has overgrown quartz (Qtz) grains (Sample BHS22).

Figure 5.2. Photomicrograph of fine-grained garnet (Grt) in mm-thick microbands showing garnet-rich and quartz-rich bands. Note coexisting dark green Ba-rich biotite (Bio) and magnetite (Mgt). Apatite (Ap) appears similar to garnet (Grt) but is colourless.

Figure 5.3. Photomicrograph of poikiloblastic magnetite (Mgt) in garnet-rich iron formation mesoband. Other minerals present are quartz (Qtz), apatite (Ap) and barite (Ba).

Figure 5.4. Ba-rich biotite (Bio) occurring as discrete grains adjacent to garnet (Grt) and quartz (Qtz) in garnet-rich mesoband.

Figure 5.5. (a) Photomicrograph showing alignment of amphibole (Amph) and olivine (Ol) in amphibole-rich iron formation mesoband. Opaque exsolution in amphibole revealed no compositional difference in microprobe analysis. Quartz (Qtz) encloses magnetite (Mgt) in the bottom right corner. (b). Smooth grain-boundaries between amphibole (Amph) and olivine (Ol) indicating equilibrium texture.

Figure 5.6. Photomicrograph of an aggregate in massive sulphide rock with garnet (Grt), tourmaline (Trm), gahnite (Ghn), sphalerite (Sph) and biotite (Bio).

Figure 5.7. Photomicrograph of garnet quartzite (sample TS13) showing clusters of garnet (Grt), coarser grained quartz (Qtz), sillimanite (Sill) and minor biotite (Bio).

Figure 6.1. Compositional variation with respect to (a) Fe, Mn, Ca, and (b) Fe, Mn, Mg of garnets in various rock-types. Each data point represents the average of the analyses in a single sample. (Symbols for rocks: triangle- amphibole iron formation mesoband, open square- garnet iron formation mesoband, diamond- undifferentiated schist, filled square- quartz magnetite iron formation, filled circle- massive sulphide rock, open circle- ferruginous and garnet quartzites).

Figure 6.2. Plots of mole % almandine versus (a) mole % spessartine and (b) mole % pyrope for selected garnet core and rim compositions. No preferred enrichment or depletion of cations was found within garnet of different iron formation mesobands.

Figure 6.3. Histograms showing the difference between core and rim compositions for the mole % almandine, spessartine and pyrope in garnet. The negative values reflect rim compositions are enriched in the component relative to the core and vice versa for the positive values.

Figure 6.4. Compositional variation in mole % almandine, spessartine and pyrope of garnets for (a) across garnet-rich iron formation mesoband [sample BHG4], (b) across millimetre thick microbands in amphibole-magnetite iron formation [sample TS15] and (c) across millimetre thick garnet-quartz microbands- [sample 5/1200].

Figure 6.5. Compositional variation of mole % spessartine of garnet within different rock-types in boreholes BHU 1917, BHU 1891 and BHU 2609. (Symbols in legend: S-undifferentiated schist, Q+GQ - quartzite and garnet quartzite, FQ - ferruginous quartzite, AMIF - amphibole magnetite iron formation, QMIF - quartz magnetite iron formation, MSR - massive sulphide rock, GMIF - garnet magnetite iron formation). Symbols in figure: IS - Intermediate Schist, US - Footwall Schist, HS - Hangingwall Schist.

Figure 6.6. Compositional variation (mole % spessartine) of garnet in garnet iron formation mesobands plotted on down-plunge projection of LOB. Compare with Figure 4.2.

Figure 6.7. Compositional variation of wt.% MnO in whole rock against mole % spessartine of garnet for amphibole and garnet iron formation mesobands.

Figure 6.8. Ternary diagram showing compositional variation in atomic proportions Fe^{2+}, Mn and Mg of grunerite within AMIF. Each point represents the average of the analyses in a single sample.

Figure 6.9. Plots of Fe^{2+} versus (a) Mg and (b) Mn of grunerite core and rim compositions. No preferred enrichment or depletion of the cations are shown.

Figure 6.10. Compositional variation in Fe^{2+}, Mn, and Mg of grunerite for (a) across amphibole iron formation mesoband [sample BHA9] and (b) across millimetre-thick microbands [sample TS15].

Figure 6.11. Compositional variation in atomic proportions Fe^{2+}, Mn and Mg of grunerite within different rock-types in boreholes BHU 1917, BHU 1891 and BHU 2609. (Symbols in legend: S-undifferentiated schist, Q+GQ - quartzite and garnet quartzite, FQ - ferruginous quartzite, AMIF - amphibole magnetite iron formation, QMIF - quartz magnetite iron formation, MSR - massive sulphide rock, GMIF - garnet magnetite iron formation). Symbols in figure: IS - Intermediate Schist, US - Footwall Schist, HS - Hangingwall Schist.

Figure 6.12. Compositional variation in atomic proportion Mn of grunerite within amphibole iron formation mesobands plotted on down-plunge projection of LOB. Compare with Figure 4.2.

Figure 6.13. Ternary diagram showing compositional variation of mole % fayalite (Fa), tephroite (Tep) and

forsterite (Fo) of LOB olivine. Dashed line represents compositional field of fayalite from the Pegmont deposit, Australia (Vaughan and Stanton, 1986).

Figure 6.14. Plot of mole % fayalite versus mole % tephroite for core and rim compositions of olivine. No preferred enrichment or depletion of cations are shown.

Figure 6.15. Diagrams showing the variations in mole % fayalite, tephroite and forsterite of olivine (a) across amphibole iron formation mesoband [sample BHA9] and (b) across millimetre scale microbands [sample TS15].

Figure 6.16. Compositional variation in mole % tephroite of olivine plotted on down-plunge projection. Compare with Figure 4.2.

Figure 6.17. Compositional variation with respect to atomic proportions Fe^{2+}, Mn and Mg of orthopyroxene and pyroxferroite.

Figure 6.18. Plot of atomic proportions of interlayer cations showing approximately 1:1 variation of Ba with remaining cations. Sample points include only Ba-rich biotite from the garnet (square) and amphibole (triangle) iron formation mesobands.

Figure 6.19. Plot of atomic proportions according to the substitution scheme $K^{+} + 3(Mg,Fe)^{2+} + 3Si^{4+} = Ba^{2+} + 2Ti^{4+} + 3Al^{3+}$, showing approximately 1:1 correspondence. Sample points include only Ba-rich biotite from the garnet (square) and amphibole (triangle) iron formation mesobands.

Figure 6.20. Plot of wt.% F versus X_{Mg} = Mg/(Mg+Fe) for biotite in different rock types. (Symbols for rocks: open square- undifferentiated iron formation mesobands, diamond- undifferentiated schist of the Ore Schist Formation, filled circle- massive sulphide rock, open circle- ferruginous and garnet quartzites).

Figure 6.21. Compositional variation of X_{Mg} = Mg/(Mg+Fe) and wt.% F in biotite of rock-types for boreholes BHU 2609 and BHU 1917. (Symbols: S-undifferentiated schist, Q+GQ - quartzite and garnet quartzite, FQ - ferruginous quartzite, AMIF -amphibole magnetite iron formation, QMIF - quartz magnetite iron formation, MSR -massive sulphide rock, GMIF - garnet magnetite iron formation). Symbols in figure: IS - Intermediate Schist, US - Footwall Schist, HS - Hangingwall Schist.

Figure 6.22. Plot of atomic proportion Ba against wt.% F. The Ba-rich biotite is more F-rich than the Ba-poor, with little overlap in compositions. (Symbols for rocks: same as Figure 6.19).

Figure 6.23. Compositional variation with respect to pure gahnite, spinel, hercynite for average analyses of zincian hercynite from the LOB in various rock-types. (Symbols for rocks: square- QMIF, filled circle- massive sulphide rock, open circle- garnet quartzite, triangle- schist, cross- garnet-rich aggregates within massive sulphide rock) Dashed line and dotted lines represents world wide compositions of gahnite in massive sulphide deposits and aluminous-rich sediments, respectively, (Spry, 1987; Spry and Scott, 1986).

Figure 6.24. Compositional variation with respect to ZnO versus (a) FeO and (b) MgO for zincian hercynite in various LOB rock-types. (Symbols: the same as in Figure 6.22).

Figure 6.25. Schematic stratigraphic column showing the compositional variation of the ZnO in ferroan gahnite. (Abbreviations: IS - Intermediate Schist, MMIF -massive magnetite iron formation, GQ - garnet quartzite, IF - undifferentiated iron formation, US - Footwall Schist).

Figure 6.26. Tourmaline compositions for LOB rocks plotted on a (FeO-MgO-Na_2O) ternary diagram. Superposed are tourmaline compositional fields for (1) granitoids after Powell (1968) and Nieve (1974), (2) Mine sequence, Broken Hill, Australia (Plimer, 1983) and (3) Appalachian-Caledonide massive sulphide deposits after Taylor and Slack (1984). (Symbols for rocks: filled circle - massive sulphide rock, filled square - massive magnetite iron formation).

Figure 6.27. Compositions of sphalerite in the LOB shown as mole % of ZnS, FeS and MnS. Dashed line

represents the compositional field for sphalerite from Gamsberg deposit (Rozendaal and Stumpfl, 1984).

Figure 6.28. Histograms representing compositions of sphalerite expressed as mole % ZnS, FeS, MnS and CuS.

Figure 6.29. Plot of mole % FeS versus CuS for sphalerite. The solid line represents the ZnS-$CuFeS_2$ boundary, the dashed line indicates the field of primary sphalerite and the double dashed line indicates the path of supergene alteration for the formation of secondary sphalerite (De Waal and Johnson, 1981).

Figure 6.30. Ternary plot of (FeO_{Tot}-TiO_2-MnO) showing compositional variation of oxide minerals in the LOB.

Figure 7.1. Harker binary plots of major element chemistry for garnet-rich mesobands (squares) and amphibole-fayalite-rich mesobands (triangles).

Figure 7.2. Harker binary plots of trace element chemistry for garnet-rich mesobands (squares) and amphibole-fayalite-rich mesobands (triangles).

Figure 7.3. Plot of first two principal component weights for selected major and trace elements.

Figure 7.4. Ternary plot of Si:Al:(Fe+Mn) for bulk rock compositions of garnet-rich mesobands (squares) and amphibole-rich mesobands (triangles). Fields 1 and 2 are for iron-stones and iron formations, respectively, (James, 1969). Field 3 represents combined data from Rozendaal (1982) and Moore (1989) for iron formations in Namaqualand. Fe is presented as Fe total.

Figure 7.5. Bivariate plot of Si versus Al of LOB silicate-rich mesobands, garnet-rich (squares) and amphibole-rich (triangles). Also plotted are fields for Lake Superior iron formation (solid line) (after Gross and McLeod, 1980), iron-stones (dash dot line) (Kimberley, 1979), and different types of Fe-Mn deposits (dashed lines) (Crerar, 1982).

Figure 7.6. Ternary plot of Fe:Six2:Mn showing the positions of the silicate-rich mesobands, garnet-rich (squares) and amphibole-rich (triangles) of the LOB relative to the fields of hydrothermal Fe-rich crusts (1), East Pacific Rise metalliferous sediments (2), hydrogenous Fe-Mn crusts (3), Mn nodules (4) and hydrothermal Mn-rich crusts (5) (Toth, 1980).

Figure 7.7. Ternary plot of Fe:(Co+Ni+Zn)x10:Mn showing the positions of the silicate-rich mesobands, garnet-rich (squares) and amphibole-rich (triangles) of the LOB relative to the fields of hydrothermal crusts (1), East Pacific Rise metalliferous sediments (2), hydrogenous enriched sediments (3), Fe-Mn crusts (4) and Red Sea metalliferous sediments (5), (after Bonatti et al., 1972; Toth, 1980)

Figure 7.8. Plot of Fe/Ti versus Al/(Al+Fe+Mn) showing the positions of the garnet-rich mesobands (squares) amphibole-rich mesobands (triangles), Ore Formation schists (Lipson, 1990) (dashed line) and amphibolite (Reid et al., 1987b) (solid line) relative to the relative to the mixing curve for metalliferous sediment and terrigenous matter (upper curve) and oceanic tholeiite (lower curve) (modified after Barrett, 1981). The relative positions of Red Sea metalliferous sediment (RS), East Pacific Rise metalliferous sediment (EPR), pelagic clay (PC), terrigenous matter (TM) and oceanic tholeiite (OT).

Figure 7.9. Plot of Zr versus Cr for garnet- (squares) and amphibole-rich (triangles) iron formation mesobands compared to fields for hydrogenous (dashed line) and hydrothermal (solid line) metalliferous sediments (after Marchig et al., 1982).

Figure 7.10. Plot of Y/P_2O_5 for garnet- and amphibole-rich iron formation mesobands compared to fields for hydrogenous (dashed line) and hydrothermal (solid line) metalliferous sediments (after Marchig et al., 1982).

Figure 7.11. Plot of La versus Ce for garnet- and amphibole-rich iron formation mesobands compared to sea-water ratios (solid line) and the lower limit of hydrogenous marine sediments (dashed line) (after Toth, 1980).

Figure 7.12. Ternary plot of (SiO_2x0.73)-Al_2O_3-(F_2O_3+TiO_2+CaO) showing positions of pegmatite (filled

LIST OF TABLES

ABSTRACT

The Broken Hill deposit, Aggeneys, is a metamorphosed stratiform Cu-Pb-Zn-Ag sulphide deposit situated in the mid-Proterozoic supracrustal sequence of the Bushmanland Subprovince in the Namaqualand Metamorphic Complex. The deposit comprises two superposed orebodies, each consisting mainly of massive sulphide lenses and iron formation which are hosted within a metapelitic schist close to major quartzite horizons. This study is concerned with the tectonically lower orebody (LOB). The iron formation is magnetite-rich and contains varying proportions of (Fe,Mn)-rich silicates (garnet, amphibole, olivine, orthopyroxene, pyroxenoid), quartz and Cu-Pb-Zn-sulphides. These minerals occur in mm- to 5 cm-thick bands and are often traceable over tens of metres. The well preserved banding is considered to represent bedding.

Five different varieties of silicate-rich mesobands in the iron formation can be distinguished based on the predominant mineral assemblage: (a) amphibole-olivine-quartz +/- garnet, (b) amphibole-quartz, (c) garnet-apatite-quartz +/- amphibole, (d) garnet-apatite-quartz-orthopyroxene, (e) pyroxferroite-quartz +/- amphibole and (f) quartz. These rocks all contain magnetite, and Ba-rich biotite is common but is not always present.

Silicate-rich mesobands of types (a), (b) and (c) were investigated in greater detail. The amphibole- and garnet-rich mesobands reveal no consistent chemical comparisons with silicate facies of 'Algoma' and 'Lake Superior' iron formations. Similarly, garnet- and amphibole-rich mesobands have major element contents which are inconsistent with Mn-rich and Mn-poor iron formation bands from Satnuru, India, respectively. Amphibole mesobands are considered as "immature" submarine chemical precipitates enriched in Fe, Mg, Cu and Co, whereas garnet mesobands are considered as "evolved" submarine chemical precipitates enriched in Mn, Ca, P, Pb, Ba, with significant detrital contamination of Ti, Al, Zr, Cr, Y, V, Nd, La and Ce in the latter.

Peak metamorphic P-T conditions of the Broken Hill deposit, constrained by Waters (1987) using phase equilibria for the surrounding schists, are at the upper amphibolite facies (660 ^{0}C and 4 kb). Garnet-biotite geothermometry, using the calibrations correcting for Fe-Mn-Mg-Ca mixing in garnet, yielded a favourable temperature estimate with respect to these phase

equilibria. However, corrections for Ti and Al mixing in biotite gave a spuriously low temperature. Sphalerite geobarometry yielded pressures of 10.2 - 11.3 kb, which is inconsistent with the pressure estimate obtained from the phase relations. The phase equilibria of silicate-rich iron formation were modelled in the Fe-Mg-Mn-Si-Al-O-H system. At the P-T conditions estimated for Broken Hill, the coexisting phases in assemblages (a) and (c) were stable due to significant substitution of Mn for Fe. In assemblage (b), the reluctance of amphibole to breakdown to form olivine and quartz, is due to the higher Mg content in amphibole ($X_{Mg} > 0.26$). Assemblages (d-e) result from the reduction in the activity of Fe which caused pyroxene minerals to be stable at lower pressures than predicted by phase diagrams for Fe-endmembers. The F content in biotite varies as a function of X_{Mg} rather than controlled by the activity of HF in the metamorphic fluid. Estimates of the f(HF) in the fluid are approximately 0.4 bars for the schist, 1.6 bars for the garnetiferous quartzite, 4.6 bars for garnet-rich mesobands, and 9.0 for amphibole-rich mesobands. The difference in f(HF) between iron formation bands, the schist and the garnet quartzite, indicates a chemical gradient with respect to HF existed. The preservation of the HF-chemical gradient reflects no movement of large volumes of fluid through the Lower Orebody after the formation of biotite.

The LOB behaved largely as a closed system with respect to the non-volatile species during metamorphism and consequently the present chemical pattern reflects to a great extent the original chemical system. The precursor minerals are interpreted to be similar to those associated with the Red Sea geothermal brines. The Fe-rich amphibole mesobands were probably derived mainly from a hydrous Fe-silicate precursor (e.g Fe-smectite and Fe-montmorillonite) whereas the Mn-rich garnet mesobands were most likely derived from a Mn-rich chlorite precursor (e.g. chamosite).

The silicate-rich iron formation mesobands are interpreted to have a submarine exhalative origin and to represent chemical precipitates of metalliferous brines. Garnet-rich mesobands formed under increasingly aerobic conditions whereas amphibole-rich mesobands formed under less aerobic conditions than the garnet mesobands. More than one exhaling vent might be necessary to explain the spatial distribution of garnet and amphibole iron formation mesobands.

ACKNOWLEDGEMENTS

This project was completed part-time over three years and during this period there are numerous persons to whom the author is indebted. The management of Black Mountain Mineral Development Company Limited is thanked for their permission and the funds provided for the analytical costs which made this research possible. The author is indebted to Dr. Hartwig Frimmel of the University of Cape Town who supervised the project. Dr. Frimmel's assistance throughout this thesis will remain to his credit and to my benefit. The author is grateful to Prof. John Moore of Rhodes University for his assistance in proposing the project, his supervision during the initial part of the thesis and his continued support. Dr. Pete Smith of Black Mountain Mineral Development Company Limited is acknowledged for his useful discussions and reviewing several chapters. The technical assistance on the microprobe analyser was provided by Dick Rickard of the University of Cape Town, which is much appreciated. Chandra Harris of the University of Cape Town is thanked for her assistance with the XRF analyses. Hendrik Cloete is thanked for his contribution by drafting and enhancing the quality of all the diagrams.

To my wife, Susan, for her patience and support throughout the duration of the study. It is immensely appreciated.

ABBREVIATIONS

Alm	- almandine
AMIF	- amphibole magnetite iron formation
Amph	- amphibole
And	- andalusite
Andr	- andradite
Bio	- biotite
BGZ	- Biotite Graphite Zone
Chl	- chlorite
Crd	- cordierite
Fa	- fayalite
FM	- Formation
Fo	- forsterite
Fs	- ferrosilite
Gal	- galaxite
Ghn	- gahnite
GMIF	- garnet magnetite iron formation
GQ	- garnet quartzite
Grs	- grossular
Grun	- grunerite
Hc	- hercynite
HS	- Hangingwall Schist
IS	- Intermediate Schist
Kfs	- K-feldspar
LOB	- Lower Orebody
MMIF	- massive magnetite iron formation
MSR	- massive sulphide rock
Musc	- muscovite
nd	- not detected
ND	- not determined
NMC	- Namaqualand Metamorphic Complex
NW	- north-west
OES	- Ore Equivalent Schist
PCA	- principal component analyses
Prp	- pyrope
Qtz	- quartz
QMIF	- quartz magnetite iron formation
SE	- south-east
Sill	- sillimanite
Spl	- spinel
Sps	- spessartine
Tp	- tephroite
UOB	- Upper Orebody
US	- Upper Footwall schist
Vol.%	- volume percent
Wt.%	- weight percent

1.INTRODUCTION

Broken Hill is one of four major conformable Cu-Pb-Zn-Ag sediment hosted sulphide deposits situated in a 10 x 30 km area centred on Aggeneys, approximately 110 km north-east of Springbok, South Africa (Fig 1.1). The stratiform ore bodies occur at similar stratigraphic positions in a metapelitic schist sequence close to major quartzite horizons. This sequence forms part of the supracrustal rocks within the mid-Proterozoic Bushmanland Subprovince of the Namaqua Province (see Chapter 2).

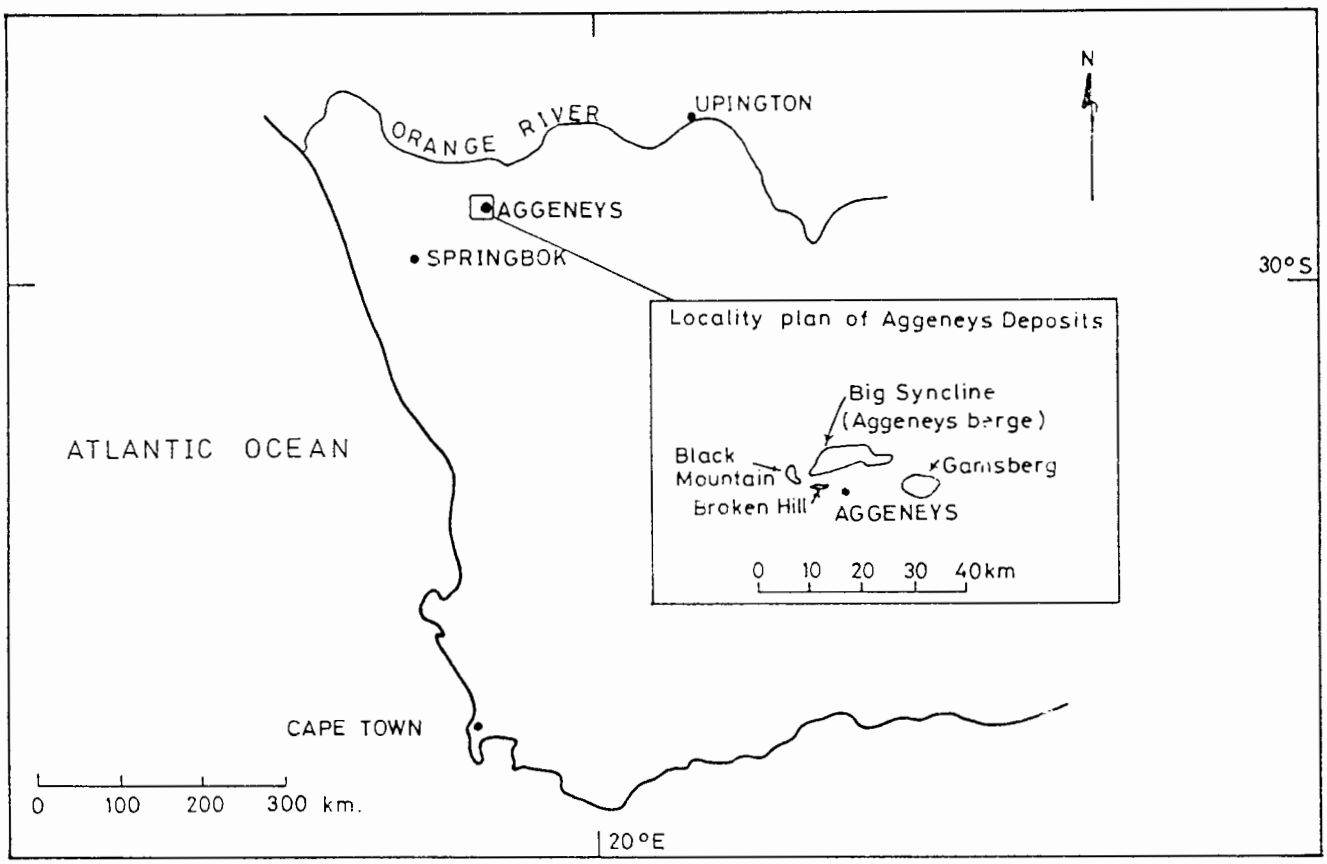

Figure 1.1. Map showing the locality of Aggeneys in the Northwest Cape Province, South Africa, with the insert showing the location of the Cu-Pb-Zn-Ag deposits.

The Aggeneys base-metal deposits can be classified as 'Broken Hill-type' (sensu Beeson, 1990). These are intermediate between volcanic- and sediment-hosted massive sulphide deposits. The characteristics of the 'Broken Hill-type' described by Beeson (1990) are:

(1) The base-metal deposits occur in geological settings where the lithological variation in the sequence from the underlying country rocks to the ore zone is noted by a change from quartzo-feldspathic gneisses, meta-volcanic rocks, quartzites to metapelites.
(2) Rocks which have been interpreted to have a volcanic origin are more common lower in the sequence than within the mineralized horizon.
(3) The stratiform orebodies are associated with a predominance of "oxidized rock-types" such as iron formations, metachert, gahnite- and garnet-bearing quartzites and tourmalinites rather than "reduced rock-types" (e.g. pyrite-bearing rocks). The varied nature of the former often have a complex association with the deposits.
(4) Facies variations are common within the iron formations.
(5) The distribution of the base-metal mineralization commonly exhibits vertical and lateral zonations.
(6) The setting of the deposits can be interpreted to have formed within basins which occur in intracratonic, rift-related environments.
(7) The deposits have been affected by metamorphic events associated with high temperature and low pressure which often reveal an anticlockwise P-T path.
(8) The deposits formed mainly within a restricted time range between 1900 and 1600 Ma.

Beeson (1990) has subdivided the 'Broken Hill-type' deposits into two sub-types where the mineralization is hosted either in calc-silicate rocks or banded iron formations. Examples of the former, as suggested by Beeson (1990) are the main orebodies of Broken Hill, Australia. Sulphide enrichment within (Fe-Mn-) silicates-quartz-magnetite assemblages in iron formations has been recognized in several base metal deposits. According to Beeson's classification, metamorphosed Proterozoic examples of such deposits are the Pegmont deposit, Australia (Vaughan and Stanton, 1986), Aggeneys-Gamsberg deposits, Namaqualand (Ryan et al., 1986; Rozendaal, 1982), Dammberg, Bergslagen district, Sweden (Ripa, 1988) and the Boquira deposit, Bahia State, Brazil (Carvalho et al., 1982).

Cu-Pb-Zn mineralization in 'Broken Hill-type' deposits has been considered by most authors to have formed syngenetically with the associated sediments. Similarly, sediment-hosted deposits like Mount Isa, Navan, McArthur River, Rammelsberg and Sullivan also have a syngenetic origin (Russell et al., 1981). Some of these large Pb-Zn deposits (e.g. HYC at

McArthur River, and Mount Isa, Australia), however, were concluded by Williams (1991) and Perkins (1991), respectively, to have an early diagenetic ore genesis. In the HYC deposit, the variation of $\delta^{34}S$ in pyrite versus that of galena and sphalerite indicate two generations of sulphide mineralization (Williams, 1991). Furthermore, the pyrite is mostly laminated whereas the galena and sphalerite are often diffuse. These features were used by Williams (1991) to interpret an early diagenetic model in which the mineralizing fluids infiltrated unconsolidated sediments.

In the syngenetic models, the mineralization involves the discharge of evolved metalliferous saline fluids on to the sea floor. The exhaled fluids were vented through faults or fractures and on cooling, they formed sulphide precipitates which were coeval with the (Fe-Mn-Si)-rich chemical sediments. The intimate association of sulphide, oxide and silicate minerals in micro- (mm), meso- (cm) and macro- (m) thick bands is likely the result of the interplay between exhalative activity, the response of chemical precipitation with respect to oxidizing and reduced conditions and the deposition of fine-grained detrital sediment.

At Broken Hill, Aggeneys, sulphide mineralization of economic importance occurs as two superposed horizons, each consisting of massive sulphide lenses and banded iron formations. The two stacked mineralized units are part of an overturned fold limb, and are referred to as the Lower Orebody (LOB) and the Upper Orebody (UOB) in their tectonic position. Ryan et al. (1986) have shown that the Broken Hill deposit displays many characteristics common to deposits of exhalative origin.

The first detailed study of the regional setting of the Aggeneys deposits was carried out by Joubert (1971). Ryan et al. (1986) have examined the stratigraphy, structure and metamorphism of the Cu-Pb-Zn-Ag deposits in the Aggeneys area. The structural setting of these deposits have been described by Colliston et al. (1989) in terms of sub-horizontal tectonics. A detailed study of the host rock-types to the Broken Hill deposit by Lipson (1990) emphasises the geochemistry of the metapelitic rocks that enclose the mineralized horizons and of the overlying quartzite horizons. Detailed documentations of the geology for the Big Syncline, Gamsberg and Black Mountain deposits have been presented by Lipson (1978), Rozendaal (1978) and Stedman (1980). Furthermore, Moore (1989) and Rozendaal (1982)

have examined the bulk compositions of numerous iron formations from these deposits and elsewhere in the supracrustal sequences of the Namaqua Province.

Previous geochemical examinations of the Broken Hill deposit have given no attention to the compositions of the individual iron formation bands. Two distinct and common types of silicate iron formation bands are garnet- and amphibole-rich. In order to use whole rock composition as a means to interpret the origin of metamorphosed banded iron formations, the chemical composition is required to remain unchanged by events subsequent to their formation as sediments. The rocks in the Aggeneys area have been subjected to regional metamorphic events under amphibolite facies conditions and consequently, any study attempting to make conclusions about the original environment using geochemistry as a tool, requires careful consideration of the effects of metamorphism. Thus, it is necessary to establish to what extent the rocks involved represented a closed system during metamorphism.

Few contributions to the mineral petrography and chemistry of the Broken Hill deposit have been made. De Waal (1974) has examined the mineralogy of Broken Hill deposit in terms of metallurgical beneficiation. Examination of the chemical heterogeneity of sphalerite was undertaken by De Waal and Johnson (1981). The formation of gahnite by desulphurisation reactions was applied to the Aggeneys deposits by Spry (1987) and Hicks (1988), and the existence of zincian hogbomite in the Aggeneys deposits has been recognized by Spry and Petersen (1989) to be a potential exploration guide for metamorphosed massive sulphide deposits. The presence of a Mn halo surrounding the Broken Hill deposit has been recognized by Stumpfl (1979) from the Mn content in garnet. Only a few compositions of silicate minerals from the Broken Hill deposit have been determined by Rozendaal (1982) and Hicks (1988). Sulphur isotope characteristics of pyrrhotite in massive sulphide rock and iron formation in the Broken Hill deposit have been examined by von Gehlen et al. (1983) and Smith (1990). Barr (1988) studied the genetic significance of Sr and Pb isotopes in barite.

Most previous studies of the Broken Hill deposit had little or no access to underground exposure. In recent years, a depth of over 500 metres has been reached in the mine where predominantly cut and fill mining methods are used. This method has the advantage of

exposing a continuum of the geology. In addition, detailed underground drilling has revealed additional information unavailable to previous interpretations. This has necessitated further examination of some aspects on the geology of the deposit. For example, a more detailed description of the rock-types, a re-evaluation of the interpretation of the structure and the effects of metamorphism on the deposit.

This study is concerned broadly with the mineralogy and composition of the LOB in light of its close association with iron formations. Examination of the mineral assemblages and their chemical compositions is carried out on the LOB rather than the UOB. The LOB body has been chosen due to the presence of well preserved banding and a greater proportion of (Fe-Mn)-silicate-rich bands in the iron formation.

More specifically, the aims of this project are:

- to document a detailed description of the LOB,
- to describe the mineral chemistry of the metamorphic assemblages within the LOB rock-types,
- to interpret the whole rock compositions of the silicate-rich iron formation bands,
- to use mineral paragenesis and phase relationships within the iron formation and schists to constrain the metamorphic conditions that have prevailed at this locality,
- to establish the precursor mineralogy of the iron formation bands prior to metamorphism,
- and finally to interpret the genesis of the silicate-rich iron formation bands.

2.REGIONAL GEOLOGY

The east-west trending Proterozoic Namaqua Province in the northwestern Cape is a polyphase deformed and medium-to-high grade metamorphosed gneissic terrane (Joubert, 1971). The western Namaqua Province contains 2000 Ma old heterogeneous basement rocks that underwent an early tectono-magmatic event at approximately 1750 Ma (Blignault et al., 1983; Moore et al., 1990). On a regional scale, the Namaqua Province is subdivided into tectonic subprovinces which show differences in metamorphic history, rock-types and structure, viz: the Gordonia, Richtersveld and Bushmanland Subprovinces (Hartnady et al., 1985; Joubert, 1986; Moore et al., 1990). Their spatial relationship, illustrated in Figure 2.1, is thought to be the result of a collision event during which a Bushmanland microcontinent accreted onto an active Richtersveld continental margin (Moore et al., 1990). During this period, sediments of the Gordonia Subprovince accumulated in a backarc basin between the Richtersveld 'arc' and the Kaapvaal craton (Moore et al., 1990).

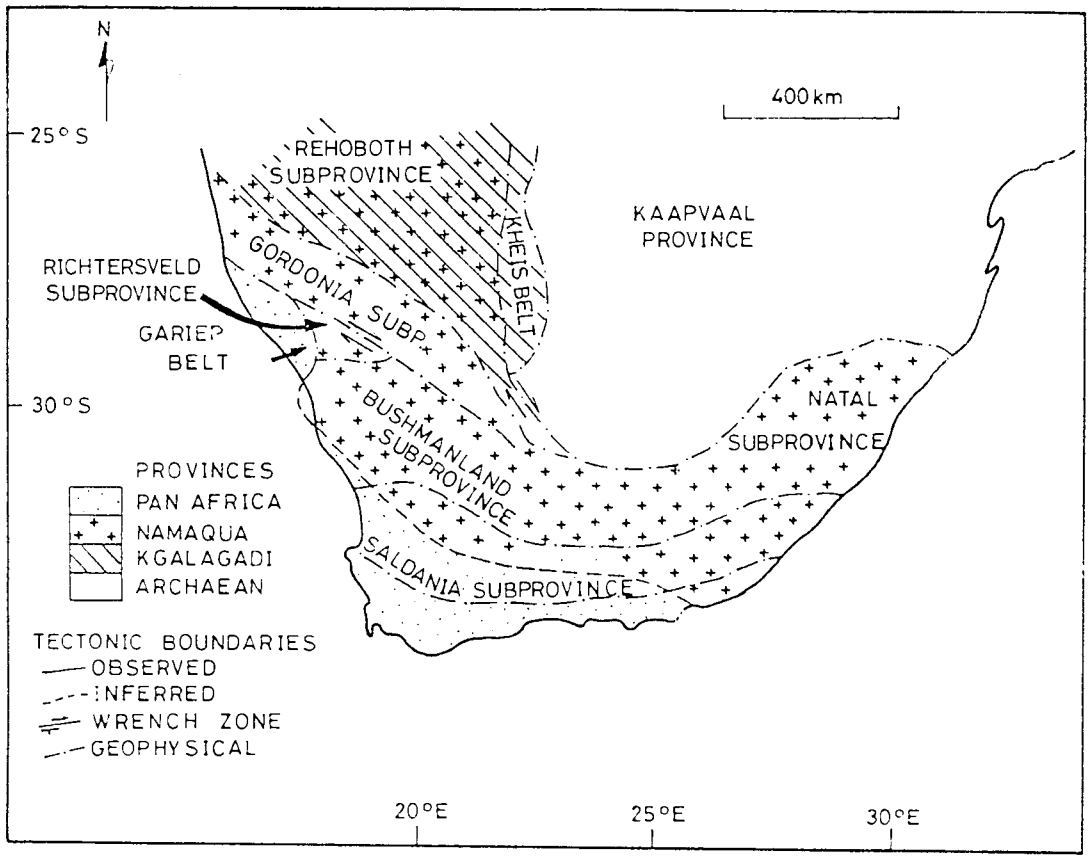

Figure 2.1. Map of Southern Africa illustrating the major provinces and subprovinces (after Hartnady et al., 1985).

Other workers (Praekelt et al., 1986; Colliston and Praekelt, 1988) have subdivided the Namaqua Province into several thrust-bound 'terranes' (Fig. 2.2) which broadly coincide with the terranes defined by Blignault et al., (1983).

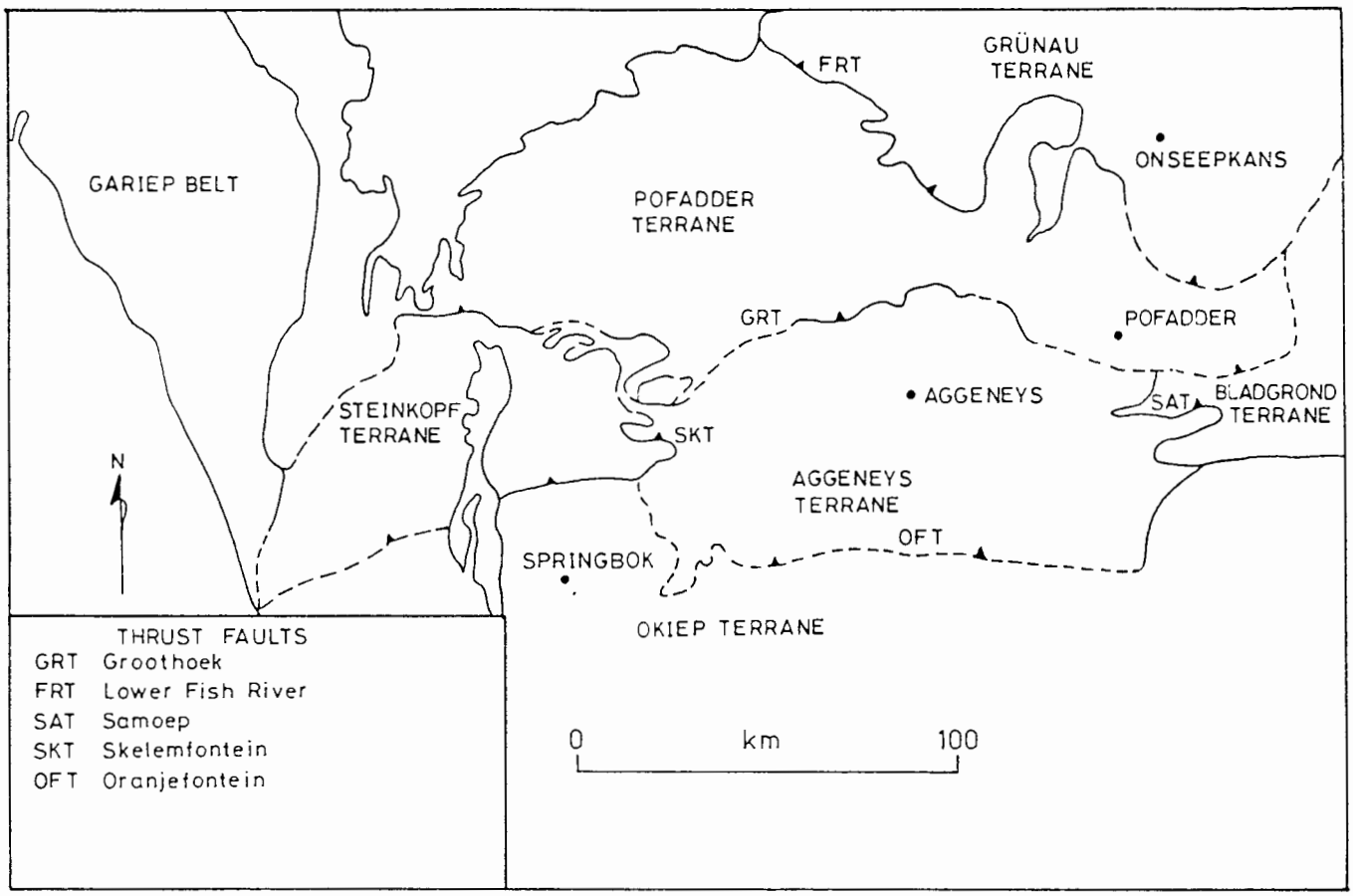

Figure 2.2. Map of Namaqua Province showing major subdivisions into fault bound "terranes" (modified after Colliston et al., 1989).

In the Bushmanland Subprovince, an extensive and relatively thin succession of younger mid-Proterozoic supracrustal rocks, referred to as the Bushmanland Group, overlies gneissic basement (Moore et al., 1990). The succession consists of a basal leucogneiss, predominantly metaquartzite/schist sequences and minor amphibolite which underwent subsequent tectonic reactivation at 1100 Ma (Moore et al., 1990). The Aggeneys base metal deposits, intimately associated with thin iron formation units, are located within a schist sequence of the Aggeneys Subgroup.

2.1.BASEMENT ROCKS

The central Richtersveld Subprovince occurs as a wedge between the Gordonia Subprovince to the north and the Bushmanland Subprovince to the south (Figs. 2.1 and 2.3). It is dominated by two basement components, an extrusive andesitic calc-alkaline meta-volcanic sequence, the Orange River Group, and intrusive I-type granitoids with a differentiated igneous suite of tonalite-granodiorite-granite compositions, the Vioolsdrif Igneous Suite (Reid, 1982; Reid et al., 1987a).

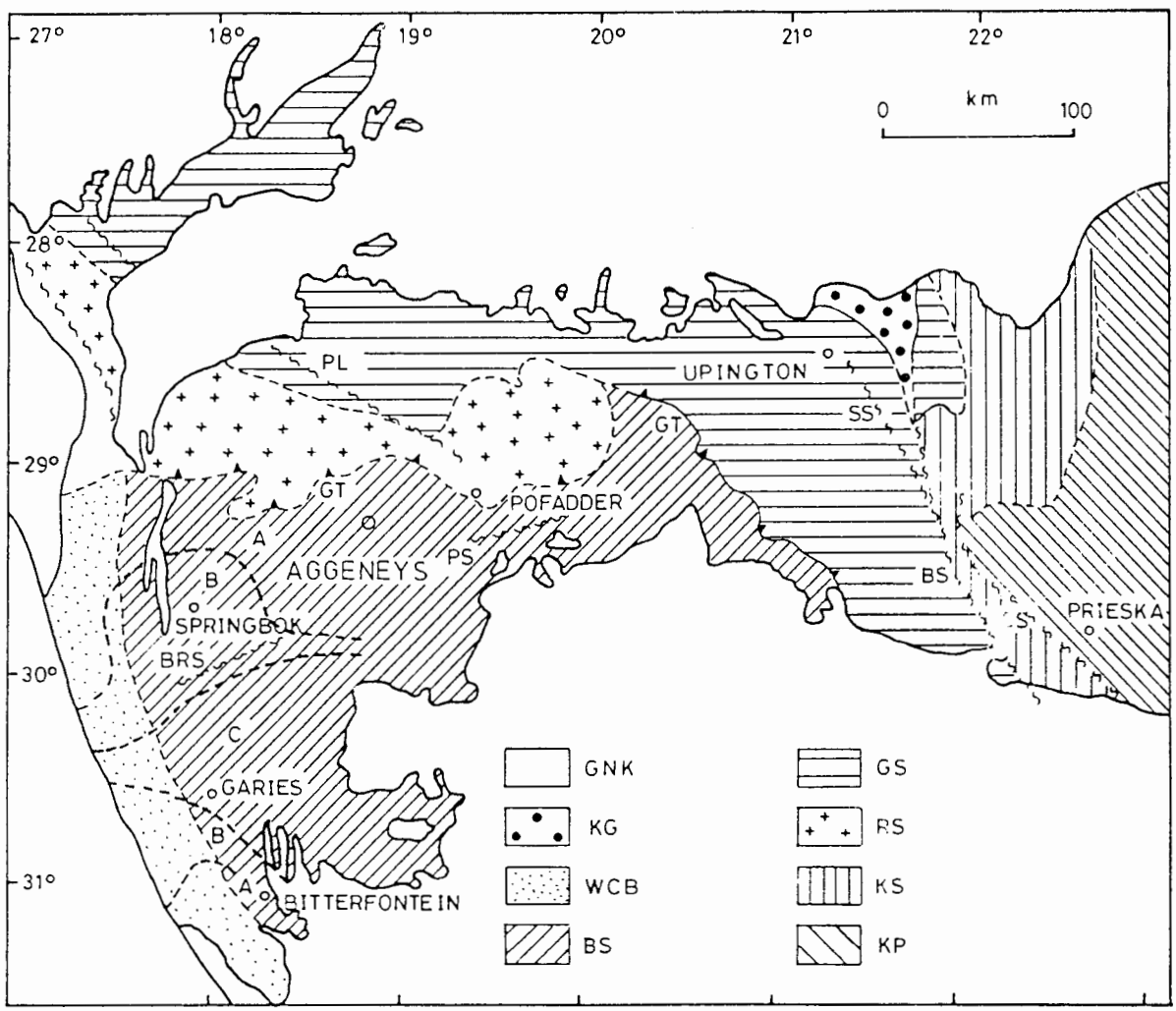

Figure 2.3. Subdivisions of the Proterozoic Namaqua Province into tectonic terranes of the Bushmanland, Richtersveld and Gordonia Subprovinces (after Hartnady et al., 1985). Superimposed are the metamorphic zones in western Namaqualand (after Waters, 1986) : A= upper granulite facies, B= lower granulite facies and C= upper amphibolite facies. Symbols in legend: GNK= Gariep, Nama, Karoo and surficial deposits, KG= Koras Group, WCB= West Coast Belt, BS= Bushmanland Subprovince, GS= Gordonia Subprovince, RS= Richtersveld Subprovince, KS= Kheis Subprovince, KP= Kaapvaal Subprovince. Shear zones: BSR= Buffels River, PS= Pofadder Shear, PL= Pofadder Lineament, SS= Strausberg, DS= Doornberg, BS= Brakbos, GT= Groothoek Thrust.

Consistent whole rock Rb-Sr, Pb-Pb and Th-Pb ages of 1996 +/- 15 Ma (Reid, 1979) are interpreted as the age of extrusion of the meta-volcanic Orange River Group. A Rb-Sr whole rock age of 1900 +/-30 Ma (Reid, 1979; 1982) and a U-Th-Pb zircon age of 1870 +/-20 Ma (Welke et al., 1979) have been determined for the Vioolsdrif Igneous Suite. For the latter intrusive granitoid suite, isotopic and geochemical evidence reveals that these rocks represent new crustal material derived from mantle differentiation (Reid and Barton, 1983). Reid (1982) suggests a two stage emplacement history for the Vioolsdrif granitoid suite. After a significant hiatus of 170 Ma (Reid, 1982), for which there is little field evidence (Blignault et al., 1983), the earlier basic to intermediate rocks were intruded by more felsic rocks at 1730 +/-20 Ma (Reid, 1982; Reid and Barton, 1983). Contrary to this model, Welke et al. (1979) suggest that the entire Vioolsdrif Suite was emplaced at 1885 Ma, and subsequent migmatization reset certain rock types at 1740 Ma.

The northerly basement component within the Gordonia Subprovince consists predominantly of metapelitic rocks of the Grunau Sequence (Blignault et al., 1983). These sediments are thought to have originally formed within a back arc basin between the Richtersveld active margin and the Kaapvaal Craton (Moore et al., 1990). The age of this basement is uncertain. However, on a regional scale, metasediments of the Grunau Sequence are intercalated with correlatives of meta-volcanic rocks of the Orange River Group. This suggests that a primary interlayering is more likely than tectonic stacking (Toogood, 1976; Blignault et. al., 1983). To the south-east of Kakamas, the Korannaland Sequence of the Gordonia Subprovince is developed which comprises a variety of rock types such as quartzo-feldspathic gneisses, calc-silicate assemblages, kinzigites, amphibolites and quartzites (SACS, 1980; Stowe, 1983). Because of distinctive assemblages of the Korannaland Sequence, the stratigraphic correlation for these rocks is uncertain (Joubert, 1986). Intense structural deformation is evident including north-west shear zones (Stowe, 1983) with dextral movement greater than 100 km.

The southern component of the heterogenous basement, the Bushmanland Subprovince, is bound by the Richtersveld and Gordonia Subprovinces to the north, and the late-Proterozoic Gariep and Saldania Subprovinces to the west and south, respectively. The Bushmanland Subprovince is dominated by orthogneisses and minor enclaves of supracrustal units (Watkeys, 1986; Moore, 1989; Moore et al., 1990). In central and northern Bushmanland, it

comprises grey porphyroblastic and banded biotite gneisses (Moore, 1977; Watkeys, 1986), where it is referred to as the Achab Gneiss. Similar Pb-Pb ages for the basement gneisses in the Aggeneys and Namiesberg areas of 2020 +/-150 Ma have been determined by Welke and Smith (1984) for whole rock and by Armstrong et al. (1988) for single zircons. Watkeys (1986) suggested from the porphyroblastic texture of the Achab Gneiss occurring in regions of low strain and the presence of xenoliths, that this gneiss might have originated as a megacrystic granite, which intruded into a "pre-Bushmanland" sequence. Correlatives of the Bushmanland basement further west, in the vicinity of Steinkopf, are the grey gneisses of the Gladkop Suite for which a whole rock Rb-Sr age of 1825+/-70 Ma has been determined (Barton, 1983).

The basement rocks of the Bushmanland Subprovince and the Richtersveld Subprovince are separated by a tectonized zone characterized, in part, by a chain of mafic/ultramafic bodies (Joubert, 1986), known as the Wortel Belt or Groothoek thrust fault (Fig. 2.3) (Theart, 1980; Blignault et al., 1983; Watkeys, 1988). These two sub-provinces are considered to have accreted to the Kaapvaal Craton as a single unit at 1400-1200 Ma (Joubert, 1986).

2.2.SUPRACRUSTAL ROCKS

The supracrustal rocks in the western Namaqua Province have been subdivided by SACS (1980) into the Okiep and the Bushmanland Groups, to the west and east, respectively (Table 2.1). The supracrustal succession, to the east, in the Namiesberg-Gamsberg-Aggeneys area, is laterally extensive, relatively thin (< 1000 m) and consists of two distinct components, a lower basal sequence comprising leucogneiss and an upper sequence of metasediments and lesser amphibolite (Moore et al., 1990). These supracrustal rocks are considered by Watkeys (1986) to rest tectonically on the heterogeneous basement. As in the wider western Namaqua Province region, the supracrustal sequence of the Bushmanland Group starts with a lower leucocratic gneiss, the Hoogoor Suite. This leucogneiss, also termed Pink Gneiss Formation, is followed by a younger sequence of metasediments that comprises metapelitic schists, quartzites, iron formations, metaconglomerates and amphibolites. In the Aggeneys area, this sequence is collectively termed the Aggeneys Subgroup. In the Namiesberg-Swartkoppies area, almost monomineralic sillimanite and sillimanite corundum rocks occur as irregular 1-100 metre stratabound lenses. Stratigraphically, these lenses are locally developed at the base

of the metapelitic schist in the Namies Schist Formation close to the leucogneiss. These lenses and also laterally equivalent tourmalinite rocks, have been interpreted by Wilner et al. (1990, 1992) to have originated from the exhalation of hydrothermal fluids. According to Wilner et al. (1990), the peraluminous rocks originated by Al-enrichment prior to metamorphism from deposition of aluminous clays and hydroxides.

Amphibolites occur high up in the Aggeneys Subgroup. They have yielded a Sm-Nd isochron age of 1649 +/- 90 Ma, which provides a minimum age for the underlying metasediments and leucogneiss (Reid et al., 1987b).

Table 2.1. Lithostratigraphy of the supracrustal sequence of the Bushmanland Subprovince.

BUSHMANLAND GROUP				OKIEP GROUP	
(SACS, 1980)*		(Colliston et al., 1989)		(SACS, 1980)*	
Subgroup		Formation		Sugroup	
Pella	quartz-muscovite-schist, conglomerate	Koeris	quartz-muscovite-feldspar-schist, amphibolite and conglomerate	Een Riet	metasediments north of Steinkopf
	iron formation				
	metaquartzite	Hotson	gneiss, quartzite, schist iron formation	Khurisberg	metaquartzite and schists of the Okiep Copper Districts and environs
	schist	T'hamma-berg	muscovite-sillimanite-schist, quartzite		
Guadom	mafic gneiss with inetrcalated metasediments			Aardvark	metaquartzites and schist of the coastal plain east of Port Nolloth
		Skelmpoort	metaquartzite, quartz-muscovite-biotite-schist		
Hom	leucocratic gneiss with intercalated metasediments			Garies	undifferentiated grey gneisses of Namaqualand
		Witputs	metaquartzite with thin quartz biotite sillimanite schist		
Aggeneys	quartz-muscovite-schist and conglomerate				
	iron formation	Wortel	quartz-biotite-sillimanite-schist, metaquartzite, amphibolite and iron formation	Bitter-fontein	metaquartzite and schists of southern Namaqualand
	metaquartzite				
	schist				

* Subgroup names given to stratigraphic successions in different geographical areas.

Similar metasedimentary sequences are found in northern Bushmanland which extend into the Richtersveld Subprovince in the Goodhouse-Pella region. Previous schemes incorporate those Orange River rocks into various subgroups (Hom, Guadom and Pella) of a more extensive Bushmanland Group, which are represented in central Bushmanland by the Aggeneys Subgroup (SACS, 1980; Blignault, 1983). Other stratigraphic models of Praekelt et al. (1983) and van Aswegen et al. (1987) do not consider the quartzite/schist sequences to be correlatives of those further south but represent a thick sedimentary pile with repeated units of cyclic sedimentation or allochtonous slices of various sources.

Colliston et al. (1989) subdivide the supracrustal rocks in the Aggeneys-Haramoep area, into at least six stratigraphic units (Table 2.1). The succession of metasediments has been interpreted to represent an upward shallowing sequence. The sequence commences with deep-water sediments (the Wortel Formation) and ends with metaconglomerates and meta-volcanic rocks (the Koeris Formation). The sub-horizontal position of the stratigraphic units is explained by Colliston et al. (1989) to be more the result of horizontal tectonics than of original deposition. Their interpretation suggests that the supracrustal inselbergs east of Aggeneys represent large scale isoclinal structures, fold nappes and sheath folds (Colliston et al., 1989). Likewise, similar structures are found within the supracrustal rocks, west of Aggeneys, at Geselskapbank (Strydom and Visser, 1986).

The inselbergs at the Black Mountain, Broken Hill, Gamsberg and Big Syncline deposits, consist mostly of quartzite, schist and leucogneiss. In the Aggeneys area, these rocks form the greater part of a relatively thin (< 1000 m-thick) sequence. Using the succession of leucogneiss-schist-quartzite-schist, the stratigraphic sequence exposed at each inselberg can be interpreted as lateral correlatives of each other. The author has not examined similar quartzite/schist successions to the north of Aggeneys. Colliston et al. (1990) have included these successions as part of a thicker (> 2000 m) stratigraphic sequence. The latter stratigraphic scheme, which has several cycles of deposition, was suggested by Moore et al. (1990) to rely heavily on a "plethora of thrust faults" to account for discontinuities in the stratigraphy. This reservation is supported, based on the author's limited inspection of the stratigraphy in the Aggeneysberge. Evidence of shearing or the development of mylonites along some inspected thrust faults in the Aggeneysberge, as shown

on the geological map compiled by Colliston et al. (1986), is not apparent. Consequently, the relatively thin stratigraphic sequence of < 1000 m has been adopted in this study.

2.3.INTRUSIVE ROCKS

The intrusive rocks constitute a large proportion of the Bushmanland Subprovince (Fig.2.4),and can be categorized either as pretectonic, syntectonic or post-tectonic with

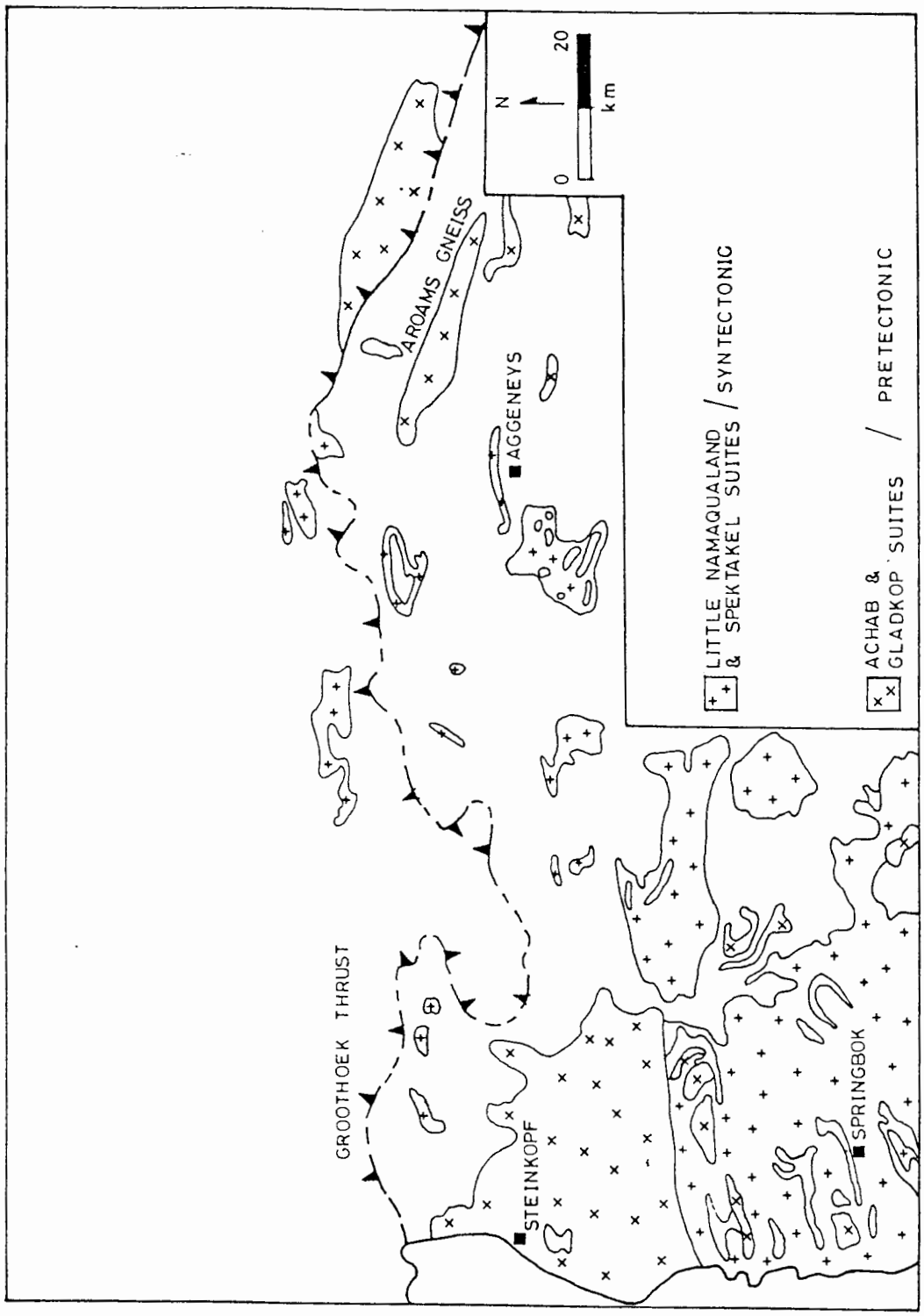

Figure 2.4. Map showing the distribution of intrusive rocks within the Bushmanland Subprovince (modified after Moore et al., 1990).

respect to the major structural event at 1100 Ma (Joubert, 1971; Blignault et al., 1983). In the Namiesberg area, east of Aggeneys, the pretectonic banded biotite gneiss (Achab gneiss) is thought to represent an early intrusive megacrystic granite (Watkeys, 1986), dated at 2020 Ma (Welke and Smith, 1984). The early syntectonic granitoids of the Little Namaqualand Suite (LNS) (SACS, 1980), are mostly augen gneisses of granitic composition (Blignault et al., 1983). These rocks occur pervasively over western Namaqualand and were emplaced syntectonically with respect to the main deformation event. In the Pella-Aggeneys area, the LNS is extensively developed and is referred to as the Aroams Gneiss. Other late syntectonic granites of the Spectakel Suite (SACS, 1980) are located in western Namaqualand (Fig. 2.4) and were emplaced during a late-to-post period with respect to the main deformation event (Clifford et al., 1975). The intrusive Cu-bearing noritoid rocks of the Koperberg Suite in the Okiep district comprise andesinite, diorite, norite and hypersthenite bodies. These are post-tectonic in relation to the major structural event and were emplaced at approximately 1070 Ma (Clifford et al., 1975)

2.4.TECTONOMETAMORPHIC EVOLUTION

Regionally, Joubert (1971) distinguished four major deformation events in the Namaqua Province. The reference to D1, D2, D3 and D4 is used in accordance with Joubert (1971) to describe the structural events. The main fabric-forming event is considered to be D2. Locally, however, there is evidence for an earlier D1 event found within the basement gneiss which is not seen in the overlying supracrustal rocks (Moore, 1977; Blignault et al., 1983). In addition, an earlier fabric expressed as small scale intrafolial isoclinal folds (F1) (Joubert, 1971) and rare inclusion trails in garnets (S1) (Waters, 1989) are found in the basement rock but not in the overlying Bushmanland Group. The D2 event is characterized by major recumbent isoclinal folds (F2), early thrusting and recrystallization of minerals in the pre-existing basement rocks at medium-to-high grade regional metamorphism (Joubert, 1971; Moore, 1977; Strydom and Visser, 1986). A striking feature of the D2 event is the parallelism between F2 fold axes and the conspicuous lineation expressed by mineral orientation, roding, boudins and mullions (Joubert, 1986). In the Aggeneys area, the F2 fold axes plunge to the north-east (Ryan et al., 1986). However, on a regional scale the attitude of F2 folds is dependent on their position within large structures formed subsequently. The ensuing and less intense D3 event is reflected by large scale open F3 folds and associated

shear zones which have modified the D2 structures. The F3 folds are open with north-dipping axial planes and shallow east-west trending plunges (Joubert, 1971). In the Aggeneys area, the D3 event formed a major asymmetric, synform with its fold closure to the west and plunges with a moderate angle to the north-east. The Broken Hill deposit is on the south limb of the structure, with Black Mountain some 6 km to the west, and Big Syncline situated along the central fold axis. The last structural event (D4) led to the development of north- and north-north-west- trending monoclinal F4 folds, and associated north-south faults and fracturing (Joubert, 1971).

Complex polyphase metamorphism in medium-to-high grade metamorphic rocks has been reported by some authors for the Bushmanland Subprovince and has been examined in considerable detail. Establishment of a tectonometamorphic scheme was first made by Joubert (1971). Further contributions from Joubert (1974), Clifford et al. (1975), Moore (1977), Lipson (1978), Blignault et al. (1983) and Jack (1980), reveal variable P-T conditions within the Bushmanland Subprovince in relation to several structural episodes. In contrast, Albat (1984) and Waters (1986, 1989) have only proposed one metamorphic event.

In the Bushmanland Subprovince, the first metamorphic paragenesis associated with the major regional metamorphic imprint M1 is syntectonic to post-tectonic with respect to D2 (Joubert, 1971; 1974; Clifford et al., 1975, Moore, 1977; Albat, 1984; Waters, 1986; 1989). Waters (1989) concludes that after the D2 event there was substantial prograde mineral growth in which peak conditions appear to have outlasted D3 and the emplacement of late tectonic granites of 1141+/- 22 Ma (Clifford et al., 1975).

Metamorphism associated with D1 is uncertain. Evidence for an earlier metamorphic event has, as yet, not convincingly been identified (reviewed by Moore, 1989) and it is further assumed that this event would likely be of lower metamorphic grade than the subsequent major thermal event (M1). Schematic plots of temperature versus time for the different interpretations for the tectono-metamorphic evolution of the Bushmanland Subprovince are illustrated in Figure 2.5. Joubert (1971) favours at least two separate prograde metamorphic events in western Namaqualand related to the D2 and D3 structures with a thermal trough between. Similarly, Moore (1977) provides textural evidence for a prograde metamorphic

event related to D2 and retrograde events related to D3 and D4 structures for the Namiesberg. In the granulite facies rocks at Kliprand, Albat (1984) recognizes textural evidence suggesting that the metamorphism proceeded via a single major prolonged thermal event M1 that reached its peak during D2. Several retrograde recrystallization episodes of restricted distribution are related to the cooling phase subsequent to the thermal peak. Albat (1984) supports this model due to the lack of evidence for any thermal trough between D2 and D3 events.

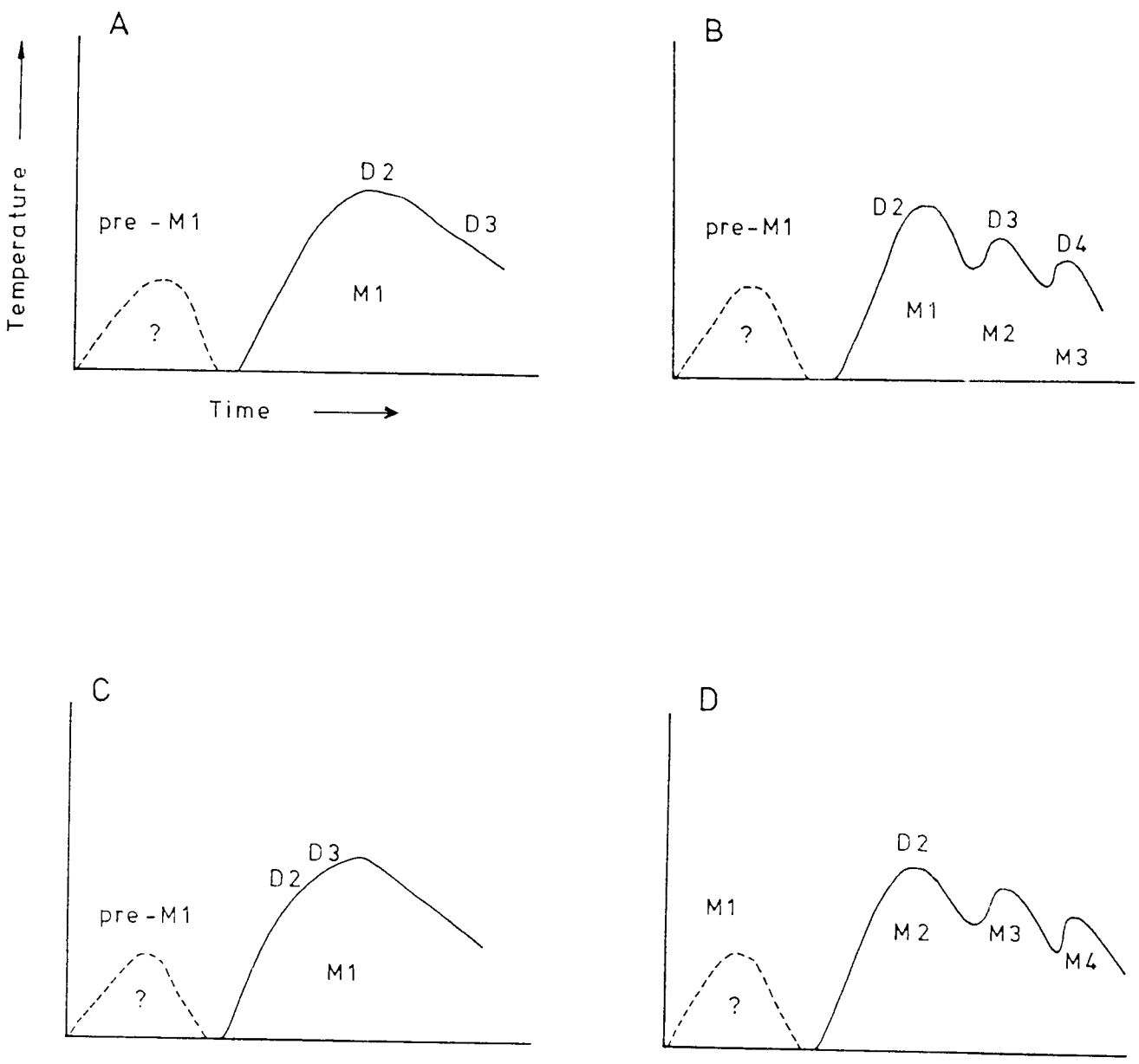

Figure 2.5. Schematic plots of temperature versus time illustrating metamorphic events in relation to deformational episodes. Model A (Albat, 1984) and model C (Waters, 1986) reflect single prograde and retrograde metamorphic events for all tectonic events; whereas Model B (Joubert, 1971) and model D (Lipson, 1978) illustrates thermal peaks and troughs for each tectonic event.

A symmetrical pattern of the metamorphic intensity within metapelitic schist and gneiss assemblages is found throughout the Bushmanland Subprovince (Fig. 2.6) (Waters, 1986). The metamorphic zonation in western Namaqualand reveals a high grade central core zone of upper granulite facies rock (zone C), trending east-west. It is flanked by lower granulite and amphibolite facies rock (zones B and A, respectively) to the north and south. Peak metamorphic parageneses in metapelitic rocks of hercynite-quartz and garnet-cordierite-K-feldspar are found in zones C and B, respectively (Waters, 1986). The Aggeneys area occurs within zone A, where peak metamorphic parageneses reflect metamorphism at the upper limit of the amphibolite facies (Chapter 3). A gradual thermal gradient defines the change in metamorphism from the amphibolite facies in the outer zone to the upper granulite facies of the central zone. Waters and Whales (1984) have documented the controls on the mineral parageneses in the transition zone between A and B. Their observation of alternating bands consisting of biotite-sillimanite-quartz and garnet-cordierite-K-feldspar assemblages formed at the same P-T conditions with $a(H_2O)$ systematically lower in the later. Mineral geothermobarometry and textural associations of equilibrium metamorphic minerals in metapelites, for the granulite terrain of zone C, have been applied by Waters (1989) to conclude an 'anticlockwise' P-T path for the Namaqua thermal event (Fig. 2.7). This P-T path is, however, not applicable to the Aggeneys area in zone A. The significance of this P-T path is that the rocks experienced constant or increasing pressure during the retrograde high T history (Waters, 1986). The P-T evolution is explained by Waters (1986) to be the result of voluminous addition of granitic magmas.

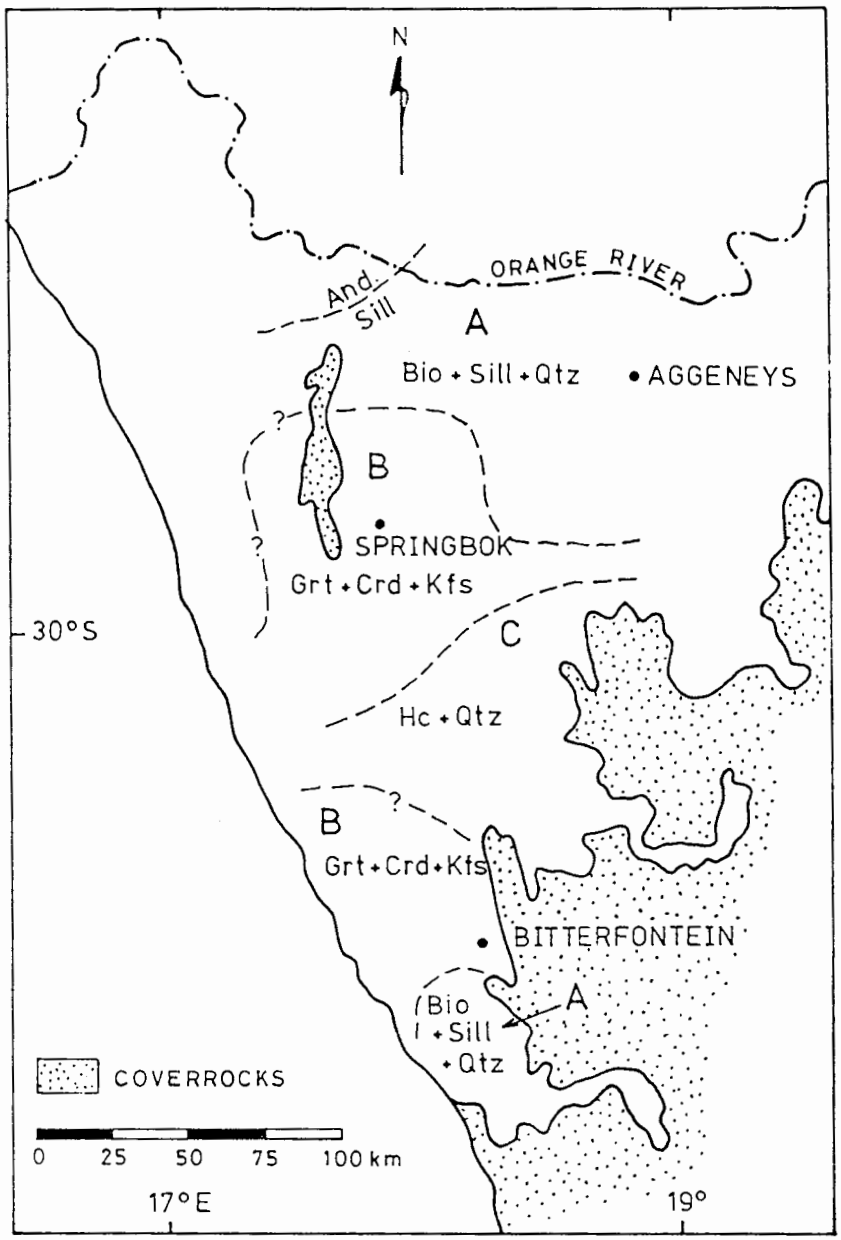

Figure 2.6. Metamorphic map of western Namaqualand, with isograds and assemblage zones determined in metapelitic rocks (after Waters, 1986). Garnet (Grt) + Cordierite (Crd) + K-feldspar (Kfs) persist through the Hercynite (Hc) + Quartz (Qtz) zone. Metamorphic zones: A= upper amphibolite facies, B= lower granulite facies and C= upper granulite facies. Andalusite-sillimanite boundary is from Blignault et al. (1983).

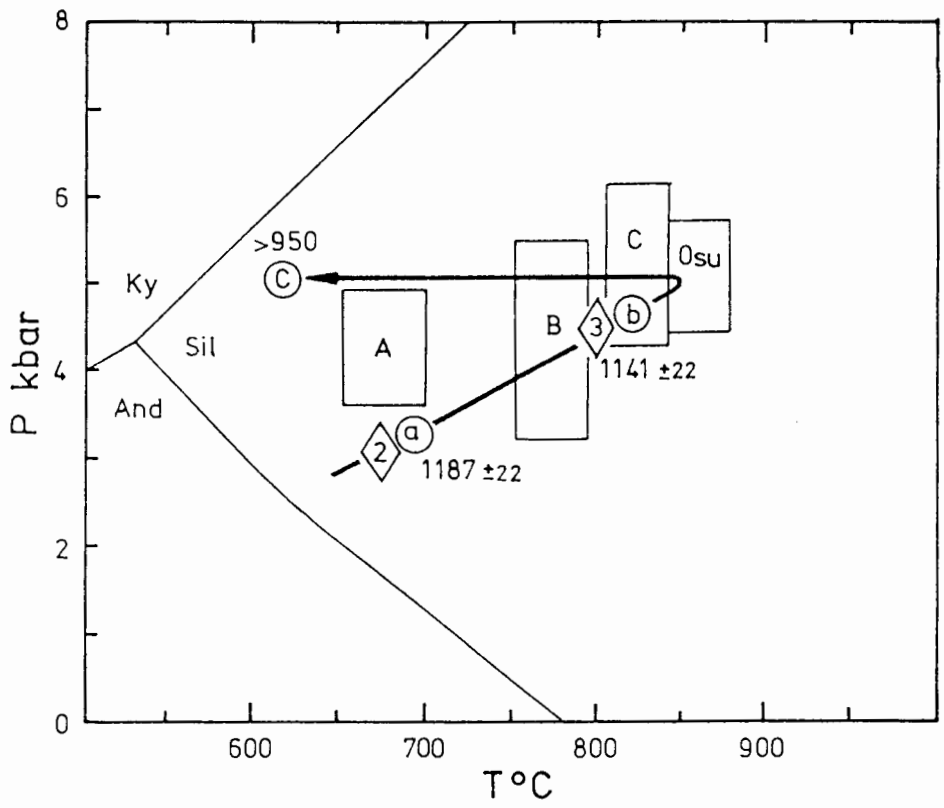

Figure 2.7. A P-T diagram for the Namaqua event in the western Bushmanland Subprovince. The boxes represent the P-T variation for the zones delineated in Figure 2.6. The solid arrow illustrates the P-T-t path within the granulite zone C. The numbers within the triangles, 2 and 3, represent the structural events D2 and D3 with respective ages after Clifford et al. (1975). Circles: a= Rb-Sr whole rock isochron on supracrustal granulite rocks, b= Rb-Sr whole rock isochron on late-tectonic granite gneiss and c= cooling history on U-Pb mineral ages. (after Waters, 1989).

3.GEOLOGY OF THE AGGENEYS AREA

In the Aggeneys-Gamsberg-Namiesberg areas, the outcrop of rock belongs to a basal sequence of the Bushmanland Subprovince and an overlying supracrustal succession of the Bushmanland Group (Fig. 3.1). The latter is preserved as isolated inselbergs. In this Chapter, the Bushmanland Group is taken to include only those supracrustal rocks in central Bushmanland of the Aggeneys Subgroup and exclude similar rocks to the north along the Orange River. Various stratigraphic schemes have been used to subdivide the supracrustal succession in the Aggeneys area (Joubert, 1974; Moore, 1977; Rozendaal, 1978; Ryan et al., 1986; Colliston et al., 1989; Lipson, 1990). Schematic subdivisions of the lithostratigraphy based on the "thinner" stratigraphic sequence at Aggeneys, Gamsberg and Namiesberg are shown in Table 3.1. The stratigraphic scheme of Lipson (1990) has been adopted in this study because it is founded on the geology of Broken Hill and can be correlated with the lithostratigraphic sequences of the inselbergs elsewhere in the Aggeneys area.

3.1.LITHOSTRATIGRAPHIC DESCRIPTION

3.1.1.Basement Rock-types

The basal sequence to the supracrustal succession in central Bushmanland comprises porphyroblastic and banded grey gneisses, the Achab Gneiss. In central Bushmanland, it underlies most of the supracrustal successions and has been recognized at Namiesberg (Moore, 1977), Gamsberg (Rozendaal, 1978), in the Aggeneysberge (Lipson, 1980), north of Namiesberg and north-west of the Aggeneysberge (Watkeys, 1986). The Achab Gneiss has limited outcrop and occupies mainly the low-lying area and suboutcrops extensively below the surficial sand and calcrete cover. Also exposed in the Achab Gneiss are minor lensoid xenoliths of calc-silicate rock found close to the overlying leucogneiss (Ryan et al., 1986; Moore, 1977).

In regions of low strain, the porphyroblastic Achab Gneiss consists of coarse porphyroblasts of K-feldspar with a fine- to medium-grained matrix of biotite, quartz and plagioclase, whereas in regions of high-strain, a banded gneiss is developed with thin veins (5-10 mm) of plagioclase and quartz (Watkeys, 1986).

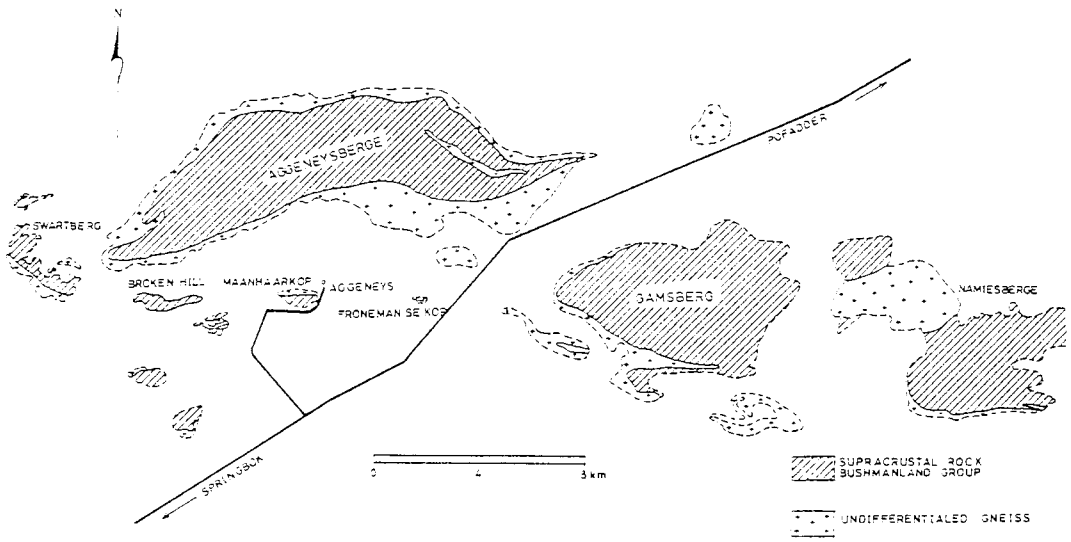

Figure 3.1. Map showing the distribution of combined porphyroblastic and leucogneisses, and supracrustal rocks in the Aggeneys-Namiesberg areas (modified after Colliston et al., 1986).

To the west of the Aggeneysberge and in the Achab area, the earliest fabric encloses the porphyroblasts and this texture is thought by Watkeys (1986) to represent recrystallized phenocrysts. Watkeys (1986) has interpreted the Achab Gneiss as a megacrystic granite which intruded a "pre-Bushmanland sequence" at about 2000 Ma. The granitic origin is in agreement with Lipson (1980). The contact with the overlying leucocratic gneiss is sharp. No conclusive evidence is found for a sedimentary or an intrusive contact between these two gneisses and Watkeys (1986) suggests a "tectonic dislocation".

3.1.2. Leucocratic Gneiss

The leucocratic gneiss, referred to as the Hoogoor Gneiss (SACS, 1980), develops to a maximum thickness of 200 metres in the Aggeneys area (Ryan et al., 1986). The leucogneiss is found in close association with the underlying augen gneiss and forms the basal portion of the supracrustal sequence. Weathered samples have an orange appearance, whereas fresh rock has a distinctive pink-appearance and has also aptly been called the Pink Gneiss (Moore, 1977; Rozendaal, 1978). The leucogneiss is generally well banded, equigranular, granoblastic gneiss devoid of megacrysts or augen (Moore, 1989). The rock consists of quartz, microcline, perthite, plagioclase and minor amounts of biotite and opaque minerals (Ryan et

Table 3.1. Generalized lithostratigraphy of the inselbergs in the Aggeneys area.

Aggeneys (Ryan et al.,1986)	Broken Hill (Lipson, 1990)	Gamsberg (Rozendaal, 1978)	Namiesberg (Moore, 1977)		
				<----	
AMPHIBOLITE + LIGHT GREY GNEISS FM. conglomerate, grey gneiss with minor amphibolite		NOUSEES MAFIC FM. conglomerate, psammitic schist, amphibolite			
	SHAFT SCHIST FM. qtz-bio-musc-sill-schist				
AGGENEYS ORE FM. qtz-bio-musc-sill-schist, iron formation	BIOTITE GRAPHITE ZONE bio-graphite-schist	GAMS IRON FM. iron formation			AGGENEYS SUBGROUP Supracrustal sequence
	ORE SCHIST FM. qtz-bio-musc-sill-schist, iron formation				
WHITE QUARTZITE FM. metaquartzite, schist	BROKEN HILL QUARTZITE FM. metaquartzite, schist	PELLA QUARTZITE FM. metaquartzite, schist	metaquartzite, ferruginous quartzit		
ALUMINOUS SCHIST FM. qtz-bio-musc-sill-mgt-schist	NAMIES SCHIST FM. qtz-bio-musc-sill-mgt-schist	NAMIES SCHIST FM. metapelitic schist, iron formations	qtz-bio-sill-musc-schist, sill-rich rocks		
PINK GNEISS FM. quartzo-felspathic gneiss	LEUCOCRATIC GNEISS quartzo-felspathic gneiss	HOOGOOR GNEISS FM quartzo-felspathic gneiss	pink gneiss		
				<----	
AUGEN GNEISS FM porphyroblastic gneiss	porphyroblastic gneiss	porphyroblastic and banded grey gneisses	minor amphibolite, calc-silicate rocks	<----	Basal sequence
			porphyroblastic and banded grey gneisses		

al., 1986). Thin discontinuous lenses of schist, quartzite and amphibolite within the leucogneiss have been reported by Ryan et al. (1986). The leucogneiss has a sharp contact with the overlying Namies Schist Formation.

The leucocratic gneisses exhibit a narrow range of chemical composition, particularly the constancy of SiO_2/Al_2O_3 ratio (Lipson, 1980; Moore, 1989) and have persistently high K_2O values (5-7 wt.%). Their compositions as suggested by Moore (1989) are comparable with major recent acid ash flow tuffs and other high-silica rhyolites and are likely to have originated from a degraded rhyolitic protolith (Moore, 1989) or sub-aerially deposited from calc-alkaline rhyolitic tephra (Duncan et al., 1984). In marked contrast, Colliston et al. (1989) interpret the leucogneiss as an intrusive granitoid. Although the author has not observed any evidence for an intrusive contact as suggested by Praekelt (pers com, 1992), the conformable nature of the leucogneiss with respect to the enclosing rocks over throughout most of the Aggeneys area, constrains the likelihood of an intrusive origin.

3.1.3.Namies Schist Formation

Overlying the leucogneiss is a muscovite-sillimanite-biotite-quartz metapelitic schist of the Namies Schist Formation. This unit has an average thickness of 100 metres in the vicinity of Broken Hill and Maanhaarkop. Opaque minerals comprise up to 5 vol.% of the rock with magnetite most common and lesser chalcopyrite. The schist is strongly foliated, coarse-grained, quartz-rich schist and exhibits textural variations which are nodular to mottled. The nodules consist of a quartz-sillimanite-muscovite assemblage which occurs mostly in proximity to the underlying leucogneiss (Lipson, 1990). In outcrop, the schists weather dark-brown to grey where relatively quartz-poor, and lighter grey in the more quartz- and muscovite-rich rock. Lipson (1990) describes biotite in excess of muscovite lower in the unit and an increase in muscovite at the expense of the biotite towards the underlying but stratigraphically higher quartzite. The Namies Schist has a large modal variation where a lower quartz content is found closer to the gneiss and increases towards the quartzite. Towards the top of the unit, quartzite bands mark a gradational change to the overlying Broken Hill Quartzite Formation (Lipson, 1990).

3.1.4. Broken Hill Quartzite Formation

In the Aggeneys area, the quartzites of the Broken Hill Quartzite Formation serve as a resistant cap to the ranges of hills and form prominent ridges. The E-W trending Broken Hill Quartzite Formation has an average thickness of 95 metres (Lipson, 1990). In the Aggeneysberge, it varies in thickness from 5 to 900 metres and thickness in excess of 100 metres is attributed to duplication by isoclinal folding (Lipson, 1978).

Within this major quartzite horizon is a sillimanite-muscovite-biotite-quartz metapelitic schist which hosts local irregular discontinuous lenses of quartz magnetite iron formation. The negative weathering of this schist gives the effect of dividing the quartzite into two horizons (e.g. at Broken Hill and Black Mountain). The lower quartzite is darker in colour than the upper, which is white to grey, and the latter exhibits a glassy appearance. Both quartzite horizons consist of at least 95 vol.% recrystallized quartz, with small contents of muscovite, sillimanite, biotite and opaque minerals. Heavy mineral layers within the quartzite comprise ilmenite, zircon and rutile. These layers have thicknesses defined by one-to-two mineral grains. At Froneman se Kop, these layers are interpreted to define foresets of cross-bedding which have been used to indicate polarity of the stratigraphic sequence (Lipson et al., 1978).

The quartzites have compositions dominated by high silica contents, at least 98 wt.% SiO_2 (Lipson, 1990). Two contrasting genetic models, either detrital or chemogenic ones, have been proposed for the formation of the quartzite. Lipson (1990) suggests that the quartzite was derived from metamorphism of a highly mature detrital sandstone or quartz arenite which was deposited as a partially submerged beach barrier. In marked contrast, Moore (1989) suggests that high levels of dissolved silica were derived from degraded acid volcanic rocks and precipitated as chert in a shallow water environment.

3.1.5. Aggeneys Ore Formation

A 200-metre-thick sillimanite-muscovite-biotite-quartz metapelitic schist stratigraphically overlies the major quartzite horizons. This stratigraphic horizon hosts the iron formations associated with the Cu-Pb-Zn-Ag stratiform orebodies. Interbanded within the succession are thin lenses of quartz-rich schist and calc-silicate rocks. A similar succession hosts the iron-formation-related ore horizons of the Gamsberg deposit, the Gams Iron Formation

(Rozendaal, 1978). In the Aggeneys area, the upper part of the Aggeneys Ore Formation is a homogeneous schist which has little textural and mineralogical variation (Lipson, 1990). This schist contains trace to 3 vol.% of pyrite and minor graphite. In contrast, the lower part of the Aggeneys Ore Formation has wider textural variations (banded and foliated) and has distinct accessory mineral assemblages which include magnetite, garnet and chalcopyrite. Lipson (1990) has subdivided the metapelitic schist of the Aggeneys Ore Formation into two stratigraphic units, the lower Ore Schist Formation which hosts the iron formation and the upper Shaft Schist Formation. This subdivision has been adopted in this study and more detailed descriptions of these rocks are given in Chapter 4.

3.1.6.Amphibolite\ Gneiss\ Conglomerate Assemblage

In the Aggeneys area, the top of the stratigraphic sequence is well developed at a few localities. This sequence was referred to as the Grey Gneiss Formation by Ryan et al. (1986). In the eastern part of the Aggeneysberge, "quartzite grades into bands of metaconglomerate, which, in turn, are interbanded with a variable succession of gneisses and amphibolite" (Ryan et al., 1986). The metaconglomerate is poorly sorted and contains significant amounts of matrix gahnite. At Gamsberg, the top of the stratigraphic succession has been called the Nousees Mafic Formation (Rozendaal, 1978). It comprises quartz-pebble and iron formation-pebble conglomerates which overlie the quartzite and iron formation horizons. Overlying the conglomerates are psammitic schists interbanded with amphibolite and calc-silicate units (Rozendaal, 1982).

The amphibolites comprise plagioclase, hornblende and minor quartz, with subordinate amounts of biotite, epidote, diopside, magnetite, K-feldspar and garnet (Reid et al., 1987b). These mafic rocks have 4-9 wt.% MgO and are enriched in Ni relative to modern basalts. They are thought to represent metamorphosed tholeiitic basalts that were formed in a back-arc extensional basin (Reid et al., 1987b).

3.1.7.Lithostratigraphic Correlation

In the intensely deformed Bushmanland Subprovince, correlating lithostratigraphic units of the isolated inselbergs is tenuous as there exists the possibility of large scale dislocations. Specific stratigraphic horizons which include the schist (Namies Schist Formation) situated

between the leucogneiss and quartzite, the whiter quartzite overlain by a darker quartzite and the pyrite-bearing schist above the quartzite enabled Lipson (1990) to correlate the stratigraphic successions at Broken Hill-Gamsberg-Namiesberg as lateral equivalents. The Namies Schist Formation at Broken Hill has rock-types and a mineralogy similar to the schist between the quartzite and leucogneiss at Gamsberg (Rozendaal, 1978). At Gamsberg, the mineralized iron formation lies above the major quartzite horizon.

At Broken Hill, the Namies Schist Formation structurally overlies the quartzites which in turn are above the Ore and Shaft Schist Formations. A similar structural sequence is recognized at Klein Kop and Maanhaarkop (Fig. 4.2), which are small hills to the east, with the exception that no orebody is found within the Ore Schist Formation (Lipson, 1990). Other features, including a schist within the quartzite, outcrops of calc-silicate bands within the pyritic schist and borehole intersections of a garnet quartzite within schist below the dark quartzite, are recognized by Lipson (1990) to infer a correlation between these hills.

These stratigraphic considerations coupled with the polarity within the succession at Froneman se Kop (Lipson et al., 1986) indicate that Broken Hill is an overturned sequence.

3.2. Metamorphism

The earliest metamorphic paragenesis for the supracrustal rocks reflects metamorphism of amphibolite facies. Metapelitic rocks are schistose, comprising rock-types with quartz + biotite + muscovite + sillimanite (+/- garnet +/- K-feldspar), and mafic rocks contain quartz + plagioclase + hornblende (+/- biotite) parageneses.

Various metamorphic schemes proposed for the Aggeneys area include several prograde and retrograde events. In the Aggeneys area, the general consensus is that prograde metamorphism occurred simultaneously with and might have outlasted D2. For the high grade rocks in the Namiesberg, Moore (1977) equates metamorphic episodes M1-M3 with deformational events D2-D4, respectively. Assemblages consisting of K-feldspar + sillimanite + cordierite in pelitic schist, and diopside in the amphibolite indicate peak P-T conditions for prograde metamorphism (M1) to have reached 650-750 ^{0}C and 5-7 kb (Moore, 1977). The peak metamorphic conditions associated with D2 deformation in the

Aggeneysberge have been estimated by Lipson (1978) at 670-690 ^{0}C and 4.5 kb, and at Gamsberg, Rozendaal (1978) has established peak metamorphic conditions of 630-670 ^{0}C and 2.8-4.5 kb. Rare intergrowths of sillimanite and K-feldspar are considered by Lipson (1990) to be the best indicators of the peak prograde metamorphism.

Widespread retrograde metamorphism (M2) evident from the hydration of K-feldspar and sillimanite to muscovite and quartz, and the recrystallisation of biotite in the schists has been suggested by Moore (1977). Quartz-muscovite-sillimanite nodules with deeply embayed grain boundaries and microcline porphyroblasts enclosed by a sheath of fine-grained muscovite and quartz were suggested by Lipson (1978) to be evidence for the retrograde reaction:

Locally in the Namiesberg, a second retrograde metamorphic event with assemblages of chlorite, zoisite and clinozoisite are closely associated with the D4 structures (Moore, 1977). Similarly, in the Gamsberg, retrograde chlorite in existing foliation planes have been documented by Rozendaal (1975).

In the Broken Hill schists, Waters (1987) observed coarse-grained cross-cutting flakes of muscovite associated with and replacing fibrolitic sillimanite knots. In this study, some muscovite and quartz are in textural equilibrium at peak metamorphic conditions (660 ^{0}C and 3.5-4.0 kb). Consequently, it remains uncertain to what extent muscovite was produced by prograde and by retrograde metamorphism. The coarse-grained muscovite in stable association with other coexisting phases (e.g. quartz, sillimanite and K-feldspar) at peak metamorphism might be explained by the high F contents of the white micas. The significant F contents in muscovite could have the effect of increasing the temperature of the muscovite-quartz break reaction.

4. GEOLOGY OF BROKEN HILL

4.1.LOCAL SETTING

A section through Broken Hill and its environs shows a broadly symmetrical distribution of rock-types, with gneisses and quartzites exposed at Plant Hill to the south, a thick variable central sequence of schists which host the sulphide-rich lenses, and more quartzites, schists and gneiss to the north (Fig. 4.1). This sequence has been interpreted by Lipson (1990) as being duplicated limbs of a major isoclinal fold. This interpretation is, however, ambiguous and depends on the correlation of the footwall gneiss in the south with the hangingwall gneiss in the north. At Plant Hill, the gneiss has cm-thick quartz and feldspar bands and mm-thick biotite foliations. Small isoclinal folds with an amplitude less than 1 m are common in this gneiss and contrast markedly in appearance with the more homogeneous gneiss north of Broken Hill. Furthermore, the bulk compositions (unpublished company data) of these gneisses indicate distinctly different rock-types, which might suggest that the gneiss at the two localities represent different stratigraphic units. The gneiss at Broken Hill has K_2O consistently enriched with respect to Na_2O ($K_2O/Na_2O > 2.2$), whereas at Plant Hill, K_2O is generally depleted relative to Na_2O ($K_2O/Na_2O = 0.17\text{-}1.13$).

4.2.HOST ROCKS

Surface exposure of the major lithological units at Broken Hill is shown in Figure 4.2. The Pink Gneiss Formation (leucocratic gneiss) occurs at the base of the supracrustal sequence at Broken Hill, and underlies (from older to younger) rocks of the Namies Schist, Broken Hill Quartzite, Ore Schist (hosting LOB and UOB) and Shaft Schist Formations (Figure 4.3). Mine geologists have informally subdivided the Ore Schist Formation into the Hangingwall Schist (HS), the Intermediate Schist (IS) and the Upper Footwall Schist (US), with respect to the tectonic position of the LOB and UOB rock-types. For detailed descriptions of the schists and their whole rock compositions, the reader is referred to Lipson (1990). To the east and west of the mineralized horizon are garnet-rich bands interbanded with schist. This banded garnet-schist unit is the lateral equivalent of the LOB and UOB successions, the Ore Equivalent Schist (OES) (Lipson, 1990). The Ore Schist Formation overlies a biotite-graphite schist, the Biotite Graphite Zone (BGZ), which separates the former from the Shaft Schist Formation.

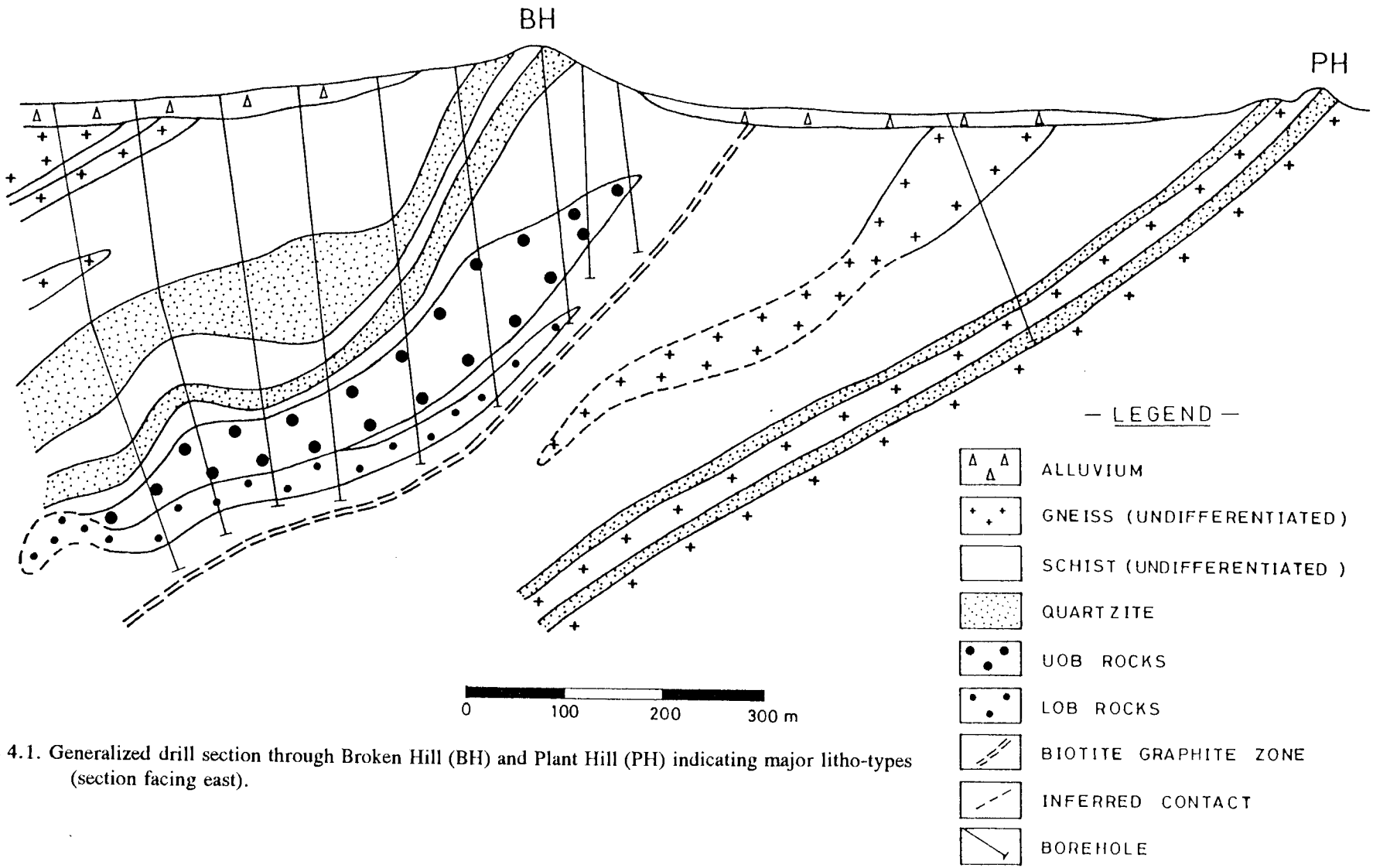

Figure 4.1. Generalized drill section through Broken Hill (BH) and Plant Hill (PH) indicating major litho-types (section facing east).

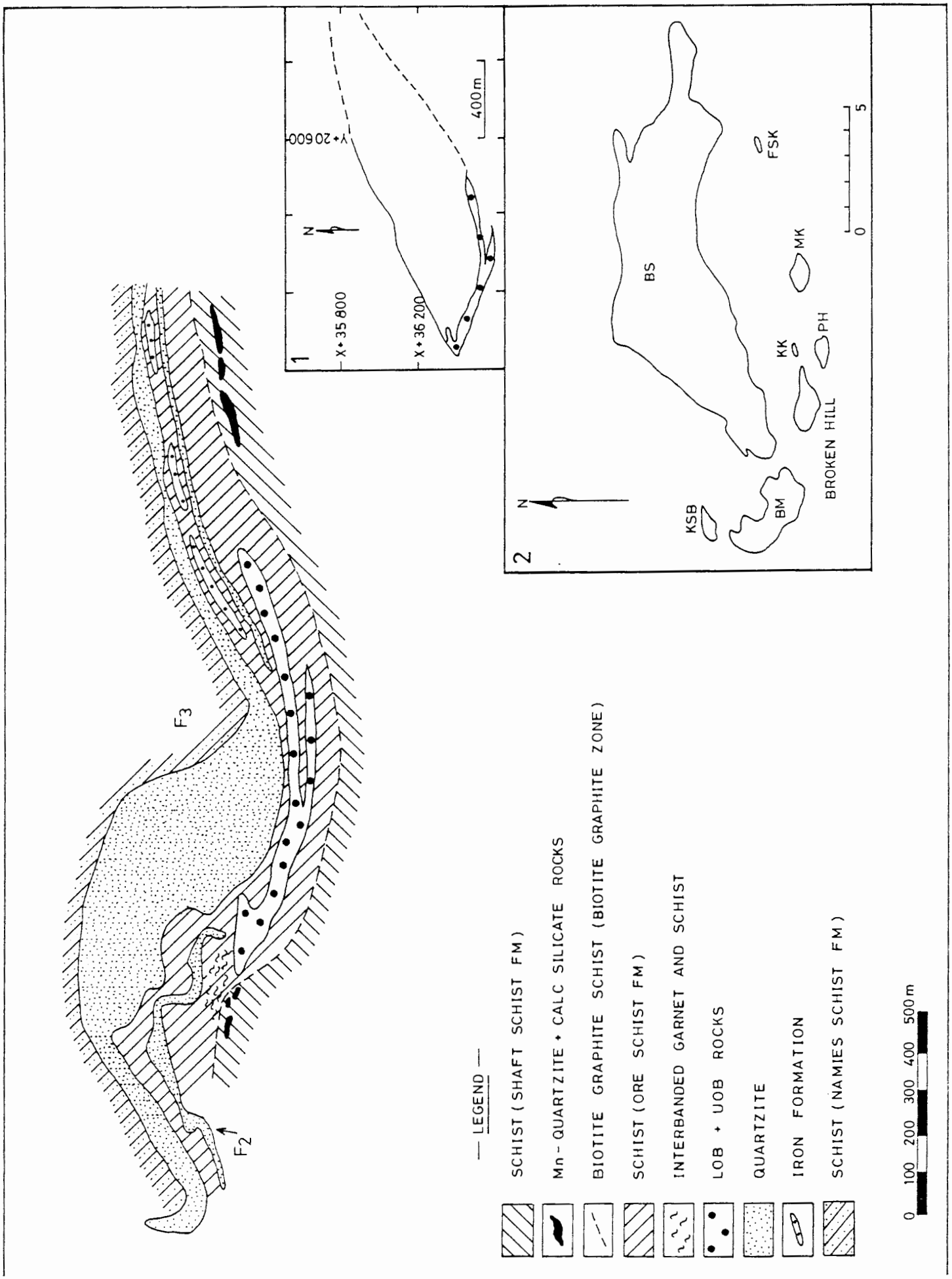

Figure 4.2. Schematic geological map of the Broken Hill deposit showing major rock-types exposed at surface. Insert 1: down-plunge projection of LOB and UOB relative to the surface exposure. Insert 2: locality of Broken Hill with respect to other inselbergs in the area, BS- Big Syncline (Aggeneysberge), FSK- Froneman se Kop, MK- Maanharkop, PH- Plant Hill, BM- Black Mountain, KK- Klein Kop, KSB- Klein Swartberg (modified after Lipson, 1990).

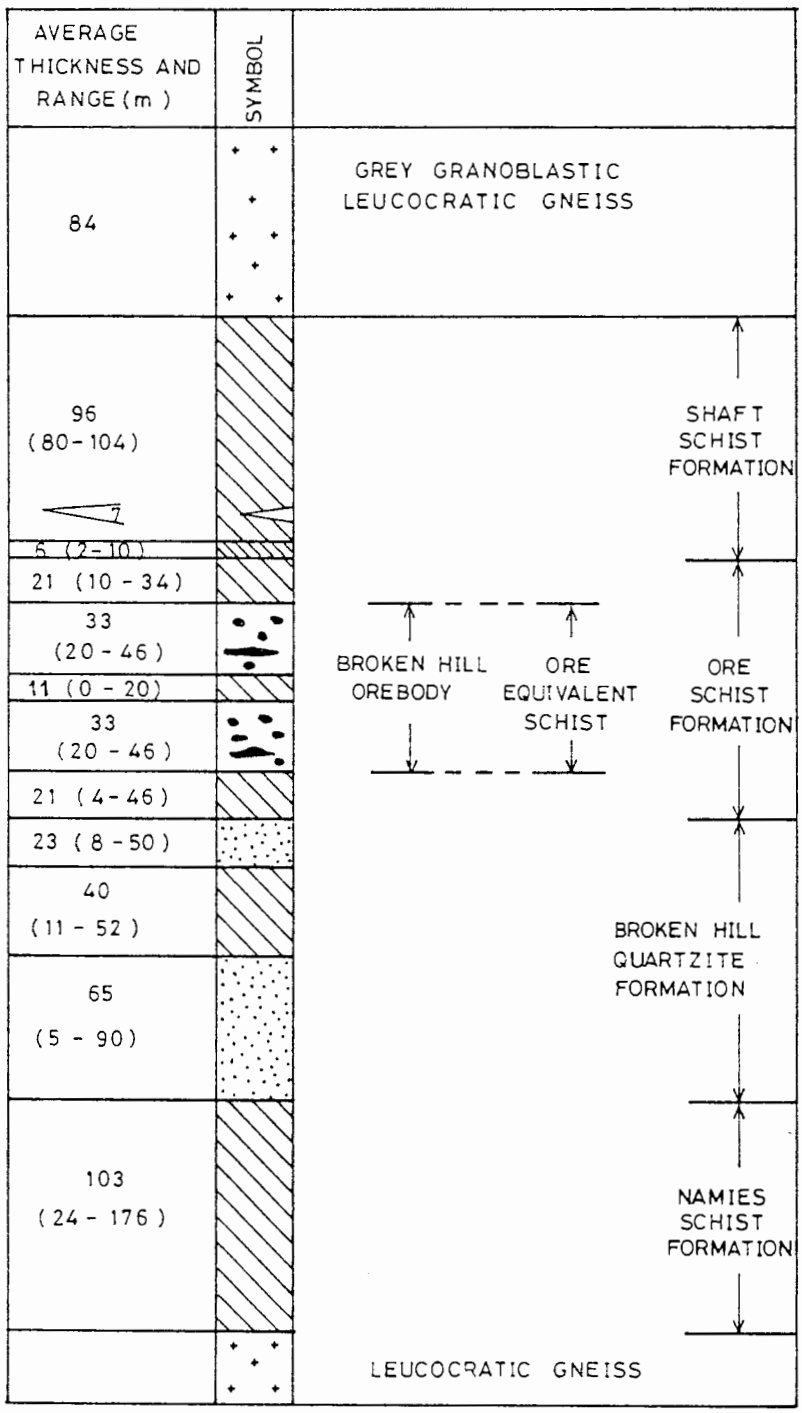

Figure 4.3. Stratigraphic column at Broken Hill (modified after Lipson, 1990).

Amphibolite and metaconglomerate found higher in the sequence of the Amphibolite and Grey Gneiss Formation is not developed at Broken Hill.

4.2.1.Hangingwall Schist

The Hangingwall Schist (HS) is a banded and foliated muscovite-sillimanite-biotite-quartz-schist. This schist has an average thickness of 21 m. The HS crops-out on the south slope of the Broken Hill inselberg. The schists are light brown in appearance and are medium-to-coarse-grained (0.5 to 2 mm). Quartz occurs throughout the rock but is concentrated locally in 5-10 mm thick quartzite bands. Biotite coexists with muscovite, with the former generally predominating (see Chapter 5). Garnet is predominantly disseminated, but less common, it is found in mm-thick bands. Disseminated magnetite grains (< 1 mm) and thin (5-10 cm) quartz magnetite iron formation lenses are often associated with the HS. Minor disseminated chalcopyrite grains (< 2 mm) are common within the iron formation lenses and might be found within the schist. Local lenses of pegmatite are 1-20 cm to several metres in thickness and consist predominantly of coarse-grained (5-30 mm) K-feldspar, quartz and minor muscovite. The pegmatite lenses are often conformable with the banding in the schist and Lipson (1990) suggested that they were formed by in-situ anatexis during peak metamorphism. Recrystallized quartz lenses of similar thickness are also conformable with the banding in the schist and are thought to be derived from the metamorphic segregation of silica in the original sediment.

4.2.2.Intermediate Schist

The Intermediate Schist (IS) is a muscovite-biotite-sillimanite-quartz-schist. Its thickness ranges from 20 m in the east and pinches out to 50 cm in the west where it grades into a garnet-biotite-quartz schist (see Chapter 4.3.2). Thin quartz-rich lenses within the IS, are sheared, boudinaged and folded. Where the IS is sheared, the quartz lenses contain sillimanite. This schist differs from the HS by its coarser-grained sillimanite (up to 10 mm in length), its absence of thin quartz magnetite iron formation lenses, and the rare occurrence of disseminated chalcopyrite.

4.2.3.Upper Footwall Schist

The Upper Footwall Schist (US) is a medium-to-coarse-grained (0.5 to 2 mm) muscovite-

sillimanite-biotite-quartz schist and has the same textures as the HS. The average thickness of the US is 20 m and varies from 10 to 35 m-thick. It differs from the HS by the complete absence of magnetite. Coarse-grained remobilized galena and chalcopyrite are situated locally at 1-5 m from the LOB.

4.2.4.Biotite Graphite Zone

The sharp transition between the Ore Schist Formation and the Shaft Schist Formation is defined by the 2-10 m thick biotite-graphite-schist of the Biotite Graphite Zone (BGZ). In addition, it contains accessory pyrite 'platelets' which are parallel to the foliation. The BGZ is often associated with lenses of pegmatite and recrystallized quartz veins. At the mine, it is referred to as the Weak Zone where it is associated with precarious ground conditions in the underground development.

4.2.5.Shaft Schist Formation

The Shaft Schist rarely crops-out due to its soft nature and negative weathering characteristic. The rock consists of biotite, muscovite, elongated quartz, sillimanite, pyrite and minor graphite. The schist is medium-grained (0.1-1 mm) and highly foliated. It occurs as a homogeneous unit and exhibits little textural and mineralogical variation (Lipson, 1990). Pegmatite and recrystallized quartz lenses, similar to those in the Ore Schist Formation, are also common in the Shaft Schist Formation. Visible distinctions between the schist of the Shaft Schist and the Ore Schist Formations are the darker, green appearance, the presence of pyrite 'platelets' parallel to the foliation and the complete absence of garnet in the former.

Conformable within the Shaft Schist Formation are lenses of calc-silicate rock and Mn-rich quartzite which occur 10 m from the BGZ (Lipson, 1990). These lenses are restricted to the easterly and westerly margins of the deposit (Fig. 4.2).

4.3.LOWER AND UPPER OREBODY ROCKS

The superposed UOB and LOB rock-types that are hosted within the Ore Schist Formation crop-out at surface with a strike length of 1000 m. The economically mineralized horizons at surface and within the upper levels (above 3 level) have a strike length >700 m, but are confined to <300 m in length beyond 17 level. The UOB extends further to the east than the

LOB. Both the LOB and UOB have average thicknesses of approximately 33 m. A generalized plan showing the distribution LOB and UOB rock-types is given in Figure 4.4.

4.3.1.Ferruginous quartzite and garnet-bearing quartzite

Ferruginous quartzite (FQ) and garnetiferous quartzite (GQ) partly or completely enclose the iron formation and massive sulphide lenses of the UOB and LOB, respectively. The GQ generally contains between 3 and 8 vol.% garnet (locally it has as much as 35 vol.%) and lacks magnetite. In contrast, the FQ contains up to 10 vol.% magnetite with accessory garnet.

The FQ occurs as a consistent lithological horizon that overlies the iron formation in the UOB (Figs. 4.4-4.6). It generally has a massive appearance with thin tectonically disrupted magnetite-rich bands. The contact between the FQ and the iron formation in the UOB is gradual over 5-15 cm. Towards the iron formation, there is a distinct increase in the number and thickness of magnetite bands. Trace amounts (<0.5 vol.%) of chalcopyrite are found in proximity to the iron formation, together with little galena and sphalerite. Pyrite and pyrrhotite were not observed. At the NE margin down-plunge extent of the Broken Hill deposit, 1-4 m-thick lenses of GQ are developed in the FQ.

The GQ occurs as a 1-5 m-thick discontinuous unit which overlies and underlies the iron formation of the LOB (Fig. 4.5). At the SE margin, the GQ completely encloses the LOB iron formation (Figs. 4.4-4.5). Above the iron formation, the GQ often has a brecciated texture (Fig. 4.7). The GQ in places appears as a pseudo-clast-supported conglomerate. It comprises sub-rounded quartzite clasts (1-2 cm) with fine-grained (<0.5 mm) matrix garnet.

4.3.2.Iron formation

Iron formation constitutes a major portion of the lithological sequence at Broken Hill. The iron formations are magnetite-rich and contain varying proportions of silicate-rich bands. The nature and percentage of silicate-rich bands have been used to describe four distinct iron formations which are recognizable as macrobands. The iron formations are:

1. Quartz-magnetite iron formation (QMIF)
2. Amphibole-olivine-magnetite iron formation (AMIF)

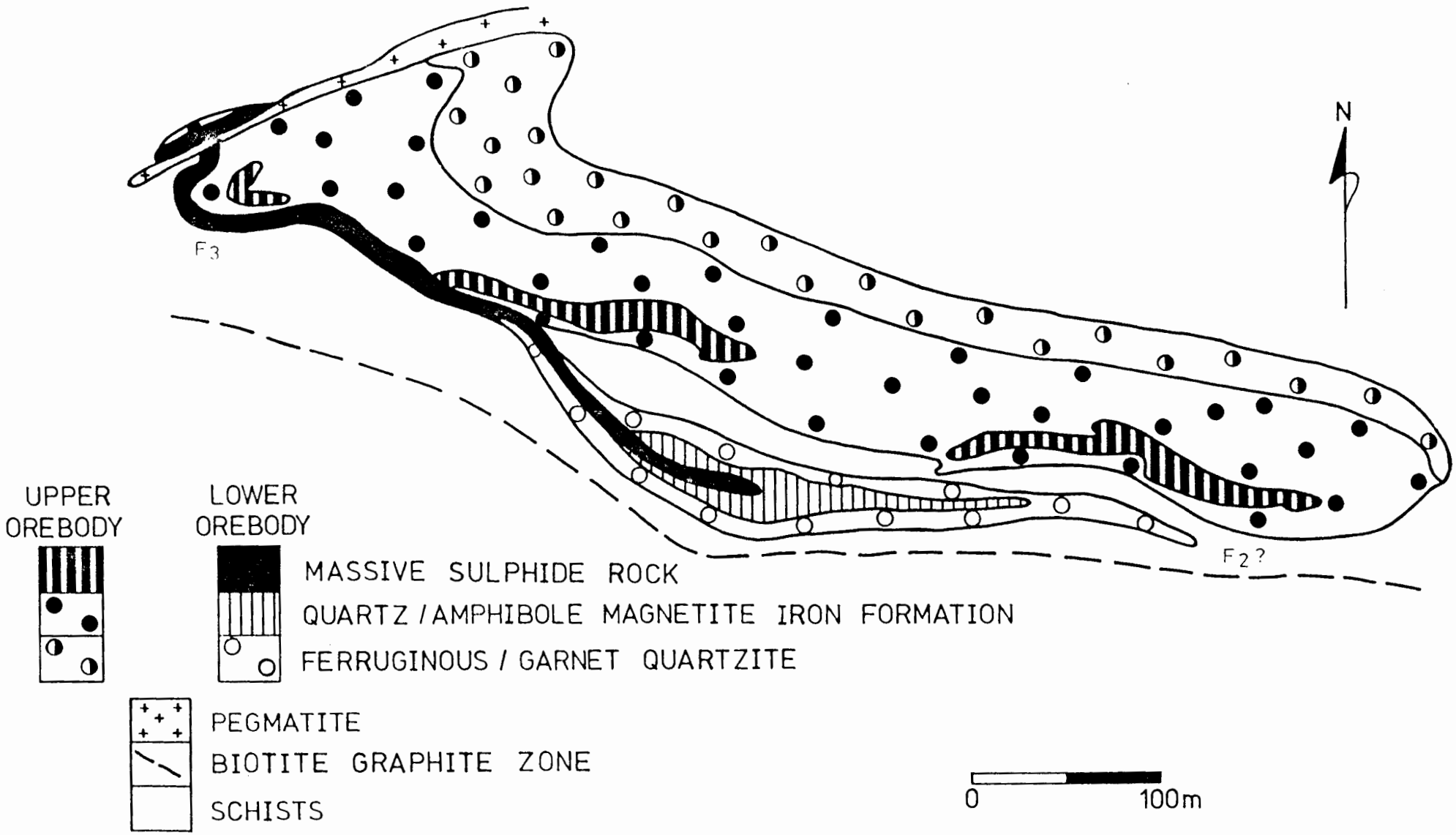

Figure 4.4. Generalized plan of 8 level showing the discontinuous UOB massive sulphide lenses and a continuous LOB massive sulphide lens both enclosed by banded iron formation rock and, ferruginous quartzite and garnet quartzite, respectively (modified after Smith, 1986; used with permission).

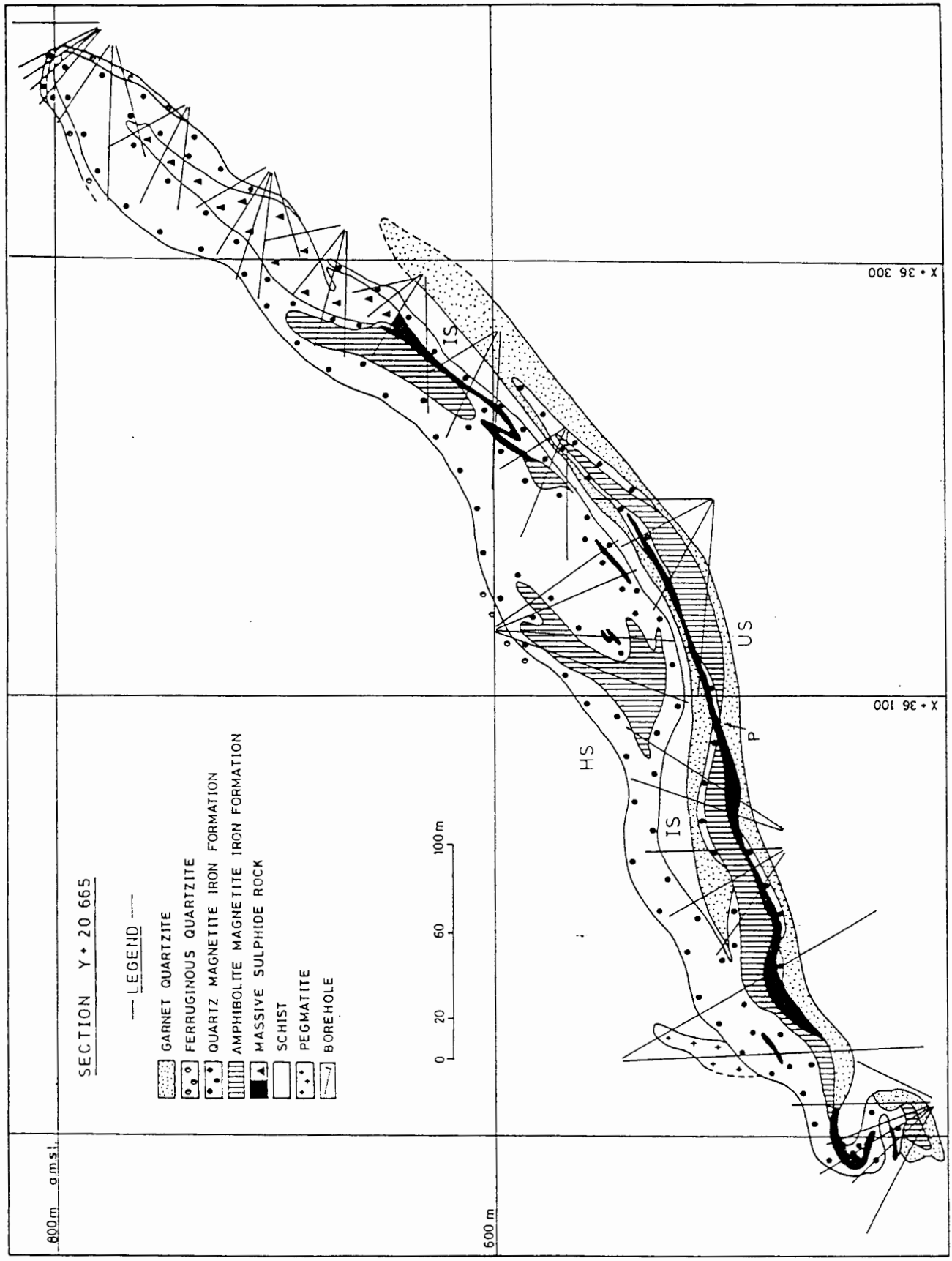

Figure 4.5. Interpreted N-S drill section (Y+20665) through the LOB and UOB successions. See text for annotation of "P". HS - Hangingwall Schist, IS - Intermediate Schist, US - Upper Footwall Schist.

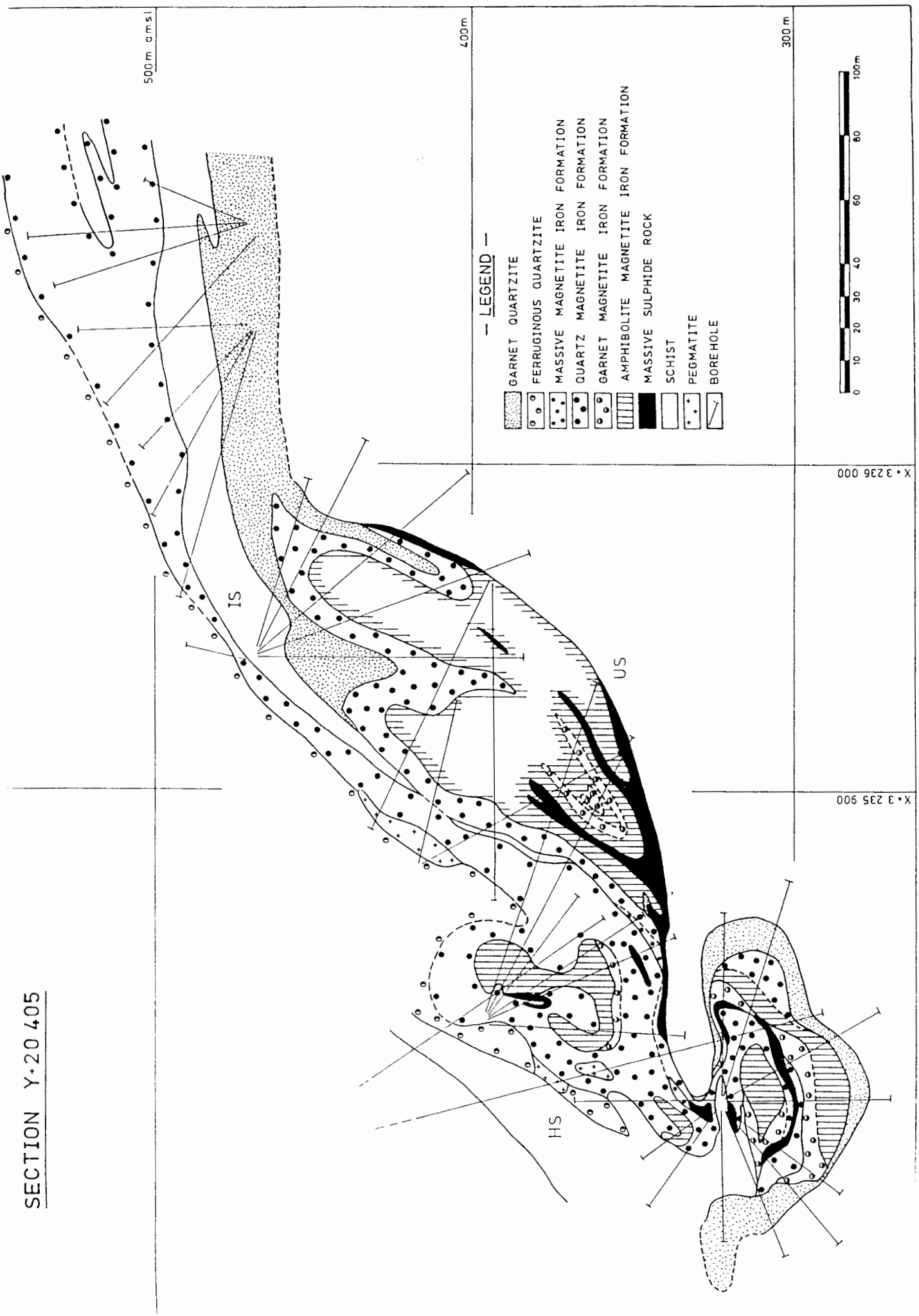

Figure 4.6. Interpreted N-S drill section (Y+20405) through the LOB and UOB successions. Compare with Figure 4.5.

Figure 4.7. Garnet quartzite with breccia texture. Location: borehole BHU2659.

3. Garnet-magnetite iron formation (GMIF)
4. Massive magnetite iron formation (MMIF)

The QMIF is essentially a bimineralic rock with quartz and magnetite bands. Quartz is, however, not always the exclusive silicate phase because minor proportions (< 5 vol.%) of amphibole, garnet and biotite might be present. The massive magnetite iron formation (MMIF) lacks banding and has a massive appearance. It characteristically contains >75 vol.% magnetite. The AMIF and GMIF contain significant proportions of (Fe-Mn)-rich silicate minerals, but have fewer and thinner magnetite bands compared to the QMIF. Although the AMIF and GMIF might be regarded as endmembers, each iron formation might contain subordinate garnet and amphibole bands, respectively. The subdivision of the iron formation-types is illustrated in Figure 4.8. The highest percentage silicate mineral determines the iron formation-type. The nomenclature used for the distinction of the iron formations is consistent with the definitions employed by the mine geologists. This is essential because the drill records of the various iron formation intersections logged by mine geologists and the author were used to interpret the N-S drill-sections. In the discussion that follows, the spatial distribution and a brief description of the iron formations are given.

Detailed descriptions of the iron formations' mineralogy and textures are given in Chapter 5.

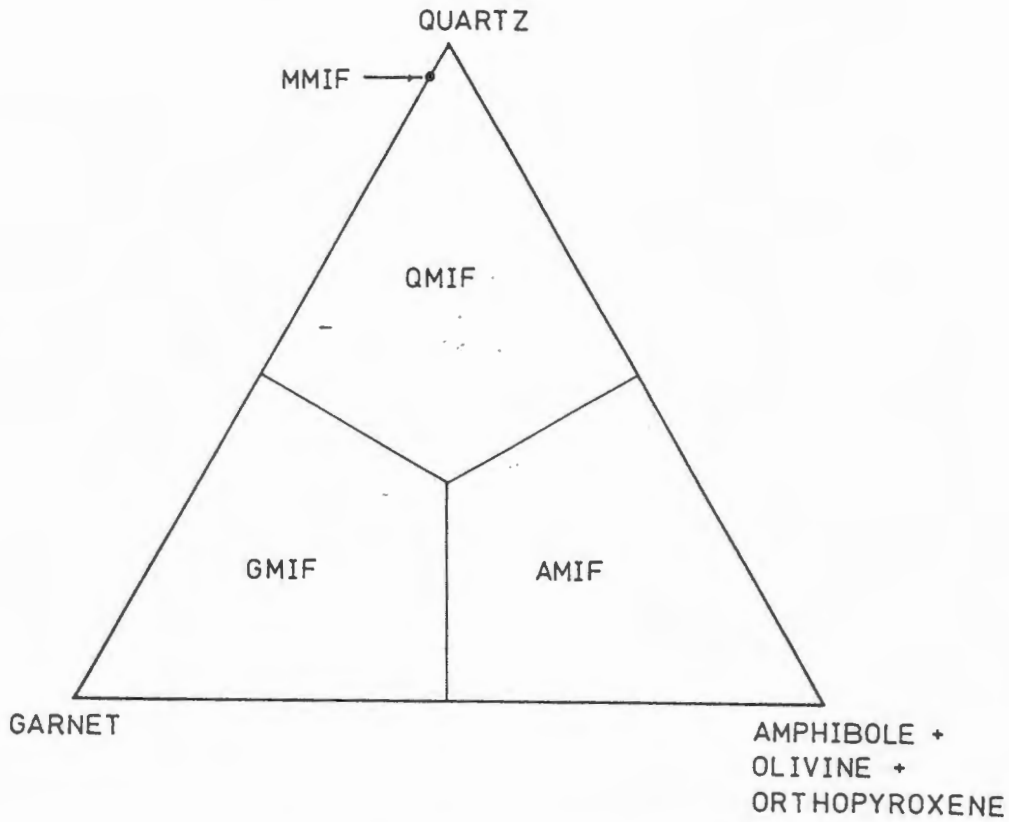

Figure 4.8. Ternary diagram showing QMIF, AMIF, GMIF and MMIF iron formation-types as a function of their silicate mineral contents. MMIF- massive magnetite iron formation, QMIF- quartz magnetite iron formation, GMIF- garnet magnetite iron formation and AMIF- amphibole magnetite iron formation.

QMIF is the most common iron formation in the UOB succession. It is developed as a thin unit (10 cm - 5 m) which underlies the massive sulphide lenses. Where the QMIF overlies the massive sulphide rock it is generally between 2 m and 20 m in thickness. The iron formation within the UOB succession has significantly greater magnetite contents than the iron formation in the LOB. At the NW margin of the deposit, a hybrid of AMIF and GMIF is persistently developed above the massive sulphide lens of the UOB. Similarly, lenses of AMIF with variable thickness (2 to 8 m) were found in the central and eastern regions of the UOB.

Throughout the LOB succession, banded iron formation rock both overlie and underlie the massive sulphide rock of the LOB. These iron formations often have a symmetrical distribution (Figs. 4.4-4.5). The distribution and thickness of the LOB iron formation is illustrated with an isopach map (Fig. 4.9). The iron formation at the NW margin has been excluded because of uncertainties arising from pinch and swell effects due to folding and shearing. Where the iron formation thickness below the massive sulphide lens is greater than that above, there is a linear trend that follows the plunge of the deposit.

Within the LOB succession, QMIF encloses the AMIF at the SE margin (Figs. 4.5 and 4.6). At this locality, the banded texture of the QMIF is generally well preserved which contrasts with the more massive appearance at the NW margin where the rock is poorly banded. The banding within the AMIF and GMIF is more spectacular (Fig. 4.10) and mesobands are traceable over tens of metres (Fig. 4.11). The GMIF is best delineated below the massive sulphide lens at the NW margin of the LOB (Figs. 4.5, 4.6).

Where the QMIF, AMIF and GMIF are close to the massive sulphide lens, there are often economic concentrations of Cu, Pb and Zn mineralization in the iron formation. Galena, sphalerite and chalcopyrite occur either as conformable mm-thick bands, or as finely disseminated grains. Less common are discordant veinlets and remobilized aggregates. The occurrence of the discordant galena bands were not always observed to be spatially related to folding.

The massive magnetite iron formation (MMIF) is restricted to the NW margin of the deposit where it occurs as the lateral equivalent of the IS, and has been used to distinguish LOB from UOB rock-types. The lateral transition is noted by a thinning of the IS into a 30-100 cm-thick garnet-biotite-magnetite-schist which is interbanded with the MMIF further towards the west. The MMIF ranges in thickness from several centimetres where it has been attenuated to several metres in folded areas. The MMIF is also characterized by distinctive garnet and tourmaline porphyroblasts (Fig. 4.12).

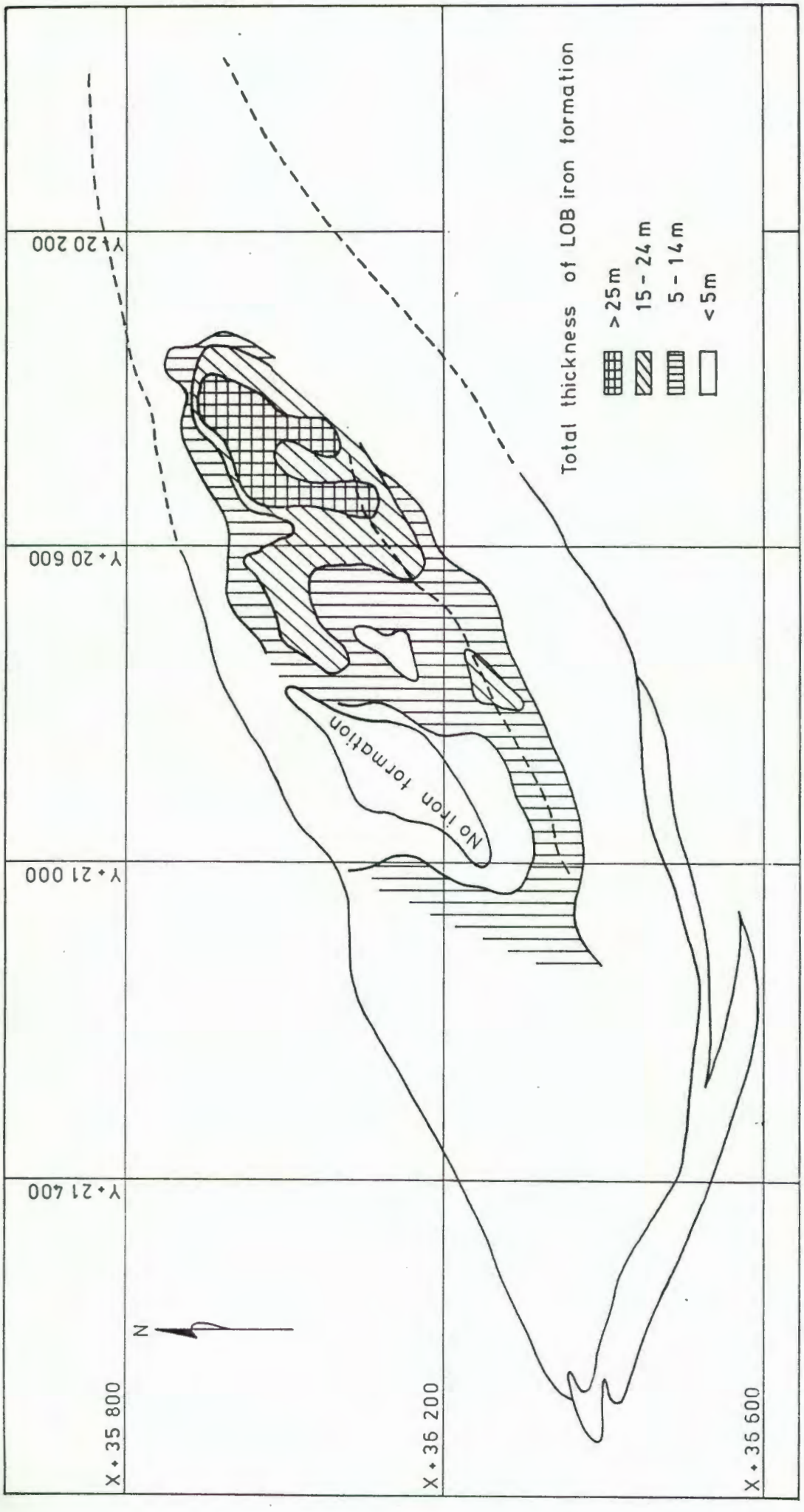

Figure 4.9. Isopach map showing the total thickness of the LOB iron formation. The iron formation along the NW margin of the deposit was excluded due the effects of folding. Compare with Figure 4.2.

Figure 4.10. Photograph of amphibole magnetite iron formation showing alternating amphibole- and garnet-rich mesobands.

Figure 4.11. Banded garnet magnetite iron formation at the NW margin of the LOB. Location: stope 11/0700 lift 7. Scale: Magnet-pen has 14 cm length.

Figure 4.12. Massive magnetite iron formation with coarse-grained porphyroblasts of garnet and tourmaline. Location: stope 8/1100 lift 8.

4.3.3.Massive sulphide rock

The massive sulphide rock has a sulphide content of at least 25 vol.%. With lesser proportions of sulphide, the rock is referred to as sulphide quartzite.

The UOB massive sulphide rock is developed as three separate lenses at equivalent stratigraphic positions in the upper part of the mine from above 12 level (Fig. 4.4). However, below 12 level, the UOB massive sulphide rock is confined to the NW margin of the deposit where it is developed as a unit of <1 to 2 m in thickness. The massive sulphide lenses of the UOB succession are enclosed by iron formation of variable thickness (Chapter 4.3.2.) and locally, they might be in contact with IS. Sulphide mineralization in the UOB is coarser-grained (2-10 mm) than the LOB ($<$1-2 mm). At the NW margin, the UOB massive sulphide rock consists of alternating garnet and galena mesobands (1-2 cm-thick). In the central and eastern lenses above 12 level, the UOB massive sulphide rock is poorly banded and has a massive appearance. Brecciated textures are less common.

The LOB massive sulphide rock occurs as a thin continuous lens with sharp lower and upper contacts. The thickness ranges from 2-3 cm where, due to local shearing it is developed as a mylonite, and distended intersections of 12 m in thickness are the result of isoclinal folding. Generally, the massive sulphide rock has a persistent thickness in the range of 2-5 m. The rock-types that are in contact with the massive sulphide rock lens include schist, garnet quartzite and banded iron formation (Fig. 4.4-4.6).

The LOB massive sulphide rock is medium-grained (0.5-1.0 mm) with pyrrhotite predominating over galena, sphalerite, chalcopyrite and varying proportions of quartz (see Chapter 5). At the central and the SE margin of the LOB, the massive sulphide rock has mm- to- cm-thick quartz and pyrrhotite bands which are typically wispy but might be continuous for tens of centimetres (Fig. 4.13a). At the deformed NW edge of the deposit, banding is poorly preserved in the massive sulphide rock with massive and breccia textures being common (Fig. 4.13b). Where the massive sulphide rock is in contact with US, it contains significant quantities of muscovite and minor biotite which are conformable with the banding. Despite the ductile nature of the LOB massive sulphide rock, it is seldom injected into the underlying schist and into the overlying iron formation. Fine-grained sulphide mylonites of 5 to 20 cm thickness are common along the margins of the massive sulphide rock (Fig. 4.13b). This is the result of shearing. The sulphide mylonites are generally galena-rich but are also rarely pyrrhotite- and chalcopyrite-rich varieties. This durchbewegung texture contains small proportions of rounded quartz and garnet.

Biotite-rich lenses, varying from 10-20 cm in length (common) to 3 m (rarely) are stratabound within the massive sulphide rock and at the interface with the US at the NW margin. These lenses are enclosed by a mm-thick rim of gahnite followed by chalcopyrite and galena. Also common in this vicinity, are coarse-grained (5-25 mm) aggregates rich in garnet, quartz, tourmaline, gahnite and biotite.

(a)

5 cm

(b)

5 cm

Figure 4.13. Photographs showing the nature, textures and features in the LOB massive sulphide: (a) massive sulphide rock with banding of pyrrhotite and quartz and disseminated galena within bands (b) massive sulphide rock with massive texture and galena-rich mylonite developed along the contact with garnet quartzite. Location: stope 13/0700 lift 10.

4.3.4.Pegmatite

Pegmatite occurs as either conformable lenses within the LOB and UOB rocks or forms discordant contacts. The former are common at the interface between the massive sulphide rock in the LOB and the US, and between the QMIF in the UOB and the IS. The thickness of these pegmatite lenses is generally 0.2-1.5 metres but might only be several centimetres. The discordant pegmatite-type can be up to 10 m-thick in places. This pegmatite is most common at the NW edge where it is associated with shearing and folding of the LOB, UOB and country rocks.

The discordant pegmatite predominantly consists of quartz and Pb-rich feldspar (amazonite), with minor proportions of garnet, muscovite, tourmaline, gahnite, galena, pyrrhotite and chalcopyrite. The mineralogy of the pegmatite, to some extent, mimics that of the enclosing schist and massive sulphide rock. Lipson (1990) suggested that the constant pegmatite to schist ratio within the Ore Schist Formation indicates an in-situ origin as a result of partial melting.

The conformable pegmatite at the interface of schist and iron formation/ or massive sulphide rock have low variance assemblages. This pegmatite essentially consists of amazonite and quartz. These are considered to be of metasomatic origin and related to element exchange along a steep geochemical gradient between the galena-bearing rock and the schist (see Chapter 8).

4.4. METAL ZONATION

Two distinct metal distributions, vertical and lateral, are recognizable in the Broken Hill deposit. The Pb/Zn ratio in the LOB massive sulphide rock horizon is distinctly less than 3 whereas in the UOB, the Pb/Zn ratio is typically greater than 5 but may be as high as 30. The total Cu+Pb+Zn metal content within the UOB massive sulphide rock is often greater than 20 wt.%. The massive sulphide rock in the LOB has typical Cu+Pb+Zn metal contents of 10 wt.%. Furthermore, the massive sulphide rocks of the LOB and UOB successions exhibit distinct Cu/(Cu+Pb+Zn) ratios. In the massive sulphide rock, the value for this ratio is significantly greater for the UOB (0.08) than for the LOB (0.025) (Smith, 1989).

The LOB and UOB massive sulphide lenses also exhibit well developed, strongly elongate lateral Cu-Pb-Zn zoning that parallel the plunge of the orebody and the regional structural trend. In the LOB massive sulphide rock horizon, there is a clear decrease of the Cu/(Cu+Pb+Zn) ratio from W to E (Fig. 4.14). Furthermore, there is no evidence to suggest that the higher Cu contents found at the NW edge have been concentrated in the hinges of small folds. However, at the Black Mountain deposit, local concentrations of Cu in fold hinges has been reported by Stedman (1980). The only localized concentrations of Cu and Pb are restricted to minor remobilized galena and chalcopyrite aggregates in the iron formation. Consequently, the distribution of Cu, Pb and Zn in the LOB massive sulphide lens is believed to reflect the original depositional pattern.

The Cu, Pb and Zn distributions within the iron formations are more complex and poorly defined compared to the massive sulphide rock. The base metal distribution is only considered for the LOB. Generally, there is significant Cu-enrichment within the QMIF at the NW margin compared to the AMIF and GMIF at the SE margin. However, the GMIF below the massive sulphide lens at the NW margin also has low Cu contents.

4.5.STRUCTURE

The tectonic events (D1-D4; sensu Joubert, 1971) which are evident in the wider Bushmanland region were considered by Ryan et al. (1986) to have deformed the Broken Hill orebodies and manifest themselves in predominantly polyphase folding (F1-F4). The separate LOB and UOB orebodies plunge parallel to the major regional structural trends. Along the NW margin, the two orebodies merge and have been deformed by two phases of folding. Along the SE margin, the UOB extends further than the LOB, and both orebodies appear not to have been as strongly deformed as in the NW margin of deposit. The LOB and UOB rock-types exhibit a variety of contrasting tectonic features and fabrics. It is not always possible to relate these structures unambiguously to the regional D1-D4 tectonic regime, particularly in the incompetent massive sulphide units.

No evidence was found to suggest an early F1 fold. Ryan et al. (1986) have proposed that the repetition of the iron formation about a fold axis situated above the UOB massive sulphide lenses was the result of duplication by an isoclinal F1 fold. Evidence for their

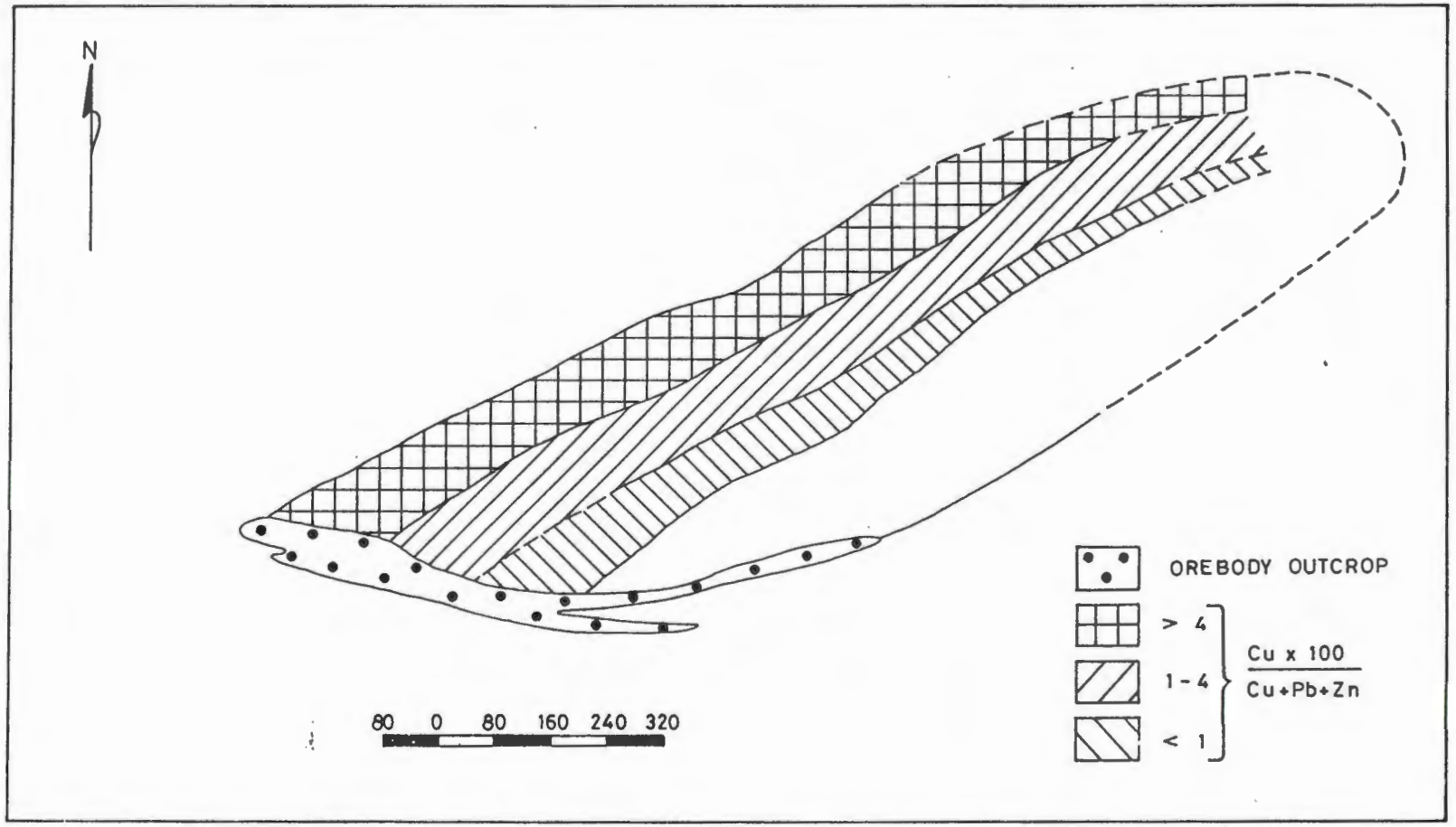

Figure 4.14. Down-plunge projection showing the variation of CuX100/(Cu+Pb+Zn) within LOB massive sulphide rock. Cu decreases from west to east (modified after Smith, 1989; used with permission). Compare with Figure 4.2.

proposed F1 fold is lacking. The thick sequence of iron formation overlying the UOB massive sulphide lenses contrasts with the thinner iron formation below the UOB. The latter should represent a sheared limb of the F1 fold which was not observed. Further consequence of their F1 ought to be evident in the repetition of the ferruginous quartzite below the UOB massive sulphide horizon, which is absent.

The intense D2 deformational event found throughout the Bushmanland Subprovince has been recognized at Broken Hill. The E-W trending quartzites along the Broken Hill ridge show only minor F2 kinks with a geometry that indicates a left lateral sense of movement (Fig. 4.2). These kinks in the surface quartzite are presumed to be of the same fold generation as the isoclinal folds seen in the OES at surface and the isoclinal folding of the LOB at the NW edge of the deposit (Figs. 4.5-4.6). The latter has the same geometry to the kinks in the quartzite. In addition to the different geometry of these folds, further evidence is required to substantiate that the inferred F2 folds are in fact an older fold generation than the F3.

A large F2 fold has also been suggested by Ryan et al. (1986) to have a fold hinge at the SE margin of the LOB and its fold axis trending through the massive sulphide lens. Their proposed F2 fold was suggested to account for the symmetrical sequence of iron formation around the massive sulphide lens. Reservations concerning the duplication of the LOB rock-types by large isoclinal F2 folding have been expressed by Mourant and Smith (1986). This is verified from the lack of folding in underground exposures at the SE margin, in the area of the expected fold closure. Furthermore, the lateral Cu/(Cu+Pb+Zn) metal-zonation might not be preserved if the massive sulphide has been isoclinally folded. Despite this evidence which refutes a large F2 fold at the SE margin, an isoclinal fold with an amplitude of approximately 10 metres has been observed in the surface outcrop. Consequently, apart from F2 folding at the NW margin, it has been assumed that the LOB is duplicated by an F2 fold at the SE margin (sensu Ryan et al., 1986).

At surface, deformation of the quartzite horizons is shown by a large open F3 fold which has a geometry that indicates a right lateral sense of movement (Fig. 4.2). This F3 fold and the F2 kinks in the quartzite plunge at moderate (20-30^0) angles towards the NE. Intense shearing associated with the F3 event has caused the lower quartzite horizon to disappear in

places above the orebody. The F3 Z-shaped fold geometry is also found for both the LOB and UOB rock-types at the NW edge of the deposit. The F3 fold parallels the open flexure within the quartzite, and is persistent from surface to the down plunge extent at 21 level. As a result of the folding, the massive sulphide lens is significantly attenuated and distended particularly in the hinge and along the limbs, respectively. Prominent lineations within the enclosing metapelitic schist trend parallel to the plunge of the fold. Associated with the F3 folding are NE trending shear zones that truncate both LOB and UOB rock-types.

Between 13 and 16 levels, the LOB thickens dramatically, by a factor of at least three, due to stacked isoclinal infolds of iron formation and massive sulphide rock (Fig. 4.6). The geometry of these folds indicates a right lateral sense of movement. They lack the along-plunge continuity and S-shape geometry of normal F2 structures and disappear entirely in the upper levels of the mine. The region in which this major isoclinal folding is found (ie. mainly the 15/600 and 16/600 stopes) is associated with comparatively more complex deformation. It is uncertain whether they represent an F2 fold or are a manifestation of a locally thicker LOB succession which was folded by the D3 event. These folds have amplitudes ranging from 10 to 20 m.

North-trending structures including fractures, monoclinal folds and faults with small displacement are ascribed to D4. Monoclinal folds (F4), trending NW indicated by Ryan et al. (1986) are not conspicuously apparent in underground exposures. These folds were interpreted by the latter authors to occur where there is thickening of the UOB in a N-S direction. Vertically dipping faults with limited displacement (maximum 10 metres) are found locally on 2,3 and 17 levels (Fig. 4.15). The LOB and UOB rock-types are up-thrown by these faults to the west.

The variable nature of the footwall rock underlying the LOB massive sulphide horizon might represent a "pseudo stratigraphy" analogous to Joma Ore Body, Norway (Marshall, 1990) which is thought to be the result of thrusting. There is no obvious evidence to imply widespread thrusting in the LOB succession. A discordant relationship of the lithological units is shown at point P on the drill-section of Figure 4.5. This might suggest at least some evidence for local sub-horizontal tectonism. This feature is anomalous and it is only found in

a single drill-section and would support an F2 fold mechanism.

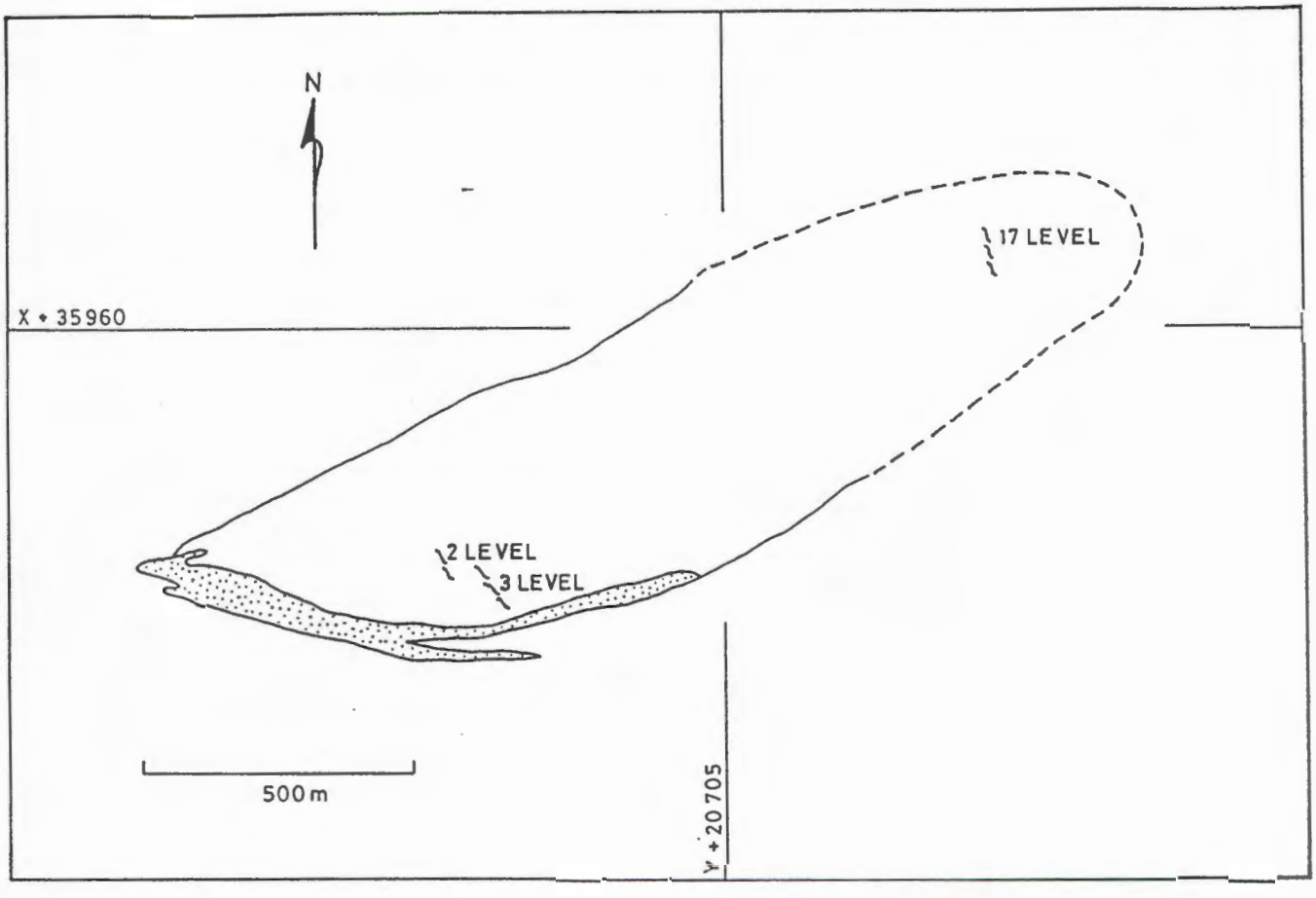

Figure 4.15. Position of faults on down plunge projection. Compare with Figure 4.2.

5.PETROGRAPHY

Thin sections of schist and LOB rock-types including iron formation, massive sulphide rock, aggregates and biotite lenses within the massive sulphide rock, and garnetiferous quartzite were examined. Particular attention was given to thin sections of samples from the silicate-rich iron formation bands that were analysed for bulk composition.

5.1.SCHIST

The foliation within the schist from the Ore Schist Formation is defined by biotite, muscovite, sillimanite and elongated quartz. Fresh core samples of this rock generally have a grey appearance but become darker with increasing proportions of biotite. The schists examined consist predominantly of quartz and biotite, with lesser proportions of muscovite and sillimanite (Table 5.1). Trace amounts (< 1 vol.%) of chlorite are often associated with fractures.

Table 5.1. Percentage modal proportions of minerals in the Ore Schist Formation.

	BHS22 (US)	1917-N6 (HS)
Quartz	21	40
Muscovite	25	5
K-feldspar	2	-
Garnet	Sc	1
Biotite	12	22
Sillimanite	20	15
Sericite	20	18

(-) not observed.
Modal proportions estimated from microscopic inspection.
US- Upper Footwall Schist. HS- Hangingwall Schist.

In thin-section, most biotite grains were found partly altered to sericite, in particular at the ends of the long axis. Biotite grains are mostly coarse-grained (1-1.5 mm) and fewer grains are 1.0-0.5 mm in size. Biotite grain shapes are mostly subhedral. The biotite is often in contact with unaltered muscovite which is of similar grain-size. The muscovite appears to be mimetic along the foliation defined by the biotite, with fewer finer-grained cross-cutting muscovite. The euhedral muscovite commonly has rounded inclusions of quartz (0.2 mm). The edges of most muscovite grains have been altered to fine-grained sericite (<0.1 mm). The finer-grained mica occurs in small aggregates that cut across euhedral muscovite (Fig. 5.1). Quartz grains (<1 mm) are highly strained and elongated. In all samples of schist, fine-grained sericite was observed to have grown around and within quartz grains. In some samples, quartz grains define < 0.75 mm-thick bands which have subordinate amounts of biotite. Sillimanite occurs either as a fibrolitic or nodular variety. Quartz and sillimanite intergrowths are ubiquitous. Poikiloblastic garnet grains are elongated parallel to the foliation and have a similar grain-size as quartz. Inclusions of quartz (0.2 mm) in garnet have the same orientation as the foliation.

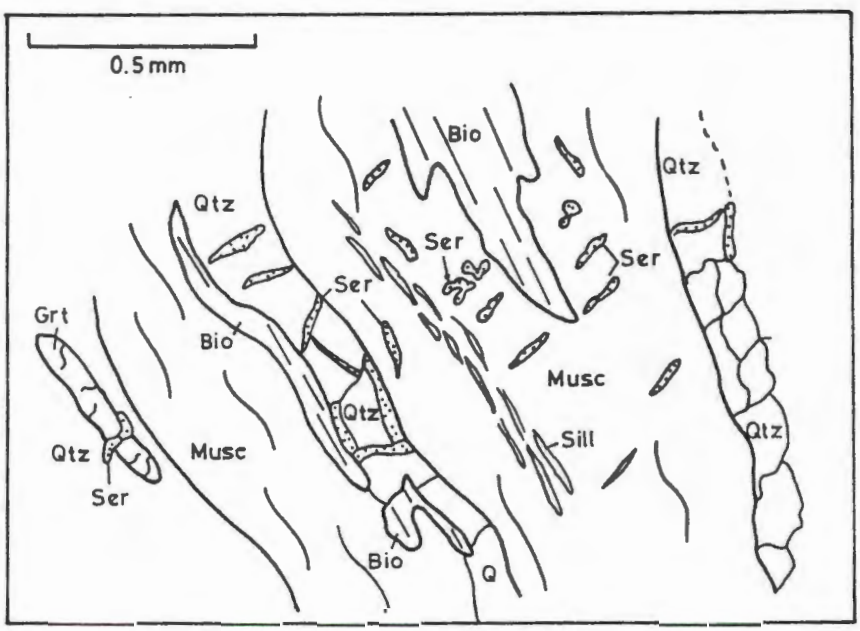

Figure 5.1. Foliated garnet-biotite-sillimanite-muscovite-quartz schist of the US. Note overgrowth of muscovite (Musc) on biotite (Bio). Fine-grained mica, sericite (Ser), cross-cuts coarser grained euhedral muscovite and has overgrown quartz (Qtz) grains (Sample BHS22).

K-feldspar porphyroblasts have been reported by Lipson (1990) to comprise 2-5 vol.% of the schist. The K-feldspar is often poikiloblastic and exhibit perthitic intergrowths (Lipson, 1990). The K-feldspar porphyroblasts were not observed in the five thin-sections of schist examined in this study.

5.2.IRON FORMATION

The three iron formation varieties, GMIF, AMIF and QMIF were defined in Chapter 4 by their proportions of silicate-rich bands. Each iron formation, where preserved, exhibits remarkable compositional banding which represents bedding. The banding is evident from the sharp mineralogical change where amphibole-, garnet-, quartz- and magnetite-rich layering is between 1 and 10 cm-thick. At this scale, the banding is referred to as mesobands. In thin section, delicate 1-2 mm-thick bands are defined as microbands. These are noted by changes in the proportion of mineral phases and by alternating layers with distinct mineral paragenesis. For example, microbands that contain 65 vol.% garnet and 35 vol.% quartz alternate with those that contain 65 vol.% quartz and 35 vol.% garnet or alternate with bands almost entirely of amphibole and olivine. Contacts between individual silicate bands are generally sharp and well defined. Garnet-rich bands grading within <1 to 2 cm into fayalite-amphibole-rich bands are rare.

5.2.1.Garnet mesobands

Garnet mesobands are commonly 1-3 cm thick, but seldom wider than 5 cm and mesobands with thicknesses up to 20 cm are rare. The garnet mesobands are interbanded with amphibole, olivine, quartz and magnetite mesobands which can be traced over tens of metres. The distinct reddish colour of garnet bands contrasts with other bands which have a darker appearance. This colour contrast serves as an excellent marker for recognizing folding within the iron formation.

Modal proportions of minerals within garnet mesobands are shown in Table 5.2. Within some mesobands there are up to 5 mm-thick bands that have varying proportions of quartz and garnet. Garnet is mostly fine-grained (0.2-0.4 mm) and almost always occurs as equidimensional grains that show no sign of a dimensional fabric. Fine inclusions (0.1-0.2 mm) of quartz, magnetite, sphalerite and zircon are often found in a coarser-grained (0.5-1.0

mm) garnet. These inclusions were unlikely to have formed as exsolved phases in garnet but were engulfed by the growth of garnet. Optically, the garnet grains are homogeneous. Garnet coexists with apatite of similar grain size. Where microbanding was found, garnet and apatite form small clusters (1-1.5 mm) which occur as mm-thick bands that alternate with quartz-rich microbands (Fig. 5.2). Quartz grains exhibit equigranular textures and are generally coarser-grained (0.3-0.7 mm) than garnet and apatite. Mutual quartz boundaries are straight to curved and intersect at triple point junctions. In some samples, quartz is elongated parallel to the banding.

Table 5.2. Percentage modal proportions of minerals in garnet iron formation mesobands.

	BHG1	BHG2	BHG4	BHG6	BHG13	BHG15	BHG16	BHG17
Quartz	25	33	33	22	10	45	36	39
Amphibole	-	-	-	-	15	-	-	8
Olivine	-	-	-	-	-	-	-	4
Garnet	62	34	27	64	63	23	51	25
Biotite	-	4	15	Sc	-	3	-	2
Apatite	8	14	14	7	7	1	2	4
Sillimanite	-	-	-	-	Tr	-	-	-
Zircon	-	-	-	-	-	-	Sc	-
Chlorite	-	Sc	-	-	-	-	-	3
Magnetite	5	14	8	6	4	15	10	14
Sulphides	-	-	2	Tr	-	12	-	Sc
Gahnite	-	-	Tr	-	-	Tr	-	-
Barite	Tr	Tr	-	Tr	-	-	1	1

(-) not observed.
Modal proportions estimated from 300 point counts.

Other minerals comprising minor percentages are magnetite, biotite, barite, amphibole, sphalerite and chlorite in decreasing proportions. Anhedral to subhedral magnetite is coarse-grained (1-4 mm) and is disseminated within the finer-grained garnet-quartz-apatite 'matrix'. Some grains are poikiloblastic with inclusions of garnet (Fig. 5.3). Magnetite has irregular grain boundaries and is often enclosed in quartz. Biotite with green-brown pleochroism has high barium concentrations (Chapter 6.5). Biotite has a random orientation and in a few samples it exhibits a marked dimensional orientation parallel to the banding. It might either

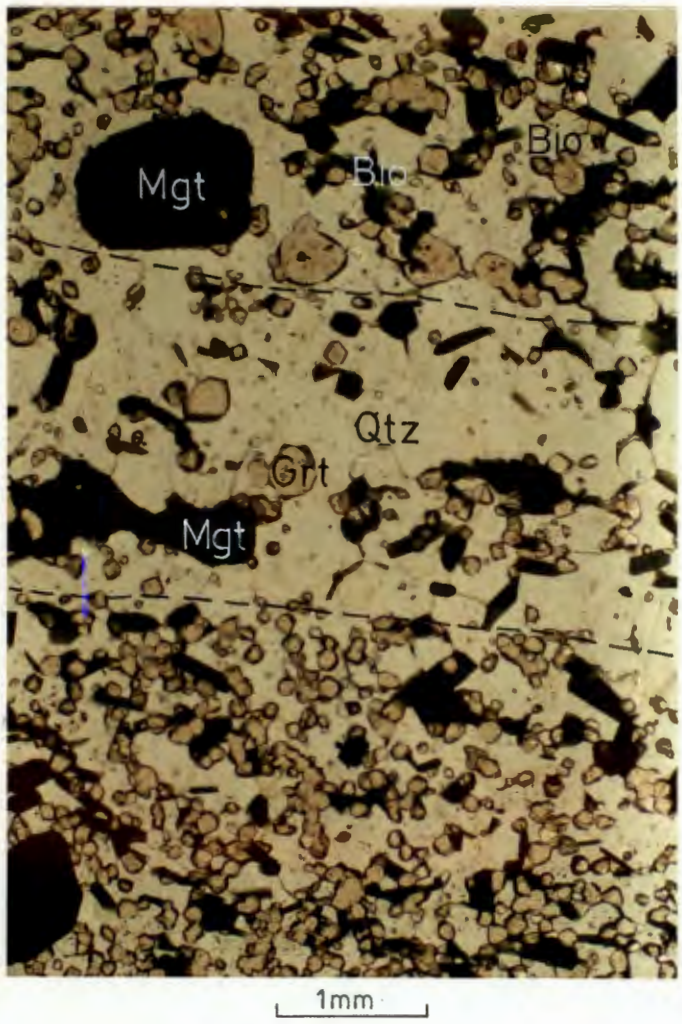

Figure 5.2. Photomicrograph of fine-grained garnet (Grt) in mm-thick microbands showing garnet-rich and quartz-rich bands. Note coexisting dark green Ba-rich biotite (Bio) and magnetite (Mgt). Apatite (Ap) appears similar to garnet (Grt) but is colourless.

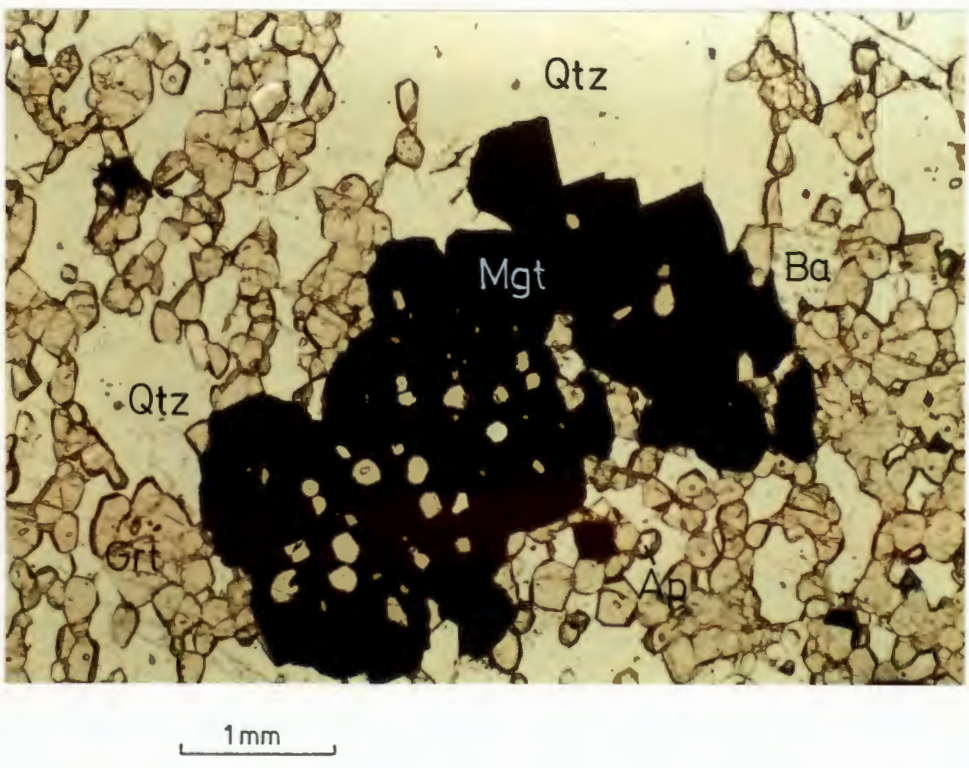

Figure 5.3. Photomicrograph of poikiloblastic magnetite (Mgt) in garnet-rich iron formation mesoband. Other minerals present are quartz (Qtz), apatite (Ap) and barite (Ba).

partly envelope garnet exhibiting an embayed texture or occur as fine discrete grains adjacent to garnet (Fig. 5.4). Minor barite coexists with or without biotite. Barite occurs as subhedral grains and it is slightly more coarse-grained than the garnet (0.4-0.5 mm). Amphibole was observed to have equilibrium textures with garnet. The amphibole is medium-grained (0.5-1.0 mm) and is mostly disseminated in the garnet mesobands. Only one sample, BHG15, contained significant sphalerite and galena. These sulphide minerals have anhedral forms. Chlorite occurs in 0.2 mm-thick fractures and locally, it forms as pseudomorphs after garnet.

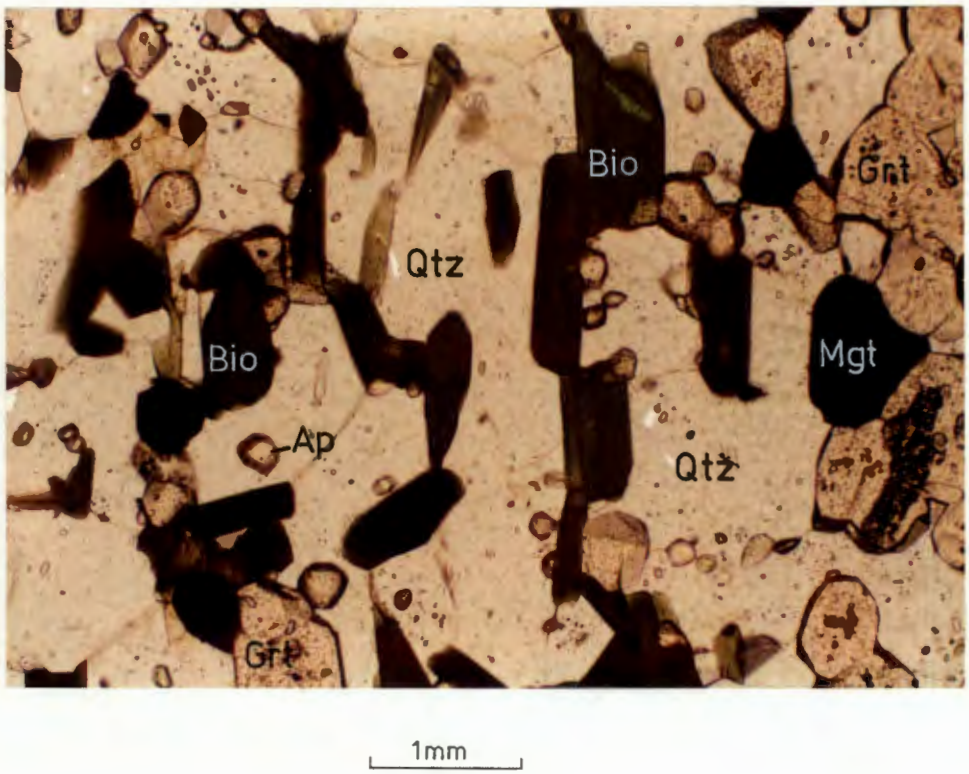

Figure 5.4. Ba-rich biotite (Bio) occurring as discrete grains adjacent to garnet (Grt) and quartz (Qtz) in garnet-rich mesoband.

5.2.2. Amphibole-olivine mesobands

Hand specimens of amphibole-rich bands have a dark green colour. Lighter appearances occur with increased proportions of olivine and quartz. These bands consist predominantly of amphibole, olivine, quartz and magnetite (Table 5.3).

Amphiboles occur as euhedral to subhedral laths which exhibit prominent polysynthetic twinning. Amphiboles are colourless-to-light green. The long axes of amphiboles are mostly

Table 5.3. Percentage modal proportions of minerals in amphibole iron formation mesobands.

	BHA 5	BHA 7	BHA 8	BHA 9	BHA 10	BHA 11	BHA 12	BHA 18	BHA 19	BHA 25
Quartz	28	2	39	12	9	26	67	18	20	39
Amphibole	37	6	21	31	15	19	19	52	24	5
Olivine	30	62	-	24	45	38	-	22	48	36
Garnet	-	1	1	14	8	2	-	-	2	2
Biotite	1	1	8	-	-	-	-	-	-	-
Apatite	-	3	Tr	Sc	1	Sc	-	-	-	-
Sillimanite	-	-	Tr	-	-	2	-	2	-	-
Opague	4	24	34	15	18	14	14	2	6	16
Sulphides	-	-	-	Tr	-	-	-	-	-	1
Barite	-	-	-	-	Tr	Sc	-	-	-	

(-) not observed.
Modal proportions estimated from 200 point counts.

parallel to the banding (Fig. 5.5 a-b), but in places some amphibole with a random orientation is found. Their grain-size varies between 0.5 mm and 3 mm with an average of approximately 2 mm. Amphibole in many thin sections, but not all grains, exhibits exsolution of an opaque mineral which has a brown black colour. Olivine and quartz are often embayed into amphibole and their grain boundaries are sharp and smooth. This texture indicates equilibrium conditions for the assemblage. Olivine grains are subhedral to anhedral with prolific micro-fractures. Less common is poikiloblastic olivine which has inclusions of quartz, magnetite and lesser amphibole. Quartz grains vary in size 0.5 and 1.0 mm. Quartz grains in mutual contact with each other exhibit serrated grain-boundaries. Magnetite is subhedral to anhedral. Magnetite occurs either as fine-grained (<0.2 mm) anhedral blebs interstitial to silicate minerals or as isolated subhedral grains. Microbands of magnetite with thicknesses < 2 mm have irregular contacts with the silicate bands. In all thin sections examined, magnetite appears unstable. Biotite is mostly present in accessory proportions in only few of the mesobands. If present, green-brown pleochroic biotite usually occurs as either subhedral laths or as minor euhedral blocky micas. Biotite is randomly orientated relative to the banding. Garnet in the amphibole mesobands is medium-to-coarse-grained

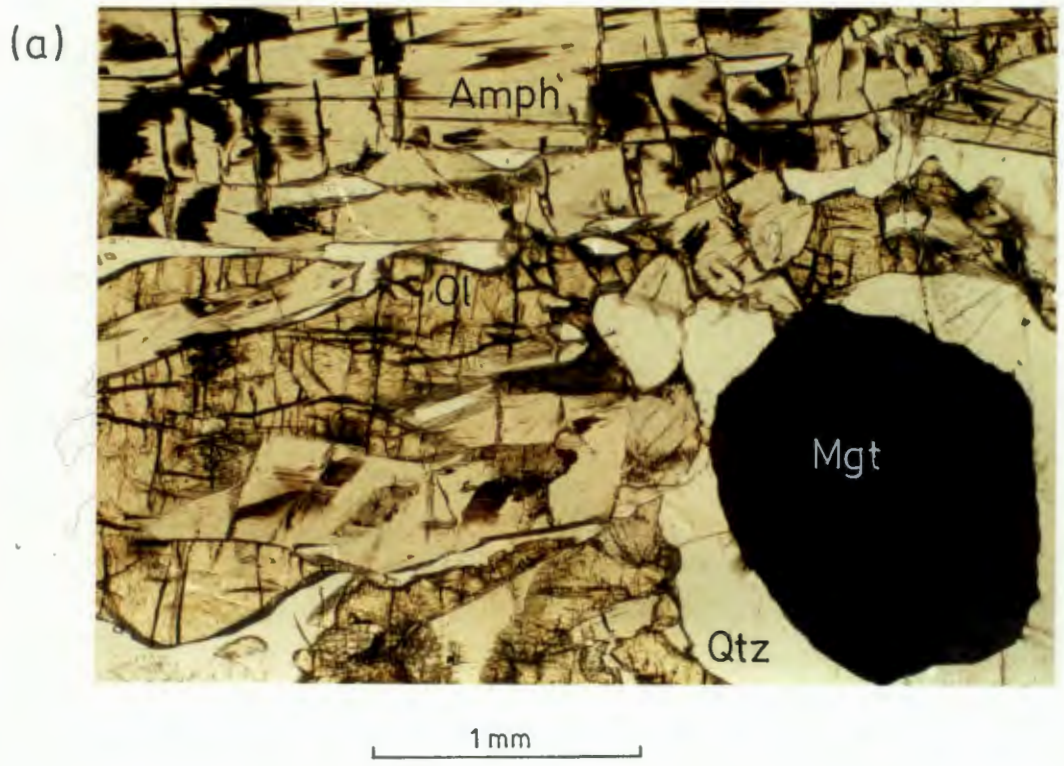

Figure 5.5. (a) Photomicrograph showing alignment of amphibole (Amph) and olivine (Ol) in amphibole-rich iron formation mesoband. Opaque exsolution in amphibole revealed no compositional difference in microprobe analysis. Quartz (Qtz) encloses magnetite (Mgt) in the bottom right corner. (b). Smooth grain-boundaries between amphibole (Amph) and olivine (Ol) indicating equilibrium texture.

(0.5-1.2 mm). Garnet is mostly poikiloblastic and contains significant quartz, amphibole, and magnetite and minor sphalerite inclusions. These garnets are highly embayed by quartz, olivine and amphibole.

5.2.3.Quartz mesobands

Quartz mesobands in the LOB are seldom homogeneous and are defined by their high content of quartz with subordinate proportions of silicate minerals and magnetite (Table 5.4). The quartz mesobands in the QMIF are generally <1 cm in thickness and the banding has commonly been tectonically disrupted. These bands have a light grey colour and their appearance becomes darker with increasing contents of magnetite.

Table 5.4. Percentage modal proportions of minerals in quartz-rich mesobands.

	10/700	BHU1891-13
Magnetite	30	10
Quartz	65	65
Amphibole	-	1
Biotite	Sc	6
Sillimanite	-	Sc
Garnet	3	15
Apatite	-	1
Sulphide	2	-

(-) not observed.
Sc - scarce (<0.5 vol.%).
Modal proportions estimated from microscopic inspection.

In thin section, quartz-rich mesobands are characterized by significant microbanding with thicknesses generally <1 mm. This microbanding is defined by alternating compositional bands that are nearly pure SiO_2 (mostly quartz) and Fe-rich ones (magnetite). Quartz is mostly medium-grained (0.3-0.4 mm) and is granoblastic in texture within individual microbands. Also common is fine-grained (<0.15 mm) quartz which occurs in thin (1 mm)

elongated mylonitic lenses (mortar texture) within microbands. Quartz grains have extreme undulose extinction and the grain boundaries are sutured. Other microbands consist mostly of garnet-biotite-quartz and rarely of pyroxferroite-amphibole-quartz. Magnetite is medium-grained (0.2-0.4) and occurs as anhedral "blebs".

5.2.4.Massive magnetite iron formation

Massive magnetite iron formation has a black appearance. It consists predominantly of magnetite with lesser biotite, muscovite, quartz, garnet, tourmaline, K-feldspar, gahnite and sphalerite (Table. 5.5). Hand specimens appear homogeneous and locally contain coarse-grained porphyroblasts of garnet (1-6 cm), tourmaline (0.5-1.5 cm) and books of green biotite (1-2 cm).

Table 5.5. Percentage modal proportions of minerals in the massive magnetite iron formation.

	BHM15	TS6
Magnetite	75	80
Quartz	10	7
Muscovite	8	-
Biotite	2	4
Gahnite	-	2
Chlorite	2	2
Sillimanite	1	-
Garnet	2	-
Feldspar	-	5

(-) not observed.
Modal proportions estimated from microscopic inspection.

In thin section, magnetite is medium-to-coarse-grained (0.2-1.5 mm) with a granoblastic texture. Mutual grains have straight common boundaries. Interstitial biotite, muscovite and quartz are fine-grained (0.2-0.5 mm) and exhibit anhedral to subhedral forms. These minerals have serrated-type sutured grain boundaries with magnetite.

Highly strained elongated quartz and muscovite define a poorly developed foliation parallel to the banding. In sample TS6, coarse-grained (< 3 mm) quartz has a webbed texture with anhedral magnetite. Poikiloblastic garnets are anhedral with deeply embayed edges. Some garnets exhibit replacement by chlorite. Two varieties of biotite were identified: (i) medium-grained (0.2-1.0 mm), pleochroic yellow, subhedral grains, and (ii) coarse-grained (>5 mm) pleochroic pale green euhedral grains. The former type coexists with muscovite of similar grain-size and forms webbed textures with anhedral magnetite. The latter type, however, has limited distribution and appears to be unaffected by the intense deformation.

Tourmaline porphyroblasts are pleochroic grey blue, poikiloblastic and have embayed edges. The inclusions within the tourmaline occupy as much as 50 vol.% of the individual grains. Fine-to-medium-grained (0.1-0.3 mm) anhedral magnetite comprises 95 vol.% of the inclusions whereas garnet and gahnite occur as minor proportions.

Galena and sphalerite are either scarce or were not identified in the thin sections examined. Where observed, the sulphide minerals are fine-grained and exhibit anhedral forms. Sphalerite is often parallel with the fabric. Coarse-grained remobilized sphalerite common in MMIF at the west fold closure was not examined in this study. The other common Zn-rich phase is medium-grained (<1 mm) anhedral gahnite. It occurs as thin streaks between magnetite grains. Gahnite is also locally developed with a webbed texture enclosing magnetite grains. Thin 0.1-0.2 mm wide fractures truncate all other grains and are filled with chlorite.

5.3. MASSIVE SULPHIDE ROCK

The massive sulphide rock of the LOB is either banded, massive in appearance or occurs as a fine-grained mylonite. Because of its high pyrrhotite content, the massive sulphide rock has a bronze colour.

The banded variety has 1-5 mm-thick pyrrhotite-rich bands alternating with quartz-rich bands of similar thicknesses. Banding is typically wispy and discontinuous (10-30 cm in length) which is the result of tectonic disruption. It was assumed that banding was originally continuous rather than its development as thin lenticular bands. There appears to be no

preserved soft-sediment slump structures. Pyrrhotite bands have irregular contacts with the quartz-rich bands. Pyrrhotite, galena, sphalerite and chalcopyrite are generally fine-to-medium-grained (0.1-1.0 mm) and exhibit a variety of grain forms (anhedral and euhedral). Galena often shows annealing with pyrrhotite. Sphalerite often contains inclusions of chalcopyrite and pyrrhotite. Chalcopyrite is mostly disseminated and interstitial with respect to the silicate minerals.

Quartz is medium-grained (0.15-0.6 mm) and is anhedral. Quartz in contact with pyrrhotite exhibits irregular serrated grain boundaries. Colourless euhedral muscovite occurs as a minor constituent (<5 vol.%), is medium-grained (<1 mm) and is partly replaced by sericite. Quartz and muscovite are not found in contact with each other, with the exception of sample TS15 where quartz is embayed into muscovite. Fibrolitic intergrowths of sillimanite are common in the muscovite. Red-brown biotite is an accessory mineral and appears altered. Garnet has a similar grain-size to quartz. Garnet is often partly replaced by chlorite. Gahnite occurs as fine subhedral-to-euhedral grains which commonly exhibit poikiloblastic textures. Inclusions within gahnite are sphalerite and quartz. Equant grains of gahnite are often enveloped by biotite grains and vice versa.

Mica-rich lenses within the massive sulphide rock consist mostly of colourless muscovite with minor pleochroic red biotite. Muscovite occurs as coarse (1.0-1.5 mm), euhedral, blocky grains that are randomly orientated and meet in triple point junctions. Few grains have fine-grained (<0.15 mm) sericite along the rims. Enclosing the muscovite-rich lenses is a 1-to-3 mm thick rim of coarse-grained (>1.0 mm) gahnite. The embayed muscovite and biotite with gahnite exhibit smooth grain boundaries which are curved-to-straight, indicating an equilibrium assemblage.

Aggregates within the massive sulphide rock are garnet- and quartz-rich. Subordinate amounts of tourmaline, biotite, gahnite, sphalerite and biotite occur as minor portions. All minerals are coarse-grained (1- 30 mm) and have euhedral crystal forms (Fig. 5.6).

5.4.GARNET QUARTZITE

Garnet quartzite in hand specimen has a light grey colour but becomes more red in

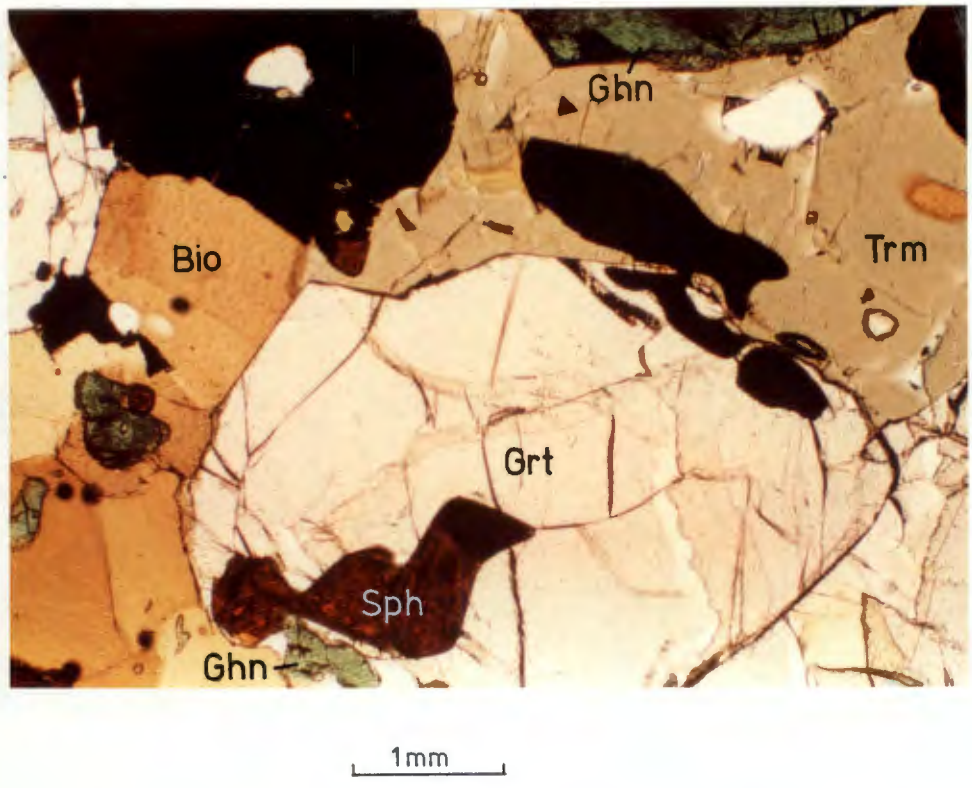

Figure 5.6. Photomicrograph of an aggregate in massive sulphide rock with garnet (Grt), tourmaline (Trm), gahnite (Ghn), sphalerite (Sph) and biotite (Bio).

Table 5.6. Percentage modal proportions of minerals in garnet quartzite.

	TS13	BHGQ23	1917-N2
Quartz	39	68	70
Garnet	50	25	19
Biotite	1	1	5
Apatite	4	4	2
Sillimanite	3	-	-
Gahnite	Tr	-	3
Chlorite	Tr	-	-
Opaque	2	2	Tr
Sulphides	Sc	-	-

(-) not observed.
Modal proportions estimated from microscopic inspection.

appearance with increasing proportions of garnet. Modal proportions of garnet quartzite reveal high contents of quartz generally in excess of 70 vol.% with subdominant garnet and biotite (Table 5.6). The garnet quartzite contains minor (<5 vol.%) apatite, sillimanite, magnetite and K-feldspar and trace contents (<1 vol.%) of gahnite, sulphide, chlorite, zircon and staurolite.

In thin section, some garnet quartzite samples have 1-3 mm-thick microbands of quartz which alternate with garnet-biotite-apatite-rich microbands (Fig. 5.7). Quartz grains form equant granoblastic textures but are more commonly elongated parallel to the microbanding. Quartz varies from 0.4 to 1.5 mm in size and have sutured mutual grain-boundaries. The intimate association of garnet and biotite defines a foliation parallel to the micro-banding. Garnet is medium-grained (0.2-0.4 mm) and occurs as equant grains. Similar to the garnet mesobands and micobands, garnet in the GQ occurs mostly in clusters forming a granoblastic polygonal texture (Fig. 5.7).

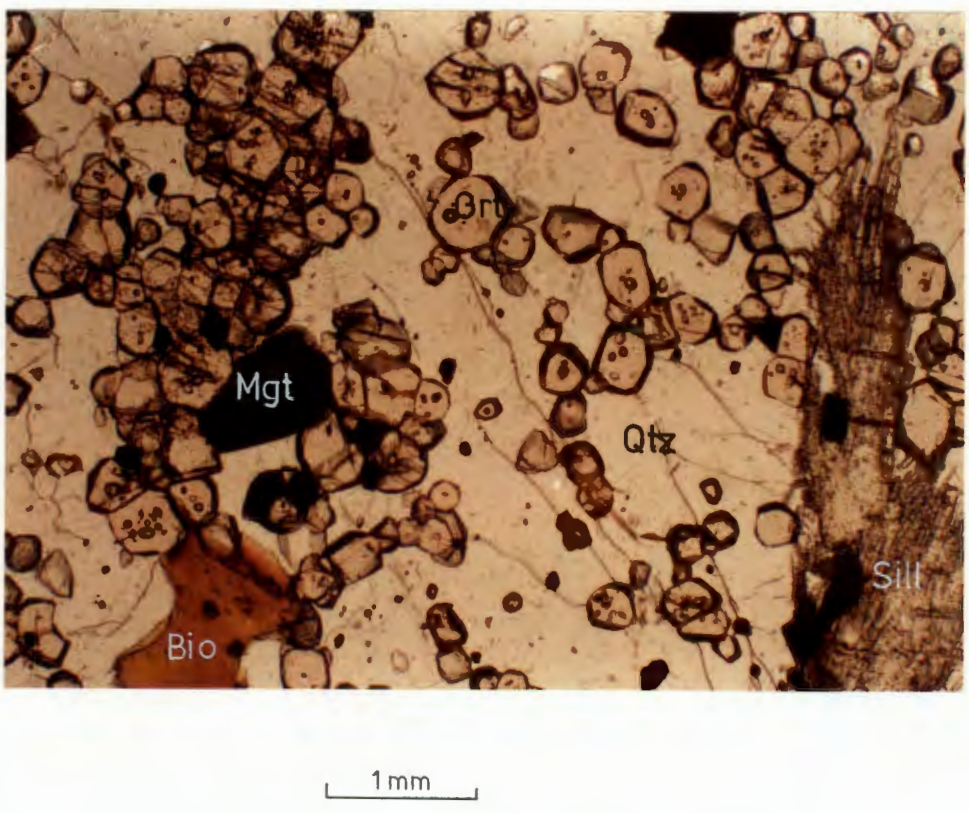

Figure 5.7. Photomicrograph of garnet quartzite (sample TS13) showing clusters of garnet (Grt), coarser grained quartz (Qtz), sillimanite (Sill) and minor biotite (Bio).

Garnet also contains fine-grained (<0.15 mm) inclusions of quartz, apatite, magnetite and minor zircon. Garnet in contact with biotite has straight grain boundaries defining equilibrium textures. Apatite has similar grain-shapes as garnet but with a more restricted grain-size (0.2-0.3 mm). Sillimanite was found as fibrolitic nodules in samples 3-2609 but more persistently it occurs as thin needle-like grains. Chlorite occurs either in <1 mm-thick fractures or as a replacement of garnet and biotite. Gahnite is scarce (<0.5 vol.%) and was found in close association with garnet and biotite. Where associated with garnet, gahnite is medium-grained (<0.4 mm), and has an anhedral form. In some cases, gahnite has partly replaced garnet. Anhedral staurolite is scarce and only a single grain was recognized. It occurs as a relict mineral in close association with gahnite.

6.MINERAL CHEMISTRY

The compositions of the minerals examined were determined by electron microprobe analysis. The technique, standards, lower limits of detection and errors are described in Appendix A.

6.1.GARNETS

Garnets in the LOB are associated with a variety of rock-types. In order of decreasing modal proportions, these are banded iron formation, garnet quartzite, massive sulphide rock and ferruginous quartzite. Garnets are mainly almandine-spessartine solid solution with small pyrope and grossular components (Fig. 6.1a-b). A total of 147 garnet compositions was determined from 38 slides. The total Fe content is expressed as FeO. The data were normalized on the basis of 24 oxygens and the Fe_2O_3 content was calculated assuming Fe^{3+} to fill vacant octahedral sites only. The Mn content in garnet within the various rock-types is variable. Average spessartine contents in garnet analysed for the individual rock-types are 20.9 mole % in the ferruginous and garnet quartzite, 43.1 mole % in the massive sulphide rock, 14.1 mole % in the metapelitic schists, 42.9 mole % in the amphibole iron formation mesobands and 40.1 mole % in the garnet iron formation mesobands (Table 6.1). The spessartine component in garnet is most variable within the garnet iron formation mesobands compared with the former four rock-types (Fig. 6.1a-b). A general trend is also shown for all the garnet compositions. The pyrope content in garnet is low for almandine-poor compositions. The pyrope content increases as the garnet compositions becomes more almandine-rich.

The amount of andradite component in the garnet is generally very low (Table 6.1) indicating that most of the iron in the garnets is in the reduced divalent form. The andradite component is smallest in the massive sulphide rock compared to the schist and silicate-rich iron formation mesobands. Within the iron formation, amphibole-rich iron formation mesobands are characterized by higher andradite component in garnet than the garnet-rich iron formation mesobands. This is directly correlated with a higher proportion of magnetite in the amphibole-rich iron formation bands.

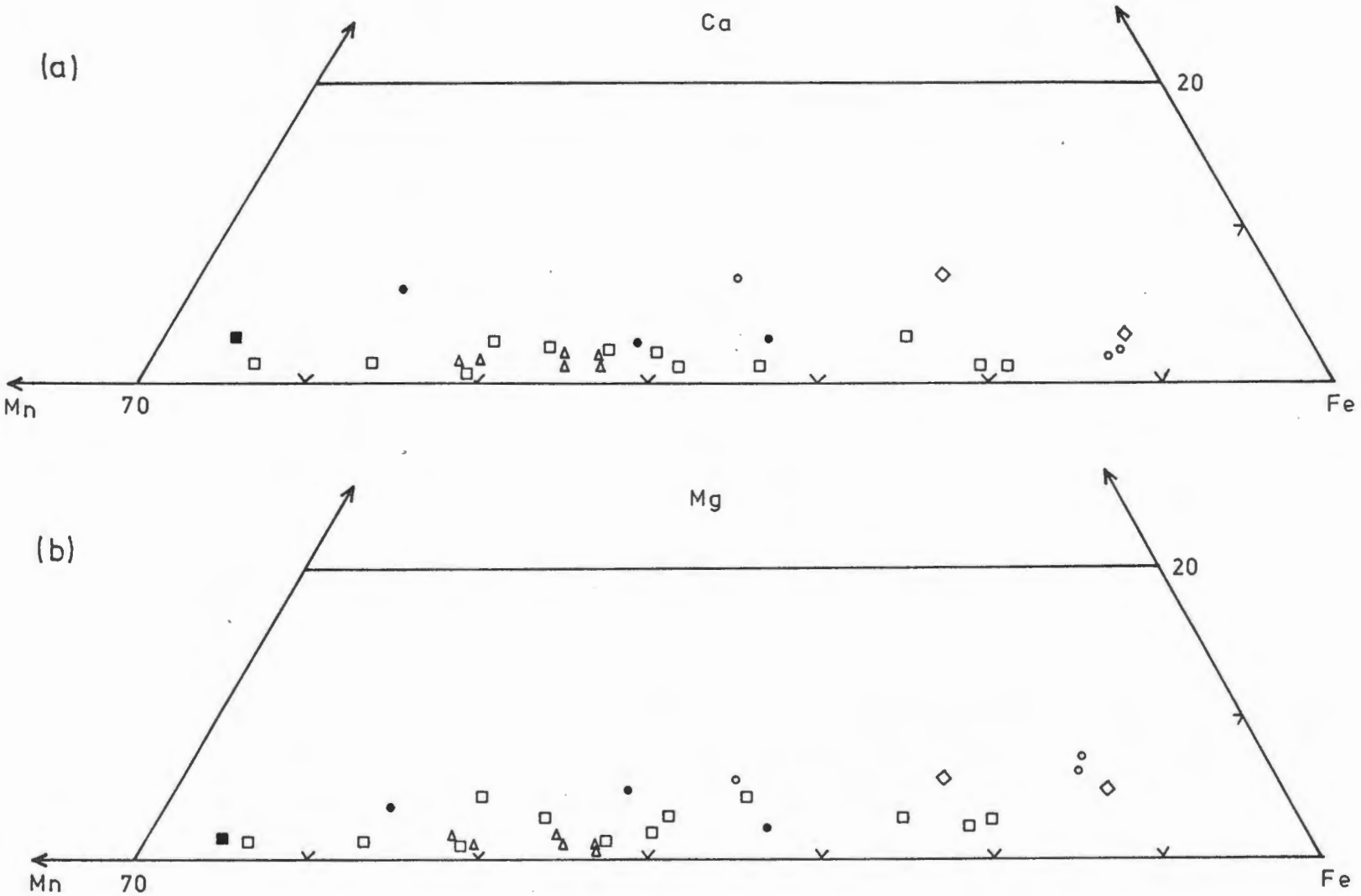

Figure 6.1. Compositional variation with respect to (a) Fe, Mn, Ca, and (b) Fe, Mn, Mg of garnets in various rock-types. Each data point represents the average of the analyses in a single sample. (Symbols for rocks: triangle- amphibole iron formation mesoband, open square- garnet iron formation mesoband, diamond- undifferentiated schist, filled square- quartz magnetite iron formation, filled circle- massive sulphide rock, open circle- ferruginous and garnet quartzites).

Table 6.1. Average electron microprobe analyses of garnet.

wt. %	Schist (HS+US) (N=3)		MSR (N=2)		Garnet mesoband (N=9)		Amphibole mesoband (N=10)		GQ and FQ (N=5)	
	Ave.	1σ	Ave.	1σ	Ave.	1σ	Ave.	1σ	Ave	1σ
SiO_2	36.24	0.37	36.57	0.20	36.48	0.13	36.30	0.11	36.79	0.15
Al_2O_3	21.06	0.30	20.90	0.04	20.41	0.11	20.31	0.11	21.15	0.13
FeO	34.11	1.84	21.84	4.48	25.66	2.21	24.36	1.17	31.62	3.48
MnO	6.31	1.30	19.06	3.77	17.05	2.24	19.06	1.09	9.37	3.42
MgO	1.15	0.15	1.00	0.23	0.52	0.09	0.33	0.03	1.60	0.16
CaO	1.57	0.54	1.44	0.84	0.48	0.07	0.52	0.03	0.94	0.38
Total	100.44		100.81		100.60		100.88		101.47	
SiIV	5.86	0.04	5.94	0.01	5.97	0.00	5.95	0.01	5.92	0.01
AlIV	0.13	0.04	0.06	0.01	0.03	0.00	0.05	0.01	0.07	0.01
T site	6.00	0.00	6.00	0.00	6.00	0.00	6.00	0.00	6.00	0.00
AlVI	3.87	0.03	3.94	0.01	3.91	0.02	3.86	0.02	3.94	0.02
Fe^{3+} *	0.14	0.04	0.08	0.01	0.09	0.02	0.14	0.02	0.07	0.02
O site	4.03	0.01	4.02	0.00	4.01	0.00	4.01	0.00	4.02	0.00
Fe^{2+}	4.60	0.27	2.88	0.62	3.41	0.30	3.18	0.16	4.18	0.46
Mn	0.86	0.17	2.62	0.51	2.36	0.31	2.64	0.15	1.27	0.47
Mg	0.27	0.04	0.24	0.06	0.12	0.02	0.08	0.00	0.38	0.37
Ca	0.27	0.09	0.25	0.14	0.08	0.01	0.09	0.00	0.16	0.06
A site	6.01	0.01	6.00	0.00	5.99	0.00	6.00	0.00	6.01	0.00
Alm	74.56	3.91	47.39	9.94	54.93	4.26	51.84	2.60	68.76	7.73
Sps	14.08	2.87	43.07	8.51	40.13	4.26	42.98	2.42	20.95	7.70
Prp	4.48	0.59	3.94	0.91	2.01	0.31	1.31	0.10	6.34	0.61
Grs	4.40	1.54	4.11	2.33	1.40	0.16	1.49	0.08	2.66	1.10
Andr	2.37	0.67	1.31	0.23	1.52	0.28	2.35	0.28	1.12	0.34

Cations calculated on the basis of 24 oxygens.
* calculated from formula where Fe^{3+} fills octahedral sites.
nd - not detected (K_2O, Na_2O and TiO_2).
N - number of samples.

In the discussion that follows, the variation of garnet composition or lack of it, was examined on four scales, viz: (1) individual grains, (2) microbands (3) mesobands and (4) macrobands. The significance of the distribution of Mn in garnet is discussed in Chapter 8.

In general, single garnet crystals (0.2 - 1.5 mm) are relatively homogeneous. Slight differences in composition between cores and rims of garnet in three iron formation mesobands are shown in Figure 6.2. Compositional differences of all the analyses are summarised in Figure 6.3, which shows enrichment of Fe and Mn in rims whereas cores are enriched in Mg. Uniform garnet compositions in the Aggeneys area have previously been reported by Lipson (1978), Stumpfl (1979) and Rozendaal (1982). Similarly, Stanton and Williams (1978) reported that single garnets in iron formation at Broken Hill, Australia, which have experienced high-grade metamorphism, exhibit uniform core and rim compositions. In contrast, single manganiferous garnets within stratabound deposits in the Eastern Alps which are situated in low-grade metamorphic terrains (greenschist facies, up to 400 ^{o}C) are chemically heterogeneous (Stumpfl, 1979). This is to be expected considering significantly lower diffusion rates of Fe, Mg, Mn and Ca in garnet at these lower temperatures (Spear, 1991).

Garnets show no marked compositional changes from one mineral grain to the next on the scale of 1-30 mm within mineralogically homogeneous mesobands (Fig. 6.4a-b). There may be more significant compositional changes across millimetre thick microbands (Fig. 6.4c). Garnet compositions are also homogeneous along bands on the scale of 1-20 mm.

Within the LOB, there is a marked compositional variation of garnet from one lithology to the next. The variations of Fe, Mn and Mg are shown for boreholes BHU 1917, 1891 and 2609 which represent typical profiles through the LOB sequence (Fig. 6.5). The high spessartine contents between 37.6 and 49.8 mole % in garnet within the massive sulphide rock are comparable with the spessartine contents in the garnet and amphibole iron formation mesobands. The spessartine content remains enriched in the iron formation enclosing the massive sulphide rock. There is a marked change in the Mn content in garnet between the iron formation and the overlying ferruginous and garnet quartzite (BHU 1917 and BHU 2609). The ferruginous and garnet quartzite typically have garnet with Mn contents less than

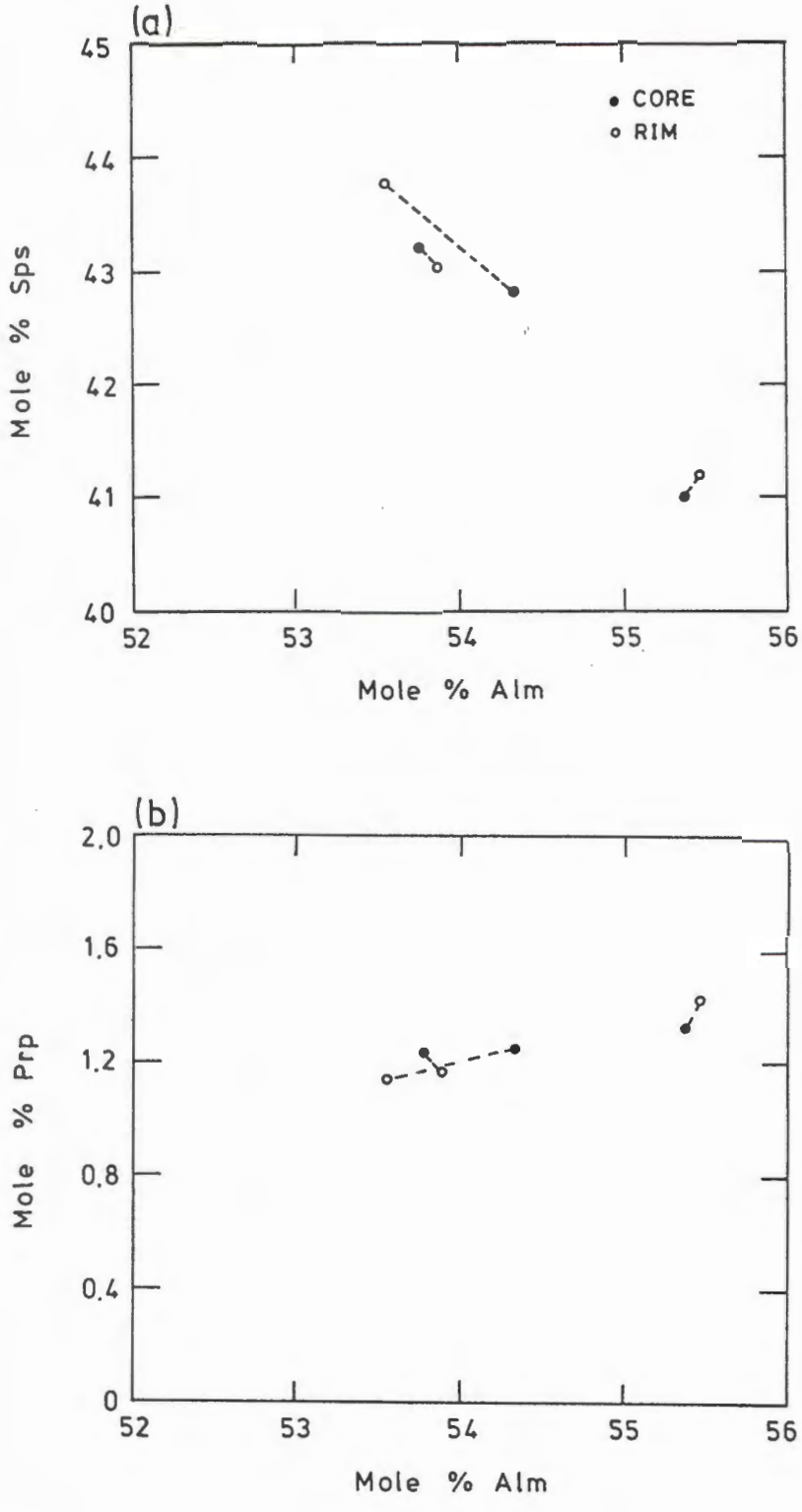

Figure 6.2. Plots of mole % almandine versus (a) mole % spessartine and (b) mole % pyrope for selected garnet core and rim compositions. No preferred enrichment or depletion of cations was found within garnet of different iron formation mesobands.

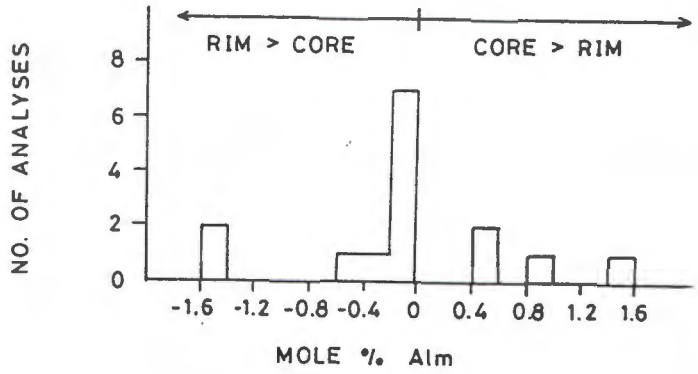

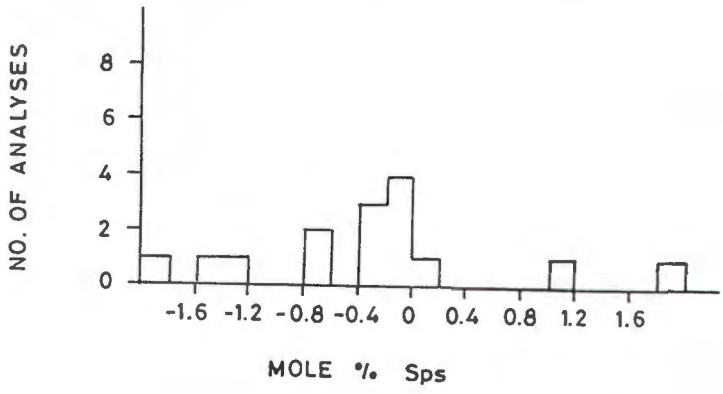

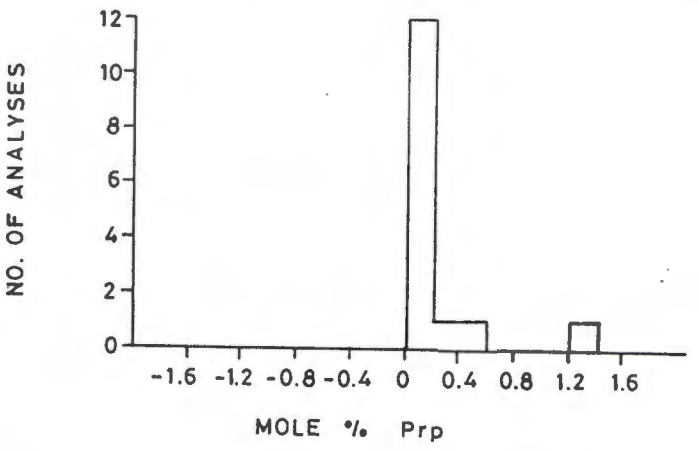

Figure 6.3. Histograms showing the difference between core and rim compositions for the mole % almandine, spessartine and pyrope in garnet. The negative values reflect rim compositions are enriched in the component relative to the core and vice versa for the positive values.

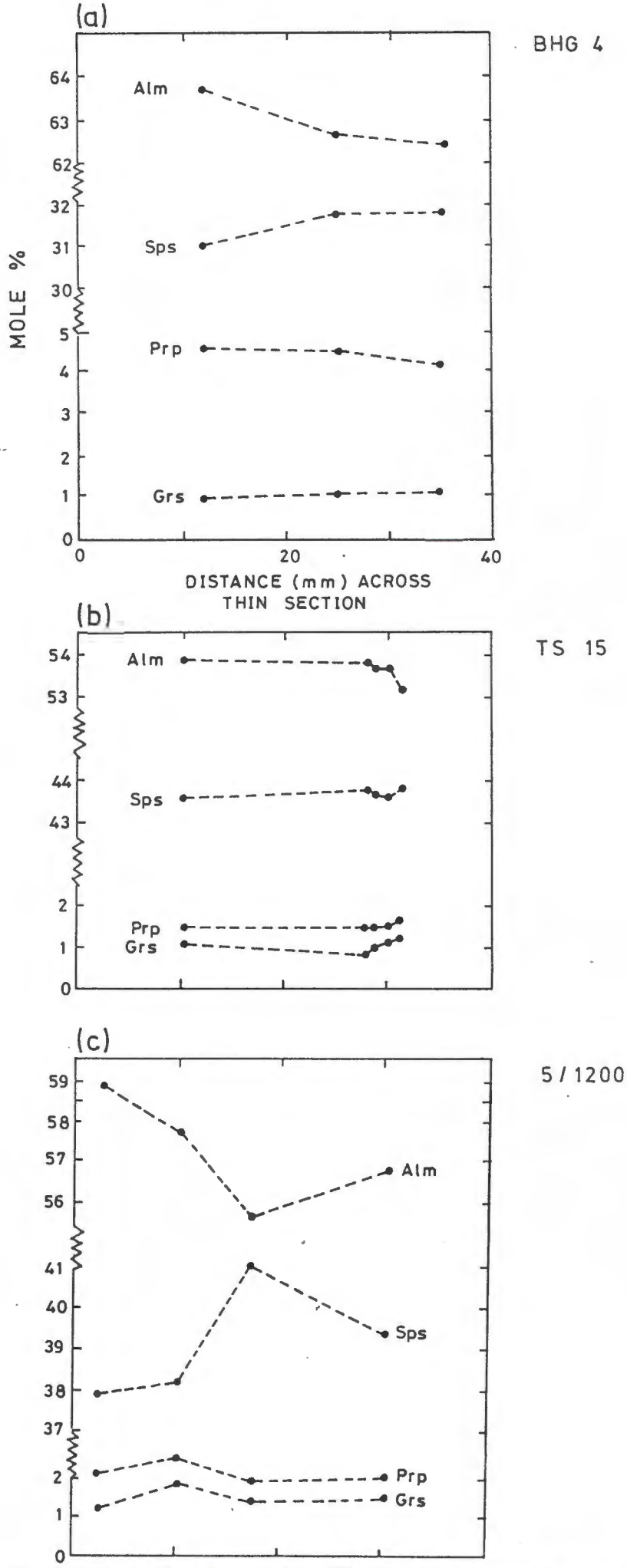

Figure 6.4. Compositional variation in mole % almandine, spessartine and pyrope of garnets for (a) across garnet-rich iron formation mesoband [sample BHG4], (b) across millimetre thick microbands in amphibole-magnetite iron formation [sample TS15] and (c) across millimetre thick garnet-quartz microbands- [sample 5/1200]

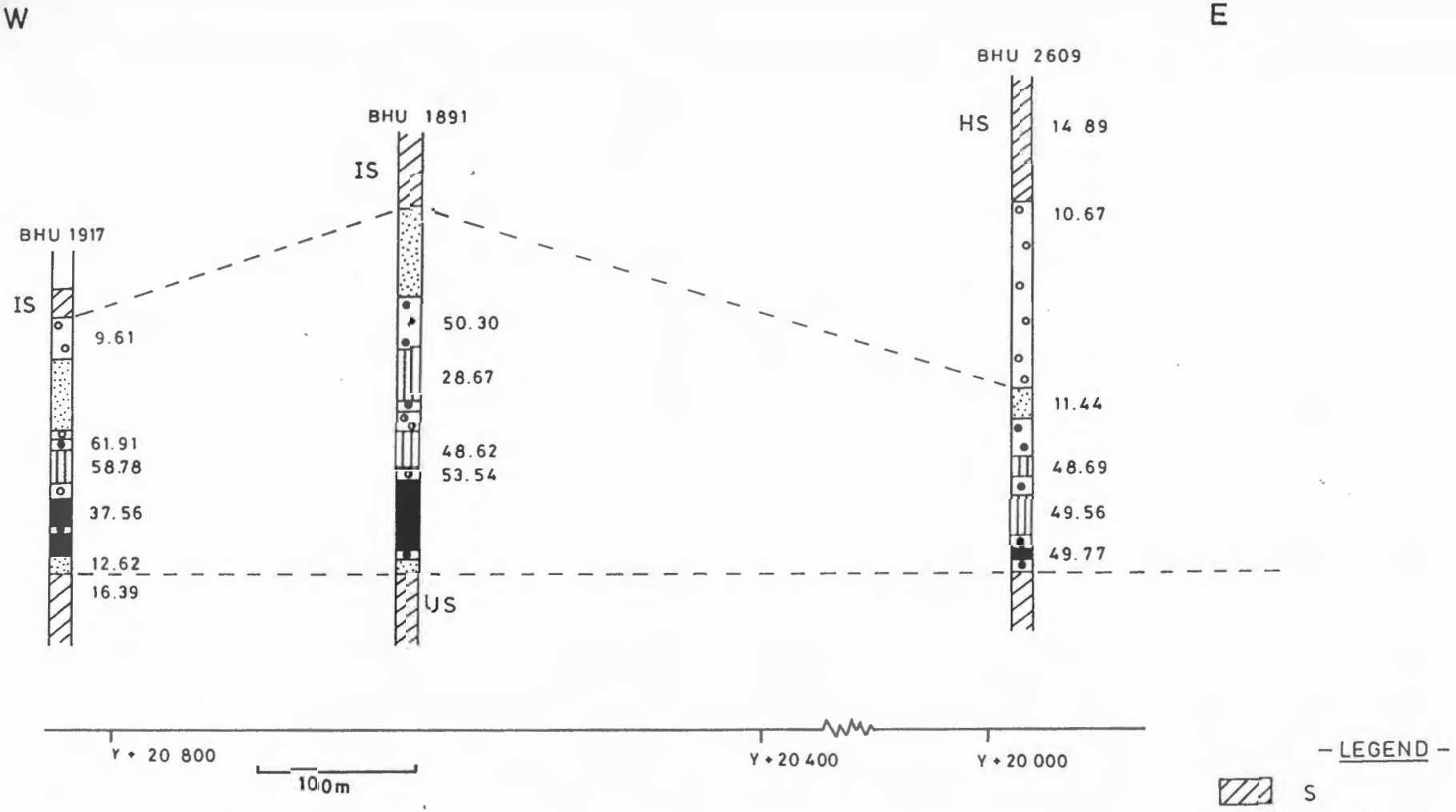

Figure 6.5. Compositional variation of mole % spessartine of garnet within different rock-types in boreholes BHU 1917, BHU 1891 and BHU 2609. (Symbols in legend: S-undifferentiated schist, Q+GQ - quartzite and garnet quartzite, FQ - ferruginous quartzite, AMIF - amphibole magnetite iron formation, QMIF - quartz magnetite iron formation, MSR - massive sulphide rock, GMIF - garnet magnetite iron formation). Symbols in figure: IS - Intermediate Schist, US - Footwall Schist, HS - Hangingwall Schist.

13 mole % spessartine (Fig. 6.5). Garnets within the underlying and overlying metapelitic schist are depleted in Mn, compared with the iron formation and massive sulphide rock. Typical spessartine contents in garnet within the underlying schist is 16.39 mole % and within the overlying schist is 14.89 mole %. Thus, there is a general decrease of the spessartine component in garnet with increasing distance away from the massive sulphide rock and iron formation horizons. The Mn content of garnet is, however, variable from one iron formation macroband to the next (Fig. 6.5). On the scale of the mine, the lateral variation of spessartine within garnet iron formation mesobands shows no consistent trend from east to west, and a general decrease in the down plunge direction (NE) (Fig. 6.6). The trends have probably been obscured by the variation of spessartine within garnet in the vertical directions.

A plot of wt.% MnO of whole rock composition against the mole % spessartine in garnet (Fig. 6.7) illustrates the dependency of garnet in garnet-rich mesobands on whole rock composition. The schist sample has a composition which rests on the general trend line. On the contrary, the mole % spessartine in garnet within amphibole-rich mesobands is independent of the MnO content in the whole rock. The reason for this is that in the garnet iron formation mesobands and the schist, garnet is the only mineral that will incorporate significant Mn, whereas in the amphibole iron formation bands, Mn is also partitioned into amphibole and olivine.

6.2. AMPHIBOLE

Amphiboles of the monoclinic cummingtonite-grunerite series, which range from $Fe_2Mg_5Si_8O_{22}(OH)_2$ to $Fe_7Si_8O_{22}(OH)_2$,are the most common amphiboles in metamorphosed iron formations (Robinson et al., 1982). The amount of solid solution of cations other than Fe^{2+} and Mg in the cummingtonite-grunerite series is generally limited except for Mn^{2+}.

Amphiboles have complex structures and, for effective comparison, analyses are cast into a reasonable structural formula based on site occupancies (Robinson et al., 1982). Many amphiboles contain both Fe^{2+} and Fe^{3+} which are indistinguishable from microprobe analysis. The partitioning of Fe^{2+} and Fe^{3+} into the chemical formula on the basis of chemical limits and crystal-chemical limits has been evaluated by Robinson et al. (1982).

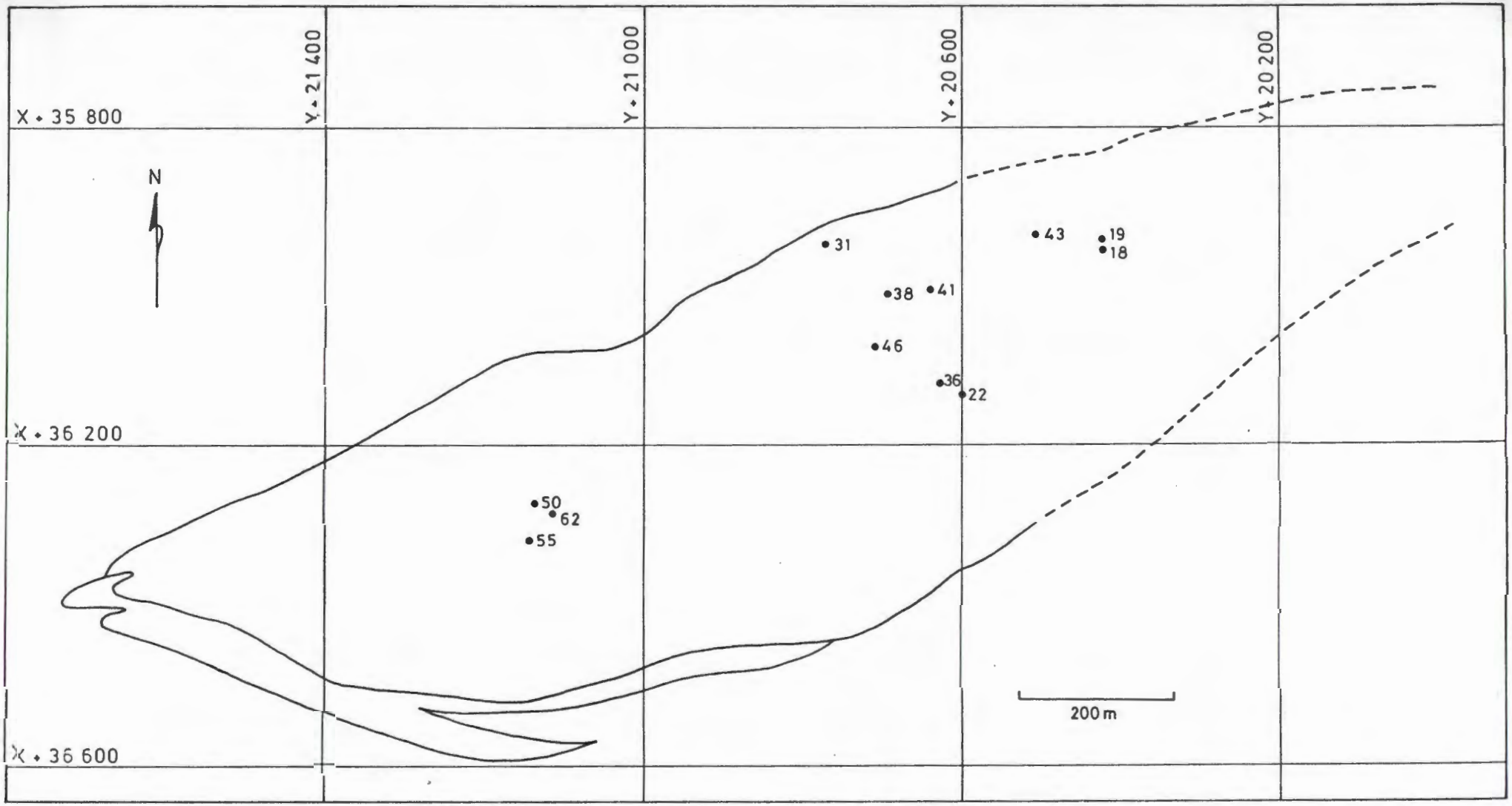

Figure 6.6. Compositional variation (mole % spessartine) of garnet in garnet iron formation mesobands plotted on down-plunge projection of LOB. Compare with Figure 4.2.

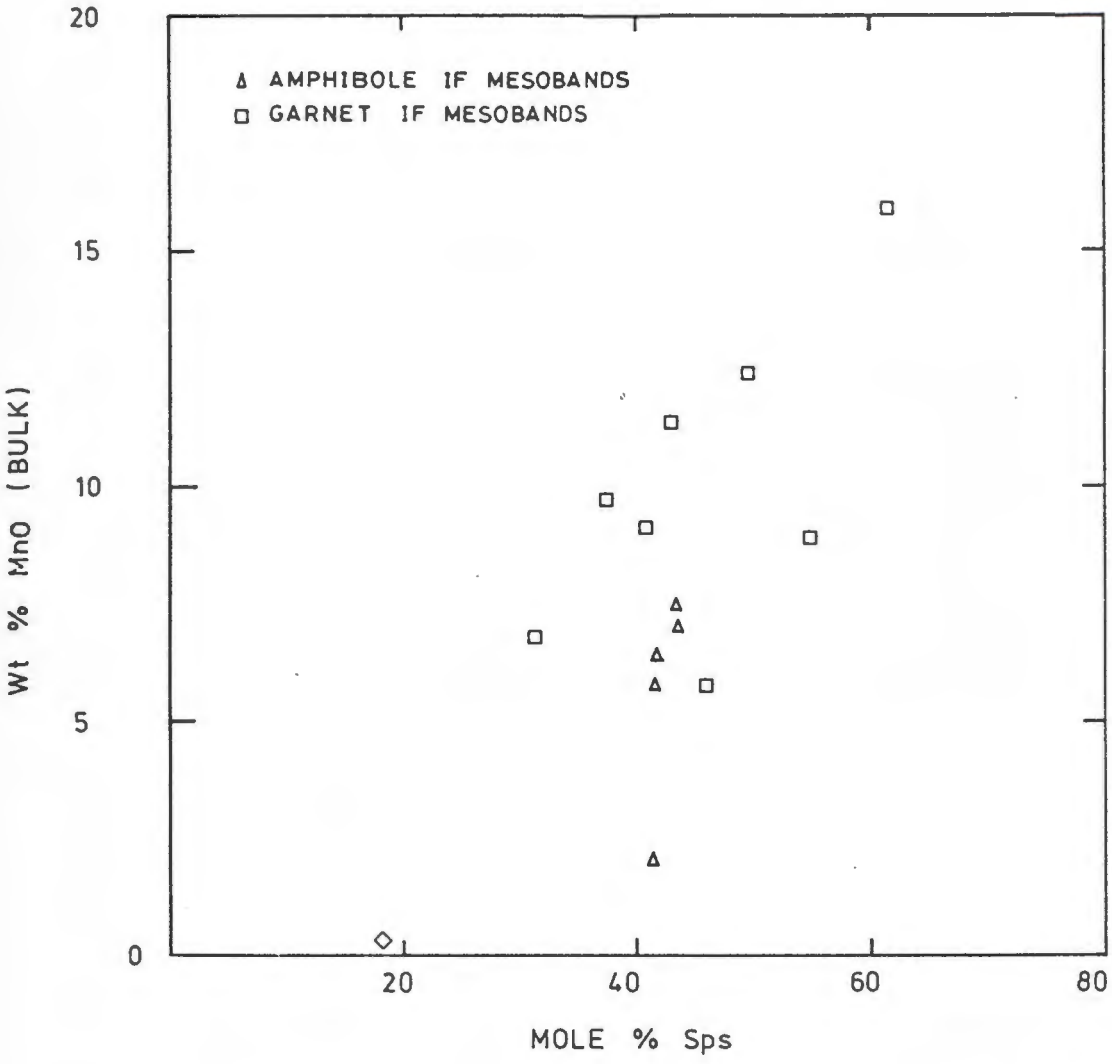

Figure 6.7. Compositional variation of wt.% MnO in whole rock against mole % spessartine of garnet for amphibole and garnet iron formation mesobands.

Following this procedure suggested by Robinson et al. (1982) for Fe-Mg amphiboles, amphibole formulas were normalized with the total cations summing 15, exclusive of Na and K. Using this procedure, all Na and K (which are low in these analyses) are excluded from the M4 site which results in Ca being excluded from the A-site. In this normalization, Mn, Fe and Mg are maximized in the M4 site.

In the LOB, (Fe-Mn-Mg)-rich amphibole is restricted to the iron formation. Chemically, the amphiboles are Fe-rich with lesser Mn and Mg, and are virtually Ca-free. Representative and

average grunerite compositions are shown in Table 6.2. The amphiboles have compositions of manganoan grunerite, with (FeO + MnO) > 40 wt.%. A ternary plot of the atomic proportions Fe^{2+}-Mn-Mg within the M123 and M4 sites (Figure 6.8) illustrates the compositional variation of grunerite within the iron formation. The scatter of data points forms a crude trend parallel to the Fe-Mg tie line. Fe^{2+} and Mg cations form the major substitution scheme in the grunerite with near constant dilution by Mn. Generally, there is greater Mn substitution in Mg-rich amphibole.

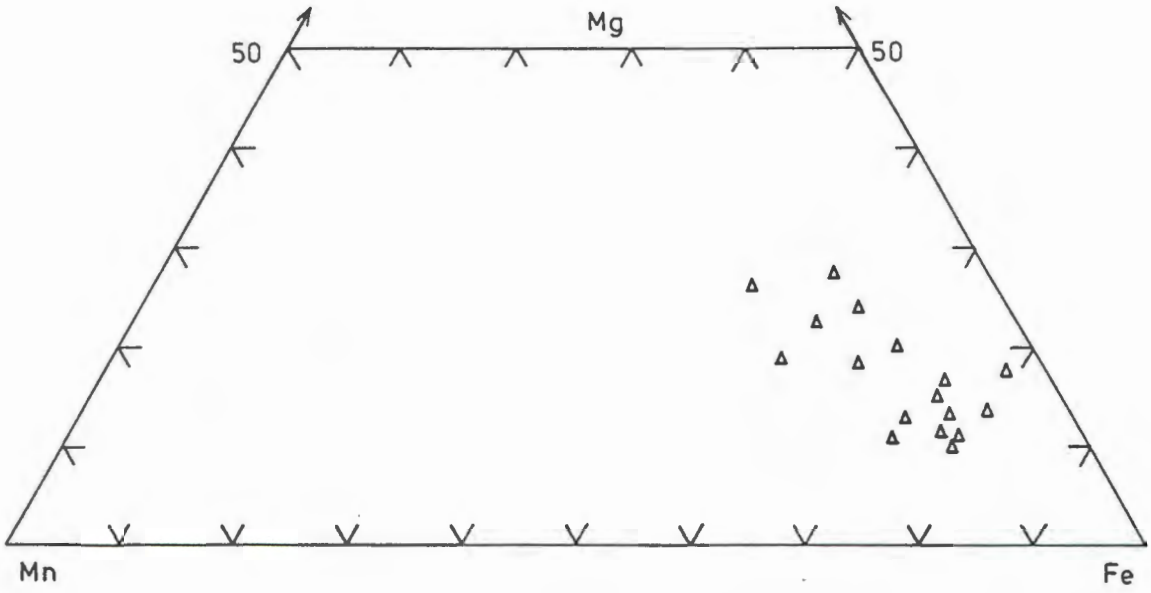

Figure 6.8. Ternary diagram showing compositional variation in atomic proportions Fe^{2+}, Mn and Mg of grunerite within AMIF. Each point represents the average of the analyses in a single sample.

The difference between core and rim compositions, expressed as atomic proportions, is less than 0.07 enrichment or depletion in Fe, Mg and Mn (Fig. 6.9). The core and rim compositions exhibit no preferred trend of enrichment and depletion of Fe, Mn and Mg. The differences are so small that single grains can be regarded as essentially homogeneous.

Within each mesoband and across millimetre-thick microbands, the grunerite compositions show no significant variation in Mn content (Fig. 6.10). There is, however, considerable

Table 6.2. Average electron microprobe analyses of amphibole.

	AMIF BHA10 (n=3)	Average of all amphibole (N=15)
wt. %	Ave 1σ	Ave 1σ
SiO_2	47.99 0.229	48.53 0.169
Al_2O_3	0.65 0.009	0.71 0.061
FeO	39.07 0.118	36.84 0.954
MnO	5.54 0.067	6.51 0.573
MgO	4.21 0.096	4.75 0.409
CaO	0.08 0.006	0.04 0.087
Na_2O	0.23 0.009	0.25 0.033
Total	97.77 0.434	97.63 0.086
Si IV	7.78 0.027	7.83 0.014
Al IV	0.12 0.002	0.12 0.011
Fe^{3+}	0.09 0.028	0.03 0.006
T site	8.00 0.000	8.00 0.000
Al VI	0.00 0.000	0.00 0.002
Fe^{3+}	0.14 0.027	0.07 0.009
Mg^{2+}	1.02 0.023	1.14 0.095
Fe^{2+}	3.83 0.004	3.77 0.009
M123 site	5.00 0.000	5.00 0.000
Fe^{2+}	1.22 0.007	1.09 0.073
Mn	0.76 0.007	0.88 0.076
Ca	0.15 0.001	0.00 0.001
M4 site	2.00 0.000	2.00 0.000
Na	0.07 0.003	0.08 0.010
A site	0.07 0.003	0.08 0.010
$Fe^{\#}$	0.721	0.696 0.019
$Mg^{\#}$	0.146	0.163 0.013
$Mn^{\#}$	0.109	0.127 0.011

Cations calculated on the basis of 22 oxygens.
Total Fe reported as FeO.
nd - not detected (K_2O).
n - number of points.
N - number of samples.
- atomic proportion in M123 + M4 sites.

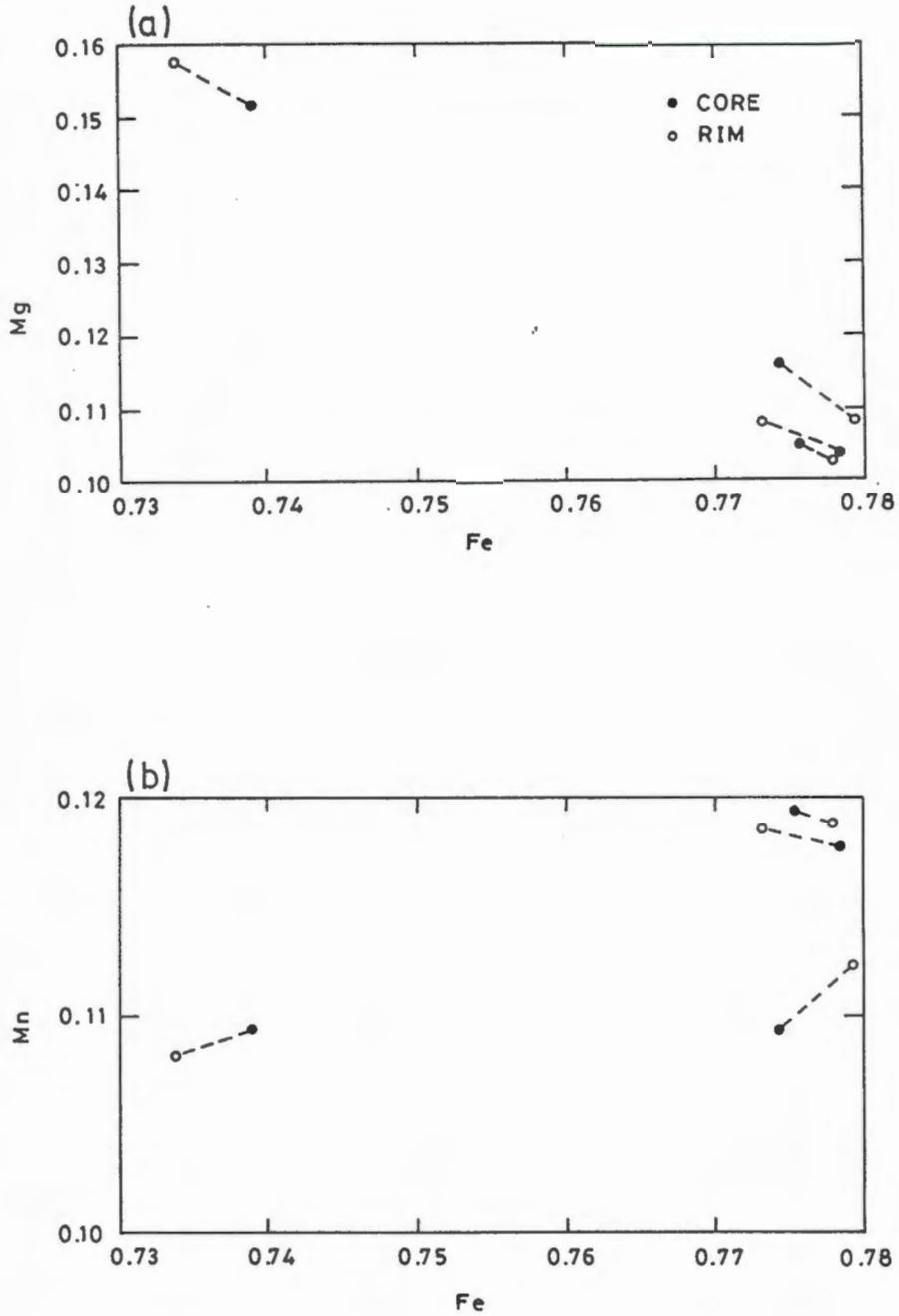

Figure 6.9. Plots of Fe^{2+} versus (a) Mg and (b) Mn of grunerite core and rim compositions. No preferred enrichment or depletion of the cations are shown.

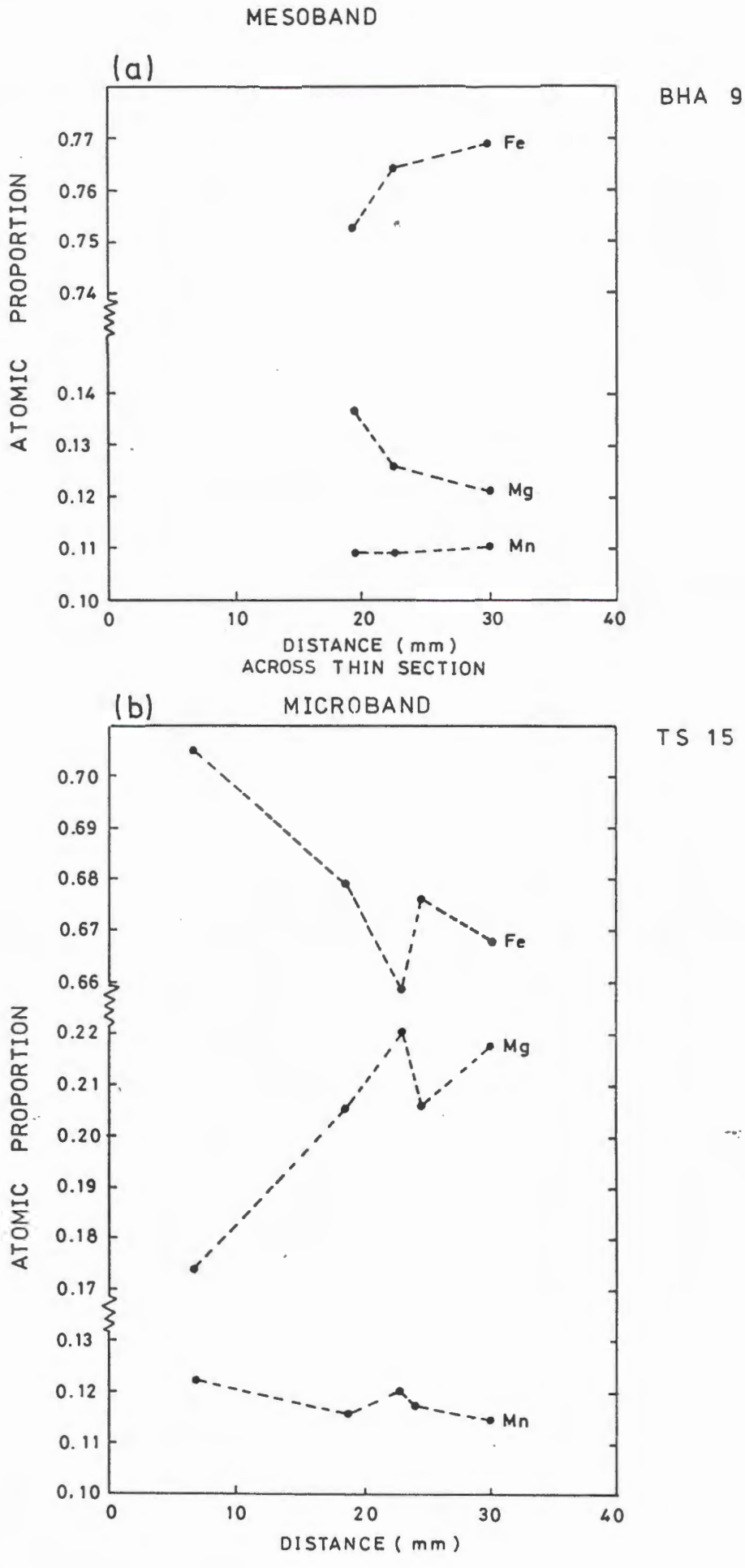

Figure 6.10. Compositional variation in Fe^{2+}, Mn, and Mg of grunerite for (a) across amphibole iron formation mesoband [sample BHA9] and (b) across millimetre-thick microbands [sample TS15].

variation in the mole percentage of Fe and Mg across millimetre-thick microbands in sample TS15, over a distance of 10 mm. Further marked variation in the Fe, Mg and Mn contents in grunerite occurs between mesobands from one iron formation unit to the next (Fig. 6.11). The atomic proportion of Mn in grunerite shown in borehole BHU2609 decreases towards the top of the structural sequence. This is accompanied by a decrease in Mg and an increase in Fe. The trend parallels the variation of Fe, Mg, and Mn in garnet for the same borehole. The same observation is, however, not supported by the grunerite compositions analysed from borehole, BHU 1891, where the variation of cation concentrations is inconsistent with those in BHU2609.

The sample distribution of analysed grunerite with its atomic proportion of Mn is shown in Figure 6.12. There is a general decrease of the Mn content down the plunge of the LOB from the SW to the NE. A few samples, however, have atomic proportions of Mn that are inconsistent with this trend. These irregular values are attributed to variations across the macrobands of the iron formation (i.e. a vertical change).

6.3.OLIVINE

Olivine coexists with grunerite, and contains almandine-spessartine garnet in some amphibole-rich mesobands and in microbands of the iron formation. Representative chemical analyses of olivine and the average of 10 samples are given in Table 6.3. The tephroite contents in fayalite varies between 5 and 17 mole %. The forsterite content is very low and is generally less than 2.5 mole %. Consequently, olivine has compositions between fayalite and tephroite, also referred to as knebelite. Cr_2O_3, NiO and CaO were below the detection limits in all cases. A small Zn component was determined for samples TS4 and TS15 with ZnO contents < 1 mole %. A ternary diagram (Fig. 6.13) of Fe, Mn and Mg shows LOB olivine to plot along the Fe-Mn tie line. LOB fayalite is Mn-enriched compared with compositions from other sulphide-bearing metamorphosed iron formations, e.g Pegmont deposit, Australia (Vaughan and Stanton, 1986) (Fig. 6.13). The average composition for all samples is 82.8 mole % fayalite, 15.3 mole % tephroite and 1.9 mole % forsterite. The variation of manganoan fayalite composition between iron formation mesobands is small. This is shown by the standard deviation (1σ) of Fe, Mn and Mg for all samples (Table 6.3). Similarly, manganoan fayalite is reported to have homogeneous compositions throughout the Pegmont

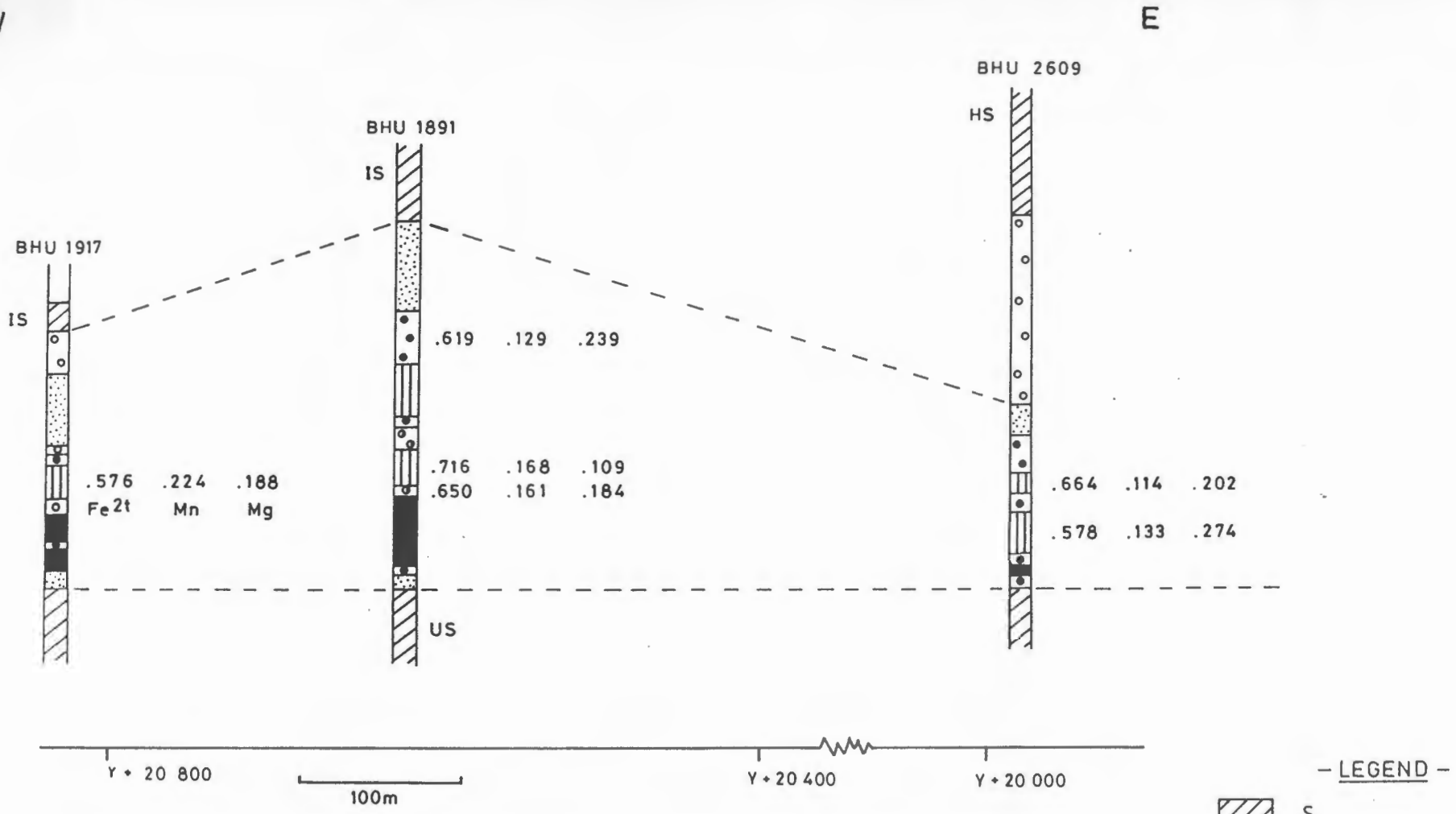

Figure 6.11. Compositional variation in atomic proportions Fe^{2+}, Mn and Mg of grunerite within different rock-types in boreholes BHU 1917, BHU 1891 and BHU 2609. (Symbols in legend: S- undifferentiated schist, Q+GQ - quartzite and garnet quartzite, FQ - ferruginous quartzite, AMIF - amphibole magnetite iron formation, QMIF - quartz magnetite iron formation, MSR - massive sulphide rock, GMIF - garnet magnetite iron formation). Symbols in figure: IS - Intermediate Schist, US - Footwall Schist, HS - Hangingwall Schist.

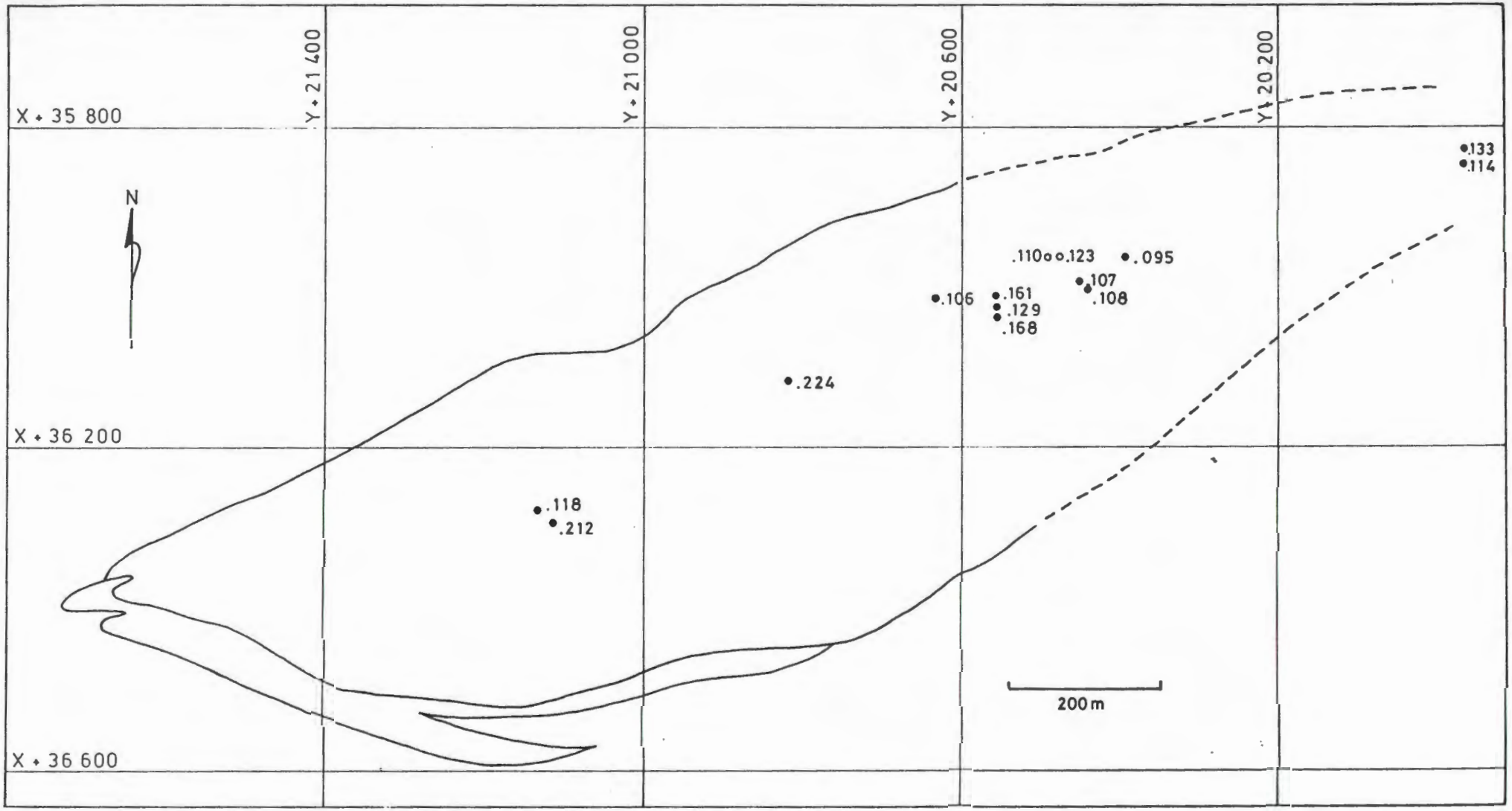

Figure 6.12. Compositional variation in atomic proportion Mn of grunerite within amphibole iron formation mesobands plotted on down-plunge projection of LOB. Compare with Figure 4.2.

Table 6.3. Average electron microprobe analyses of olivine.

wt.%	AMIF TS15 (n=11)	Average All samples (N=10)	1σ
SiO_2	29.62	29.71	0.079
FeO	57.50	58.97	0.791
MnO	11.41	10.78	0.947
MgO	1.15	0.75	0.969
ZnO	0.13	ND	ND
Total	99.81	100.26	
Si	1.00	0.99	0.001
Fe^{2+}	1.62	1.66	0.023
Mn	0.33	0.30	0.026
Mg	0.06	0.03	0.004
Zn	0.00	-	-
Cations	3.00	3.01	0.001
Mole % Fa	80.86	82.80	1.245
Mole % Tp	16.26	15.32	1.338
Mole % Fo	2.89	1.88	2.433

Cations calculated on the basis of 4 oxygens.
Total Fe determined as FeO.
ND - not determined.
nd - not detected (TiO_2, Cr_2O_3, NiO and CaO).
n - number of points.
N - number of samples.

deposit, Australia (Vaughan and Stanton, 1986).

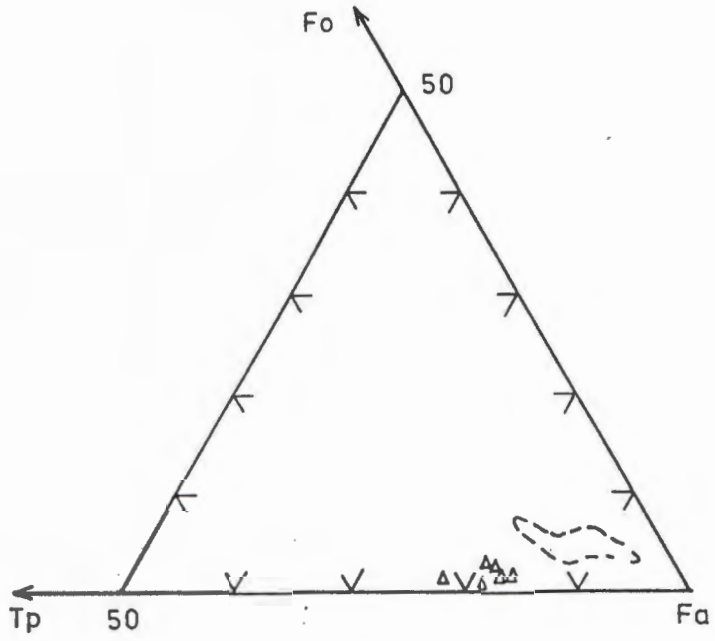

Figure 6.13. Ternary diagram showing compositional variation of mole % fayalite (Fa), tephroite (Tep) and forsterite (Fo) of LOB fayalite. Dashed line represents compositional field of fayalite from the Pegmont deposit, Australia (Vaughan and Stanton, 1986).

Differences between core and rim compositions of manganoan fayalite (with grain-sizes 0.4 - 1.0 mm) are small. The maximum difference between core and rim compositions for Fe, Mn and Mg contents are 1.06, 0.99 and 0.11 mole percent fayalite, tephroite and forsterite, respectively. Some samples have core compositions which are slightly depleted in Fe and enriched in Mn, relative to the rim compositions. The opposite is found for the distribution of Fe and Mn between core and rim compositions for other samples (Fig. 6.14). For 6 analyses, cores and rims reveal no preferred trend for enrichment or depletion of Fe and Mn.

Manganoan fayalite has uniform composition within each mesoband. The amount of fayalite, tephroite and forsterite in LOB olivine across millimetre-thick microbands (sample TS15) and across mesobands (sample BHA9) shows no marked compositional variation (Fig. 6.15).

The distribution of olivine samples examined is shown in Figure 6.16 with their corresponding Mn contents. The samples were all collected from the centre of the LOB and

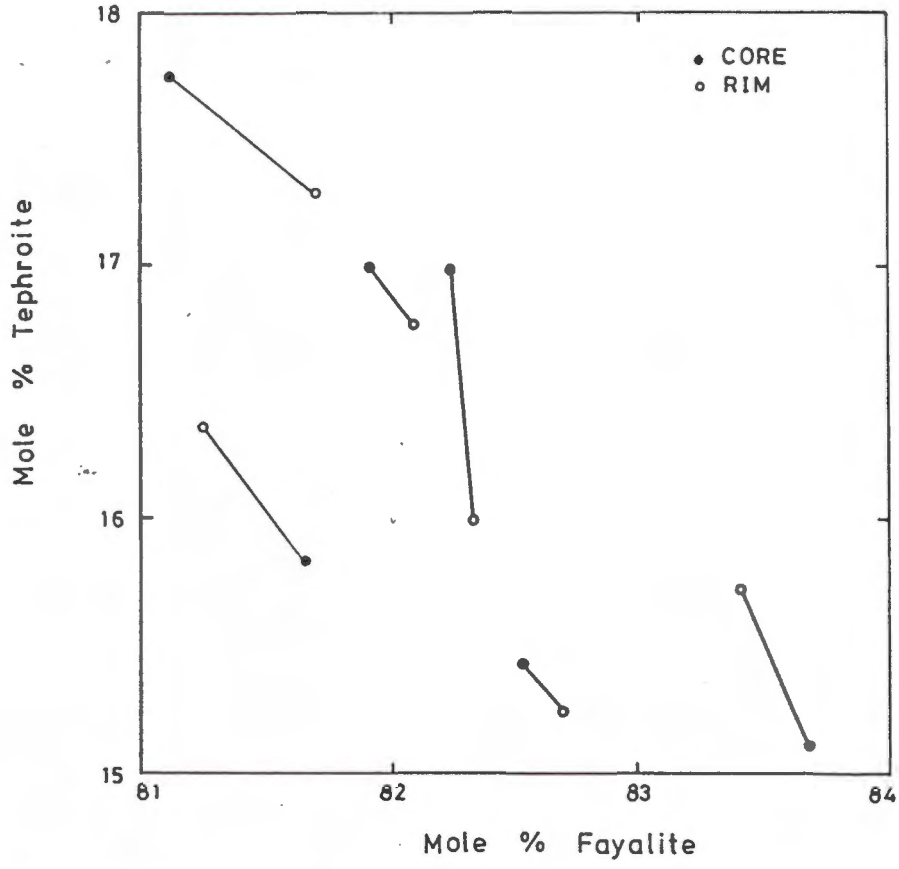

Figure 6.14. Plot of mole % fayalite versus mole % tephroite for core and rim compositions of olivine. No preferred enrichment or depletion of cations are shown.

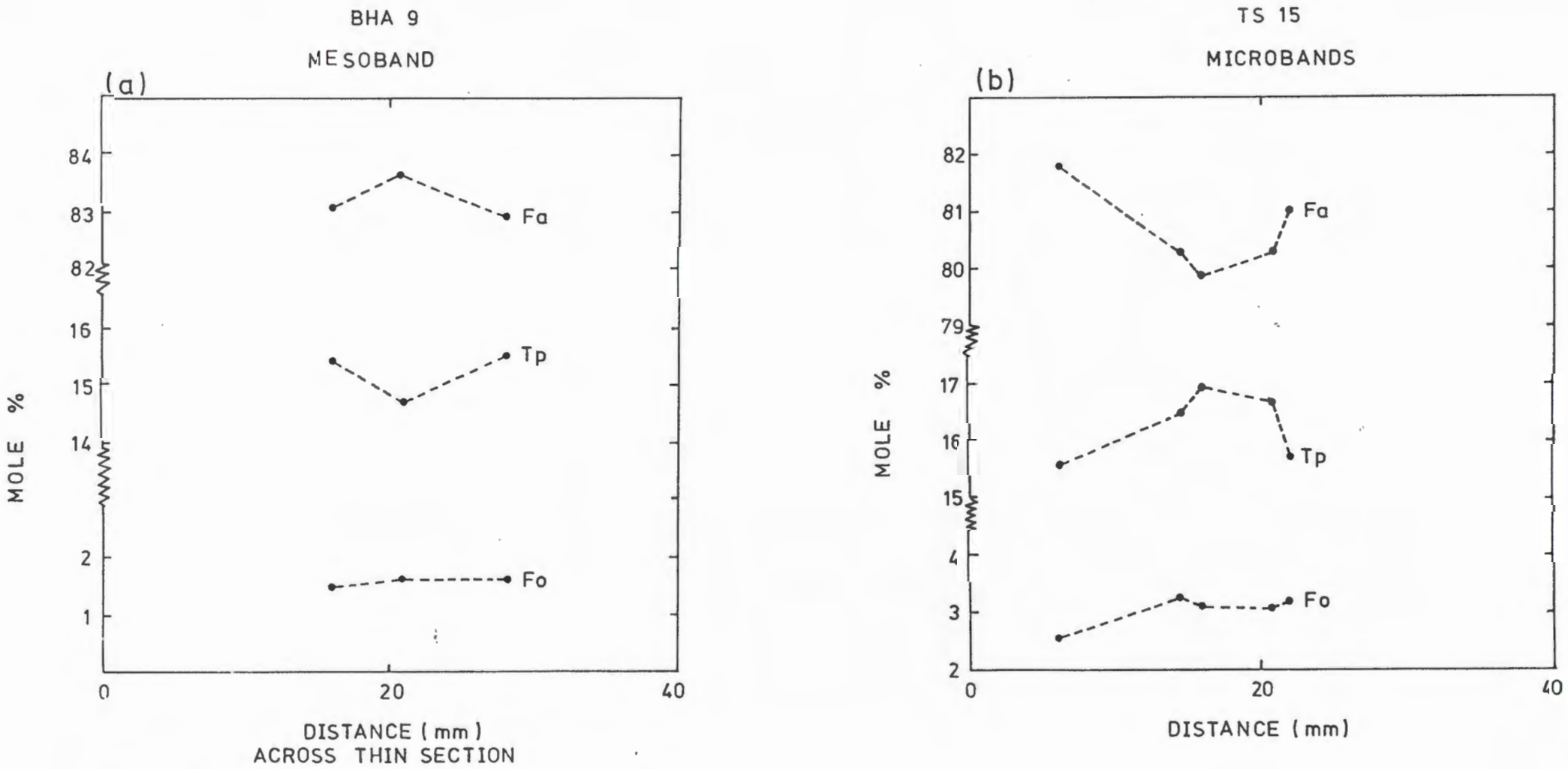

Figure 6.15. Diagrams showing the variations in mole % fayalite, tephroite and forsterite of olivine (a) across amphibole iron formation mesoband [sample BHA9] and (b) across millimetre scale microbands [sample TS15].

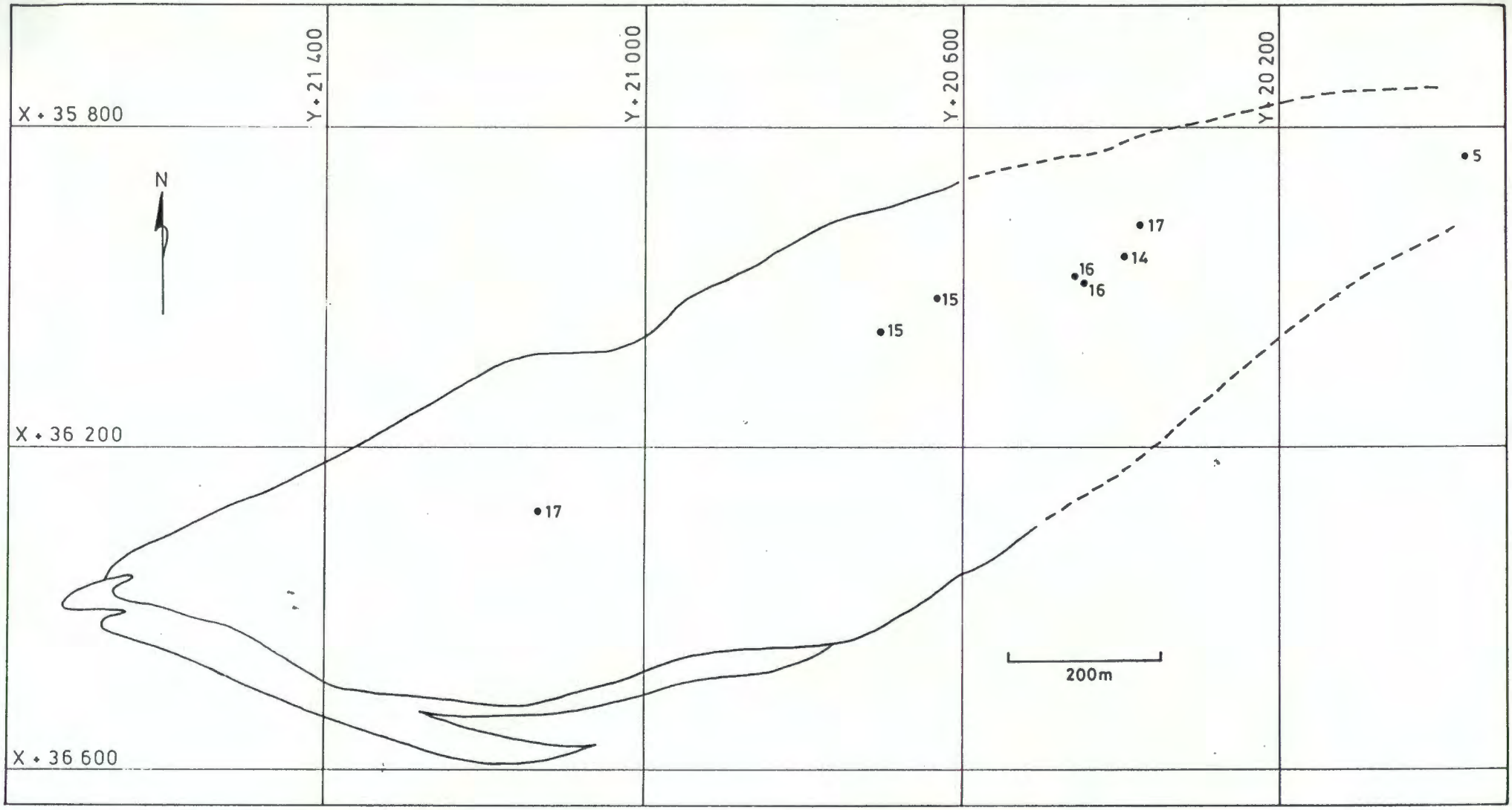

Figure 6.16. Compositional variation in mole % tephroite of olivine plotted on down-plunge projection. Compare with Figure 4.2.

no conclusion can be drawn about possible east-west compositional variation. The tephroite content in olivine within iron formation mesobands is generally enriched in the up-plunge region and depleted in the down-plunge region. The iron formation mesobands within the central region exhibits olivine with variable tephroite contents.

6.4.ORTHOPYROXENE AND PYROXFERROITE

Orthopyroxene is an accessory mineral within the iron formation and was only observed in one sample (5-1200). It coexists with garnet and quartz but is not associated with olivine. The composition of orthopyroxene is shown in Table 6.4. CaO was not detected in orthopyroxene. In addition, Mn is enriched relative Mg in orthopyroxene (Fig. 6.17). The analysed orthopyroxene is referred to as manganoan ferrosilite.

Table 6.4. Representative and average analyses of orthopyroxene and pyroxferroite.

wt. %	Orthopyroxene 5/1200 (n=1)	Pyroxferroite (n=10, N=4)	1σ
SiO_2	46.59	45.83	0.224
Al_2O_3	0.20	0.01	0.014
FeO	40.85	26.17	0.291
MnO	7.78	25.47	0.467
MgO	4.13	1.74	0.095
CaO	nd	0.31	0.178
Total	99.54	99.55	
Si IV	1.99	1.99	0.004
AL IV	0.01	0.00	0.000
T site	2.00	1.99	0.003
Fe^{2+}	1.46	0.95	0.010
Mn	0.28	0.93	0.018
Mg	0.26	0.11	0.006
Ca	0.00	0.01	0.000
M1,M2 sites	2.00	2.01	0.007

Cations calculated on the basis of 6 oxygens.
Total Fe reported as FeO.
n - number of points.
N - number of samples.
nd- not detected (TiO_2).

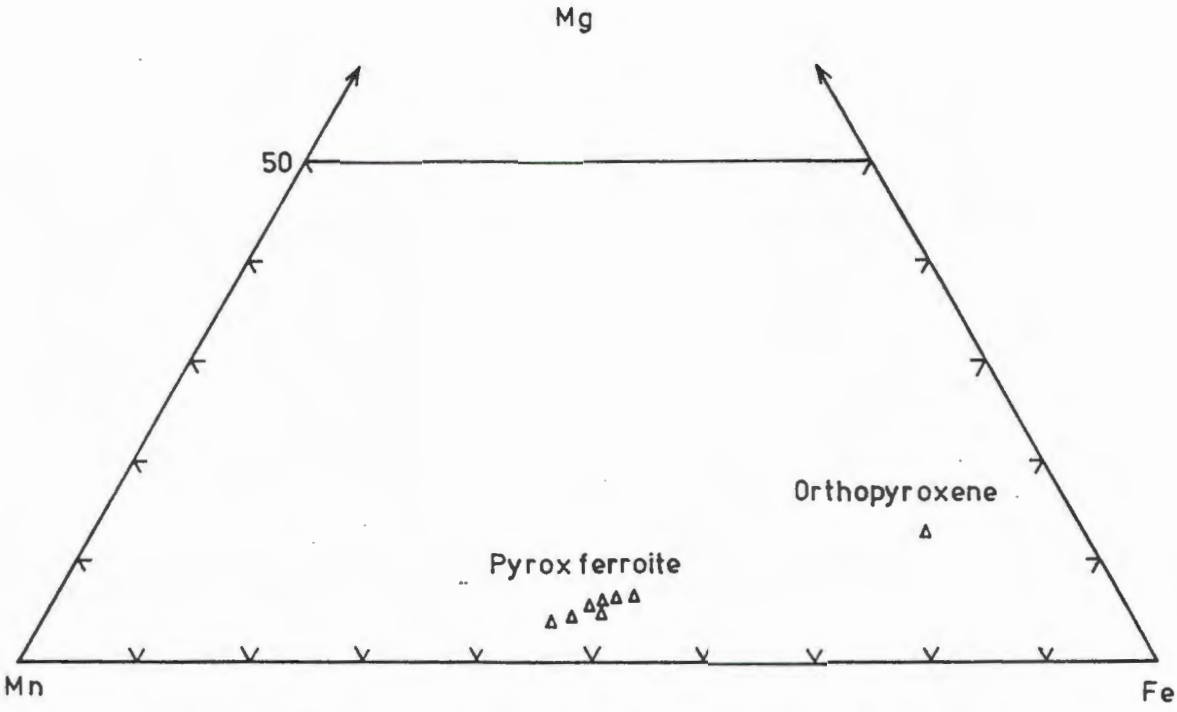

Figure 6.17. Compositional variation with respect to atomic proportions Fe^{2+}, Mn and Mg of orthopyroxene and pyroxferroite.

More common than orthopyroxene is pyroxferroite which occurs with varying proportions within the amphibole magnetite iron formation. It was generally found in textural contact with quartz. Amphibole is generally absent in the presence of pyroxferroite. In a single thin-section, pyroxferroite was found as a product of the breakdown of amphibole. Pyroxferroite is a typical mineral in metamorphosed manganiferous iron formations. It has been described, for example, from Gamsberg (Rozendaal, 1982) and the Pegmont deposit, Australia (Vaughan and Stanton, 1986).

In the LOB iron formation, pyroxferroite is found in association, apart from quartz, with manganoan grunerite and spessartine-rich garnet. The composition of pyroxferroite is essentially that of a Fe-Mn solid-solution with a low Mg content and insignificant traces of Ca (Table 6.4, Fig. 6.17).

6.5.BIOTITE

Apart from the metapelitic schists, biotite is present as an accessory mineral in the massive sulphide rock, in silicate-rich mesobands of the iron formation, in massive magnetite iron formation and in garnet quartzite. Biotite is not always present in individual garnet- and amphibole-rich iron formation mesobands. Three optically distinct biotites were recognized in the LOB which exhibit either brown-red, green-brown or pale green pleochroism. These various biotites have distinctly different chemical compositions which represent annite-phlogopite, kinoshitalite and titanian-deficient compositions, respectively. Representative compositions of biotite are shown in Table 6.5.

Biotite exhibiting strong green-brown pleochroism, is confined to the silicate-rich iron formation mesobands and is Ba-rich. The average composition for this biotite (Table 6.5) has the formula:

$$(Ba_{.8}K_{.6}Na_{.1})(Mg_{1.8}Fe_{3.5}Mn_{.2}Ti_{.2}Al_{.2})(Si_{5.1}Al_{2.9})O_{20}[OH_{1.9},F_{2.1}]$$

The classification of micas into true and brittle micas is done on the basis of the magnitude of the layer charge per formula unit, which is ideally -1.0 and -2.0, respectively, (Bailey, 1984; Guggenheim, 1984). True micas have K or Na and brittle micas Ca and Ba in the interlayer sites. Barium-rich micas have been reported in magnetite-rich rock from Wilayatra, Ceylon (Pattiaratchii et al., 1967), nephelinites in Hawaii (Mansker et al., 1979), along a contact metamorphic zone between plutonic rock and phyllite from the Alaska Range (Solie and Su, 1987), within stratabound mineralized schist in the Scottish Dalradian (Fortey and Beddoe-Stephens, 1982), and from the Nodatamagua Mine, Japan (Yoshii et al., 1973).

Ba-rich biotite from Broken Hill has a Ba/K ratio of 1.25/1 which is within the range defined for kinoshitalite (Yoshii and Maeda, 1975). Mansker et al. (1979) assign Ba entirely to interlayer sites on a 1:1 basis, by substituting for K+Na+Ca. This relationship is valid for the LOB barian biotites with correlation coefficient (r) of -0.89 (Fig. 6.18). The resulting charge imbalance is corrected for by substituting $Ba^{2+} + Al^{3+} = K^{+} + Si^{4+}$ (Mansker et al., 1979).

Table 6.5. Representative and average electron microprobe analyses of biotite.

wt. %	Garnet mesoband BHG2 (n=3)	Amphibole mesoband BHA5 (n=3)	Schist (US) BHS22 (n=1)	MSR TS12 (n=4)	Grt.-bio-schist BH3 (n=1)	GQ TS13 (n=3)
SiO_2	28.38	28.70	34.30	40.46	34.70	36.73
TiO_2	1.58	0.67	5.05	0.18	1.69	1.21
Al_2O_3	15.16	14.75	21.06	12.53	20.30	19.27
FeO	27.52	29.27	23.37	11.57	26.26	21.01
MnO	0.95	1.59	0.23	0.54	nd	nd
MgO	5.69	4.70	5.55	18.97	6.12	10.30
BaO	12.36	10.88	nd	nd	nd	1.06
Na_2O	0.17	0.22	nd	0.30	8.49	0.19
K_2O	2.23	3.04	7.73	8.96	8.49	6.59
F	4.54	4.98	0.84	5.75	1.89	1.49
Cl	nd	nd	nd	nd	nd	nd
Total	98.51	98.80	98.13	99.26	99.87	98.42
Si IV	5.01	5.10	5.16	6.02	5.27	5.42
AL IV	2.99	2.90	2.84	1.98	2.73	2.48
T site	8.00	8.00	8.00	8.00	8.00	8.00
Al VI	0.17	0.19	0.89	0.22	0.91	0.94
Ti VI	0.20	0.09	0.57	0.02	0.19	0.06
Fe^{2+}	4.06	4.35	2.94	1.44	3.34	3.04
Mn	0.14	0.24	0.03	0.07	-	-
Mg	1.50	1.25	1.24	4.21	1.39	1.96
O site	6.07	6.12	5.67	5.96	5.83	5.99
Ba	0.86	0.76	-	-	-	0.00
Na	0.06	0.08	-	0.09	0.12	0.05
K	0.50	0.69	1.48	1.70	1.65	1.49
A site	1.41	1.52	1.48	1.79	1.77	1.54
OH	1.46	1.20	3.60	1.29	3.09	3.29
F	2.54	2.80	0.40	2.71	0.91	0.71
X_{Mg}	0.27	0.22	0.30	0.75	0.29	0.39

Cations calculated on the basis of 22 oxygens.
Total Fe reported as FeO.
nd - not detected.
n - number of points
X_{Mg}= Mg/(Fe+Mg)

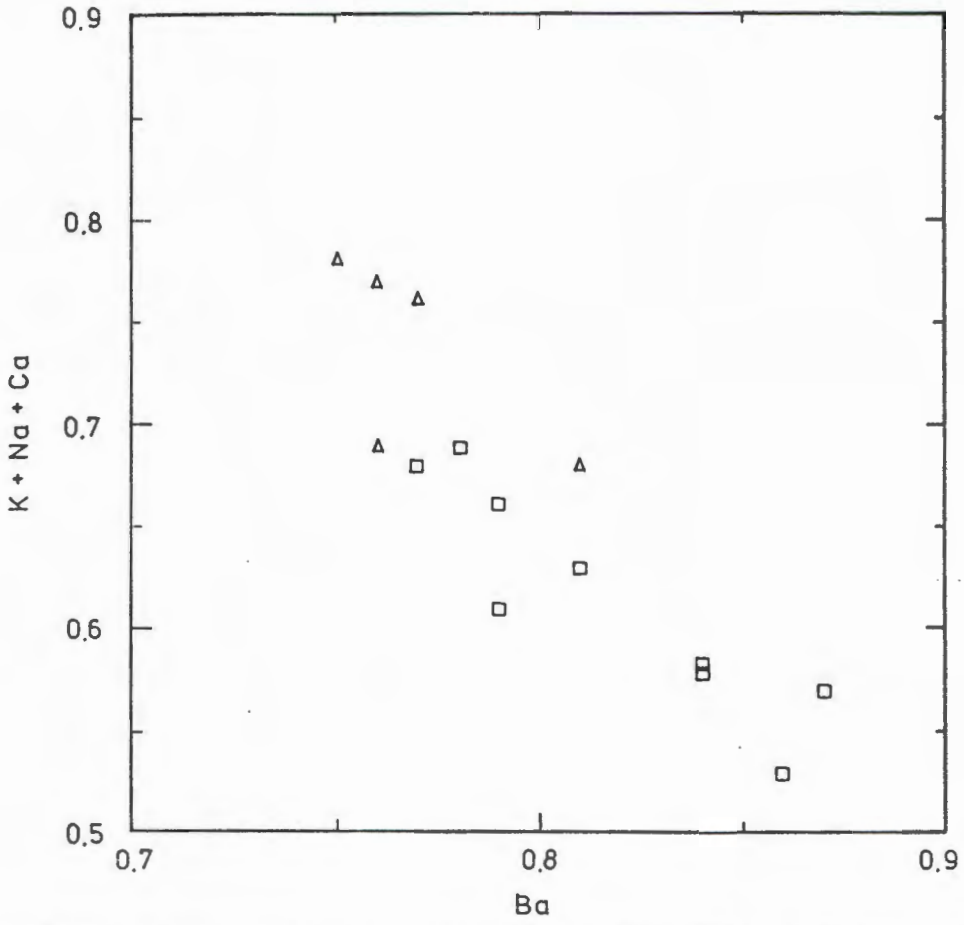

Figure 6.18. Plot of atomic proportions of interlayer cations showing approximately 1:1 variation of Ba with remaining cations. Sample points include only Ba-rich biotite from the garnet (square) and amphibole (triangle) iron formation mesobands.

Their substitution scheme:

$$Ba^{2+} + 2Ti^{4+} + 3Al^{3+} = K^{+} + 3(Mg,Fe)^{2+} + 3Si^{4+}$$

holds grossly true for Broken Hill barian biotites with r= -0.91 (Fig. 6.19).

In the barian biotites, differences of Ba and K between core and rim compositions are negligible indicating the presence of intra-crystalline diffusion. Homogeneous biotite compositions prevail throughout individual silicate-rich iron formation mesobands. Ba is generally enriched in biotite within garnet iron formation mesobands relative to the amphibole iron formation mesobands (Fig. 6.18).

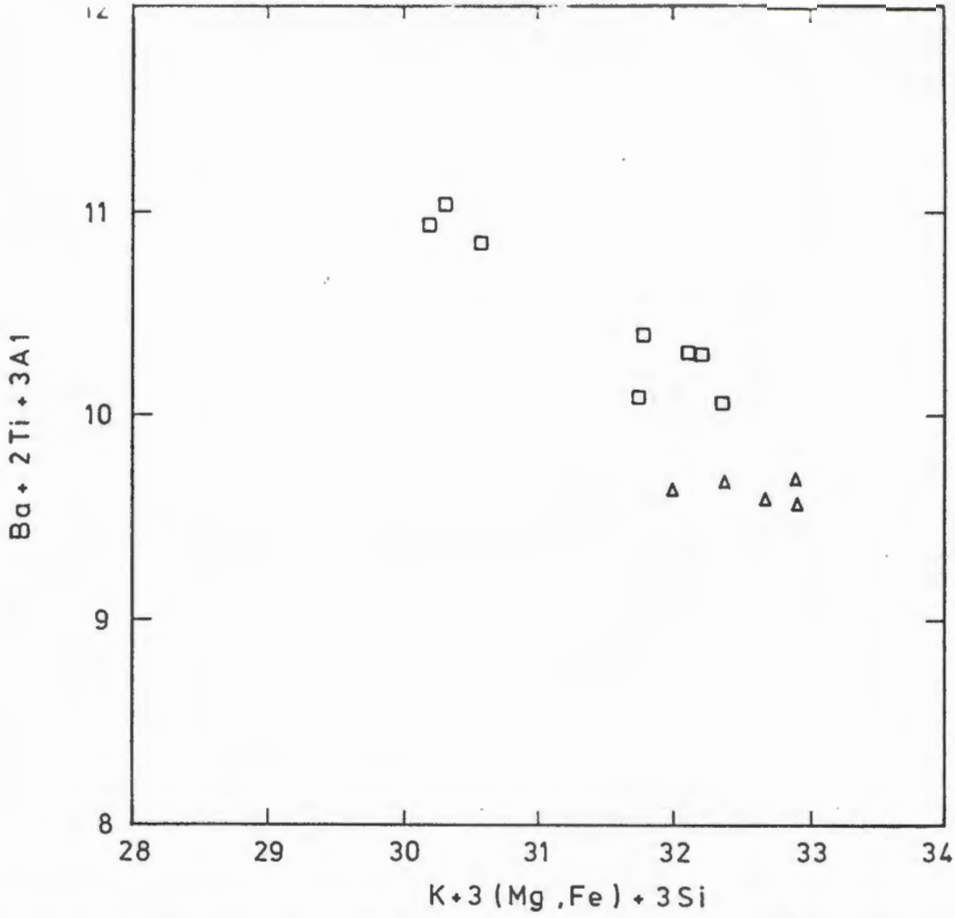

Figure 6.19. Plot of atomic proportions according to the substitution scheme $K^+ + 3(Mg,Fe)^{2+} + 3Si^{4+} = Ba^{2+} + 2Ti^{4+} + 3Al^{3+}$, showing approximately 1:1 correspondence. Sample points include only Ba-rich biotite from the garnet (square) and amphibole (triangle) iron formation mesobands.

The formation of the barian biotites is not fully understood. Ba-rich biotites reported in the literature form in high temperature environments under both low and high pressures. Hatch et al. (1957) showed that high melting points up to 1450 °C are characteristic of synthetic F-rich analogues of kinoshitalite. Thus, high temperatures seem to be necessary for the formation of Ba-rich biotite.

Other LOB biotites are K- rich and are distinguished from the Ba-rich variety by either brown-red or pale green pleochroism. The latter have TiO_2 concentrations below detection limits and have an average formula:

$(Ba_{.0}K_{1.6}Na_{.1})(Mg_{3.3}Fe_{1.9}Mn_{.1}Ti_{.0}Al_{.6})(Si_{5.6}Al_{2.4})O_{20}[OH_{2.2},F_{1.8}]$.

whereas the former have an average formula:

$(Ba_{.1}K_{1.4}Na_{.1})(Mg_{1.9}Fe_{2.9}Mn_{.1}Ti_{.2}Al_{.8})(Si_{5.4}Al_{2.6})O_{20}[OH_{2.9},F_{1.1}]$.

Apart from the non-detectable Ti content in the pale green variety, the chemical formulae reveal marked differences between the atomic proportions of Fe and Mg.

The K-rich biotites within and around the LOB contain variable amounts of F. It is evident from Fig. 6.20, that the F content in biotite for the iron formation bands and massive sulphide rock varies as a function of X_{Mg}. The variable F contents in biotite within the metapelitic schists and garnet quartzites are, however, to a large extent independent of X_{Mg}. If samples from different rock-types are considered in stratigraphic sequence (example BHU 2609 and BHU 1917), the F content and the X_{Mg} values generally diminish further away from the massive sulphide lens (Fig. 6.21). The significance of this variation might be considered either a function of whole rock composition, temperature or metamorphic fluid interaction (discussed in Chapter 8).

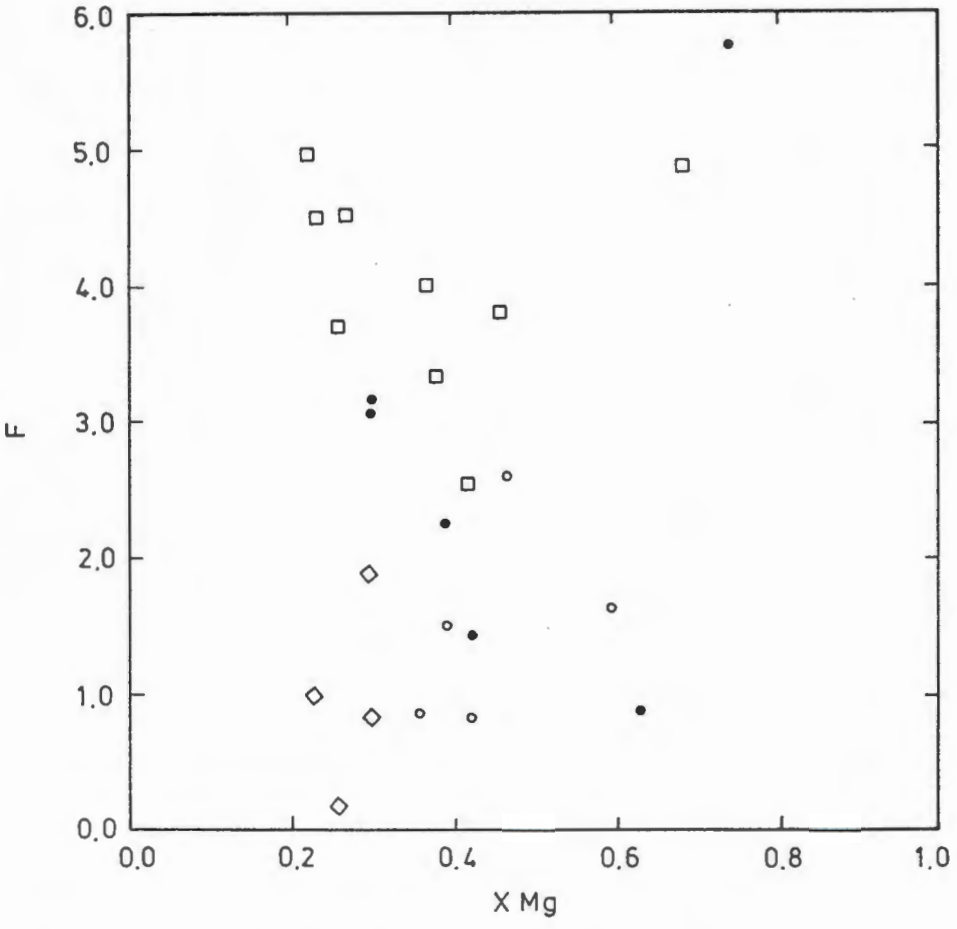

Figure 6.20. Plot of wt. % F versus X_{Mg} = Mg/(Mg+Fe) for biotite in different rock types. (Symbols for rocks: open square- undifferentiated iron formation mesobands, diamond- undifferentiated schist of the Ore Schist Formation, filled circle- massive sulphide rock, open circle- ferruginous and garnet quartzites).

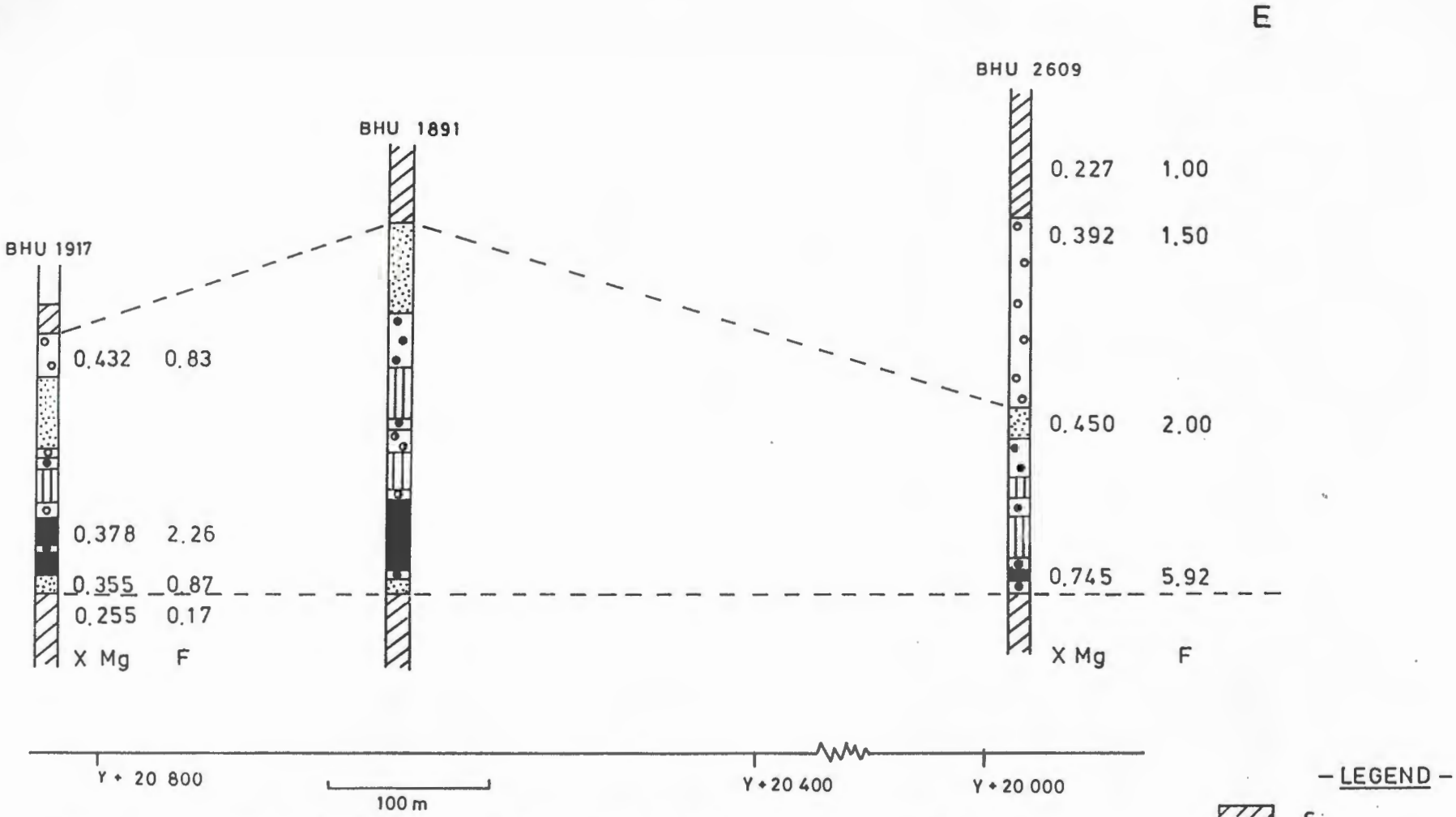

Figure 6.21. Compositional variation of $\dot{X}_{Mg}$ = Mg/(Mg+Fe) and wt.% F in biotite of rock-types for boreholes BHU 2609 and BHU 1917. (Symbols: S-undifferentiated schist, Q+GQ - quartzite and garnet quartzite, FQ - ferruginous quartzite, AMIF -amphibole magnetite iron formation, QMIF - quartz magnetite iron formation, MSR -massive sulphide rock, GMIF - garnet magnetite iron formation). Symbols in figure: IS - Intermediate Schist, US - Footwall Schist, HS - Hangingwall Schist.

A comparison of Ba and F concentrations in the two mica types (Fig. 6.22) reveals that Ba-rich biotites are also enriched in F. Similar F enrichments in Ba-rich micas were found in the Alaska Range by Solie and Su (1987). It is envisaged that the distinct biotite compositions reflect variation of different bulk rock and/or fluid compositions. However high F contents associated with Ba-rich biotites suggest that fluid composition may have been a controlling factor in formation of the different biotite.

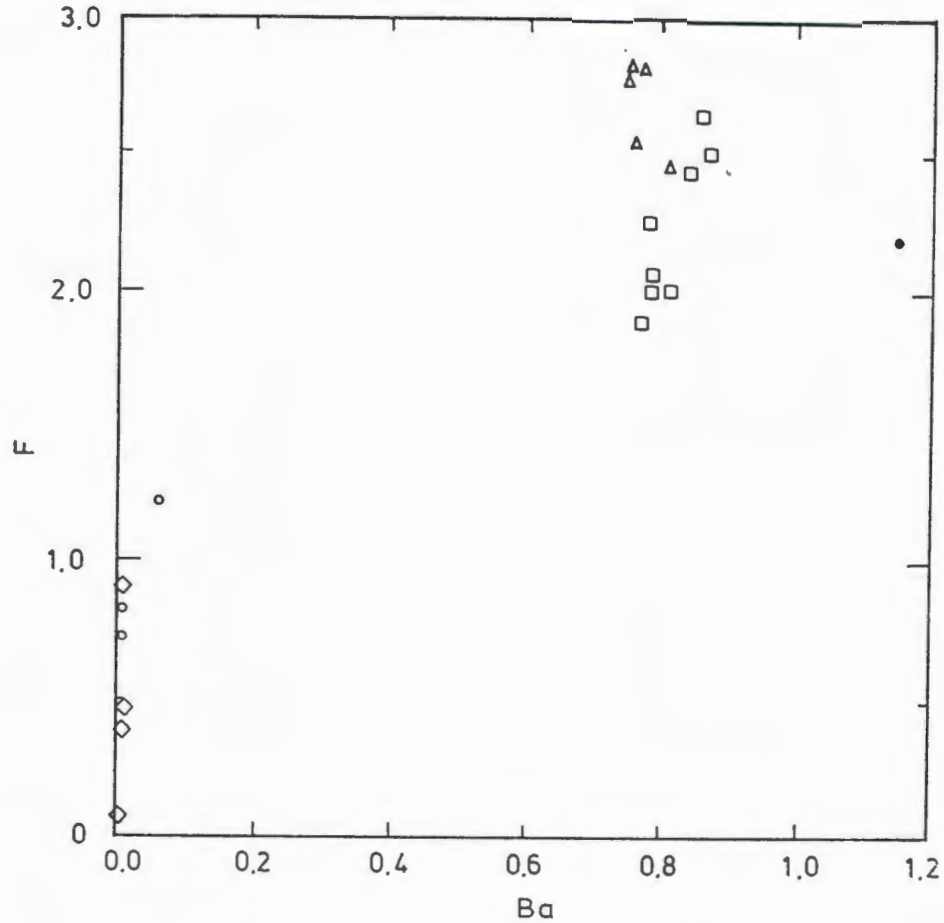

Figure 6.22. Plot of atomic proportion Ba against wt.% F. The Ba-rich biotite is more F-rich than the Ba-poor, with little overlap in compositions. (Symbols for rocks: same as Figure 6.19).

6.6.MUSCOVITE

White mica was analysed from samples within massive sulphide rock, within an aggregate of the massive sulphide rock and within the schist around the LOB. The composition of the white micas is very similar in the various rock-types. It corresponds to an almost ideal muscovite (Table 6.6). The muscovite is Ti-bearing (1.1 wt.% TiO_2) and has small amounts of Fe (2.26 wt.% FeO) and Mg (1.07 wt.% MgO). Muscovite in the massive sulphide rock (sample TS5) and schist (sample 1917-N6) have small Ba concentrations (0.66 wt.% BaO).

Table 6.6. Average electron microprobe analyses of muscovite.

wt. %	MSR TS5 (n=5)	1σ	Average of all samples (N=5)	1σ
SiO_2	44.33	0.636	46.19	0.622
TiO_2	1.56	0.078	1.10	0.201
Al_2O_3	34.29	0.324	35.19	1.129
FeO	1.73	0.069	2.26	0.634
MgO	1.52	0.007	1.07	0.273
BaO	0.66	0.803	1.94	0.146
Na_2O	0.54	0.086	0.30	0.070
K_2O	9.18	0.722	8.89	0.319
F	0.63	0.393	0.97	0.368
Total	94.46		96.20	
Si IV	6.01	0.067	6.12	0.042
AL IV	1.98	0.067	1.87	0.042
T site	8.00	0.000	8.00	0.000
Al VI	3.50	0.005	3.62	0.105
Ti VI	0.16	0.008	0.11	0.201
Fe^{2+}	0.19	0.007	0.25	0.073
Mg^{2+}	0.30	0.002	0.21	0.056
O site	4.17	0.008	4.20	0.024
Ba	0.03	0.042	0.01	0.007
Na	0.14	0.002	0.08	0.018
K	1.59	0.126	1.50	0.066
A site	1.76	0.106	1.59	0.080
OH	3.72	0.168	3.58	0.159
F	0.27	0.168	0.41	0.159

Cations determined on the basis of 20 oxygens.
Total Fe reported as FeO.
n - number of points.
N - number of samples.

6.7.GAHNITE

Gahnite occurs in massive sulphide rock, quartz magnetite iron formation, massive magnetite iron formation, garnet quartzite and pegmatite. Gahnite was also found along the perimeter of biotite-rich lenses within the massive sulphide rock. Representative analyses of the gahnite from various rocks are given in Table 6.7 and the compositional variation shown in Figure 6.23 is indicative of ferroan gahnite. The range for ferroan gahnite is ($Gahnite_{46-69}$,$Hercynite_{19-49}$,$Spinel_{2-5}$,$Galaxite_{0-1}$). The ferroan gahnite analysed is depleted in the spinel component compared with gahnite in rocks associated with metamorphosed massive sulphide deposits elsewhere in the world (Fig. 6.23). Gahnite in the garnet quartzite has, however, considerably higher hercynite component and compares well with hercynite from world wide aluminous metasediments (Spry and Scott, 1986).

Plots of wt.% FeO and MgO versus ZnO reveal the variable composition of gahnite in the different rock types (Fig. 6.24a-b). FeO ranges between 7.64 and 19.47 wt.%, and MgO between 0.30 and 1.17 wt.%. In Figure 6.24, a strong antipathetic correlation ($r = -0.99$) between FeO and ZnO indicates the substitution of Fe for Zn.

Compositional zoning of ferroan gahnite grains enclosed within magnetite in quartz magnetite iron formation from Broken Hill has been examined by Spry (1987). In the thin sections examined, optically zoned gahnite was only observed in a garnet quartzite rock (sample TS13). Spry (1987) reports that relative to the rims, the cores are significantly enriched in Zn and depleted in Fe, with minor depletions in Mg and Mn. This zoned gahnite was only recognized in the quartz magnetite iron formation, and it was suggested by Spry (1987) that the Zn became depleted during the growth of ferroan gahnite.

ZnO variations of gahnite on the scale of a thin section range from nearly uniform, (1σ = 0.17 wt.%) in quartz magnetite iron formation to the maximum variation (1σ = 2.74) in garnet quartzite. The variation of the Zn component in ferroan gahnite at this scale is either controlled by sphalerite of different composition within the same rock or variations in the oxygen and sulphur fugacity.

Table 6.7. Average electron microprobe analyses for gahnite.

wt.%	MSR TS11 (n=12)	GQ TS13 (n=6)	QMIF TS3 (n=4)	MSR# BH1 (n=2)
SiO_2	nd	nd	nd	nd
TiO_2	nd	0.02	nd	nd
Al_2O_3	55.06	54.41	55.38	54.90
Cr_2O_3	0.08	0.34	nd	nd
FeO	9.44	22.62	9.01	10.57
MnO	0.31	0.13	0.35	0.23
MgO	0.98	1.17	0.70	0.33
ZnO	33.49	20.86	34.48	33.56
Total	99.36	99.53	99.92	99.59
Al	1.96	1.91	1.97	1.96
Cr	nd	0.01	nd	nd
Fe^{3+}	0.04	0.08	0.03	0.04
Fe^{2+}	0.20	0.49	0.19	0.23
Mn	0.01	0.00	0.01	0.01
Mg	0.04	0.05	0.03	0.02
Zn	0.75	0.46	0.77	0.75
Cations	3.00	3.00	3.00	3.01
Fe^{2+}/Zn	0.27	1.08	0.25	0.30

Cations determined on the basis of 4 oxygens.
Total Fe determined as FeO.
Fe^{3+} - calculated from formula.
n - number of points.
nd - not detected.
- gahnite rim around biotite-rich lens in massive sulphide rock.

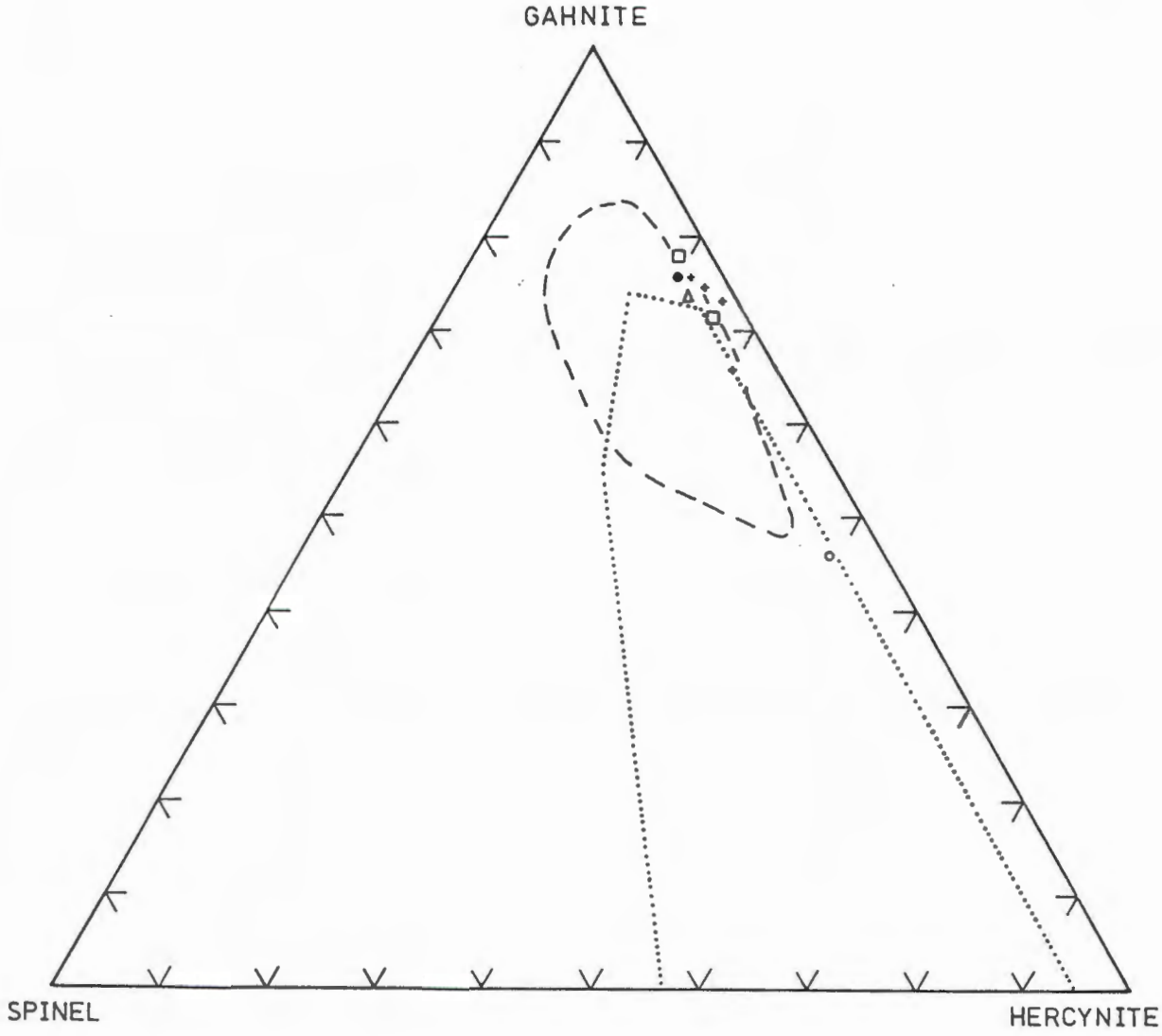

Figure 6.23. Compositional variation with respect to pure gahnite, spinel, hercynite for average analyses of zincian hercynite from the LOB in various rock-types. (Symbols for rocks: square- QMIF, filled circle- massive sulphide rock, open circle- garnet quartzite, triangle- schist, cross- garnet-rich aggregates within massive sulphide rock) Dashed line and dotted lines represents world wide compositions of gahnite in massive sulphide deposits and aluminous-rich sediments, respectively, (Spry, 1986; Spry and Scott, 1986a).

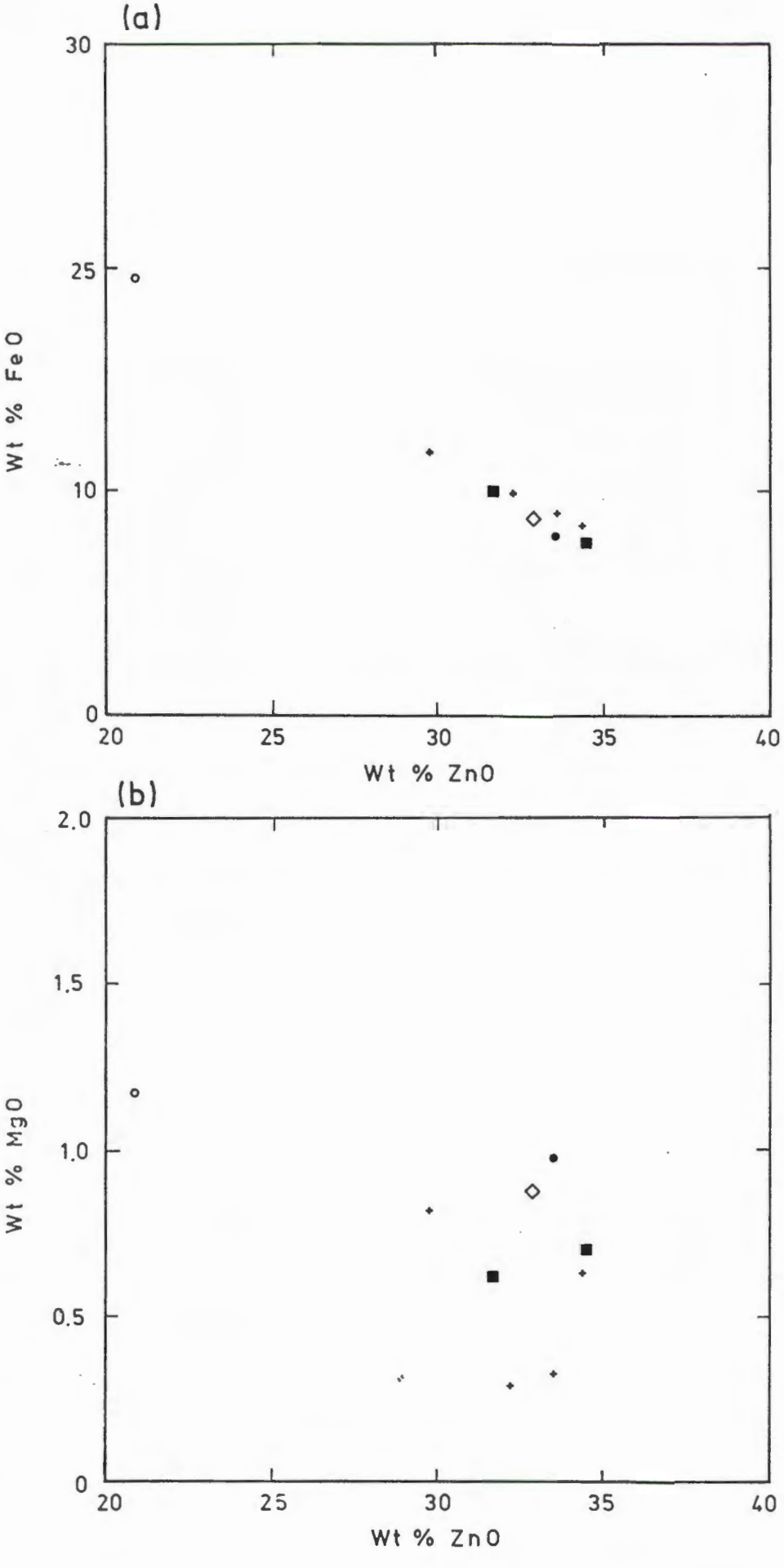

Figure 6.24. Compositional variation with respect to ZnO versus (a) FeO and (b) MgO for zincian hercynite in various LOB rock-types. (Symbols: the same as in Figure 6.22).

The compositional variation of gahnite within the various rock-types across the stratigraphy has been examined in borehole BHU2609 (Fig. 6.25). The gahnite in massive sulphide rock within the ore zone is enriched in Zn relative to garnet quartzite (TS13) higher in the structural sequence.

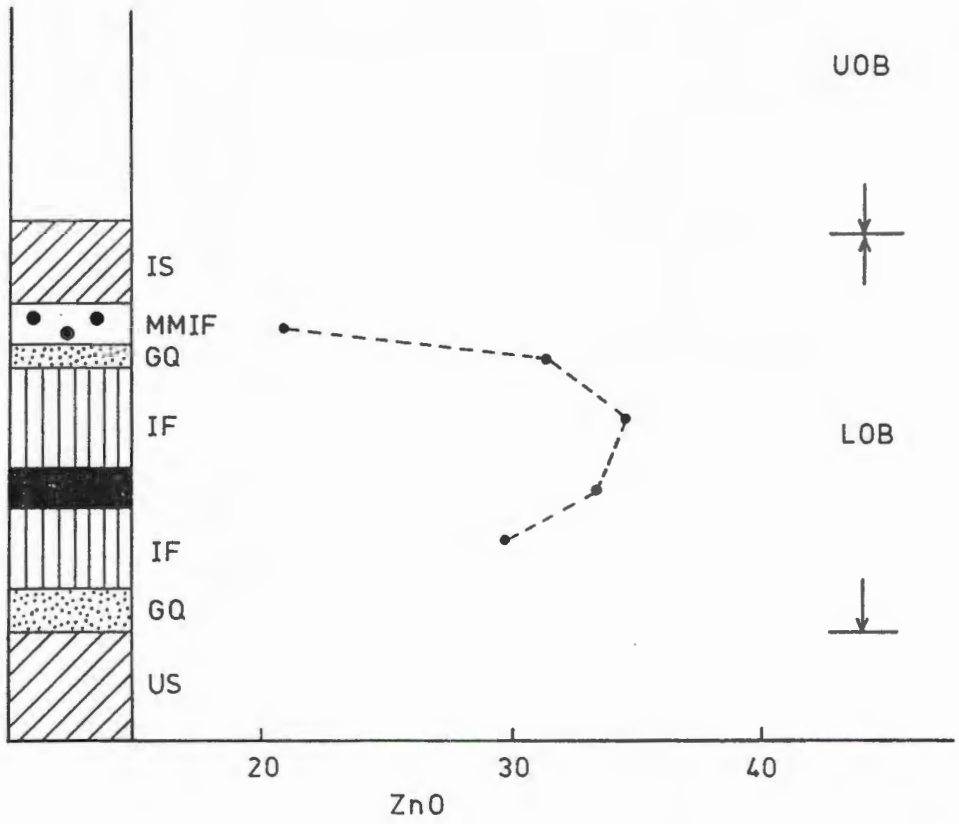

Figure 6.25. Schematic stratigraphic column showing the compositional variation of the ZnO in ferroan gahnite. (Abbreviations: IS - Intermediate Schist, MMIF -massive magnetite iron formation, GQ - garnet quartzite, IF - undifferentiated iron formation, US - Footwall Schist).

6.8.TOURMALINE

Tourmaline occurs as an accessory mineral disseminated in massive sulphide rock, within garnet-rich aggregates in the massive sulphide rock, in pegmatite, and rarely within silicate-rich mesobands in the iron formation. In the massive magnetite iron formation, tourmaline commonly forms coarse-grained porphyroblasts within fine-grained magnetite matrix.

Analyses of tourmalines from the massive sulphide rock, garnet-rich aggregates and massive magnetite iron formation are given in Table 6.8. The tourmalines from these rocks show small variations in the distribution of SiO_2 but larger for Al_2O_3. The FeO content varies from 5.00 to 14.14 wt.% and the MgO content ranges from between 3.73 and 7.64 wt.%. Only tourmaline within the massive sulphide rock has higher MgO than FeO contents. In the rocks examined, tourmaline has a limited range of Na_2O (1.94-2.44 wt.%) and CaO (0.56-0.99 wt.%). CaO in tourmaline is depleted in the massive magnetite iron formation compared to the other rock-types. TiO_2 variations are small, with 0.65 wt.% in massive sulphide rock, 0.49 wt.% in garnet-rich aggregates and 0.17 wt.% in the massive magnetite iron formation. Despite the high Mn content in the host rock only small amounts of Mn (<0.2 wt.% MnO) were detected in the tourmaline. All tourmaline grains analysed in the LOB have high F contents varying between 0.61 and 1.16 wt.%.

Major element oxides indicate tourmaline from granitic rocks to be chemically distinct from those associated with massive sulphide deposits. In a ternary MgO-Na_2O-FeO diagram (Fig. 6.26) tourmalines associated with granite, aplite and pegmatite from Southwest England (Power, 1968) and Northern Portugal (Neiva, 1974) plot within the region of the schorl apex (FeO/(FeO+MgO) = 0.86-0.91) whereas those associated with massive sulphide deposits from the Appalachian-Caledonides (Taylor and Slack, 1984) plot close to the dravite end-member composition (FeO/(FeO+MgO) = 0.02-0.4).

The FeO/(FeO+MgO) ratio of LOB tourmaline in the various rocks varies between 0.40 and 0.79. In the massive sulphide rock this ratio is 0.42 which is similar to that obtained in tourmaline from the Mine Sequence of Broken Hill district, Australia, (Plimer, 1983). Tourmalines in garnet-rich aggregates and massive magnetite iron formation have exceptionally high FeO/(FeO+MgO) ratios of 0.70 and 0.79, respectively. The high schorl component is related to the exceptionally Fe-rich bulk composition, in analogy to tourmalines from Broken Hill, Australia (Stevens and Stroud, 1983).

Table 6.8. Representative electron microprobe analyses of tourmaline.

wt. %	MSR (TS5) (n=1)	MMIF (BH2) (n=1)	Aggregate in MSR (BH4) (n=1)
SiO_2	35.21	35.15	34.30
TiO_2	0.66	0.23	0.49
Al_2O_3	35.36	32.33	30.63
FeO	5.69	11.81	14.14
MnO	0.16	0.00	0.20
MgO	6.97	5.37	3.73
CaO	1.09	0.55	0.90
Na_2O	1.92	2.42	2.14
K_2O	0.11	0.00	0.07
F	0.61	1.16	0.94
Cl	nd	nd	nd
Total	87.78	89.02	87.54
Si	6.24	6.39	6.43
Ti	0.09	0.03	0.07
Al	7.39	6.92	6.76
Fe^{2+}	0.84	1.80	2.22
Mn	0.02	0.00	0.03
Mg	1.84	1.45	1.04
Ca	0.21	0.11	0.18
K	0.02	0.00	0.02
Na	0.66	0.85	0.78
Cations	17.32	17.55	17.52
$Fe^{2+}/Fe^{2+}+Mg+Mn$	0.45	0.69	0.79

Cations calculated on the basis of 27 oxygens
Total Fe reported as FeO.
n - number of points.
MSR - massive sulphide rock.
MMIF - massive magnetite iron formation.

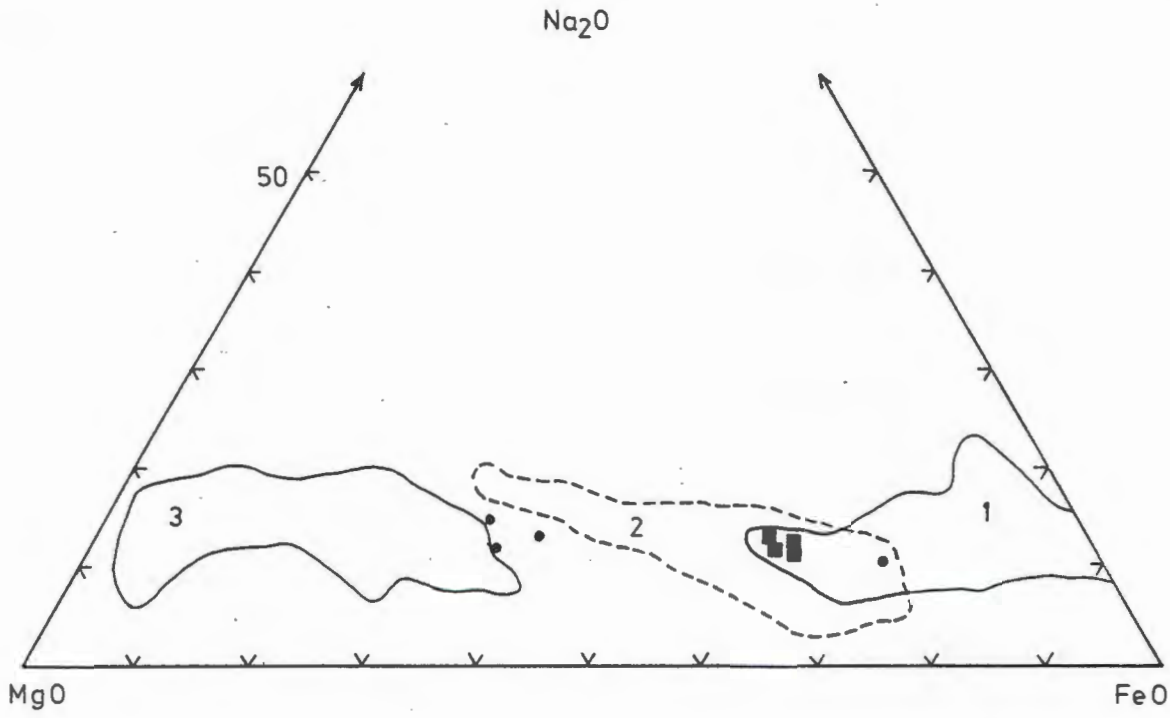

Figure 6.26. Tourmaline compositions for LOB rocks plotted on a (FeO-MgO-Na_2O) ternary diagram. Superposed are tourmaline compositional fields for (1) granitoids after Powell (1968) and Nieve (1974), (2) Mine sequence, Broken Hill, Australia (Plimer, 1983) and (3) Appalachian-Caledonide massive sulphide deposits after Taylor and Slack (1984). (Symbols for rocks: filled circle - massive sulphide rock, filled square - massive magnetite iron formation).

Within massive sulphide deposits in the Appalachians and Caledonides, tourmaline has a $Na_2O/(Na_2O+CaO)$ ratio that varies from 0.31 to 0.91 with an average of 0.66 (Taylor and Slack, 1984). In the LOB, the $Na_2O/(Na_2O+CaO)$ ratio is limited between 0.62 and 0.87 which is within the range of tourmaline from worldwide massive sulphide deposits.

The halogen content, in particular F, of Fe-rich igneous tourmaline is variable between 0 and 1 wt.% F (Power, 1968; Neiva, 1974) and might not be necessarily suitable to discriminate between those from massive sulphide deposits which have F contents that vary from 0.06 to 0.71 wt.% (Taylor and Slack, 1984). Plimer (1983) suggested that the F/Cl ratio is more appropriate to distinguish tourmaline in igneous rock from that in massive sulphide deposits. Tourmaline in igneous rocks have F/Cl ratios ranging from 2 (Neiva, 1974) to 21 (Power,1968), compared with an average F/Cl ratio of 33 found in massive sulphide deposits (Taylor and Slack, 1984). In the LOB, tourmalines analysed have Cl contents below the detection limit of 0.001 wt.%, whereas F contents are on average 0.85 wt.%, yielding a

F/Cl ratio of at least 500. The marked difference of F/Cl ratio of tourmaline in the LOB compared with that reported by Taylor and Slack (1984) for tourmaline from massive sulphide deposits is thought to result from different fluid compositions and possibly different temperature of formation.

6.9.STAUROLITE

Zincian staurolite occurs as an accessory mineral in garnet quartzite, and was only observed in sample TS13. It is characterized by a high Zn content (Table 6.9), and a formula of $(Zn_{1.4}Mg_{.1}Fe_{1.1})Al_{18.0}Si_{8.2}O_{46}(OH)_2$ can be derived for this zincian staurolite.

Table 6.9. Microprobe analyses of zincian staurolite from Broken Hill and elsewhere in Namaqualand.

wt.%	GQ (this study)	Gamsberg Spry and Scott (1986)	Namaqualand Moore and Reid (1989)
SiO_2	29.90	27.37	24.40
TiO_2	nd	0.26	0.29
Al_2O_3	56.04	54.08	52.58
FeO	4.65	8.99	10.70
MnO	nd	2.22	0.25
MgO	0.21	0.64	1.75
ZnO	6.67	2.84	4.63
Total	97.46	96.40	97.60
Si	8.19	7.72	7.71
Ti	nd	0.06	0.06
Al	18.09	19.97	17.45
Fe	1.07	2.12	2.52
Mn	nd	0.53	0.06
Mg	0.08	0.27	0.73
Zn	1.35	0.59	0.96
Cations	28.77	29.25	29.50

Cations determined on the basis of 46 oxygens.
Fe total reported as FeO.
nd - not detected.

Zincian staurolite has been reported from elsewhere in Namaqualand by Moore and Reid (1989) and from the Gamsberg by Spry and Scott (1986). Staurolite in the garnet quartzite has a higher ZnO component, 6.67 wt.% compared to those from Gamsberg for which Spry and Scott (1986) determined 2.84 wt.% ZnO, and Kraaifontein, Namaqualand, which have 4.63 wt.% ZnO (Moore and Reid, 1989). The latter authors propose the formation of zincian staurolite by hydration reaction with gahnite, quartz and sillimanite under retrograde metamorphic conditions via the reaction:

$$4ZnAl_2O_4 + 3SiO_2 + 5Al_2SiO_5 + H_2O = Zn_4Al_{18}Si_8O_{46}(OH)_2$$

This reaction is supported by textural evidence where euhedral staurolite partly encloses anhedral gahnite, indicating staurolite growth after gahnite. Spry and Scott (1986) suggested that at Gamsberg zincian spinel may have formed by the prograde breakdown of staurolite. Their evidence is from the ragged appearance of staurolite coexisting with euhedral gahnite. Consequently, remnant zincian staurolite appears to have survived breakdown reactions in the formation of zincian hercynite at upper amphibolite grade.

In the garnet quartzite studied here, no textural evidence was observed to suggest that staurolite served as a precursor to gahnite, or that staurolite formed from the hydration reaction of Moore and Reid (1989). An alternative zincian staurolite forming reaction has been proposed by Spry and Scott (1986):

$$2ZnS + 9Al_2SiO_5 + H_2O + 2O_2 = Zn_2Al_9Si_4O_{23}(OH) + SiO_2 + 2S_2$$

This reaction is similar to that for gahnite formation (modified after Spry and Scott, 1986).

6.10.SPHALERITE

High modal proportions of sphalerite (up to 8 vol.%) are found in massive sulphide rock and quartz magnetite iron formation, and smaller modal proportions, generally between 1-2 vol.%, in the iron formation and garnet quartzite. Sphalerite forms equilibrium assemblages with pyrrhotite, pyrrhotite-pyrite and pyrrhotite-magnetite, with or without chalcopyrite. In thin-section, some sphalerite is characterized by fine intergrowths of chalcopyrite-like

sulphide, referred to as "chalcopyrite disease" (sensu Barton, 1978).

Analyses of 46 sphalerite grains from eight rocks were determined. Typical sphalerite compositions are given in Table 6.10. The compositional data plot along the ZnS-FeS tie line in Figure 6.26. Compared to sphalerite from Gamsberg (Rozendaal, 1982), those from Broken Hill are significantly depleted in MnS. The compositional variations of the major sulphide components in all sphalerite grains analysed are illustrated as histograms in Figure 6.27. The average FeS content of all sphalerite is 14.00 mole % but varies between 5.67 and 16.73 mole %. The CuS and MnS components for sphalerite are small, with average contents of 0.05 and 0.45 mole %, respectively.

Table 6.10. Average electron microprobe analyses of sphalerite.

wt.%	QMIF TS3 (n=7)	MSR TS5 (n=6)	MSR TS11 (n=7)	MSR TS2 (n=5)	AMIF TS15 (n=11)
S	34.27	34.07	33.88	34.16	34.13
Zn	57.12	56.97	57.14	56.89	59.63
Fe	8.13	8.43	8.51	8.78	5.56
Mn	0.31	0.06	0.27	0.07	0.16
Cu	0.02	0.00	0.04	0.06	0.04
Total	100.06	100.07	99.84	99.97	99.52
ZnS*	84.90	84.34	84.70	84.51	89.84
FeS*	14.21	14.60	14.76	15.27	9.81
MnS*	0.58	1.05	0.48	0.13	0.29
CuS*	0.03	0.01	0.06	0.09	0.07

* mole percent (normalized).
n - number of points.
MSR - massive sulphide rock.
AMIF - amphibole magnetite iron formation rock.
QMIF - quartz magnetite iron formation rock.

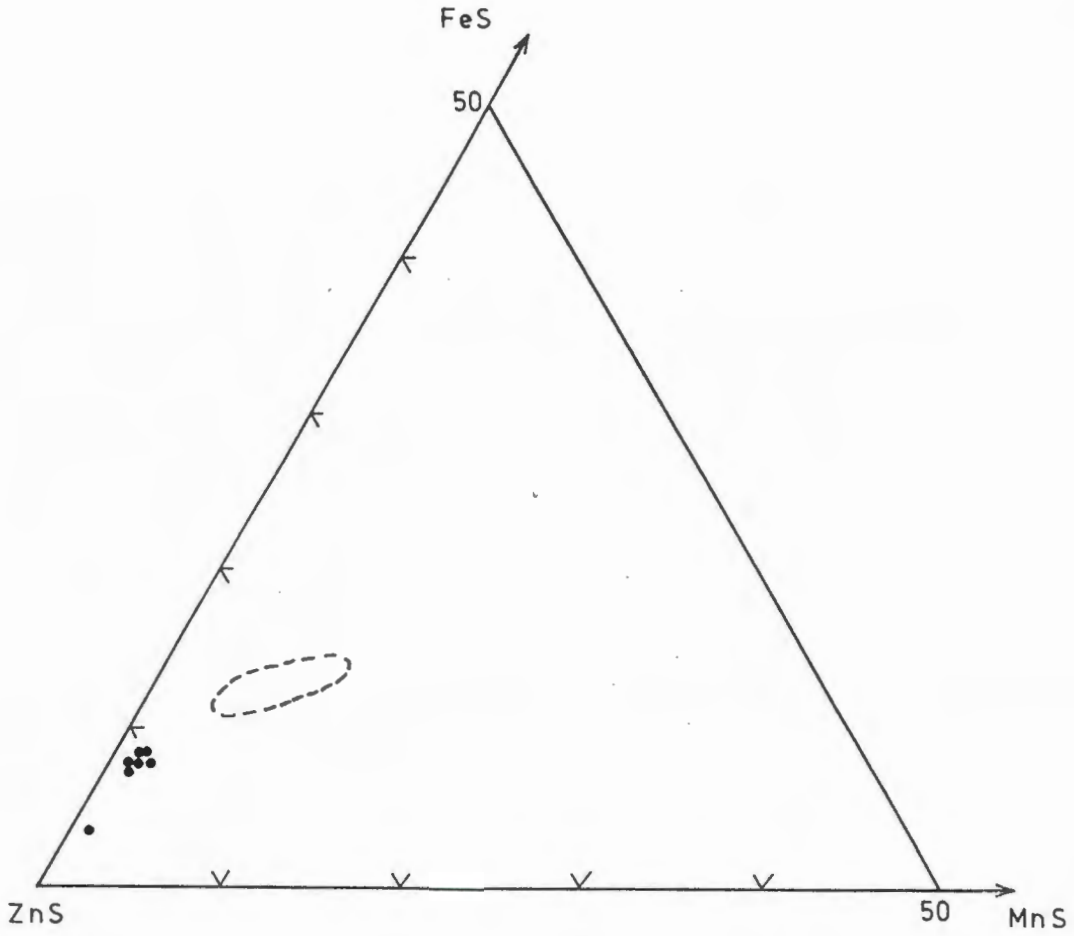

Figure 6.27. Compositions of sphalerite in the LOB shown as mole % of ZnS, FeS and MnS. Dashed line represents the compositional field for sphalerite from Gamsberg deposit (Rozendaal and Stumpfl, 1984).

The FeS content of sphalerite coexisting with pyrite and pyrrhotite in massive sulphide rock is 15.08 mole % (sample TS5). A similar value of 14.94 mole % was determined for sphalerite in the pyrite-pyrrhotite-magnetite assemblage and 15.23 mole % for a magnetite assemblage (sample TS12). Uniform FeS contents in sphalerite are indicated by the standard deviations (1σ) of 0.86 (n=6), 0.40 (n=8) and 0.53 (n=7) mole % within three samples, (TS5, TS3 and TS12), respectively. The FeS contents in LOB sphalerite reported here are higher than for sphalerite in equilibrium with pyrite and pyrrhotite reported by De Waal and Johnson (1981) which has a mean of 13.7 mole %. The FeS contents in sphalerite in equilibrium with pyrrhotite was shown by De Waal and Johnson (1981) to vary between 14 and 22 mole %. It is uncertain whether their samples of massive sulphide rock and iron formation are representative of both the LOB and the UOB successions.

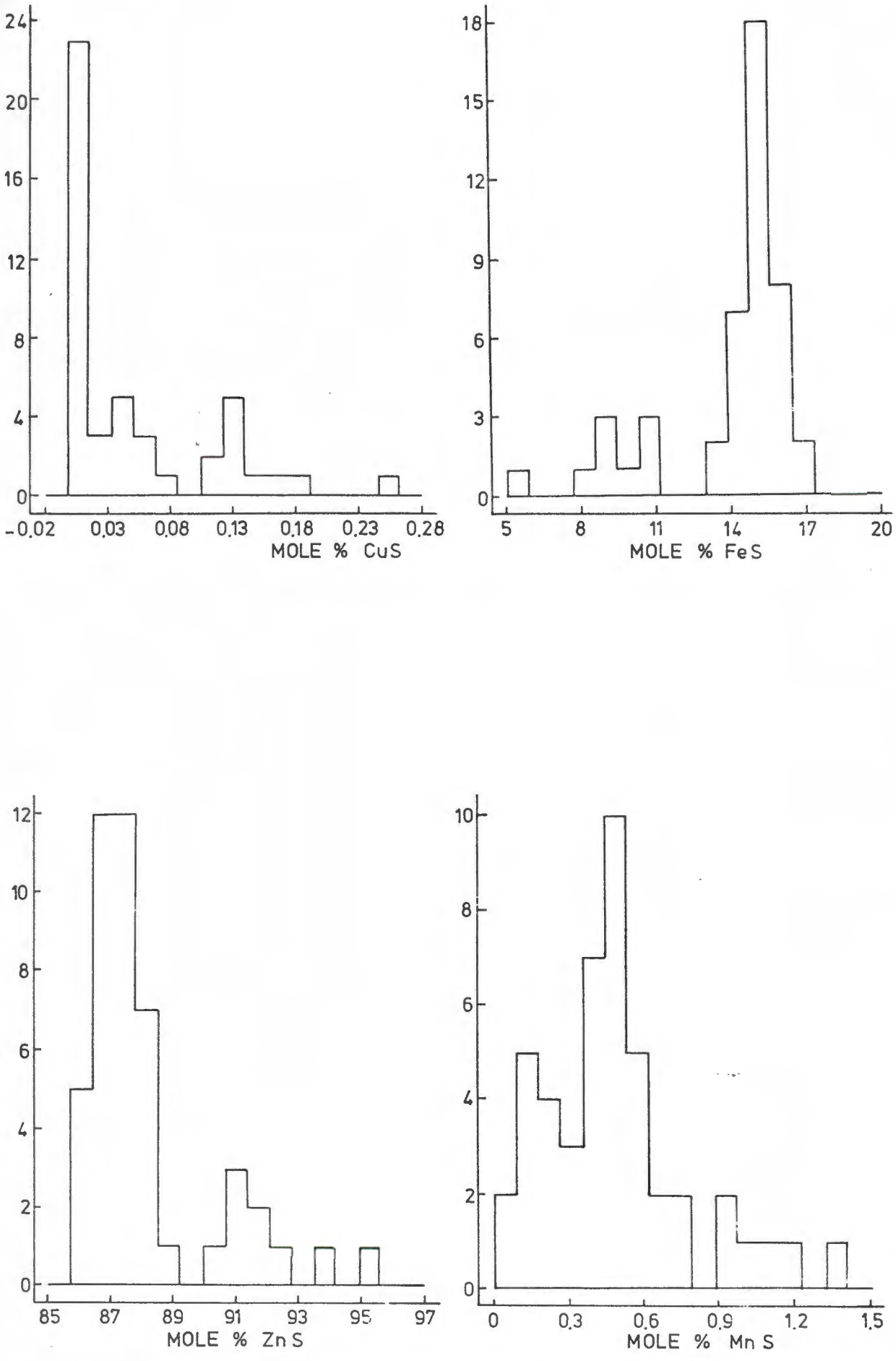

Figure 6.28. Histograms representing compositions of sphalerite expressed as mole % ZnS, FeS, MnS and CuS.

In a single sample (TS15) within the AMIF, sphalerite shows a high variation in FeS which ranges from 5.68 to 13.32 mole %. This variation is explained by the presence of two optically distinct types of sphalerite. These are differentiated in thin-section under normal transmitted light by their red-brown and yellow colours for the FeS-enriched and depleted types, respectively. Both types of sphalerite have the same textures and form equilibrium assemblages with silicate minerals and magnetite. Sphalerite compositional heterogeneity in the Broken Hill deposit, Aggeneys, has previously been reported by De Waal and Johnson (1981). These authors recognized variable FeS and CuS contents between a primary and a secondary "neoformed" sphalerite. The latter is situated within the oxidation zone under near-surface conditions. Sphalerite examined in this study have a maximum CuS content of 0.25 mole %, well within the 1.6 mole % limit characteristic of primary sphalerite (De Waal and Johnson, 1981). Sphalerite in sample TS15 plots within the field for primary sphalerite (Fig. 6.28) but approaches the ZnS-$CuFeS_2$ boundary. This is the expected path of change of the chemistry for supergene alteration where Fe depletion (<4.5 mole % FeS) is accompanied by Cu enrichment. The variable FeS content in sphalerite in sample TS15 is, however, not accompanied by significant enrichment in CuS. This sample was collected far from the sub-surface oxidation zone and the low FeS content in this sphalerite is unlikely to be a result of local alteration. It may be speculated that changes in the oxygen and sulphur fugacities caused the decrease in the FeS content of sphalerite.

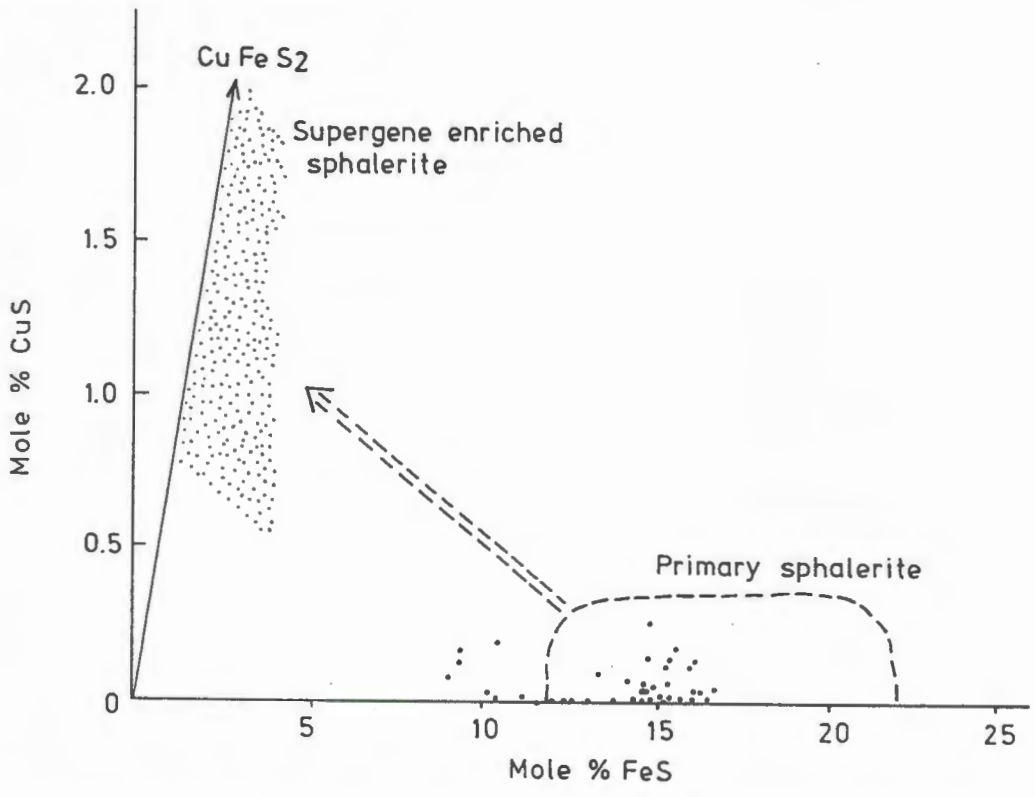

Figure 6.29. Plot of mole % FeS versus CuS for sphalerite. The solid line represents the ZnS-$CuFeS_2$ boundary, the dashed line indicates the field of primary sphalerite and the double dashed line indicates the path of supergene alteration for the formation of secondary sphalerite (De Waal and Johnson, 1981).

6.11.OXIDES

Typical microprobe analyses for magnetite, ilmenite and rutile are given in Table 6.11 and their compositional variation is shown in a ternary ($FeO+Fe_2O_3$)-TiO_2-MnO diagram (Fig. 6.30). The total Fe was determined as FeO which was recalculated for FeO and Fe_2O_3 components.

Table 6.11. Representative electron microprobe analyses for oxide minerals.

wt.%	Magnetite IF (n=1)	Magnetite FQ (n=1)	Ilmenite GQ (n=1)	Ilmenite MSR (n=1)	Rutile MSR (n=1)
TiO_2	0.49	0.12	52.90	50.54	99.49
Al_2O_3	0.15	0.67	nd	nd	nd
$Fe_2O_3^*$	67.21	67.94	ND	ND	ND
FeO	31.22	31.25	44.24	43.55	0.23
MnO	nd	nd	2.77	4.72	nd
Total	99.06	99.97	99.91	98.82	99.72
Ti	0.01	0.00	1.01	0.97	1.00
Al	0.01	0.03	0.00	0.00	0.00
Fe^{3+}	1.96	1.96	0.00	0.06	0.00
Fe^{2+}	1.01	1.00	0.95	0.87	0.00
Mn	0.00	0.00	0.06	0.10	0.00
Cations	3.00	3.00	2.00	2.00	1.00
O	4	4	3	3	2

nd - not detected (SiO_2, MgO, CaO, Cr_2O_3, ZnO and NiO.
* - calculated from formula by microprobe on-line facility.
ND - not determined.
IF- iron formation, FQ- ferruginous quartzite, GQ- garnet quartzite, MSR- massive sulphide rock.
n - number of analyses.

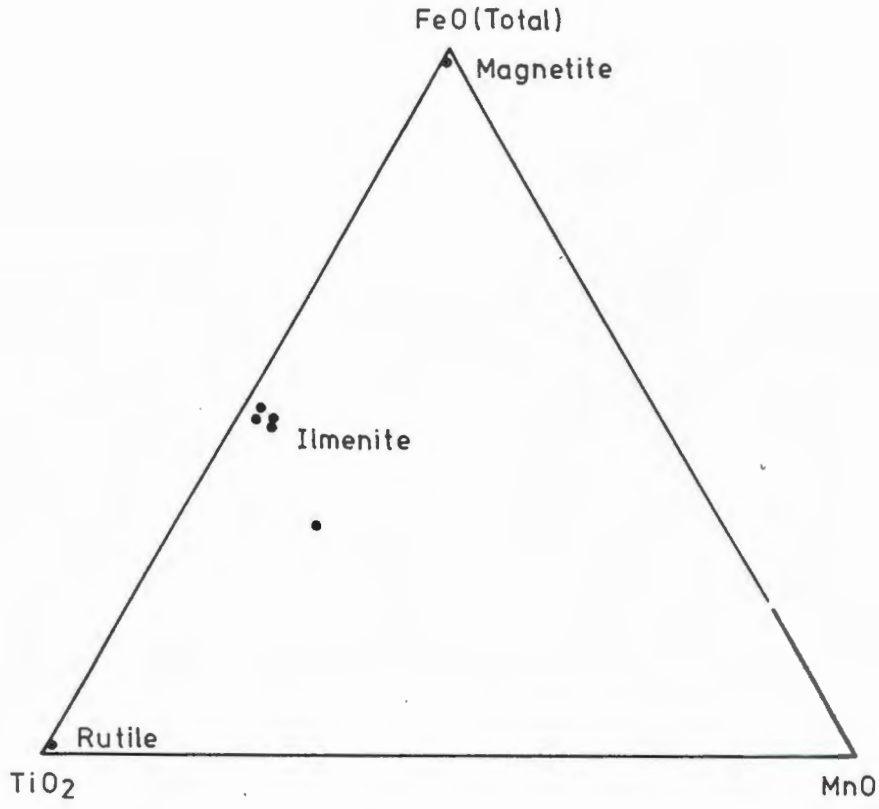

Figure 6.30. Ternary plot of ($FeO_{T\alpha}$-TiO_2-MnO) showing compositional variation of oxide minerals in the LOB.

Magnetite in the banded iron formation, ferruginous quartzite, garnet quartzite and massive sulphide rock has nearly ideal Fe_3O_4 compositions. Typical impurities are TiO_2, MnO and Al_2O_3. Concentrations of MgO, ZnO, Cr_2O_3 and NiO were below the detection limits in all of the analyses (Appendix A) and the SiO_2 content is less than 0.15 wt.%. The FeO and Fe_2O_3 contents for 22 analyses in 10 rocks have means of 30.91 wt.% (1σ = 0.20) and 67.27 wt.% (1σ = 0.18), respectively, indicating the homogenous composition of magnetite.

Ilmenite is invariably present in the form of single, disseminated grains. Ilmenite probed in massive sulphide rock and garnet quartzite have low MnO contents (4.72 and 2.20 wt.% MnO, respectively). A single grain of Mn-rich ilmenite analysed in garnet quartzite (TS13) has a MnO content of 16.47 wt.%. Rutile in contact with ilmenite in massive sulphide rock is nearly pure TiO_2 (99.51 wt.%).

6.12.DISTRIBUTION OF Fe^{2+}-Mg-Mn IN GARNET, AMPHIBOLE, OLIVINE, ORTHOPYROXENE AND PYROXFERROITE

Manganiferous iron-rich garnet, amphibole, olivine, orthopyroxene and pyroxferroite occur in varying proportions within the amphibole-rich iron formation bands in the LOB iron formation. The coexisting silicate pairs for which the exchange of Fe-Mg-Mn is considered are (i) amphibole-garnet (ii) amphibole-olivine (iii) olivine-garnet and (iv) garnet-orthopyroxene.

A variety of atomic ratios are available to quantify the Fe-Mg-Mn distribution between coexisting phases. For example, distribution coefficients for Mn are calculated either with the 'total' atomic ratio (e.g. Mn/ SUM cations in octahedral site) or with partial atomic ratios (e.g. Mn/(Fe+Mg+Mn). The distribution of X_{Mn} between the silicate phases is represented as K_D.Mn and the distribution of Fe is represented by K_D.FeMg, with X_{Mn}= Mn/(Mn+Mg+Fe) and X_{Fe}=Fe/(Fe+Mg), respectively. Definitions of the distribution coefficients K_D.Mn and K_D.FeMg are given below. For each silicate pair, the mean composition of the analysed core positions was used. In all cases, Fe is considered in the divalent oxidation state.

$$K_D.FeMg = \frac{X_{Fe}^a}{(1-X_{FE}^a)} x \frac{(1-X_{Fe}^b)}{X_{Fe}^b} = \frac{(Fe^{2+}/Mg)^a}{(Fe^{2+}/Mg)^b}$$

$$K_D.Mn = \frac{X_{Mn}^a}{(1-X_{Mn}^a)} x \frac{(1-X_{Mn}^b)}{X_{Mn}^b} = \frac{(Mn/Fe^{2+}+Mg)^a}{(Mn/Fe^{2+}+Mg)^b}$$

The silicate phases in the iron formation have considerable Mn contents even in the presence of garnet which is well known to behave as a reservoir for Mn. The proportion of Mn within the various silicate phases of the samples is indicated by the mole fractions (Table 6.12). Pyroxferroite has a larger mean X_{Mn} with less variation than garnet. The X_{Mn} values for olivine, amphibole and orthopyroxene are similar. The Mn-bearing minerals are listed below

in order of decreasing X_{Mn}.

pyroxferroite	>	garnet	>	olivine	>	orthopyroxene	>	amphibole
0.463		0.410		0.146		0.140		0.136

Similarly, the Fe-bearing minerals are listed in the order of decreasing X_{Fe}.

olivine	>	garnet	>	pyroxferroite	>	orthopyroxene	>	amphibole
0.967		0.967		0.893		0.850		0.805

The distribution coefficients are listed in Table 6.13. The distribution coefficients reveal the preference of Mn for garnet over amphibole, olivine and orthopyroxene. Mn slightly favours partitioning into olivine rather than amphibole. K_D.Mn is similar for orthopyroxene and olivine with respect to coexisting garnet.

Fe compared with Mg is strongly partitioned into garnet rather than coexisting amphibole and orthopyroxene. Between garnet-olivine and olivine-amphibole pairs, the partitioning of Fe and Mg is not strongly differentiated with only a slight preference of Fe over Mg.

The small standard deviations (1σ) of K_D.FeMg and K_D.Mn are constant from one iron formation band to the next. Bearing in mind that all these iron formation bands must have experienced very similar P-T conditions and have similar whole rock compositions, no significant variations in the K_D-values are expected.

Table 6.12. Table of mole fractions for Fe and Mg in iron formation silicate minerals.

SAMPLE	GARNET Fe/Fe+Mg	GARNET Mn/Fe+Mg+Mn	AMPHIBOLE Fe/Fe+Mg	AMPHIBOLE Mn/Fe+Mg+Mn	OLIVINE Fe/Fe+Mg	OLIVINE Mn/Fe+Mg+Mn	OPX+PYROXFERR. Fe/Fe+Mg	OPX+PYROXFERR. Mn/Fe+Mg+Mn
BHG1	0,950	0,440						
BHG2	0,980	0,420						
BHG4	0,940	0,320						
BHG6	0,980	0,500						
BHG13	0,970	0,620	0,720	0,180				
BHG16	0,970	0,380						
BHG17	0,970	0,550						
BHG23	0,920	0,470						
BHA5			0,880	0,120	0,990	0,170		
BHA7	0,980	0,420	0,880	0,110	0,980	0,150		
BHA9	0,980	0,420	0,850	0,110	0,980	0,150		
BHA10	0,980	0,440	0,830	0,110	0,970	0,160		
BHA11	0,980	0,440	0,830	0,110	0,970	0,160		
BHA12			0,660	0,210				
BHA18			0,820	0,100	0,970	0,140		
BHA19					0,990	0,170		
BHA8	0,980	0,420						
BHS22	0,930	0,200						
TS1								
TS2	0,960	0,230						
TS3								
TS4	0,970	0,200						
TS5								
TS6								
TS7								
TS8	0,950	0,370						
TS9								
TS10	0,970	0,180						
TS11								
TS12	0,920	0,530						
TS13	0,930	0,120						
TS14	0,920	0,110			0,970	0,050		
TS15	0,970	0,440	0,770	0,120	0,970	0,160		
1891-6			0,780	0,160				
1891-8	0,980	0,490	0,870	0,170				
1891-13	0,970	0,510	0,720	0,130				
1891-11	0,980	0,290						
1917-8							0,890	0,450
1917-10							0,900	0,480
1917-N5	0,920	0,320						
1917-N2								
1917-13	0,920	0,390						
2609-8	0,960	0,500						
5-1200	0,970	0,400					0,850	0,140
BH1	0,970	0,400						
BH2								
BH3	0,940	0,100						
BH4								
BH5								
1782-26	0,890	0,460						

Table 6.13. Table of equilibrium constants Kd (Mn) and Kd (Fe) between silicate pairs.

	GARNET -AMPHIBOLE		GARNET -OLIVINE		AMPHIBOLE -OLIVINE		GARNET -ORTHOPYROXENE	
	Kd(FeMg)	Kd(Mn)	Kd(FeMg)	Kd(Mn)	Kd(FeMg)	Kd(Mn)	Kd(FeMg)	Kd(Mn)
SAMPLE								
BHG1								
BHG2								
BHG4								
BHG6	0,080	0,180						
BHG13								
BHG16								
BHG17								
BHG23								
BHA5					0,889	0,667		
BHA7	0,125	0,178	1,069	0,247	0,898	0,722		
BHA9	0,103	0,164	0,963	0,247	0,867	0,667		
BHA10	0,115	0,152	0,813	0,241	0,867	0,632		
BHA11	0,113	0,152	0,892	0,241	0,856	0,632		
BHA12								
BHA18					0,845	0,647		
BHA19								
BHA8								
BHS22								
TS1								
TS2								
TS3								
TS4								
TS5								
TS6								
TS7								
TS8								
TS9								
TS10								
TS11								
TS12								
TS13								
TS14								
TS15	0,094	0,165	0,802	0,241	0,118	0,684		
1891-6								
1891-8	0,142	0,206						
1891-13	0,092	0,143						
1891-11								
1917-8								
1917-10								
1917-N5								
1917-N2								
1917-13								
2609-8							0,200	0,242
5-1200								
BH1								
BH2								
BH3								
BH4								
BH5								
BH11								
1782-26								

7.GEOCHEMISTRY

In the LOB of the Broken Hill deposit, alternating mesobands comprising Fe-rich silicates, oxides and sulphides are considered to be metamorphosed equivalents of iron formation. Major and trace element concentrations in the silicate-rich mesobands were determined in an attempt to resolve their origin and precursor mineralogy (see Chapter 9.1). Because of the sharp contacts between the mesobands it is assumed that individual silicate mesobands of the iron formation behaved essentially as relatively closed systems during metamorphism. In this Chapter, compositions of the different silicate mesobands are compared with each other and then statistically evaluated in order to theorize which elements are causing the mineralogical variation. Furthermore, comparison is made with other iron and manganese formations, as well as (Fe-, Mn-rich) sediments which have either a hydrothermal or a hydrogenous origin.

Whole rock specimens were sampled from broad (> 2-5 cm) homogeneous silicate-rich iron formation mesobands within the LOB. Eight garnet- and ten amphibole/olivine-rich samples were collected from an extensive area within the mine (see Appendix C). These samples are considered typical of the silicate mesoband-types which are easily recognizable in underground exposures. Other silicate-rich mesobands, orthopyroxene- and pyroxferroite-bearing, are either developed in mm-thick bands and were too small to sample or were not recognizable in hand specimen. These were not included in the whole rock geochemistry. A few additional specimens were also collected from the MMIF, GQ, amazonite-rich pegmatite rocks and schist of the Ore Schist Formation.

The silicate-rich bands are interbanded with 1-50 mm-thick bands of magnetite and lesser < 10 mm-thick sulphide bands. In places where the iron formation is deformed, discordant veinlets of coarse-grained galena might cut across the banding. Consequently, the samples were collected from those iron formation mesobands that showed no obvious signs of remobilized sulphide mineralization. Magnetite of less than 5 vol.% is thought to have co-precipitated with the silicate minerals. Silicate mesobands with low magnetite were also selected. By selecting samples with low sulphide contents, the X-ray fluorescence (XRF) analytical technique employed is to some extent optimized (see below).

The major and trace element analyses were carried out using the standard procedure for XRF

at the University of Cape Town (see Appendix A). The LOB iron formation is characterized by significant concentrations of Cu, Pb, Zn and Ba which may affect the trace element analysis due to absorbtion and enhancement effects related to the absorbtion edge of these elements. These effects may cause errors in other trace elements of up to 25%, either positively and negatively, at the concentration levels of the metals present in the sample (Moore, 1989). Furthermore, the concentrations of Cu, Pb, Zn and Ba in the samples were extrapolated from standards with considerably lower concentrations and therefore themselves are subject to increased inaccuracies. Error and detection limits are quantified in Appendix A. Finally, it should be noted that the total Fe was determined as FeO.

7.1.SILICATE MESOBANDS

7.1.1.Whole rock compositions

The average major and trace element concentrations for garnet- and amphibole-rich mesobands are presented in Table 7.1. Some whole rock compositions have low major element totals. These samples have, however, significant contents of Pb, Zn, S and Ba, which are not listed as 'major elements'.

Higher mean contents of SiO_2, Al_2O_3, TiO_2, MnO, CaO and P_2O_5 occur in the garnet-rich mesobands, whereas the amphibole-rich mesobands are enriched in FeO and MgO. The contents of K_2O, Na_2O and H_2O are similar in both mesoband-types and their combined contribution to the total whole rock composition is < 0.30 wt.%. Further chemical distinction between the two silicate mesobands is illustrated by Harker binary plots (Fig. 7.1).

On average, the sum of SiO_2, MnO and FeO accounts for more than 85 and 90 wt.% of the total bulk compositions of garnet- and amphibole-rich mesobands, respectively. The higher mean SiO_2 content of 51.51 wt.% in garnet-rich mesobands in comparison with 42.89 wt.% in the amphibole-rich mesobands is attributed to the higher modal quartz content in the former. A characteristic feature of the latter is the significantly and persistently higher mean FeO content. The amphibole-rich mesobands have an average FeO content of 44.21 wt.% FeO, which is twice the average FeO content in the garnet-rich mesobands (23.05 wt.%).

Table 7.1. Average compositional data and standard deviation (1σ) of XRF analyses of garnet- and amphibole-rich mesobands in the LOB iron formation. (nd - not detected).

wt. %	Garnet mesobands Ave. (n=8)	1σ	Amphibole mesobands Ave. (n=10)	1σ
SiO_2	51.51	6.37	42.89	7.57
TiO_2	0.48	0.11	0.19	0.14
Al_2O_3	10.28	1.93	1.31	0.73
FeO	23.05	3.58	44.21	8.58
MnO	10.72	2.82	6.25	2.01
MgO	0.48	0.24	1.33	0.53
CaO	0.69	0.18	0.27	0.14
K_2O	0.04	0.03	0.04	0.11
Na_2O	0.17	0.18	0.17	0.11
P_2O_5	0.31	0.09	0.17	0.13
H_2O	0.06	0.07	0.04	0.03
LOI	1.22	0.29	1.24	0.62
Total	99.01		97.92	
Mn/Fe	0.46		0.14	
(ppm)				
Mo	2	1	2	1
Nb	9	4	4	4
Zr	212	25	45	41
Y	33	6	6	4
Cr	60	6	22	11
Ni	23	23	11	10
V	45	11	26	21
Rb	11	13	6	18
Sr	47	16	30	29
Th	4	7	nd	
U	1	2	nd	
La	44	10	14	4
Ce	70	10	18	13
Nd	25	5	5	8
Co	14	11	32	23
Sc	7	1	3	1
S	7308	4446	14378	14547
Cu	47	55	256	270
Pb	11798	13159	7679	14789
Zn	3050	3963	4662	3829
Ba	2743	2665	2076	6277

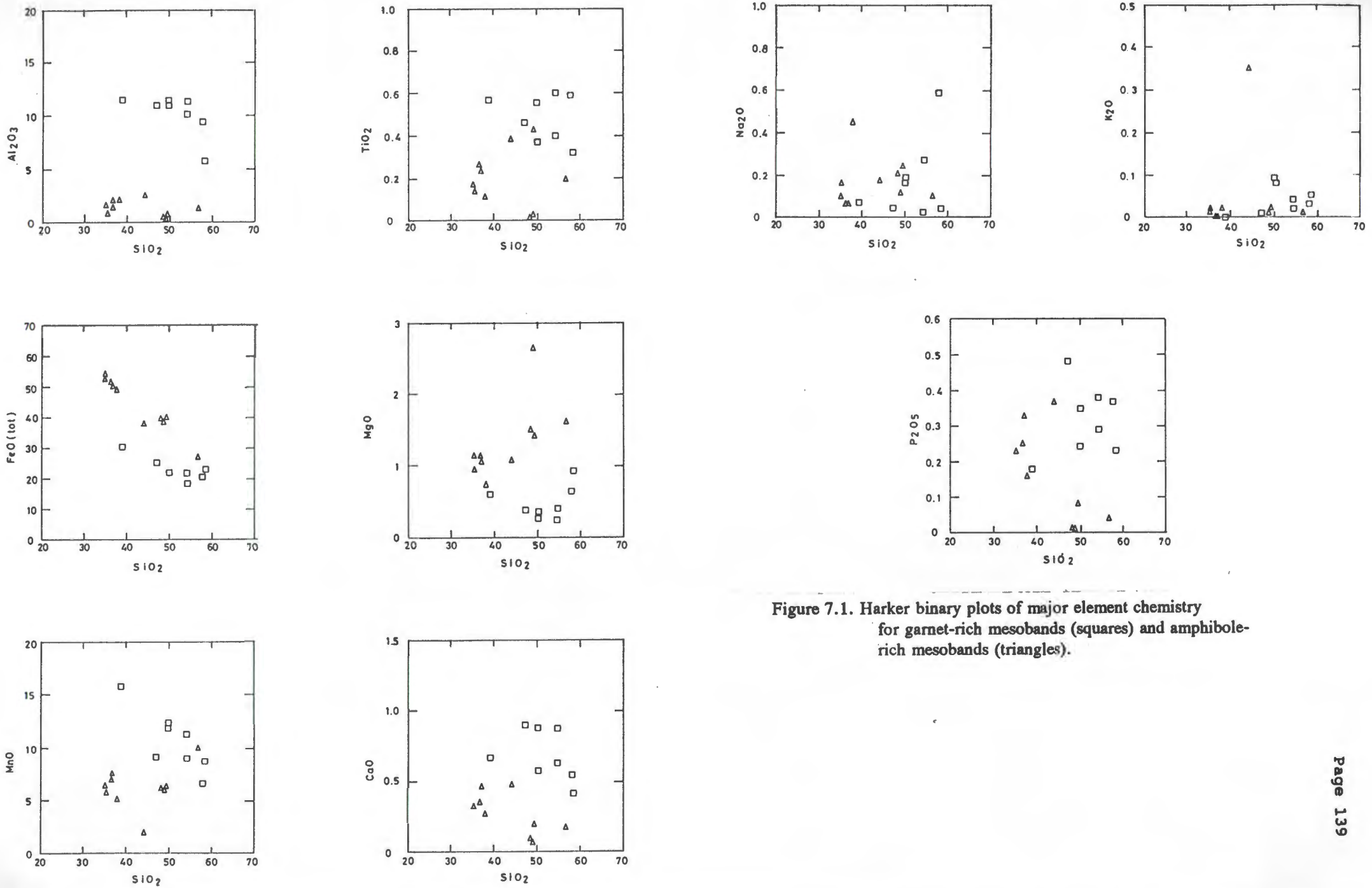

Figure 7.1. Harker binary plots of major element chemistry for garnet-rich mesobands (squares) and amphibole-rich mesobands (triangles).

Fe-rich silicate minerals and magnetite are the result of the higher FeO content in the amphibole-rich mesobands, whereas in the garnet-rich mesobands, almandine-spessartine garnet is held responsible for most of the Fe. In addition, only minor magnetite in the garnet-rich mesobands accounts for a small percentage of the total FeO. The persistently higher MnO content in the garnet-rich mesobands is related to the garnet's propensity for this element. Mn preferably partitions into garnet rather than into olivine and amphibole (see Chapter 6.12). Garnet-rich mesobands have lower bulk Fe/Mn ratios than amphibole-rich mesobands. Consequently, strong fractionation of Fe and Mn exists between the respective silicate mesobands. Garnet-rich mesobands show high Al and Ti concentrations relative to the amphibole-rich mesobands. The high Al_2O_3 and TiO_2 contents in the garnet-rich mesobands are similar to the absolute contents in the metapelitic schist of the Ore Schist Formation (cf. whole rock composition of schist sample BHS22 in Appendix D). The occurrence of biotite in the silicate mesobands is random and is reflected in variable, but generally low K_2O and Na_2O contents. The small percentage of CaO and P_2O_5 in the silicate mesobands is related to the presence of apatite. Apatite occurs with higher modal proportions in garnet-rich mesobands than amphibole-rich mesobands which reflects the CaO and P_2O_5 distribution in the respective mesoband-types.

7.1.2.Trace element distribution

Garnet- compared with amphibole-rich mesobands are significantly enriched in Zr, Ce and Cr and slightly enriched with respect to Sr, Y, La, Nd, V, and Ni concentrations (Table 7.1). Mo, Rb, Th, Nb and U are present either at concentrations < 10 ppm or below the detection limit in both types of silicate mesobands. Amphibole-rich mesobands are persistently enriched in Co. Amphibole-rich mesobands generally have higher Cu and Zn which is related to the presence of chalcopyrite and sphalerite, whereas Pb occurs in higher concentrations within garnet-rich mesobands as galena. In addition, high but variable Ba-contents were found within the garnet-rich mesobands. The variation of Ba in these samples range from < 20 ppm to > 3000 ppm and the distribution of Ba is related mainly to the modal proportions of Ba-rich biotite and barite. Further distinction of the trace element characteristics for garnet- and amphibole-rich mesobands is illustrated with Harker diagrams in Figure 7.2.

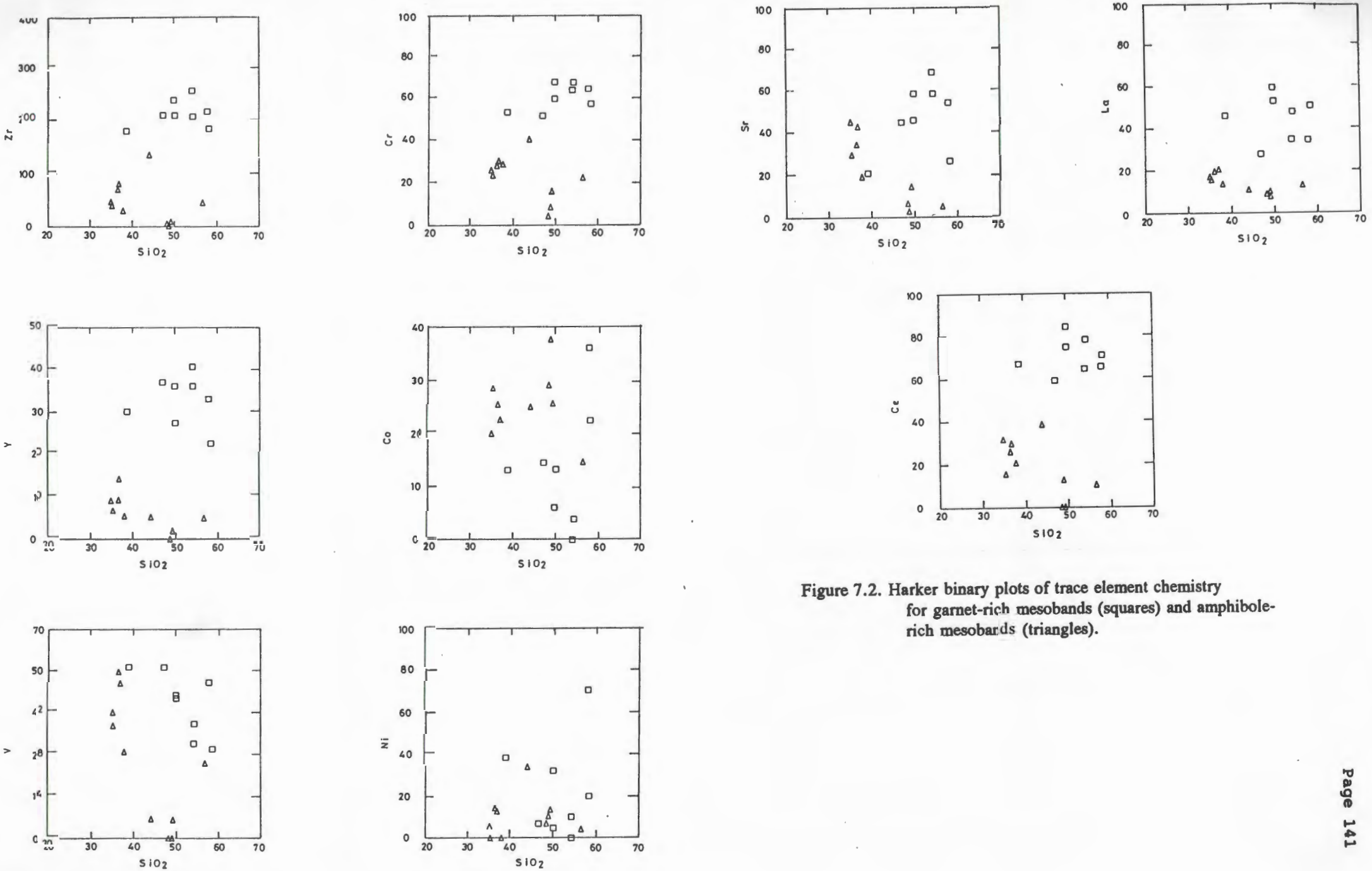

Figure 7.2. Harker binary plots of trace element chemistry for garnet-rich mesobands (squares) and amphibole-rich mesobands (triangles).

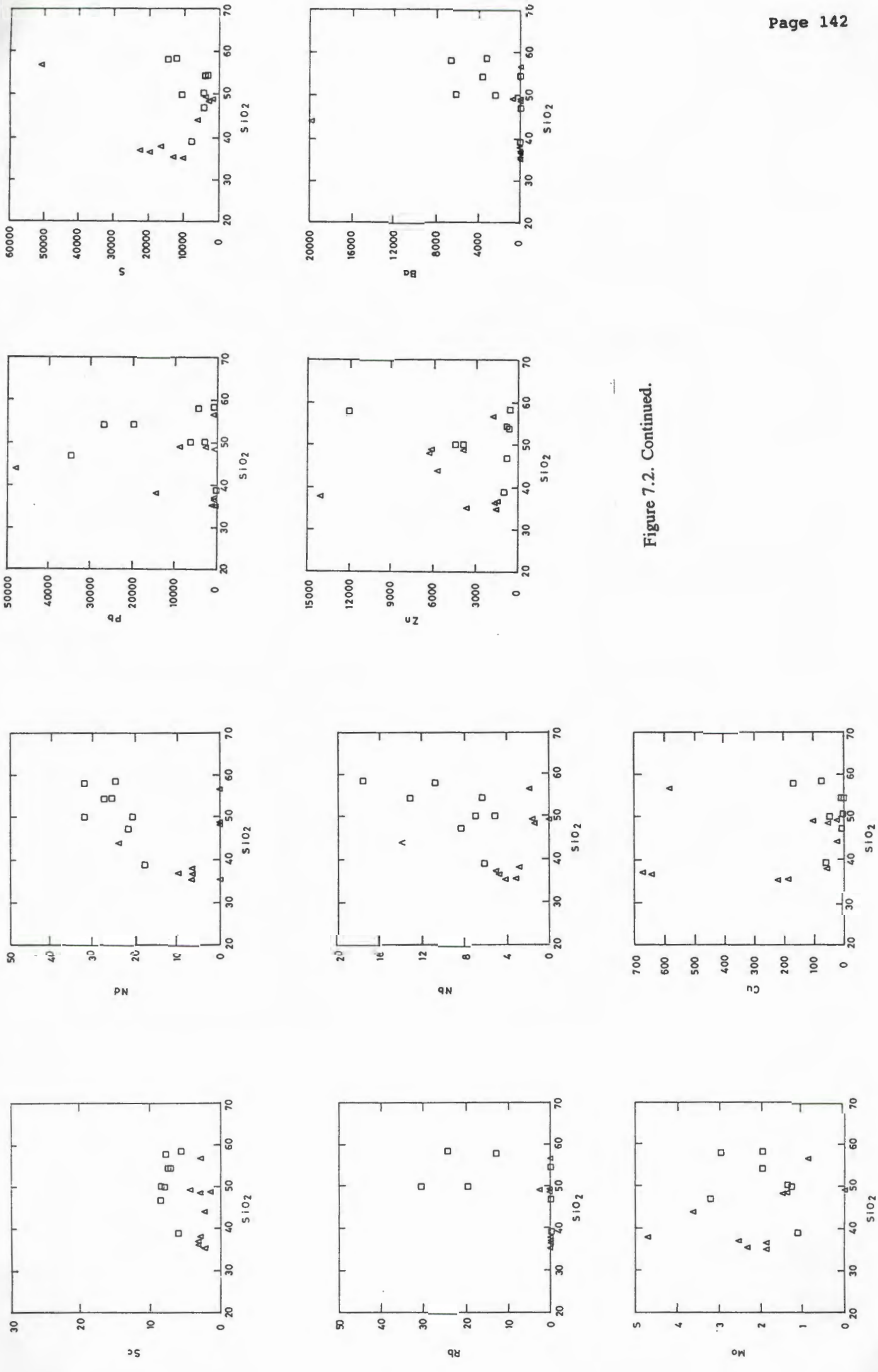

Figure 7.2. Continued.

7.1.3.Statistical treatment of data

The statistical treatment of the bulk rock data includes analysis of variance (ANOVA) and multivariate techniques such as correlation analysis and principal component analysis (PCA). The ANOVA is first used to test which major and trace elements in the garnet- and amphibole-rich mesobands, show distinct compositional differences. Correlation analysis is then used as a preliminary examination of the chemical relationships between elements for the mesobands using the combined data. Finally, PCA was used to test for linear combinations of those variables, that explain best, the variability of the major and trace elements. It should be noted that the number of samples used in the statistical treatment of the compositions is small and invalid conclusions drawn from a sample set too small may be problematical. However, by selecting samples that are considered typical and by applying significance level tests in the statistical analyses, the problem of invalid conclusions can be overcome.

7.1.3.1.Analysis of variance

The ANOVA technique is useful as it is of interest to test the effect of a nonmetric variable (e.g. silicate mesoband type) on a dependent variable (e.g. a chemical component such as SiO_2). The variance between silicate mesoband-types measures variability of composition. The variance within each silicate mesoband-type reflects the variation attributed from sources other than the selected element. A small value for the significance level test (<0.05) and a high F-test value (>4) indicate that the mean element content within each silicate mesoband-type is significantly different.

The distribution of major elements in amphibole- and garnet-rich mesobands is to some extent obvious from their mineralogy. The elements TiO_2, Al_2O_3, FeO, MnO, CaO and MgO have smaller variance within, than between each silicate mesoband type (Table 7.2). In contrast, SiO_2, P_2O_5, K_2O and Na_2O have greater variances within, than between each mesoband-type. The variance of the trace elements within the respective mesoband-types is, however, not conspicuous. The variance of Cr, Zr, Y, Nd, La, Ce and to a lesser extent, the variance of Cu, Co and V indicate that their concentrations are distinct for the two iron formation mesoband-types (Table 7.2). The remaining elements, Ni, Sr, Rb, Pb, Zn and Ba have variances greater within each mesoband-type than between them. Mo, U, Th, Nb and

Rb which have concentrations generally < 10 ppm, were not considered.

Table 7.2. Summary of ANOVA statistics for garnet- and amphibole-rich mesobands.

VARIABLE	SUM OF SQUARES FOR VARIANCE BETWEEN MESOBAND	WITHIN MESOBAND	F-RATIO	SIGNIFICANCE LEVEL
SiO2	329,66	799,70	6,6	0,0200
TiO2	0,36	0,25	22,6	0,0020
Al2O3	357,57	30,92	185,0	0,0000
FeO	1990,61	752,87	42,3	0,0000
MnO	91,13	91,02	16,0	0,0010
MgO	3,22	2,96	17,4	0,0007
CaO	0,76	0,41	29,5	0,0001
K2O	0,00	0,11	0,1	0,9399
Na2O	0,00	0,36	0,0	0,9880
P2O5	0,09	0,22	6,6	0,0205
H2O-	0,00	0,04	0,7	0,4151
Cr	6475	1301	79,6	0,0000
Zr	124049	19634	101,1	0,0000
Y	3298	421	125,2	0,0000
Ni	717	4795	2,4	0,1415
Co	1564	5770	4,3	0,0537
V	1665	4963	125,2	0,0000
Ce	12032	2023	95,2	0,0000
La	4038	966	66,8	0,0000
Sr	1234	9741	2,0	0,1738
Cu	195159	676375	4,6	0,0473
Pb	7.52 E+7	3.18 E+9	0,4	0,5533
Zn	1.54 E+7	2.41 E+8	0,8	0,4043
Ba	1.97 E+6	4.04 E+8	0,1	0,7862
S	2.22 E+8	2.04 E+9	1,7	0,2057

7.1.3.2. Correlation analysis

The existence of any strong relationship between two components of the whole rock composition can be tested with the Pearson product-moment coefficient of linear correlation. Each correlation coefficient (r) was tested for its significance level based on the Student t-test. A significance level < 0.05 was considered to imply a significant non-zero correlation.

Consequently, reasonable interpretations can still be made even from small sample populations. Correlations coefficients (r) of the components with values > 0.7 and < -0.7 with significance levels < 0.05 for the combined compositional data of garnet- and amphibole-rich mesobands is presented in Table 7.3. The discussion is limited to the combined data because the correlation coefficients were found to be essentially similar to those of the different mesoband-types.

Table 7.3. Pearson's correlation coefficients (r) for the combined compositional data of garnet- and amphibole-rich mesobands.

	SiO2	TiO2	Al2O3	FeO	MnO	MgO	CaO	Na2O	K2O	P2O5
SiO2	1,00									
TiO2		1,00								
Al2O3		0,88	1,00							
FeO	-0,86	-0,73	-0,80	1,00						
MnO			0,73		1,00					
MgO			-0,79			1,00				
CaO		0,90	0,89			-0,84	1,00			
Na2O								1,00		
K2O									1,00	
P2O5		0,76				-0,74	0,84			1,00
Nb										0,78
Zr		0,94	0,94	-0,94		-0,80	0,94			
Y		0,87	0,96	-0,75		-0,80	0,86			
Sr									0,70	0,82
La		0,76	0,87	-0,72	0,77	-0,70	0,73			
Ce		0,90	0,93	-0,74		-0,76	0,87			
Nd		0,90		-0,73		-0,74	0,88			
Cr		0,92	0,92	-0,76		-0,86	0,87			
Ni								0,79		
Sc		0,86		-0,82		-0,82	0,80			
Ba									0,95	
Zn								0,97		

All correlations with r> and < 0.70 are shown.
Significance level <0.05

For the combined data, SiO_2 exhibits a strong negative correlation with FeO which is a result of these components comprising large proportions of the bulk rock composition. Thus, an

increase in quartz is related to a decrease in garnet, amphibole, olivine and magnetite. TiO_2 varies concomitantly with Al_2O_3, CaO and P_2O_5. Furthermore, these components have strong positive correlations with Zr, Y, La, Ce, Nd, Sc and Cr. These correlations stem from the elements clustered with higher trace and major element concentrations in the garnet-rich mesobands relative to the amphibole-rich mesobands. In contrast, FeO and MgO varies antipathetically with Zr, Y, Ce, Nd, Sc, Cr. K and Ba vary concomitantly which is contrary to that expected for the substitution of the latter for the former in the interlayer sites of biotite (see Chapter 5.5). It is unlikely that Ba is associated with a clastic K-rich precursor mineral because of poor correlations of Ba with other elements TiO_2, Al_2O_3, Zr and Cr etc., which are likely to be detrital components. Consequently, it is suggested that this correlation is fortuitous. P_2O_5 and Sr exhibits a strong positive correlation, which can be related to Sr substitution of Ca in apatite. From the presence of apatite, the highly correlated CaO and P_2O_5 seems to indicate that these components are essentially restricted to this phase. CaO and MgO varies antipathetically, which is contrary to that found at Gamsberg where Rozendaal (1982) relates the association of these elements to a calcareous environment.

7.1.3.3.Principal component analysis

Principal component analysis is a useful technique for reducing the number of variables in a data set. This is achieved by finding linear combinations of the components that explain most of the compositional variation. Since there are many components that are shown to be highly correlated, there may be one or two linear combinations of these variables that can be formed to explain variations among the bulk chemistry of the silicate mesobands almost effectively as the entire data set. PCA transforms a set of correlated variables to a new set of uncorrelated variables. Thus, variables that are generally uncorrelated in the original data should be excluded from the analyses. Variables that showed no general strong correlation and/or have (r) persistently <0.5 were excluded. These were K_2O, Na_2O, H_2O and all other trace elements besides Zr, Y, La, Ce, Cr, Nd and Sc.

A property of the chemical analyses is that of constant sum of the totals which arises from the major element oxide totals that sum 100%. As a result of this constant sum, oxides which have high wt.% totals (e.g. SiO_2) will have strong negative correlations with other major element oxides with high wt.% totals (e.g. FeO), and thus SiO_2 was excluded as a variable in

the PCA.

The principal components were determined by first computing the eigen values and then expressing each as a percentage of variance for each component (Table 7.4). It is notable that the first component accounts for 80.3 % of the variance, while the next component accounts for an additional 8.9 %. For the first two components, 89.2 % of the total variability has been accounted for.

Table 7.4. Table showing the variance of each principal component 1 to 14.

PRINCIPAL COMPONENT NUMBER	PERCENTAGE OF VARIANCE	CUMULATIVE PERCENTAGE
1	80,317	80,317
2	8,880	89,197
3	4,098	93,295
4	2,220	95,516
5	1,961	97,477
6	0,983	98,460
7	0,544	99,005
8	0,395	99,400
9	0,333	99,734
10	0,116	99,850
11	0,081	99,932
12	0,037	99,970
13	0,017	98,987
14	0,012	100,000

Elements included in the analysis are:
FeO, Al2O3, TiO2, MnO, MgO, CaO, P2O5, Zr, Y, Cr, Nd, Sc, La, Ce,

Ideally, it is preferred to assign names to the principal components. This is advantageous because the variation of the data can be explained in terms of some geological processes. A plot of principal component (PC) 1 against 2, illustrated in Figure 7.3, reveals that the variables FeO and MgO plot far to the right and the remaining Al_2O_3, TiO_2, and the trace elements Zr, Y, La, Ce, Nd, Sc and Cr plot at the extreme left. Thus, component 1 differentiates to a great extent, the elements that are likely to be derived as chemical

precipitates from those that are detrital. MnO and P_2O_5 are not substantially separated by component 1. These components are, however, likely to be derived as chemical precipitates, and are differentiated from the field of detrital sediments by component 2. It could be speculated that component 2 reflects a different source or process that affected these element's concentrations.

CaO is considered to have been derived as a chemical sediment because of its good correlation (r) with P_2O_5. Its position within the detrital field challenges to a limited extent the distinction of the genetic fields shown in Figure 7.3. No explanation is offered other than that the position of CaO a function of the statistical technique or is fortuitous.

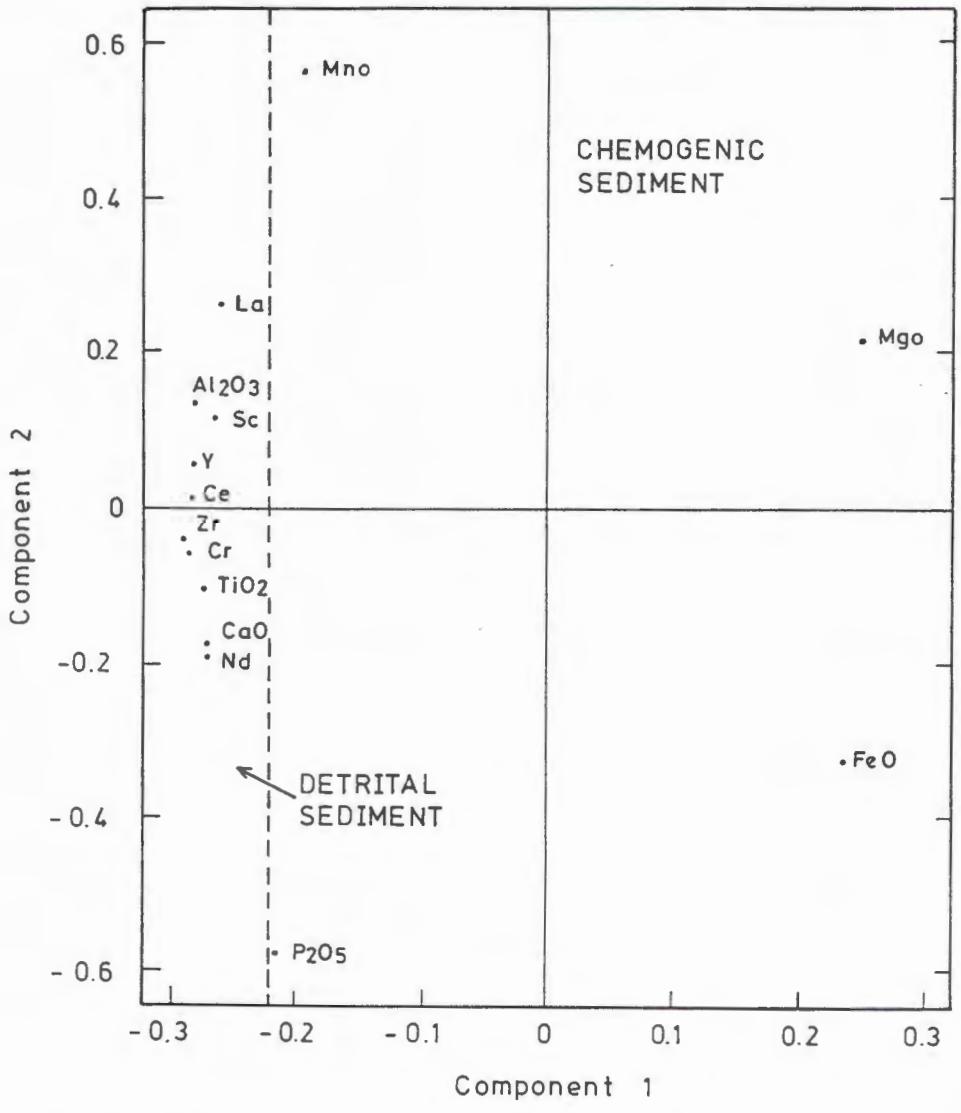

Figure 7.3. Plot of first two principal component weights for selected major and trace elements.

7.1.4. Comparison with other iron formations

Ferruginous sedimentary rocks are those that predominantly comprise chemical sediment with more than 15 wt.% Fe (James, 1954; Gross, 1965; Kimberley 1989). Ferruginous sediments are subdivided into two broad categories, ironstones and iron formations (Gross, 1980). The former consist of predominantly oolitic chamosite-siderite-goethite units with significant clay and detrital components, and is usually of Phanerozoic age. The latter, however, comprises thinly banded chemical precipitates of chert and iron-rich minerals of mainly Archaean and Proterozoic age. Iron formations are further classified on the basis of depositional environment and rock associations, whereby two important types are the Lake Superior and Algoma iron formations (Gross, 1965). Lake Superior iron formations were deposited on continental shelves, and are associated with quartzite, dolomite and black shale. In contrast, Algoma type iron formations were deposited in volcanic arcs, rift zones and deep seated fault systems together with volcaniclastic rock assemblages.

The garnet- and amphibole-rich mesobands meet the minimum Fe content required by the definition of a ferruginous sedimentary rock. Chemical distinction between ironstones and iron formations may be illustrated on a ternary Si-Al-(Fe+Mn) plot using the discrimination by James (1969) (Fig. 7.4). All the amphibole-rich mesobands studied plot within the field for iron formation. The garnet-rich mesobands occur outside this field. They have Al contents similar to ironstones, but their Si contents are too high. Both silicate mesoband-types have compositions that plot within the range defined for other iron formations in Namaqualand (Rozendaal, 1982; Moore, 1989). On a bivariate Si-Al plot (Fig. 7.5), the amphibole-rich mesobands have Si/Al ratios that coincide with the field for Lake Superior iron formations (Gross and McLeod, 1980). Si/Al ratios for both garnet- and amphibole-rich mesobands plot outside the field for ironstones (as defined by Kimberley, 1979).

In Table 7.5, the mean compositional data of garnet- and amphibole-rich mesobands are compared with the silicate facies of Algoma and Lake Superior iron formations using the data of Gross and McLeod (1980). Amphibole-rich mesobands have consistent SiO_2 contents comparable to Algoma iron formations, whereas garnet-rich mesobands are intermediate between the two iron formations. Garnet-rich mesobands have FeO contents similar to Lake Superior but are depleted in FeO with respect to Algoma iron formations whereas the

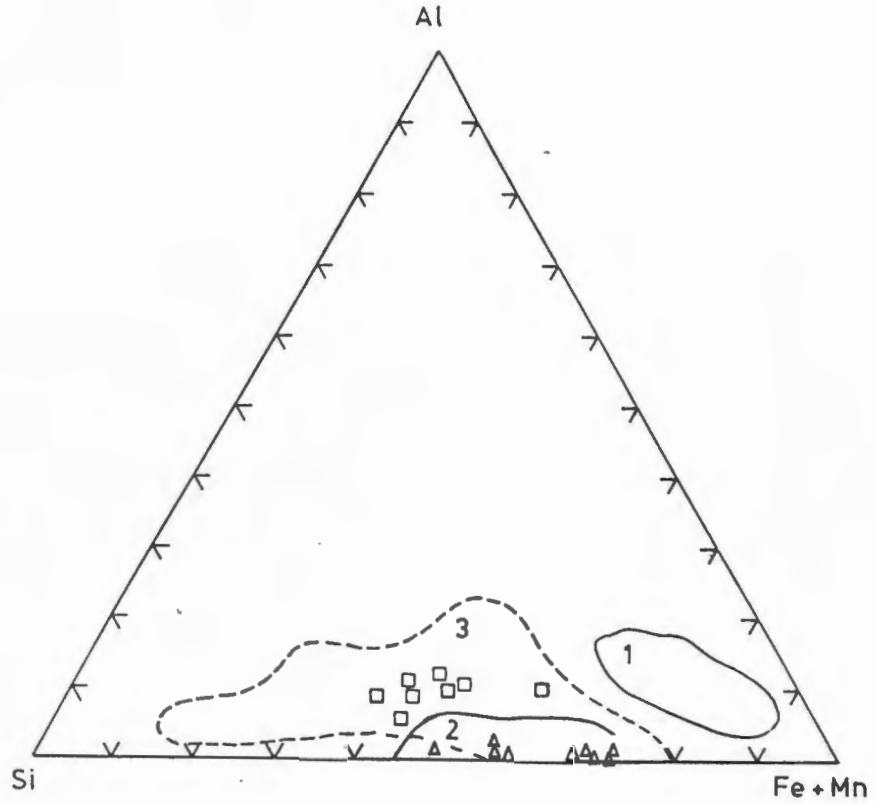

Figure 7.4. Ternary plot of Si:Al:(Fe+Mn) for bulk rock compositions of garnet-rich mesobands (squares) and amphibole-rich mesobands (triangles). Fields 1 and 2 are for iron-stones and iron formations, respectively, (James, 1969). Field 3 represents combined data from Rozendaal (1982) and Moore (1989) for iron formations in Namaqualand. Fe is presented as Fe total.

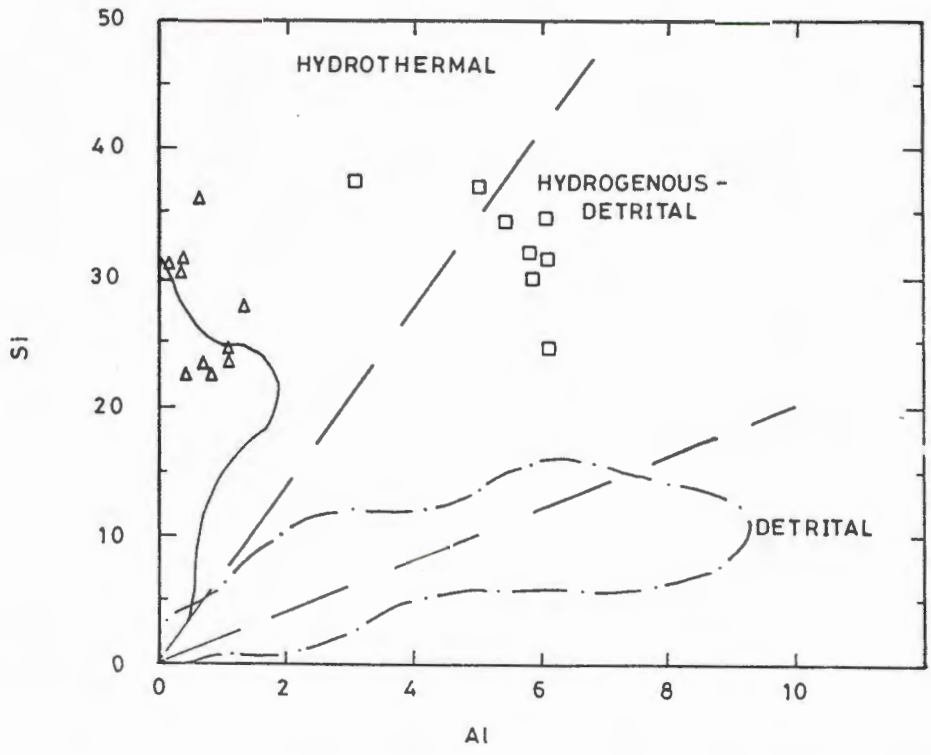

Figure 7.5. Bivariate plot of Si versus Al of LOB silicate-rich mesobands, garnet-rich (squares) and amphibole-rich (triangles). Also plotted are fields for Lake Superior iron formation (solid line) (after Gross and McLeod, 1980), iron-stones (dash dot line) (Kimberley, 1979), and different types of Fe-Mn deposits (dashed lines) (Crerar, 1982).

Table 7.5. Comparisons of average compositions for LOB silicate-rich mesobands with iron formations, silicate-rich bands and manganese formations. (nd = not detected, - = not available).

	LOB silicate mesobands		Iron formations (silicate facies)		Satnuru Iron Formation		Mamatwan Deposit
	Garnet	Amphibole	Algoma	Lake Superior	Garnet-bearing	Non-garnet bearing	
wt. %			Gross and McLeod (1980)		Bhattacharaya et al. (1990)		Nel et al. (1986)
SiO_2	51.51	42.89	46.20	59.00	47.12	52.65	4.60
TiO_2	0.48	0.19	0.19	0.19	0.79	0.77	-
Al_2O_3	10.28	1.31	7.56	2.41	4.58	2.49	-
FeO	23.05	44.21	32.91	24.13	34.49	37.25	7.64
MnO	10.72	6.25	0.94	0.44	3.68	0.08	43.06
MgO	0.48	1.33	3.89	2.73	3.19	1.61	-
CaO	0.69	0.27	0.83	2.40	3.50	1.98	15.59
K_2O	0.04	0.04	0.41	0.63	0.08	0.09	-
Na_2O	0.17	0.17	0.05	0.20	0.09	0.19	-
P_2O_5	0.31	0.17	0.42	0.10	-	-	-
H_2O	0.06	0.04	3.50	2.50	-	-	-
LOI	1.22	1.24	-	-	-	-	
Total	99.01	97.92	96.90	94.73	97.52	97.11	
(ppm)							
Mo	2	2	-	-	-	-	nd
Nb	9	4	-	-	-	-	nd
Zr	212	45	267	165	-	-	43
Y	33	6	84	43	-	-	nd
Cr	60	22	38	102	-	-	-
Ni	23	11	151	46	-	-	26
V	45	26	54	124	-	-	170
Rb	11	6	-	-	-	-	nd
Sr	47	30	28	30	-	-	200
Th	4	nd	-	-	-	-	nd
U	1	nd	-	-	-	-	nd
La	44	14	-	-	-	-	-
Ce	70	18	-	-	-	-	-
Nd	25	5	-	-	-	-	-
Co	14	32	36	27	-	-	23
Sc	7	3	11	22	-	-	-
S	7308	14378	-	-	-	-	-
Cu	47	256	-	-	-	-	46
Pb	11798	7679	-	-	-	-	61
Zn	3050	4662	-	-	-	-	47
Ba	2743	2076	70	170	-	-	2080

amphibole-rich mesobands have significantly higher FeO than both iron formations types. The enriched Mn component of both types of silicate mesobands contrast sharply with that of Algoma and Lake Superior compositions, and is more characteristic of manganiferous iron formations. Garnet-rich mesobands are enriched in TiO_2 at least two-fold, whereas the amphibole-rich mesobands have similar TiO_2 compared to the silicate facies of Lake Superior and Algoma iron formations. The Al_2O_3 content in garnet-rich mesobands compares well with Algoma silicate compositions whereas the Al_2O_3 contents in amphibole-rich mesobands is in agreement with Lake Superior silicate facies. The LOB silicate mesobands are relatively poor in MgO, CaO and K_2O compared to both Algoma and Lake Superior iron formation types.

The major element compositions of the LOB silicate mesobands vaguely resemble the silicate facies of Algoma and Lake Superior iron formations. Moore (1989) describes all-facies iron formation rock in the Aggeneys area to have Sr, Zr, Cr, V, Sc, Ni, Y, Zn and Ba concentrations that are comparable with Lake Superior iron formations. In contrast, Rozendaal (1982) describes the Gamsberg iron formation to have Al, K, P, Cu, Ni, Sr, T and V contents comparable with Algoma iron formations. The trace element characteristics of the LOB silicate mesobands compare with the silicate facies of Lake Superior and Algoma iron formations as follows (Table 7.5); the amphibole-rich mesobands are depleted with respect to Zr, Y, Cr, V, Ni and Sc, but significantly enriched in Ba, and with comparable concentrations of Co. Garnet mesobands have depleted Co, V, Ni and Sc, enriched Ba and comparable Zr and Cr concentrations compared to these iron formations-types.

It is more appropriate to compare the compositional characteristics of the studied silicate mesobands with other manganiferous mesobands in metamorphosed terrains. In Satnuru, India, bulk compositions of garnetiferous and non-garnetiferous silicate mesobands were reported by Bhattacharya et al. (1990) to be intermediate between Lake Superior and Algoma iron formations. The major element bulk compositions of the LOB are compared with the Satnuru iron formation in Table 7.5. In particular, the garnet-rich mesobands have higher Al and Mn, but lower Ti, Fe, Mg and Ca than in the Satnuru counterparts. The amphibole-rich mesobands have comparable Fe, Mg and Al but are depleted in Si and Ti compared with the non-garnetiferous iron formations from Satnuru.

7.1.5.Comparison with hydrothermal and hydrogenous marine sediments

In oceanic environments, the enrichment of submarine sediments in Fe and Mn is explained either by hydrothermal discharge and rapid deposition at active mid-ocean ridge rift systems or by hydrogenous enrichment of ocean floor sediments during the slow precipitation of iron and manganese hydroxides from sea water (Bonatti et al. 1972; Toth, 1980; Marchig et al., 1982). Marine hydrothermal sediments exhibit extreme variation in Fe/Mn ratios, antipathetic variation of silica and iron, and low trace metal contents. In contrast, hydrogenously enriched sediments have more constant Fe/Mn ratios and higher absolute trace element contents (Bonatti et al. 1972).

The chemical characteristics of hydrothermal and hydrogenous Fe- and Mn-rich deposits can be illustrated with two ternary diagrams. The first compares the relative concentrations of the major components Fe, Mn and Si (Fig. 7.6). Hydrothermal deposits concentrate along the Fe-Si tie line and at the Mn apex, whereas hydrogenously enriched deposits occupy more central fields (Bonatti et al., 1972) . The amphibole-rich mesobands plot close to the Si-Fe tie line and within the field defined for hydrothermal Fe-rich crusts. Garnet samples are more siliceous and plot outside any of the defined fields. The diagram further illustrates that in hydrothermal deposits, an increase in Si is accompanied by a decrease in Fe. The antipathetic relation between Fe and Si was statistically shown for the LOB silicate mesobands. The positions of hydrogenously enriched Fe-Mn crusts and metalliferous sediments from the East Pacific Rise (EPR) coincide (Fig. 7.6). Garnet-rich mesobands have similar Mn contents to that of the metalliferous sediment of the EPR but are enriched in Si.

The second ternary diagram of Fe-(Co+Ni+Zn)x10-Mn depicts the fields for hydrothermal and hydrogenous sediments (Fig. 7.7). The hydrothermal sediments plot along the Fe-Mn tie line and have low trace metal contents, whereas the hydrogenously enriched sediments occupy the more central position and have higher trace metal contents. Metalliferous sediments from the Red Sea (RS) and EPR are enriched in Co, Ni and Zn compared with hydrothermal crusts. Most compositions of the amphibole-rich mesobands plot within the field for hydrothermal crusts and a few within the area depicted for RS metalliferous sediments. Similarly, garnet-rich mesobands have trace element contents which in most cases plot within the field for hydrothermal sediments, with the exception of several samples which

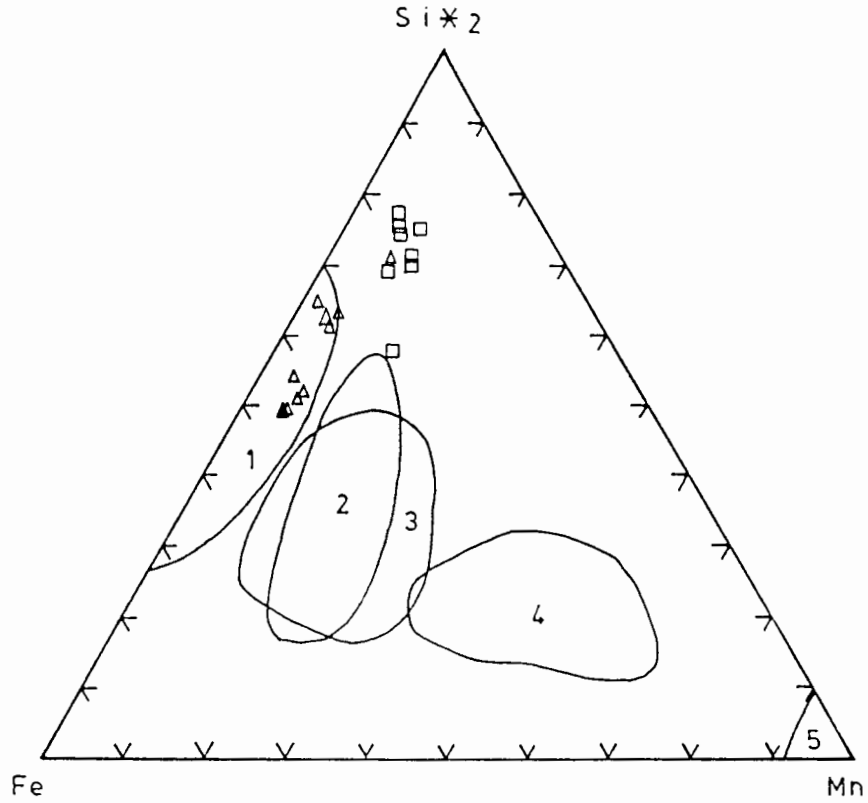

Figure 7.6. Ternary plot of Fe:Six2:Mn showing the positions of the silicate-rich mesobands, garnet-rich (squares) and amphibole-rich (triangles) of the LOB relative to the fields of hydrothermal Fe-rich crusts (1), East Pacific Rise metalliferous sediments (2), hydrogenous Fe-Mn crusts (3), Mn nodules (4) and hydrothermal Mn-rich crusts (5) (Toth, 1980).

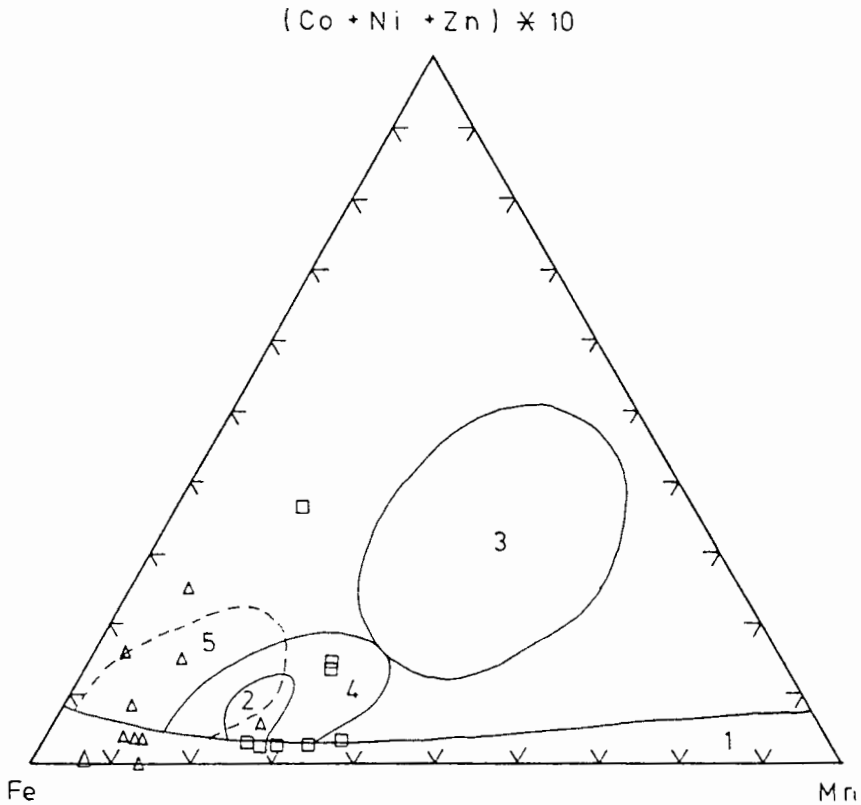

Figure 7.7. Ternary plot of Fe:(Co+Ni+Zn)x10:Mn showing the positions of the silicate-rich mesobands, garnet-rich (squares) and amphibole-rich (triangles) of the LOB relative to the fields of hydrothermal crusts (1), East Pacific Rise metalliferous sediments (2), hydrogenous enriched sediments (3), Fe-Mn crusts (4) and Red Sea metalliferous sediments (5), (after Bonatti et al., 1972; Toth, 1980)

plot in the field for hydrogenously enriched Fe-Mn crusts. This can be attributed to the presence of high concentrations of primary Zn. The diagram also clearly illustrates the strong fractionation of Fe and Mn in hydrothermal deposits and thus variable Fe/Mn ratios and low trace metal concentrations are prominent features of these deposits. The amphibole-rich mesobands have variable Fe/Mn ratios (2.7- 18.6), typical of hydrothermal iron-rich crusts, whereas garnet-rich mesobands have more constant Fe/Mn (1.6-3.1) ratios, characteristic of hydrogenous sediments (Bonatti et al. 1972) and Fe-Mn crusts which have an average Fe/Mn= 2.2 (Toth, 1980). The variable Fe/Mn is caused by fractionation of these elements with increasing pH, increasing oxidation potential and decreasing temperature which results in precipitation of Si and Fe before Mn (Toth, 1980) (opp. crit. Postma, 1985; Kimberley, 1989).

The amphibole-rich mesobands are similar to modern hydrothermal deposits, displaying higher Si/Al ratios than hydrogenous ferromanganese nodules (Fig. 7.5). Garnet mesobands have Si/Al ratios intermediate between hydrothermal and detrital sediments, and amphibole-rich mesobands have Si/Al ratios similar to sediments of hydrothermal origin (Fig. 7.5).

Bostrom (1973) devised a diagram for estimating the relative amount of mixing between pure hydrothermal metalliferous sediments which contain very little Al and terrigenous or deep-sea sediments which have significant Al using the ratios of Fe/Ti versus Al/(Al+Mn+Fe) (Fig. 7.8). Contamination of hydrothermal metalliferous sediment by deep-sea sediments (pelagic and terrigenous sediments) or oceanic tholeiitic material dilutes the hydrothermal elements Fe and Mn, whereas it enriches the elements Al and Ti. The significant Al and Ti contents in the silicate-rich mesobands, in particular the garnet-rich mesobands, were used to estimate the proportions of chemical and detrital components in the original sediment. The meta-pelitic rocks of the Broken Hill schists have comparable Fe/Ti and Al/(Al+Mn+Fe) ratios to deep-sea sediments (Fig. 7.8). Thus, it was assumed that the mixing curve of metalliferous hydrothermal sediment with deep-sea sediments shown by Barret (1981) would be grossly similar to that of Broken Hill metapelitic schists (Figure 7.8). Also considered here is the mixing curve for hydrothermal sediments and oceanic tholeiite. Although no amphibolite (meta-tholeiitic basalt) is found in the ore sequence at Broken Hill, it is found higher up in the stratigraphic sequence.

The amphibole-rich mesobands have very high Fe/Ti ratios and low Al contents which is indicative of mostly hydrothermally derived matter. Their very low Al/(Al+Fe+Mn) ratios are similar to metalliferous sediments from the East Pacific Rise (EPR) and the Red Sea (RS). Furthermore, amphibole-rich mesobands have compositions which plot on the mixing curve with oceanic tholeiite rock rather than deep-sea sediments.

The garnet-rich mesobands have compositions that plot along the mixing curve for deep-sea sediments which reflect between 50:50 and 70:30 mixtures of hydrothermal sediments from the EPR and RS with detrital material. The detrital material could have been similar in composition to the Broken Hill schists. However, contamination by material in the form of volcanic dust cannot be differentiated from the detrital material of the schists (see Fig. 7.8).

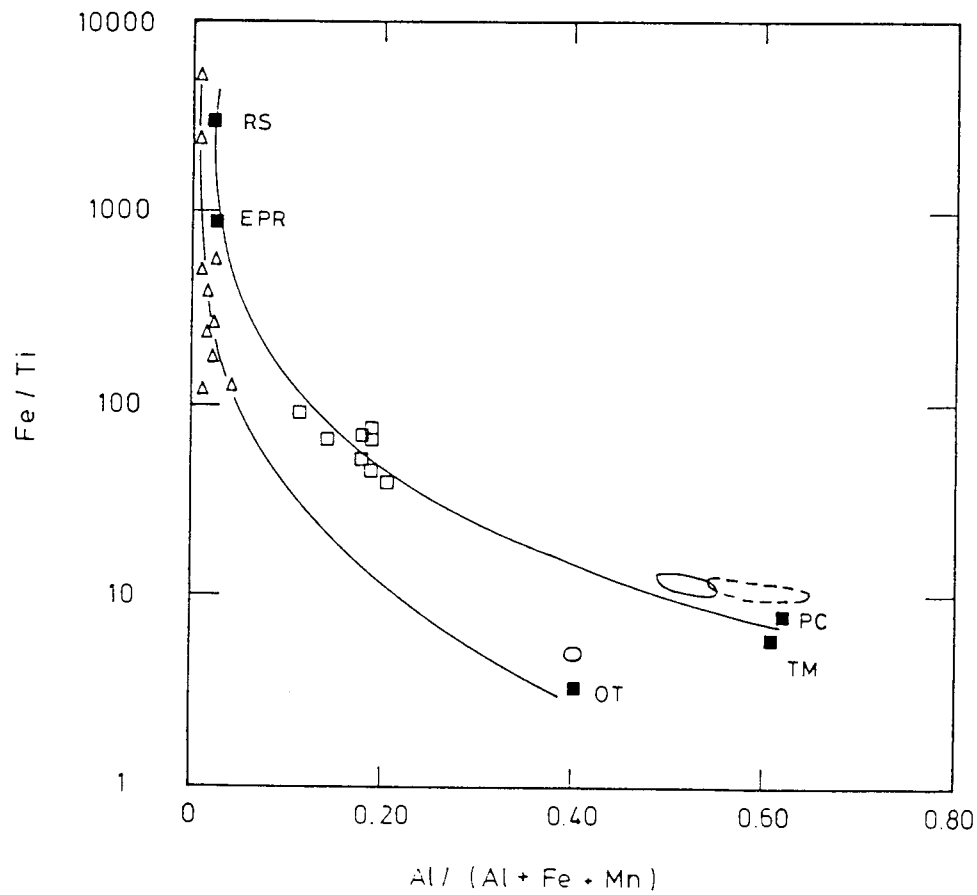

Figure 7.8. Plot of Fe/Ti versus Al/(Al+Fe+Mn) showing the positions of the garnet-rich mesobands (squares) amphibole-rich mesobands (triangles), Ore Formation schists (Lipson, 1990) (dashed line) and amphibolite (Reid et al., 1987b) (solid line) relative to the relative to the mixing curve for metalliferous sediment and terrigenous matter (upper curve) and oceanic tholeiite (lower curve) (modified after Barrett, 1981). The relative positions of Red Sea metalliferous sediment (RS), East Pacific Rise metalliferous sediment (EPR), pelagic clay (PC), terrigenous matter (TM) and oceanic tholeiite (OT).

Numerous studies have attempted to relate minor elements as geochemical criteria of depositional environment. For example, elements such as Mn, Co and Ni were considered by Sugisaki et al. (1991) to be sensitive to environmental conditions such as pH and redox potential. Consequently, their distribution in sedimentary rocks is effective in identifying depositional environments.

In hydrothermal crusts, the Co/Zn ratio is very low (with an average of 0.15), whereas higher ratios occur in Fe-Mn hydrogenously enriched crusts (average of 2.5) (Toth, 1980). Thus, whereas hydrothermal crusts are depleted in Co and Ni, they are commonly enriched in Zn. Sugisaki et al. (1991) have pointed out that for hydrogenous enrichment in reducing environments, Zn preferably precipitates out and divalent Co remains in solution, and thus the Co/Zn ratio of the sediment decreases. The opposite is found for oxidizing conditions. Garnet and amphibole-rich mesobands have Co/Zn ratios <0.01. This low ratio indicates that both mesoband-types formed as hydrothermal metalliferous sediments probably in reducing environments.

Trace element concentrations provide insight to the origin of iron formation mesobands by testing the interplay between hydrothermal and detrital input. Y is concentrated in hydrogenously enriched Fe-Mn crusts rather than in hydrothermal sediments, during the diagenetic alteration of apatite (Marchig et al., 1982). Marchig et al. (1982) suggest that, enrichment of P_2O_5, Sc, Y, La, and REE is a consequence of apatite's longer residence time in seawater because biogenic apatite is insoluble in alkaline solution. Zr is also concentrated in hydrogenously enriched Fe-Mn crusts rather than in hydrothermal sediments, because of the higher content of detrital zircon in the former. The composition of amphibole-rich mesobands plot closer to the fields for hydrothermal sediments than hydrogenously enriched sediments as shown on bivariate plots of Zr versus Cr (Fig. 7.9) and Y/P_2O_5 versus Zr/Cr (Fig. 7.10). In the garnet-rich mesobands, Zr contents are generally higher than expected for hydrogenously enriched sediments (Fig. 7.9). The garnet- and amphibole-rich mesobands have average Zr/Cr ratios of 3.5 and 1.57, respectively, and the former is similar to the ratio in the enclosing schists of the Ore Schist Formation (Zr/Cr = 2.84, from data of Lipson, 1990). This highlights that the detrital component in the iron formation mesobands and the schist were probably derived from a similar protolith.

La/Ce ratios can be used to distinguish hydrothermal sediments from hydrogenously enriched sediments. The former have extremely low absolute REE concentrations and depleted Ce contents whereas the latter are usually enriched in REE and Ce concentrations. The relative Ce enrichment in Fe-Mn crusts of hydrogenous origin, which have La/Ce ratios generally <1 (Toth, 1980), is a result of preferred adsorption of Ce to La. Absolute Ce concentrations in hydrothermal crusts are low, and the La/Ce ratio is similar to that of sea water, i.e. 2.8 (Toth, 1980). In the LOB, garnet-rich mesobands have a slightly lower mean La/Ce ratio

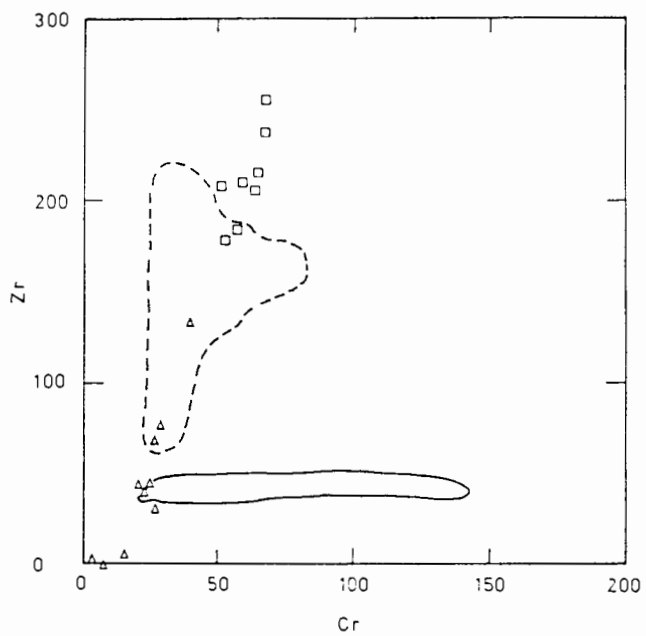

Figure 7.9. Plot of Zr versus Cr for garnet- (squares) and amphibole-rich (triangles) iron formation mesobands compared to fields for hydrogenous (dashed line) and hydrothermal (solid line) metalliferous sediments (after Marchig et al., 1982).

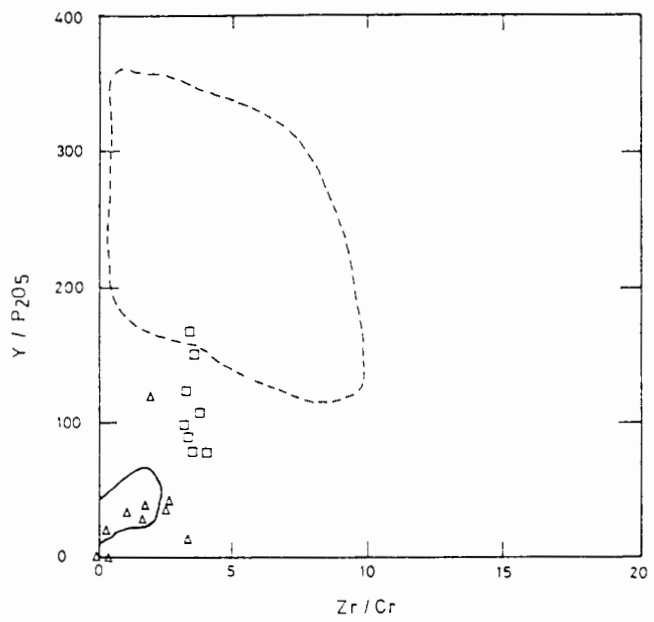

Figure 7.10. Plot of Y/P_2O_5 for garnet- and amphibole-rich iron formation mesobands compared to fields for hydrogenous (dashed line) and hydrothermal (solid line) metalliferous sediments (after Marchig et al., 1982).

(0.57) than the mean for amphibole-rich mesobands (0.86) (Fig. 7.11). Both silicate mesobands exhibit La/Ce ratios (0.54) considerably lower than that for hydrothermal deposits and are intermediate between sea water and the lower limit of hydrogenously enriched sediment.

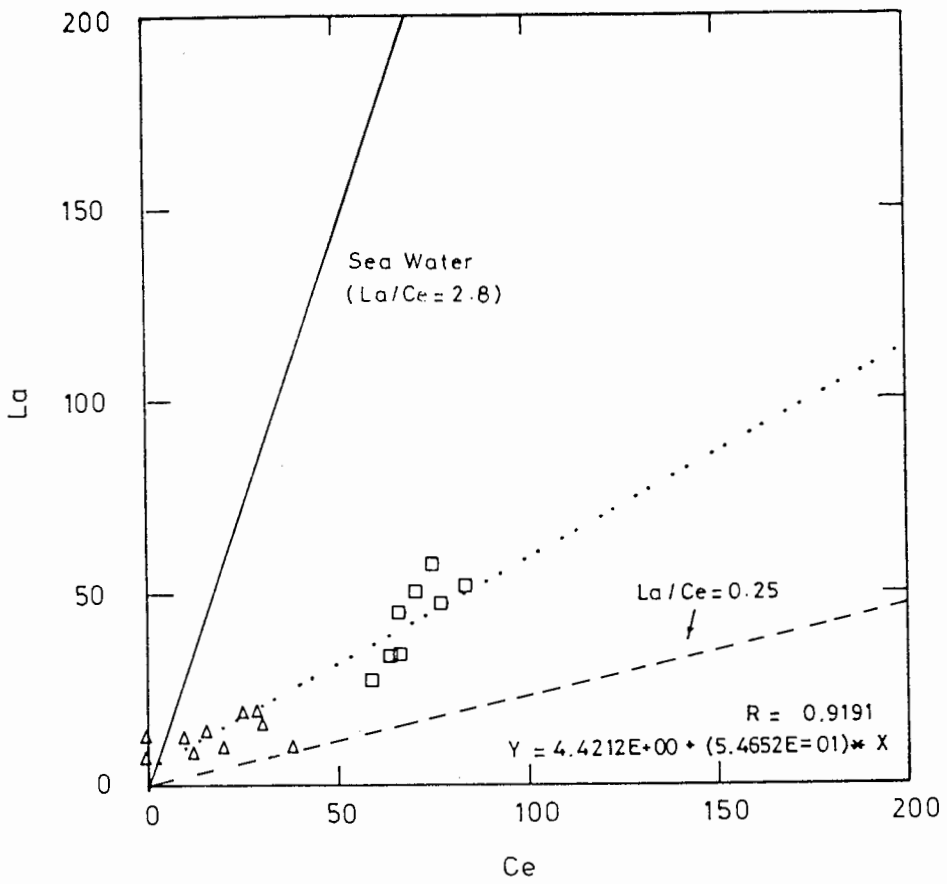

Figure 7.11. Plot of La versus Ce for garnet- and amphibole-rich iron formation mesobands compared to sea-water ratios (solid line) and the lower limit of hydrogenous marine sediments (dashed line) (after Toth, 1980).

7.1.6. Comparison with ancient manganese formations

The silicate-rich iron formation mesobands within the LOB are enriched in Mn (means of 8.30 and 4.84 wt.% for garnet- and amphibole-rich mesobands, respectively. Like iron formations, a manganese formation is a stratigraphic unit that largely consists of chemical sedimentary rock which contains >15 wt.% Mn. Manganese formations can be subdivided into two types based on genetic models related to the source of Mn, which is either hydrothermal (exhalative) or non-hydrothermal (shallow-weathering source).

The major and trace element concentrations of LOB silicate mesobands were compared with Mn-rich units of the Mamatwan deposit, northern Cape, using data from Nel et al. (1986), (Table 7.5). A higher Mn/Fe ratio (3-9) is found in the Mamatwan deposit than in LOB silicate iron formation where the average Mn/Fe ratio is 0.47 for garnet-rich mesobands and 0.15 for amphibole-rich mesobands. The LOB silicate mesobands are significantly enriched in Si and Fe but depleted in Mn and Ca compared to the Mamatwan deposit. Both deposits have similar low absolute concentrations of K, Na and Mg. The Al content in the Mamatwan deposit, although small, is ascribed to a detrital origin (Nel et al., 1986). Unlike the Mamatwan deposit, the Al contents in amphibole- and garnet-rich mesobands within the LOB are approximately one and two orders of magnitude greater, respectively.

Low trace element concentrations of Zr and Y found both in the amphibole-rich mesobands and within the Mamatwan deposit, reflect a small detrital input within these Mn-rich units (Nel et al., 1986), whereas the garnet-rich mesobands are enriched in these elements. Fe- and Mn-rich deposits which arise from rapid precipitation of exhaling fluid have low values of Ni, Co and Cr. The LOB silicate mesobands have low concentrations of these elements compared to those of the Mamatwan deposit. Similarly, to the Mamatwan deposit, trace elements such as Mo, Nb, Rb, Th and U occur with low (< 10 ppm) or non detectable concentrations, which is the case for both deposits. In particular, the low U and Th concentrations in the rift marine environment of the Northern Afar Rift, Ethiopia, (Bonatti et al., 1972) compare well with those in the LOB silicate mesobands and the Mamatwan deposit.

Higher average V and Sr concentrations occur in the Mamatwan deposit (> 170 ppm and 200 ppm, respectively) than in the silicate mesobands of the LOB. The enrichment of V and Sr can be explained in terms of the affinity of these elements for manganese (Nel et al. 1986). Furthermore, in the Mamatwan deposit, Sr is associated with a greater carbonate component and consequently low, absolute Sr in the LOB is explained by the carbonate-poor environment there. Nel et al. (1986) have shown that Ba, V, Ni and Co increase towards more distal depositional environments whereas Sr association with carbonate decreases. Ba at Mamatwan deposit occurs in similar concentration to the amphibole-rich mesobands, but is much lower than that found in the garnet-rich mesobands. As expected, Cu,Pb and Zn in the

LOB silicate mesobands are significantly higher than within the Mamatwan deposit.

7.2.PEGMATITE-TYPE ROCK

Two samples of pegmatite type-rock from the NW margin of the LOB were analysed. This rock is the discordant pegmatite variety described in Chapter 4. The samples were essentially homogeneous, comprising a low variance assemblage of amazonite feldspar and quartz. The pegmatite rock is suspected to be derived either from the partial melting of the enclosing schists as suggested by Lipson (1990) or they may have a metasomatic origin. The objective of the geochemical analysis of this rock-type is to compare its composition with the schists and to show that they have incorporated significant quantities of Pb.

The chemical composition of the pegmatite is shown in Table 7.6. The rocks are characterized by high contents of SiO_2, Al_2O_3 and K_2O. The pegmatite and schists have similar absolute SiO_2 and Al_2O_3 contents and comparable Si/Al ratios (Fig. 7.12). The pegmatite has lower Fe and Mg contents than the schist. The pegmatite rock is significantly enriched in K_2O and depleted in Na_2O with respect to the schists (Fig. 7.13). The high Pb content in the pegmatite is due to the high proportion of amazonite and the Pb content is significantly lower within the schists. This pegmatite was probably derived from the schists by incorporating K from the schists and Pb from the massive sulphide rock (see Chapter 8).

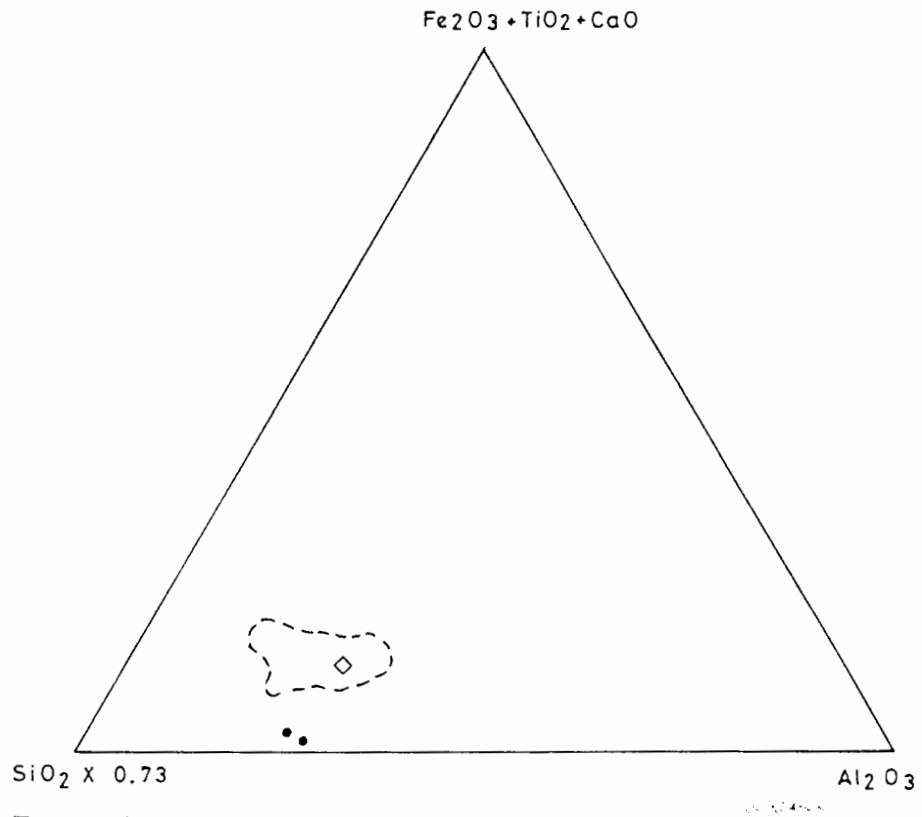

Figure 7.12. Ternary plot of (SiO_2x0.73)-Al_2O_3-(F_2O_3+TiO_2+CaO) showing positions of pegmatite (filled circle) and Broken Hill schist (diamond). Dashed line represents the compositional field of Broken Hill schists (after Lipson, 1990).

Table 7.6. Whole-rock compositions of pegmatite-type rock.

wt.%	BHF3	BHF14
SiO_2	67.20	66.96
TiO_2	0.01	nd
Al_2O_3	16.14	18.21
FeO	1.36	0.71
MnO	0.06	0.05
MgO	nd	nd
CaO	0.41	0.08
K_2O	11.84	8.03
Na_2O	0.59	1.11
P_2O_5	0.26	0.02
H_2O	0.08	0.10
LOI	0.60	1.06
Total	98.55	96.33
(ppm)		
Mo	1	1
Nb	nd	1
Zr	2	nd
Y	11	nd
Cr	12	10
Ni	3	nd
V	nd	nd
Rb	513	527
Sr	174	403
Th	nd	nd
U	nd	nd
La	18	3
Ce	44	12
Nd	20	11
Co	2	nd
Sc	1	nd
S	317	nd
Cu	328	nd
Pb	7254	10708
Zn	596	614
Ba	3141	15621

nd - not detected.

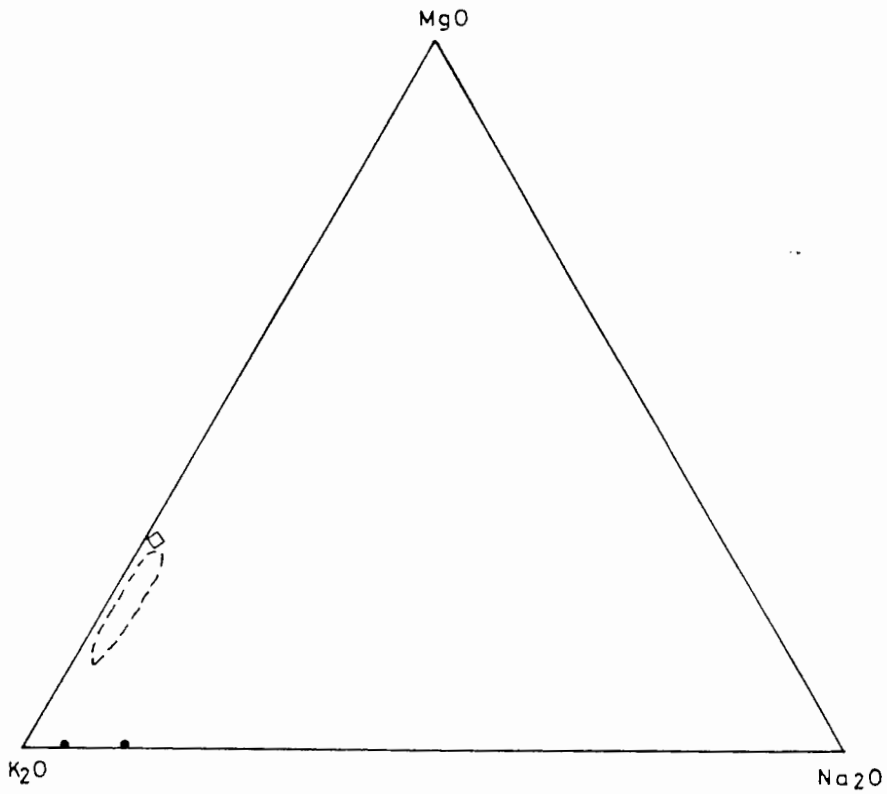

Figure 7.13. Ternary K_2O-Na_2O-MgO showing the positions of pegmatite (filled circle) and Broken Hill schist (diamond). Dashed line represents the compositional field of Broken Hill schists (after Lipson, 1990).

7.3.SUMMARY

The LOB silicate-rich iron formation mesobands are either predominantly garnet- or amphibole-olivine-rich varieties. Garnet-rich iron formation mesobands are enriched in Si, Ti, Al, Mn, Ca, P, Nb, Zr, Y, Sr, La, Ce, Nd, Cr, V, Pb, Ni and Ba. The amphibole mesobands are enriched in Fe, Mg, Cu, Co, Zn and S. Both mesoband-types reveal little difference in Na, K, H_2O and (Mo, Rb, Th, U and Sc) which occur with low concentrations.

The silicate-rich mesoband-types have Fe and Mn contents which are comparable to sediments which formed as chemical precipitates from submarine hydrothermal discharges. Amphibole mesobands have high Si/Al ratios characteristic of nearly pure hydrothermal sediments. The Si/Al and Si/Fe ratios of garnet mesobands are similar to hydrogenously enriched sediment. It was shown, however, that these mesobands have essentially also compositions comparable to submarine hydrothermal sediments but have significant detrital contamination. Except for Cu, Pb, Zn and Ba, the mesoband-types generally have low absolute trace element concentrations similar to that of hydrothermal sediments rather than

hydrogenously enriched sediments. The low concentration of trace elements within the LOB silicate-rich iron formation bands supports a submarine hydrothermal origin with rapid precipitation from Si-, Fe- and Mn-rich fluids that were also enriched in Cu, Pb, Zn and Ba. Enriched Ce concentrations in the garnet-rich mesobands relative to the amphibole-rich mesobands indicates the more rapid precipitation of elements from the submarine hydrothermal fluids during the formation of the latter.

The compositions of silicate-rich bands may be considered either as (1) chemically "immature" sediments i.e. proximal with respect to point of fluid discharge (amphibole mesobands) and chemically "evolved" sediments i.e. distal (garnet mesobands), or as (2) chemical sediments that responded to cyclic changes in the $f(O_2)$ throughout the depositional environment, or as (3) a product of differential leaching of Fe relative to Mn in the source rock. These aspects are considered further in Chapter 9.

8.METAMORPHISM

The metamorphic paragenesis of a sulphide-bearing iron formation can be considered a function of temperature, pressure, fluid composition (in particular H_2O, CO_2, HF, O_2 and S_2 fugacities), and bulk composition. Before the precursor mineralogy and genesis of the LOB iron formations are interpreted from the present chemical patterns, it is necessary to examine the effects of metamorphism. For medium- to-high grade regional metamorphism in the Namaqua Province, redistribution of elements by diffusion of ions and the movement of volatile species may have altered the original chemical system. There is little doubt that metamorphism has changed the original mineralogy of the LOB iron formation. It is also likely that the element distribution was altered during metamorphism. Consequently, it is necessary to examine the extent to which this has occurred.

8.1.EVIDENCE FOR POLYPHASE METAMORPHISM

Recognition of one metamorphic event followed by another in regionally metamorphosed rocks relies on the interpretation of the time relation of deformation (e.g. formation of a foliation, lineation or fold) and of crystallization events (e.g. growth of new minerals or recrystallization of existing ones). Spry (1976) suggested that the tectono-metamorphic evolution can be interpreted from three aspects, viz: (i) the time relation between different aspects of deformation, (ii) the time relation between crystallization of each mineral and some evidence of strain and (iii) the relative time of crystallization of each mineral. The iron formation mesobands examined in Chapter 7 were specifically selected away from fold hinges and areas of intense shearing. An interpretation of the tectonometamorphic evolution is made from the relative mineral growth relationships in the silicate-rich iron formation mesobands.

In the iron formation, prograde metamorphism is represented by amphibole-olivine-quartz, amphibole-quartz, garnet-quartz-apatite and rarely garnet-orthopyroxene-quartz, garnet-pyroxferroite-quartz and amphibole-pyroxferroite-quartz silicate assemblages. Amphiboles are mostly coarse-grained and form equilibrium textures with olivine, garnet, quartz and pyroxferroite. In the iron formation bands, amphibole, olivine and quartz exhibit either a high degree of alignment parallel to banding or are randomly orientated.

It is suggested that the prograde growth of amphibole and olivine continued after the relaxation of stress. In the garnet-rich iron formation bands, equant garnet and apatite do not show any indication of a dimensional fabric whereas quartz grains are often elongated parallel to banding. The growth of garnet appears to be unaffected by the stress associated with the fabric forming event.

Retrograde metamorphism within the iron formation is evident from crystallization of chlorite. Chlorite is associated with fractures and is particular abundant in the iron formation. The chlorite-filled fractures truncate the iron formation bands. Chlorite pseudomorphs after garnet were only observed in a few samples, indicating the restricted development of retrograde metamorphic products within the iron formation bands.

In the enclosing metapelitic schists, peak metamorphic conditions are indicated from the stable association of muscovite-quartz-K-feldspar-sillimanite. Two generations of muscovite were found. The first generation of muscovite has the same orientation as biotite and is concordant with the S2 fabric. This muscovite and quartz are in stable equilibrium at peak metamorphic conditions. Waters (1987) suggested that biotite and muscovite growth were mimicked on a strong tectonic fabric related to sub-horizontal (early D2) tectonism. In most of the schists, a second generation of fine-grained (<0.2 mm) muscovite (noted as sericite) cross-cuts primary muscovite, biotite and sillimanite. The pervasive growth of retrograde muscovite in the metapelitic schists has been recorded from many parts of the Aggeneys area (Moore, 1977; Lipson, 1978; Waters, 1987). Waters (1987) noted that the retrograde muscovite has replaced fibrolitic sillimanite. This muscovite is considered to be the product of widespread retrograde metamorphism (M2).

Chlorite has restricted occurrence in late F4 fold structures in the metapelites at Namiesberg (Moore, 1977). The limited growth of this phase was suggested by Moore (1977) to be the result of a second retrograde event. Limited chlorite within fractures in the Broken Hill schists grew during a second retrograde event (M3).

The evidence for polyphase metamorphism of the Bushmanland Subprovince in the wider Namaqualand region and in the Aggeneys area has already been presented in Chapters 3 and

4. It is generally accepted by most workers that, throughout the region, peak metamorphic conditions (M1) outlasted the most intense fabric forming event (D2). In the discussion above, it was suggested that within the LOB iron formation, growth of the peak metamorphic assemblages continued after the main fabric forming event (D2). The fabric defined by amphibole, olivine and quartz alignment in the iron formation is related to the main regional fabric (S2). The mineral growth is thought to be the result of a single prograde event. Evidence to suggest more than one prograde metamorphic event (for example, Joubert, 1971; Lipson, 1978) in the samples examined within the iron formation and the enclosing metapelitic schists was not found. Prograde mineral growth culminated before the onset of the D3 deformational event. The large open F3 fold at the NW edge of the deposit has the same metamorphic paragenesis as elsewhere in the LOB iron formation. Metamorphic assemblages expected from the M2 retrograde event evident within the schist were not found in the iron formation assemblages. The chloritic product of the second retrograde event (M3) is restricted mainly to late fractures of D4.

8.2.CONSTRAINTS ON P-T CONDITIONS

P-T estimates of the peak metamorphic conditions in the Aggeneys area have been derived from petrogenetic grids for pelitic rocks (Moore, 1977; Lipson, 1978; Rozendaal, 1978; Waters, 1987) and mafic rocks (Moore, 1977). Their estimates reveal that P-T conditions to range from 630-690 ^{0}C and 2.8-7.0 kb (Table 8.1). Waters (1987) constrained the peak P-T conditions at Broken Hill using the phase relations for the curves of (a) muscovite + quartz = K-feldspar + sillimanite + H_2O, $X(H_2O)= 1$ and (b) the Fe endmember curve for almandine + muscovite = Fe-biotite + sillimanite + quartz. The curves intersect in the P-T field (Fig. 8.1) at a temperature around 670 ^{0}C and a pressure around 4 kb.

Table 8.1. Peak metamorphic P-T conditions estimated from phase relations within metapelitic schists from the Aggeneys area.

	Namiesberg Moore (1977)	Aggeneysberge Lipson (1978)	Gamsberge Rozendaal (1978)	Aggeneys Waters (1987)	This Study
T (^{0}C)	650-750	670-695	630-670	660	670
P (kb)	5-7	3.4-4.5	2.8-4.5	3.5-4	4

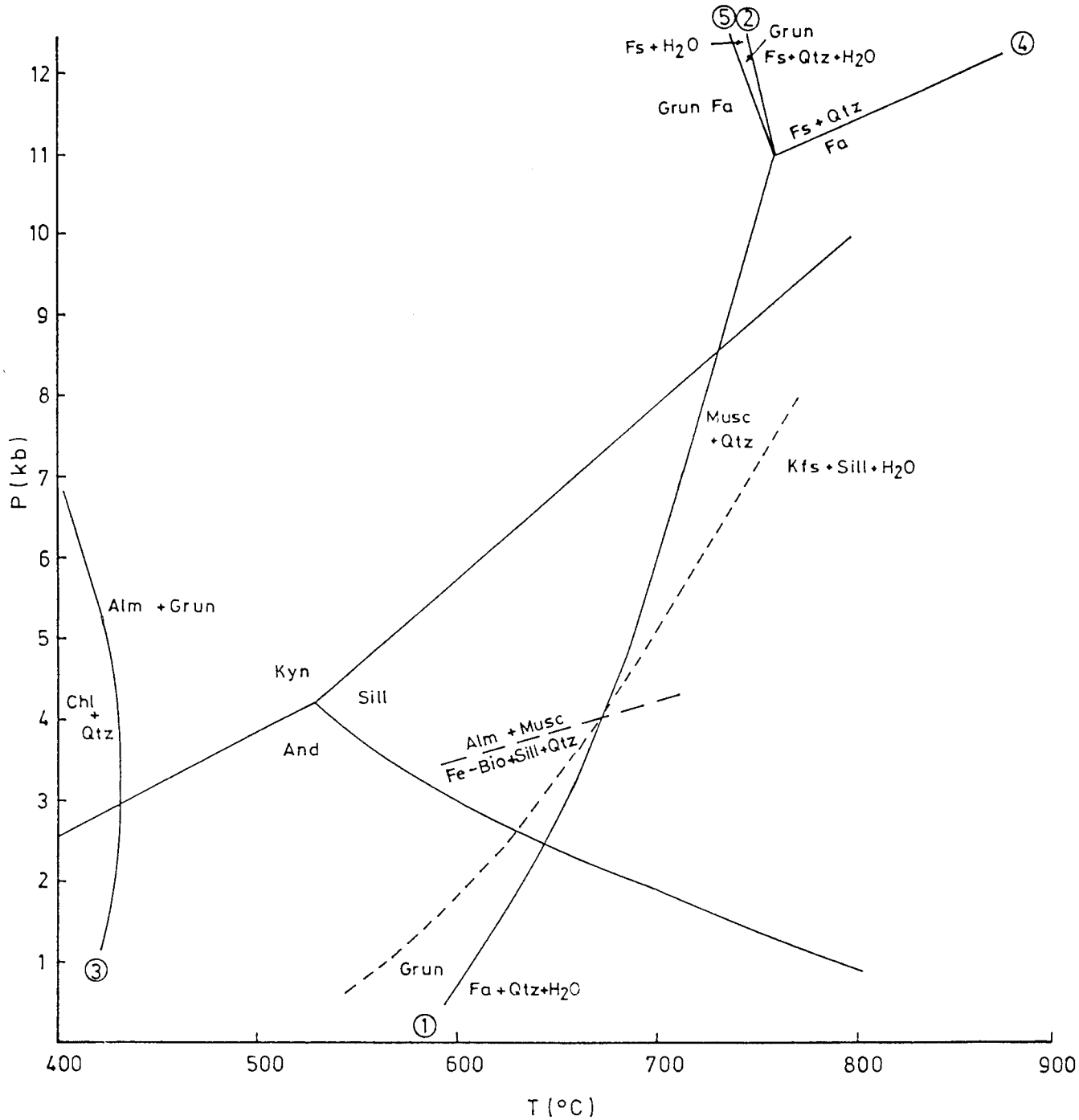

Figure 8.1. Phase equilibria for reactions (1 - 5) in the Fe-Si-O-H system with $X(H_2O) = 1$, after Miyano and Klein (1986, 1989). Kyanite-Sillimanite-Andalusite triple point is from Bohlen et al. (1991). Break-down of muscovite + quartz to K-feldspar is after Holland and Powell (1988). Fe-endmember curve for Almandine + Muscovite = Fe-biotite + sillimanite is after Tracy et al. (1976).

8.2.1.Garnet-biotite thermometry

Temperatures of peak metamorphism can be obtained using the partitioning of Fe and Mg between coexisting biotite and garnet which, expressed as K_D, is mainly a function of temperature. The Fe-Mg exchange reaction can be modelled in the Al_2O_3-K_2O-FeO-MgO system which is expressed as:

$$1/3Fe_3Al_2Si_3O_{12} + 1/3KMgAlSi_3O_{10}(OH)_2 = 1/3Mg_3Al_2Si_3O_{12} + 1/3KFeAlSi_3O_{10}(OH)_2$$

At equilibrium, the expression of the equilibrium constant (K_{Eq}) for the equation is:

$$K_{Eq}=K_D\times K_\gamma=\frac{(X_{Prp}/X_{Alm})}{(X_{Mg}/X_{Fe})^{Bio}}\times\frac{(\gamma_{Prp}/\gamma_{Alm})}{(\gamma_{Mg}/\gamma_{Fe})^{Bio}}$$

where X is the mole fraction and γ is the activity coefficient. The first part of the expression (K_D) is the distribution coefficient, and the second part (K_γ) treats the expression for non-ideal mixing. Mn and Ca do not mix ideally with Fe and Mg, and Fe-Mg mixing itself might not be ideal (Hodges and Spear, 1982; Ganguly and Saxena, 1984; Geiger et al., 1987; Hackler and Wood, 1989).

Numerous calibrations and correction factors for the garnet-biotite geothermometer are available. Empirical calibrations of K_D as a function of T (Frost, 1962; Saxena, 1969; Thompson, 1976; Goldman and Albee, 1977,) and an experimental calibration (Ferry and Spear, 1978) have been used to evaluate temperatures in medium-to-high grade pelitic and semi-pelitic rocks. Modifications to the garnet-biotite geothermometer have been made by correcting for the mixing properties of Fe-Mg-Mn-Ca in garnet and Ti-Al-Fe^{3+} in biotite.

In granulite facies rocks, Indares and Martignole (1985b) showed that differences of K_D on the thin section scale occur due to local retrograde equilibrium. Adjacent garnet rims and biotite grains are affected by diffusional Fe-Mg exchange during uplift (Florence and Spear, 1991). This can be avoided by selecting cores of garnet and matrix biotite isolated from

garnet which preserve peak temperatures (Indares and Martignole, 1985b).

The temperature estimates for garnet-biotite pairs in metapelitic schists, a garnet-rich iron formation mesoband and garnet quartzite were calculated using the calibrations of Ferry and Spear (1978), Hodges and Spear (1982), Ganguly and Saxena (1984), Indares and Martignole (1985a), and Williams and Grambling (1990). Temperatures obtained for the garnet-biotite thermometer at 4 kb are shown in Table 8.2. It is clear that there is no consistency for the temperature estimates. The calculated temperatures vary significantly from one rock-type to the next and between calibrations.

Table 8.2 Temperature estimates (^{0}C) for the garnet-biotite geothermometer using various calibrations at P= 4.0 kb.

Calibration	US schist BHS22 (n=1)	HS schist 2609-N7 (n=3)	Garnet Mesoband BHG6 (n=1)	Garnet Quartzite 1917-N2 (n=1)
FS	585	547	<400	503
HS	614	570	<400	511
GS	665	628	431	533
IM Model A Model B	534 464	520 470	<400 <400	478 454
WG	642	593	424	582

FS - Ferry and Spear (1978)
HS - Hodges and Spear (1982)
GS - Ganguly and Saxena (1984)
IM - Indares and Martignole (1985a)
WG - Williams and Grambling (1990)

n - number of garnet-biotite pairs.

Garnet compositions were determined from grains with radii <0.5 mm. Grains with radii <1 mm were suggested by Florence and Spear (1991) to be accompanied by intergranular diffusion on cooling which might have eradicated the garnet compositions that reflect peak temperatures. For this reason, temperature estimates from fine-grained garnet in the garnet iron formation mesoband and garnet quartzite rock were not considered further. Furthermore, these rocks have very low contents of K_2O in their whole rock composition and are not appropriately modelled in the Al_2O_3-K_2O-FeO-MgO system.

The discrepancy between calibrations is a function of the mixing model used and the thermodynamic mixing parameters ΔCa, ΔMn and ΔFeMg in garnet and ΔAl and ΔTi in biotite. The experimental calibration of Ferry and Spear (1978) considered ideal mixing of Fe and Mg in garnet. The temperature estimates are significantly lower than the regional estimate. The effects of non-ideal mixing between Ca and Mg in garnet as suggested by Hodges and Spear (1982) increases the temperature but it is still lower than the regional estimate. Calibrations taking into account the significantly non-ideal mixing parameters ΔCa and ΔMn of 12550 J/mol in garnet (Ganguly and Saxena, 1984) yielded temperatures comparable with the temperature constrained by the phase relations in the schists. Consideration of the ΔTi and ΔAl mixing parameters in biotite shown by Indares and Martignole (1985a) and, ΔCa and ΔMn in garnet of Ganguly and Saxena (1984) yielded very low temperature estimates. This calibration is limited to cases where Ti and Al in biotite have undergone specific reactions shown by Indares and Martignole (1985). The lower temperatures obtained are due to the high Ti and Al in the octahedral sites of the biotite. The calibration of Williams and Grambling (1990) incorporated non-ideal mixing of Ca, Mn, Fe and Mg in garnet from empirical calculations. The calibration also accommodates the effect of Fe^{3+} in biotite. The Fe^{3+} content in the biotite of this study is unknown and an all ferrous composition was assumed. By changing the ratio $Fe^{2+}/(Fe^{3+}+Fe^{2+})$, the effect of Fe^{3+} on the temperature was estimated. Values for this ratio of 0.9 and 0.8 corresponds to temperature estimates of 605 and 566 ^{0}C, respectively.

8.2.2.Sphalerite barometry

Sphalerite geobarometry is derived from the variation of FeS content in sphalerite as a function of pressure, when the activity of FeS is buffered by pyrite and hexagonal pyrrhotite (Scott, 1976). The significance of the geobarometer is the independence of mole % FeS in sphalerite with temperature (Scott, 1973). One specific requirement for the successful application of this geobarometer is that sphalerite must have equilibrated with pyrite and pyrrhotite where all sulphide grains remained in mutual contact from the onset of low grade metamorphism (Scott, 1973).

In the LOB samples, the grain contact requirement was not fulfilled. For this reason, the data of De Waal and Johnson (1981) were used. The calibration of the sphalerite geobarometer of

Bryndzia et al. (1990) was applied.

$P\ (kb) = 27.982 \log\dot{\gamma}_{FeS} - 8.549$

where $\dot{\gamma}_{FeS} = a(FeS)/X_{FeS}$

The a(FeS) is the activity of FeS for pyrite-pyrrhotite equilibrium calculated using the method of Froese and Gunter (1976). The calculations for a(FeS) are shown in Appendix B. X_{FeS} is the mole % FeS in sphalerite. The pressure estimate of 11.3 kb for the sphalerite geobarometer (X_{FeS} =0.137, after De Waal and Johnson, 1981) is significantly higher than the pressure indicated from the petrogenetic grid of Waters (1987). This pressure is also significantly higher than that derived by De Waal and Johnson (1981) using the calibration of Scott (1973). The X_{FeS} = 0.15 (this study) for LOB sphalerite not in contact with pyrite and pyrrhotite yielded a pressure of 10.2 kb.

Due to the uncertainty of the calibration, the $f(S_2)$ and the equilibrium criteria, the preferred estimated pressure is that of 4 kb from the pelitic assemblage.

8.2.3.Phase relations in the iron formation

The composition of the LOB silicate-rich iron formation bands and their associated minerals can be described by the components of the system K_2O-Na_2O-CaO-FeO-Fe_2O_3-SiO_2-MgO-MnO-Al_2O_3-TiO_2-P_2O_5-BaO-CuS-PbS-ZnS-H_2O-S-F. The phases in this system are garnet, amphibole, olivine, biotite, orthopyroxene, pyroxferroite, quartz, apatite, magnetite, galena, sphalerite, chalcopyrite, barite, sillimanite and fluid. The relationship between rock compositions and mineral assemblages in thermodynamic equilibrium is expressed by the Phase Rule. For the phases within the 18 component system above, there is a maximum of 5 degrees of freedom for the observed equilibrium assemblages. This makes it exceedingly difficult to resolve the controls on the phase equilibria. To expedite the phase relations of the iron formation rocks, it is necessary to reduce the number of components in the system by allowing several simplifying assumptions. These are:

1. The Fe_2O_3 component was not determined for silicate-rich iron formation bands whole rock compositions. The absolute Fe_2O_3 content in the mineral phases are unknown. However,

calculated Fe_2O_3 contents using normalization procedures indicate this component to be small in amphibole, garnet and biotite (Chapter 6). It is assumed that all the Fe_2O_3 is in magnetite. By ignoring magnetite as a system phase, Fe_2O_3 is excluded as a system component.

2. Garnet is the sole silicate phase that contains small quantities of CaO. Concentrations of CaO in amphibole, olivine and orthopyroxene are below the detection limit in virtually all grains analysed. Apatite is the major host for CaO and P_2O_5. The restriction of these components to apatite is confirmed by their correlation coefficient ($r=0.84$) for the whole rock compositions (Chapter 7). CaO and P_2O_5 are excluded as system components, while apatite is not considered as a system phase.

3. In order to simplify the system further, K_2O and Na_2O are excluded. K_2O is confined to biotite. Biotite is a minor phase and consequently K_2O is excluded as a system component. Na_2O occurs only in trace amounts in amphibole and is also excluded.

4. TiO_2 occurs in trace amounts in biotite and magnetite. Ilmenite and rutile were found as accessory minerals in a single thin section but were not observed within the iron formation mesobands collected for whole rock analyses. The total TiO_2 contents in the whole rock samples are consistently less than 0.6 wt.%. Therefore TiO_2 is not considered a system component, while neither ilmenite nor rutile are taken into account as system phases.

5. BaO occurs with significant concentrations in biotite within the iron formation mesobands (see Chapter 6.5). Barite is found as a minor phase in few of the garnet iron formation mesobands. Therefore, because biotite and barite are accessory minerals in these bands, BaO is excluded as a phase component.

6. The components CuS, PbS and ZnS occur with varying concentrations in the silicate-rich iron formation mesobands (Chapter 4,5 and 7). During metamorphism, the sulphide phases were assumed to have recrystallized rather than have participated in metamorphic reactions. Consequently, ZnS, CuS and PbS are excluded as system components.

7. Sillimanite is an accessory mineral in the amphibole-rich mesobands. Therefore,

sillimanite is not taken into account as a system phase.

The chemical system has thus effectively been reduced to FeO-MgO-MnO-Al_2O_3-SiO_2-H_2O-HF components by allowing the assumptions above. The equilibrium assemblages of the various silicate-rich iron formation mesobands consist of quartz, amphibole, olivine, orthopyroxene, pyroxferroite, garnet and the fluid phase. The degrees of freedom for the equilibrium assemblages in the various silicate-rich iron formation mesobands are shown in Table 8.3. The metamorphic reactions of selected phases are given in Table 8.4.

Table 8.3. Table showing the degrees of freedom for the phases in the various silicate-rich iron formation mesobands in the system FeO-MgO-MnO-Al_2O_3-SiO_2-H_2O-HF for peak metamorphic conditions.

Assemblage	Number Phases (P)	Number Components (C)	Degrees of Freedom (F)
Amph-Ol-Qtz-L	4	6	4
Amph-Qtz-L	3	6	5
Amph-Ol-Grt-Qtz-L	5	7	4
Opx-Grt-Qtz-L	4	7	5
Pyxf-Qtz-L	3	6	5

Amph - amphibole, Ol - olivine, Qtz - quartz, Grt - garnet, Opx - orthopyroxene, Pyxf - pyroxferroite, L - fluid. F=C-P+2.

Table 8.4. Possible metamorphic reactions in the FeO-Al2O3-SiO2-H2O system under medium- to- high grade metamorphic conditions.

1	2grun = 9q + 7fa + $2H_2O$
2	grun = q + 7fs + H_2O
3	70chl + 148q = 8grun + 91alm + $272H_2O$
4	5fa + q = 2fs
5	grun + fa = 9fs + H_2O

grun	= grunerite	$Fe_7Si_8O_{22}(OH)_2$
q	= quartz	SiO_2
fs	= ferrosilite	$FeSiO_3$
alm	= almandine	$Fe_3Al_2Si_3O_{12}$
chl	= Fe-chlorite	$Fe_{4.7}Al_{2.8}Si_{2.7}O_{10}(OH)_8$
fa	= fayalite	Fe_2SiO_4

The equilibria for the reactions listed in Table 8.4 in the Fe-Al-Si-O-H system have been calculated by Miyano and Klein (1986, 1989). The positions of reaction curves involving pure Fe endmembers in the P-T field are shown in Figure 8.1. Reaction curves below 400 ^{0}C are ignored because they are of no relevance to medium- to high-grade rocks of interest here. The first formation of grunerite occurs at temperatures above 400 ^{0}C by reaction (3). The curve shows that the Fe-endmember of chlorite coexisting with quartz is stable up to a temperature of approximately 430 ^{0}C. At pressures greater than 3 kb, the slope of the univariant curve becomes negative and grunerite might be formed at slightly lower temperatures. The upper stability limit of grunerite is given by reactions (1) and (2). The position of reaction curve (1) has been experimentally determined by Forbes (1977) and empirically calculated by Miyano and Klein (1986). Due to the dehydration nature of reactions (1) and (2), the slope is steep, and thus the reactions serve as good thermometers. In contrast, the solid-solid reaction (4) has a gentle slope and represents a good barometer. The univariant curves (1), (2), (4) and (5) intersect an invariant point at 760 ^{0}C and 11 kb.

For the real system at Broken Hill, substitution of particularly Mn and subordinately Mg for Fe needs to be considered. Mg substitution for Fe has the effect of increasing the temperature at which the phases for each reaction curve is stable (Haase, 1982; Miyano and Klein, 1986). For reaction curve (3), the effect of Mg for Fe substitution in coexisting chlorite, grunerite and almandine has only a minor influence on the position of the curve in P-T space (Miyano and Klein, 1989). This substitution causes the univariant curve to shift by 5 ^{0}C towards marginally higher temperatures and consequently coexisting quartz and chlorite are stable at this slightly higher temperature. The effect of Mg for Fe substitution in fayalite (X_{Fe}^{Ol}= 0.9) and ferrosilite (X_{Fe}^{Opx}= 0.9), was shown by Miyano and Klein (1986). With increasing Mg-rich compositions in these phases, the univariant curves of reactions (1) and (2) are shifted towards the right. The result is that with more Fe depleted compositions, the coexisting phases grunerite-olivine-quartz-H_2O and grunerite-orthopyroxene-quartz-H_2O are stable at higher temperatures. The substitution of Mg for Fe in reaction (4), where X_{Fe}^{Opx}= 0.9, has little effect on the temperature at which orthopyroxene-olivine-quartz assemblages coexist. The invariant point is lowered by at least 3 kb.

In many natural systems the extent of Mn for Fe substitution is generally less than Mg for

Fe. Little quantitative data are available for Mn-Fe substitution of phase equilibria within the Fe-Al-Si-O-H system. Haase (1982) suggested that because of the small amounts of Mn-Fe crystalline solid solution in iron formations, the effects on the equilibria are analogous to that of Mg-Fe. Spear and Cheney (1989) showed that in pelitic schists, the substitution of Mn for Fe in garnet, assuming ideal mixing, causes for instance, a significant expansion of the garnet + chlorite stability field. Garnet in equilibrium with chlorite and with X_{Mn} (Mn/Mn+Fe+Mg) = 0.4 is stable at temperatures approximately 50 ^{0}C higher and 125 ^{0}C lower than for the pure Fe-endmember compositions (Spear and Cheney, 1989). The silicate phases in the LOB iron formation contain significant amounts of Mn. Average X_{Mn} for the various silicate phases were shown in Chapter 6.12. The substitution of Mn for Fe increases the degree of freedom with the effect that the univariant reaction curves (1), (2) and (3) become divariant stability fields. Consequently, Mn-bearing phases are expected to become stable at lower temperatures and remain stable up to higher temperatures. This is semi-quantified in Chapter 8.4.

The addition of other volatile species reduces $X(H_2O)$ in the fluid, and increases the degree of freedom of the phase equilibria. Miyano and Klein (1986) showed, that decreasing the $X(H_2O)$ in the fluid causes the stability field of grunerite to contract towards lower temperatures at constant X_{Fe}. Using the data of Holland and Powell (1988), the univariant curves (1) and (2) are contracted by approximately 10 ^{0}C and 14 ^{0}C, respectively, for each 0.1 decrease in $X(H_2O)$.

8.2.4.Summary

The peak metamorphic temperature constrained from P-T petrogenetic grid yielded a temperature of 675 ^{0}C and pressure of 4 kb. The garnet-biotite geothermometer using the calibration of Ganguly and Saxena (1984) of the two schist samples offer the closest temperature estimate of 665 and 628 ^{0}C to that obtained from the petrogenetic grid. The pressure estimates >10 kb obtained from the sphalerite geobarometer are inconsistent with the pressure constrained from the metapelite. Constraints using phase relations in the iron formation are consistent with these peak P-T conditions, by considering qualitatively the effects of Mn in the FeO-MgO-MnO-Al_2O_3-SiO_2-H_2O-HF system.

8.3.CONSTRAINTS ON FLUID COMPOSITION

The fluid phase within the C-H-O-S system in iron formation rocks can be constrained by coexisting silicate, carbonate and sulphide phases (Ohmoto and Kerrick, 1977; Ferry and Burt, 1982). In this system, gas species are likely to include H_2O, CO_2, H_2, CO, H_2S etc. The presence of binary CO_2-H_2O fluid compositions were shown by Frost (1979), Haase (1982) and Miyano and Klein (1986, 1989) to explain the stability of phases within metamorphosed iron formations. In the LOB iron formation, C- and S-bearing species were excluded as major fluid components. The pervasive absence of carbonate phases in the LOB iron formation precludes CO_2 as a major fluid component. S-bearing gas species are unlikely to have significant contents in the fluid composition because sulphide species were assumed to be mostly involved in recrystallization. The fluid phase is speculated to be H_2O-rich with lesser contents of HF which was estimated from the composition of biotite.

8.3.1.Estimate of F and Cl fugacities

The F and Cl contents in biotite may be controlled by temperature, pressure, original bulk rock halogen content and by the exchange with a metamorphic fluid. Ferro-magnesian minerals with high X_{Mg} ratios tend to incorporate more F compared to those with low X_{Mg} ratios (Munoz, 1984). This principal of F partitioning into Fe-poor phases is commonly referred to as "Fe-F avoidance rule" and has been demonstrated by theoretical studies and for natural biotite compositions (Jacobs and Perry, 1979; Zaw and Clark, 1978; Valley and Essen, 1980). Zhu and Sverjensky (1991) showed that F favours partitioning into fluids with respect to minerals as the temperature is increased and is independent of pressure. An increase in temperature also favours the partitioning of Cl into minerals with low X_{Mg} rather than into the fluid (Zhu and Sverjensky, 1991).

It is shown in Figure 6.21, that the F content in biotite within the massive sulphide rock, garnet quartzite and iron formation varies as a function of X_{Mg}. The trend towards lower F-contents with decreasing X_{Mg} is in accordance with the "Fe-F avoidance" principal.

An estimate of the F fugacity in the fluid (f(HF)) from the composition of biotite was obtained using the equation of Gunow et al. (1980). Their equation is:

$$\log K_E = 2100/T + 1.523\ X_{Mg} + 0.461\ X_{An} + 0.079\ X_{Sid}$$
$$= \log[f(H_2O)/f(HF)] + \log[X_F/X_{OH}]$$

This equation assumes ideal solid solution between OH and F and thus the a(HF) and $a(H_2O)$ in biotite is represented by the mole fractions X_F and X_{OH}, respectively. The mole fractions for phlogopite (X_{Mg}), annite (X_{An}) and siderophyllite (X_{Sid}) are given by the equations:

$X_{Mg} = Mg/(Mg + Fe_{Tot})$

$X_{Sid} = [(3-(Si/Al))/1.75][1-X_{Mg}]$

$X_{An} = 1- (X_{Mg}+X_{Sid})$

The biotites within and around the LOB contain variable amounts of F which generally decreases with increasing distance from the massive sulphide horizon (see Chapter 6.5). T The calculated f(HF) for the analysed samples, reveal significant differences in the various rock-types (Table 8.5). The f(HF) of the metamorphic fluid during the formation of biotite, calculated for the various rock-types are: 6.41 bars in the iron formation, 2.97 bars in the massive sulphide rock, 1.65 bars in the garnet quartzite and 0.35 bars in the schist. The f(HF) calculated from the amphibole-rich iron formation mesobands was higher than for the garnet-rich mesobands (Table 8.5).

The Cl contents in biotite within the LOB rocks and schists were, however, always below the detection limit (0.025 wt.%). Because Cl prefers to partition into the mineral rather than into the fluid at high temperatures (Zhu and Sverjensky, 1991), it could be speculated that at the peak metamorphic conditions for the Broken Hill deposit, the Cl fugacity within the fluid was extremely low.

8.3.2. Estimates of oxygen and sulphur fugacities

The stability of assemblages within the iron formation is also dependent on oxygen and sulphur fugacity. At the peak metamorphic conditions established for the Broken Hill deposit, the association of nearly pure magnetite, Fe-rich olivine and quartz indicates that the ambient oxygen fugacity for amphibole mesobands was in the vicinity of the Quartz-Magnetite-Fayalite (QMF) buffer. At 670 ^{0}C and 3 kb, the oxygen fugacity in these mesobands was approximately $10^{-18.5}$ bars (Fig. 8.2) (extrapolated from Henley et al.,1984). Hsu (1968)

Table 8.5. F fugacities (bars) in the metamorphic fluid calculated from the composition of biotite.

Sample	2609-N7	BHS22	1917-N6	BHG4	BHG6	BHG2	BHA8
Rock	S	S	S	G	G	G	A
$f(H_2O)$	2551	2551	2551	2551	2551	2551	2551
X_{Mg}	0.227	0.297	0.253	0.459	0.269	0.259	0.234
X_{Sid}	0.464	0.477	0.021	0.451	0.552	0.569	0.539
XAn	0.359	0.304	0.789	0.153	0.201	0.199	0.253
X_F/X_{OH}	0.138	0.130	0.020	1.035	1.732	1.080	1.717
$\log X_F/X_{OH}$	-0.863	-0.886	-1.699	0.015	0.239	0.033	0.233
$\log f(H_2O)$ /f(HF)	3.661	3.767	4.701	3.041	2.558	2.750	2.533
f(HF)	0.557	0.436	0.051	2.321	7.066	4.539	7.481
Sample	BHA6	1917-N5	TS13	BH1	BH4	1917-13	TS12
Rock	A	GQ	GQ	MSR	MSR	MSR	MSR
$f(H_2O)$	2551	2551	2551	2551	2551	2551	2551
X_{Mg}	0.222	0.354	0.466	0.298	0.297	0.387	0.745
X_{Sid}	0.550	0.360	0.246	0.316	0.291	0.355	-0.007
XAn	0.247	0.362	0.368	0.448	0.469	0.349	0.301
X_F/X_{OH}	2.331	0.116	0.437	0.619	0.606	0.374	2.101
$\log X_F/X_{OH}$	0.367	-0.382	0.085	0.185	0.179	-0.427	0.433
$\log f(H_2O)$ /f(HF)	2.380	3.368	3.065	2.751	2.763	3.456	3.091
f(HF)	10.629	1.093	2.197	4.523	4.406	0.893	2.069

$f(H_2O)$ and f(HF) given in bars. A - amphibole iron formation mesoband, G - garnet iron formation mesoband, MSR - massive sulphide rock, S - schist, GQ - garnet quartzite.

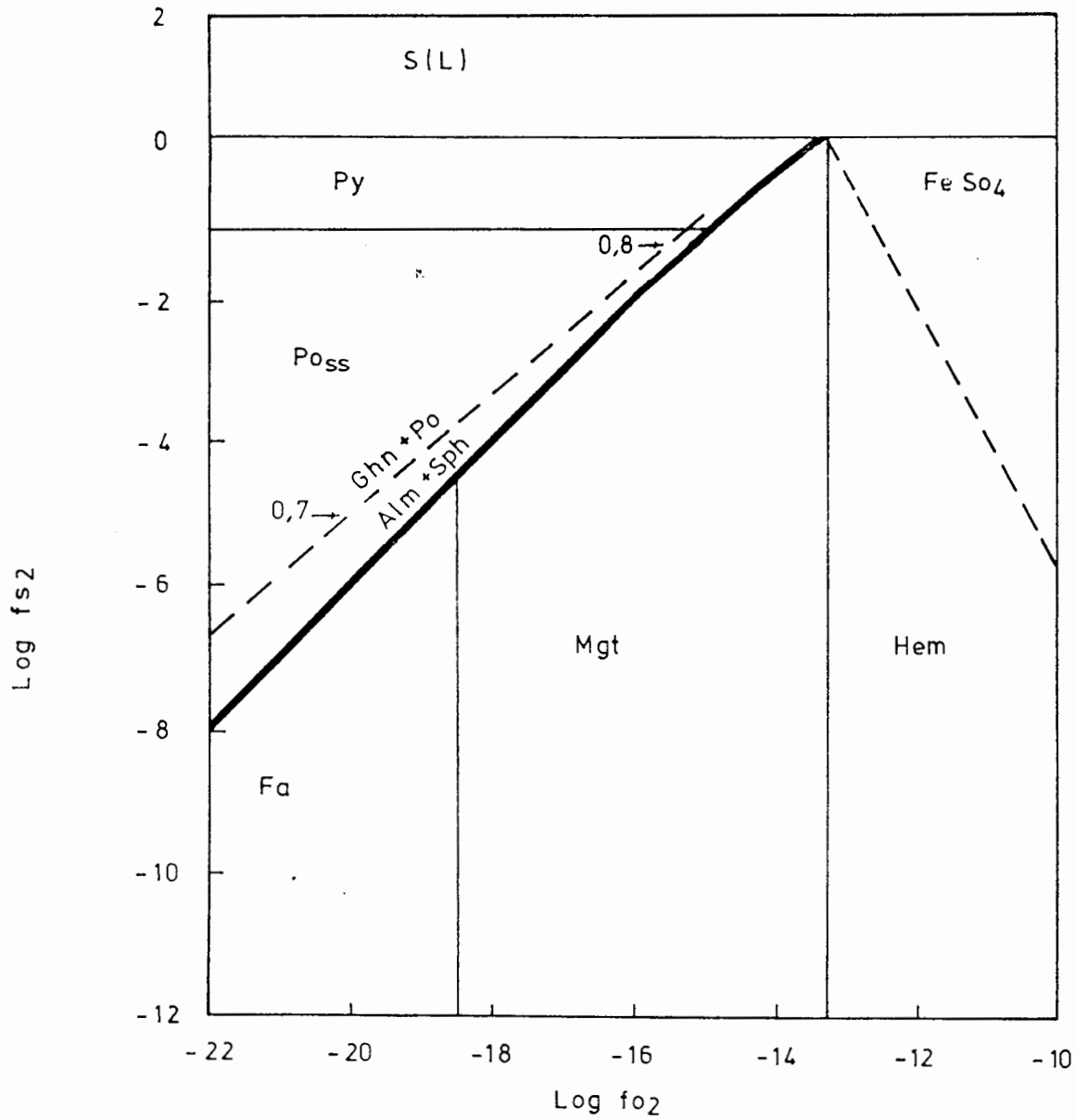

Figure 8.2. Log $f(O_2)$ - log $f(S_2)$ diagram for the system Fe-O_2-SiO_2 (after Henley et al., 1984) for T= 670 ^{0}C and P= 4 kb. The isopleth (dashed line) is taken from Spry (1987) for T= 650 $_0$C and P= 5.9 kb (P-T conditions used because of no access to these thermodynamic data). Symbols: S(L) = sulphur liquid, Po_{ss} = pyrrhotite solid solution, Fa = fayalite, Mgt = magnetite, Hem = hematite, Py = pyrite.

showed that the stability of almandine depends strongly on $f(O_2)$ with almandine being stable at oxygen fugacities up to the QMF buffer. Almandine-spessartine garnet was found to coexist with olivine and magnetite in some of the amphibole-rich mesobands. In the garnet mesobands, the $f(O_2)$ is poorly constrained and plots within the stability field for magnetite, approximately $10^{-13.3}$ - $10^{-18.5}$ bars, (extrapolated from Henley et al., 1984).

The general absence of pyrite within the LOB massive sulphide rock indicates that the sulphur fugacity $f(S_2)$ at peak P-T conditions was approximately $< 10^{-1}$ bars (Fig. 8.2). Within the massive sulphide rock, rare assemblages comprising magnetite, pyrrhotite, and pyrite indicate $f(O_2)$ and $f(S_2)$ at about $10^{-15.0}$ and $10^{-1.0}$ bars, respectively.

The $f(O_2)$ and $f(S_2)$ can also be estimated from the composition of gahnite which formed via the desulphurization reaction as proposed by Spry (1987). His reaction for gahnite from reactants garnet and sphalerite is:

$$Fe_3Al_2Si_3O_{12} + ZnS + 1.5\ S_2 = ZnAl_2O4 + 3FeS + 3SiO_2 + O_2$$

This reaction is strongly affected by variations in oxygen and sulphur fugacity (Spry and Scott, 1986). On the scale of several millimetres, however, local changes in oxygen and sulphur fugacity are thought to be less likely than variable sphalerite compositions. Different sphalerite compositions are envisaged to account for the large variation of Zn and Fe contents of ferroan gahnite within the garnet quartzite.

Given the mole fraction of gahnite in the LOB gahnite to be generally restricted between 0.75 and 0.77 (see Chapter 6.7), the $f(S_2)$ and $f(O_2)$ of the metamorphic fluid was be estimated to have been $10^{-2.6}$ - $10^{-1.7}$ and $10^{-16.6}$ - $10^{-17.8}$ bars, respectively (Fig. 8.2).

8.3.3. Local variation of F in the metamorphic fluid

It was suggested in Chapter 8.3.1 that the F content in biotite within the same rock-type was controlled by the activity of F in the metamorphic fluid. If biotites from different rock-types are considered in stratigraphic sequence (e.g. BHU 2609 and BHU 1917), then the F content in biotite varies clearly as a function of XMg (Fig. 6.21). The X_{Mg} and F content in biotite become smaller further away from the massive sulphide rock and iron formation and towards the overlying and underlying schist. The fact that the F content in biotite is dependent on X_{Mg} from one lithostratigraphic unit to the next and is dependent on a(HF) within a lithological unit indicates that a F-gradient in the metamorphic fluid existed across the lithological boundaries. The F-gradient in the fluid was steepest between the schist and the iron formation, and between the schist and the massive sulphide rock. The F-gradient was more

gentle between schist and garnet quartzite. The preservation of this F-gradient indicates that the fluid composition was buffered internally within each major lithological unit.

The estimated f(HF) of the fluid also reveals variations within the iron formation. The significant difference of f(HF) between garnet and amphibole iron formation mesobands indicates not only the internal buffering of f(HF) within each silicate band but also the primary difference in f(HF) during deposition of these two types of silicate bands.

8.4.LOB IRON FORMATION ASSEMBLAGES

Textural evidence suggests that the mineral phases present in the iron formation are in equilibrium. This is confirmed by the ternary SiO_2-FeO-MnO and SiO_2-FeO-MgO composition-assemblage diagrams (Fig. 8.3).

At the peak P-T conditions for the Broken Hill deposit (670 ^{0}C, 4 kb), the Fe-endmember compositions of coexisting grunerite, fayalite and quartz with $X(H_2O) = 1$ are stable phases. Coexisting amphibole and olivine assemblages of the LOB iron formation with their Mg-poor and (Fe-Mn)-rich compositions and fluid composition with $X(H_2O) = 1$ are also stable phases with quartz at these P-T conditions. This is due to the presence of Mn which causes the expansion of the temperature stability field for these coexisting phases. Consequently, it is not necessary to change the fluid composition by decreasing $X(H_2O)$ in order to stabilize this assemblage at the local P-T conditions.

In some iron formation bands, amphibole was not dehydrated to form olivine (e.g. sample BHA12). This assemblage contains amphibole, quartz and magnetite. Although the Mn content in this amphibole is high, the Mg content ($X_{Mg} = 0.26$) is significantly higher than that of amphibole coexisting with olivine ($X_{Mg} = 0.10$-0.15). The higher Mg content in the amphibole increases the temperature for dehydration of amphibole to olivine and quartz, reaction (1). The elevated temperature required for the amphibole breakdown was not reached. It is also concluded that the fluid composition was sufficiently H_2O-rich which did not allow any significant decrease in the temperature at which the coexisting phases would be stable. Furthermore, it is suggested that amphibole with $X_{Mn} < 0.21$ was insufficient to stabilize Mg-rich amphibole coexisting with olivine and quartz at the P-T conditions for the

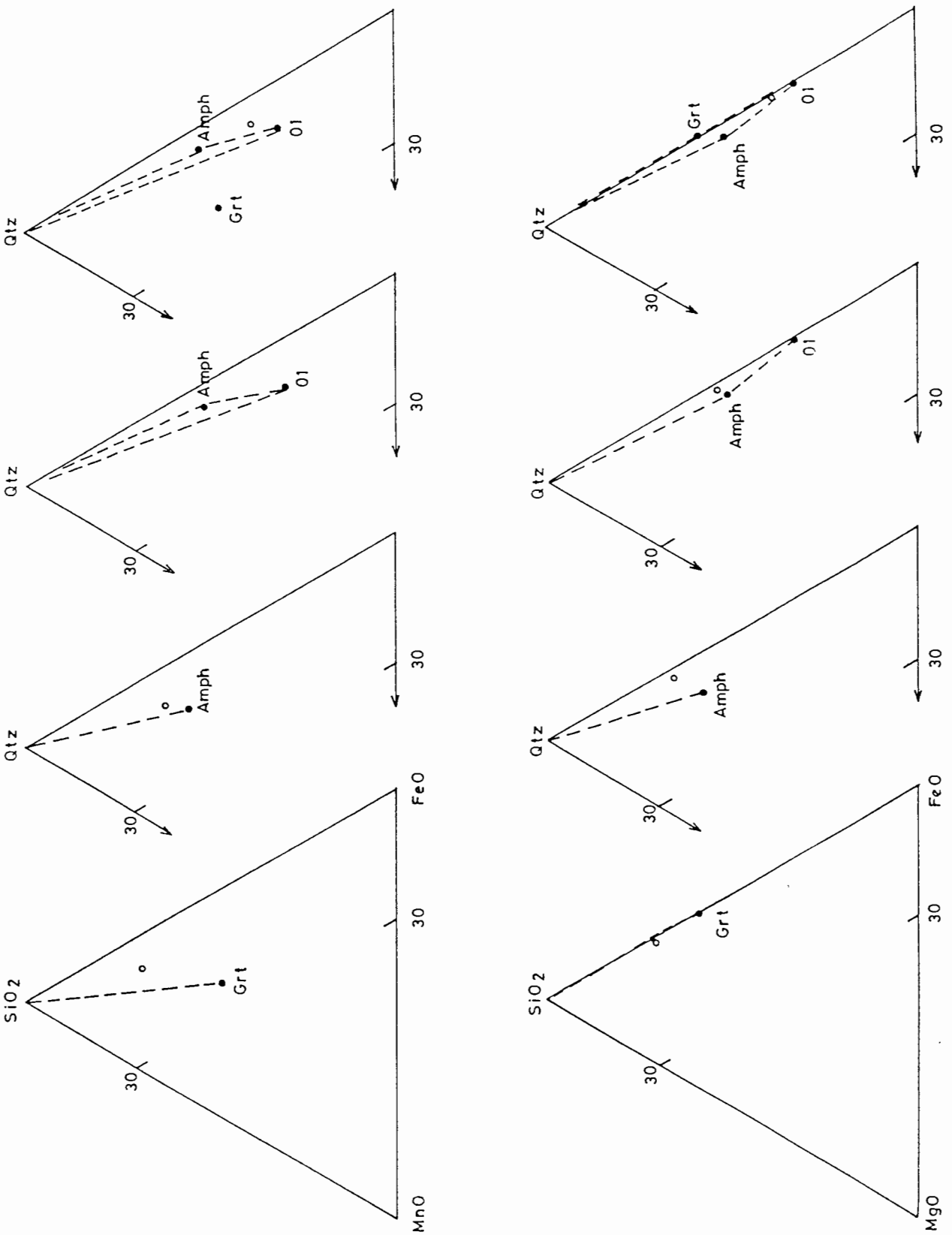

Figure 8.3. Phase relations for various silicate-rich assemblages in the systems SiO_2-FeO-MnO and SiO_2-FeO-MgO.

Broken Hill deposit.

Orthopyroxene is scarce within the LOB iron formation and was only found in one sample (5-1200) where it occurred in textural equilibrium with garnet. The garnet-orthopyroxene-quartz assemblage may have formed where amphibole dehydrated by reaction (2). The scarcity of orthopyroxene can be explained by the Fe-rich whole rock composition of the iron formation mesobands. Pressures of 11 kb are necessary for the existence of orthopyroxene where $X_{Fe}=1.0$. LOB orthopyroxene with composition $X_{Fe} = 0.73$ was accompanied by the reduction in the activity of Fe. This effectively lowered the pressure by approximately 7kb for the formation of orthopyroxene, and thus allowing its formation at the Broken Hill peak metamorphic conditions. The amphibole-pyroxferroite-quartz assemblage is uncommon, but more common is the pyroxferroite-quartz assemblage. Pyroxferroite was considered to form in a similar way as orthopyroxene by the dehydration of amphibole, reaction (2).

The absence of olivine-pyroxferroite/orthopyroxene assemblages is significant. Miyano and Klein (1986) showed the coexistence of orthopyroxene and olivine to occur within the restricted compositional range of $X_{Fe} = 0.6 - 0.8$ and $X_{Fe} = 0.80 - 0.93$ for the two phases, respectively. Orthopyroxene compositions with $X_{Fe} <=$ and $= 0.70$, will coexist with olivine at pressures < 0.5 kb. For the formation of orthopyroxene, it was suggested that low Fe contents were required. These iron contents were sufficient to stabilize orthopyroxene but were insufficiently high to form olivine. Assemblages containing, pyroxferroite have compositions close to $X_{Fe} = 0.5$ and thus cannot coexist with olivine.

8.5.COMPARISON WITH MINERAL ASSEMBLAGES IN OTHER IRON FORMATIONS

Changes to mineral assemblages and chemical compositions of iron formations have been widely recognized in regional and contact metamorphic terrains. Examples of Proterozoic iron formations from elsewhere in the world where changes in silicate assemblages have resulted from regional metamorphism have been documented for the Labrador Trough, Canada (Klein, 1978), Satnuru, Karnataka, India (Bhattacharya et al., (1990) and the Pegmont Deposit, Australia (Vaughan and Stanton, 1986). Examples of iron formations where changes in silicate mineral assemblages are the result of contact metamorphism are the Stillwater Iron Formation (Vaniman et al., 1980), Gunflint Iron Formation (Simmons et al.,

1974; Floran and Papike, 1978) and Biwabik Iron Formation (French, 1968; Bonnichsen, 1969).

The relative stabilities of minerals in iron formations at different metamorphic grades, as found by Klein (1978) are shown in Figure 8.4. Mineral assemblages characteristic of late diagenetic- to- very low grade metamorphosed iron formations, except for magnetite, were not observed in the LOB iron formation. Magnetite and quartz are stable over a wide range of P-T conditions and their presence or absence were not considered to indicate any specific P-T condition.

Garnet is prolific in the LOB, however, it is not common in many other iron formations worldwide due to their low Al_2O_3 bulk compositions (Klein, 1983). Garnet has been reported from the medium grade Negaunee Iron Formation (Haase, 1982). Spessartine-rich garnet has been reported from medium- to- high grade metamorphosed iron formations from the Pegmont Deposit, Australia (Vaughan and Stanton, 1986), the Broken Hill deposit, Australia (Stanton, 1976) and Satnuru, India (Bhattacharya, et al., 1990). Manganiferous garnets are stable over a wide range of temperatures and thus their occurrence within the LOB iron formation is not unexpected. The appearance of spessartine-rich garnet in manganiferous iron formations within high grade metamorphic regions depends largely on the whole rock Al_2O_3 content.

Pyroxene-bearing assemblages in iron formations in the Tobacco Root Mountains, Montana were suggested by Immega and Klein (1976) to have formed at P-T conditions of 4-6 kb and 650-750 ^{0}C. Assemblages bearing grunerite, pyroxene and olivine have been found in high grade metamorphosed iron formations, West Australia, which were regionally metamorphosed at temperatures around 670 +/-50 ^{0}C and pressures of 3-5 kb (Gole and Klein, 1981). Prolific orthopyroxene- and clinopyroxene-bearing assemblages are found in the Satnuru iron formation, India, which reached metamorphic grade of 740 ^{0}C +/- 60 ^{0}C and 6 kb (Bhattacharya et al., 1990). Iron formation assemblages with olivine and pyroxene also formed as a result of contact metamorphism, such as in the Bibwabik Iron Formation. Here the peak metamorphic conditions have been estimated to be 650-750 ^{0}C and 1.5-3.0 kb (Bonnichsen, 1969, 1975). The contact metamorphosed Gunflint Iron Formation with olivine-

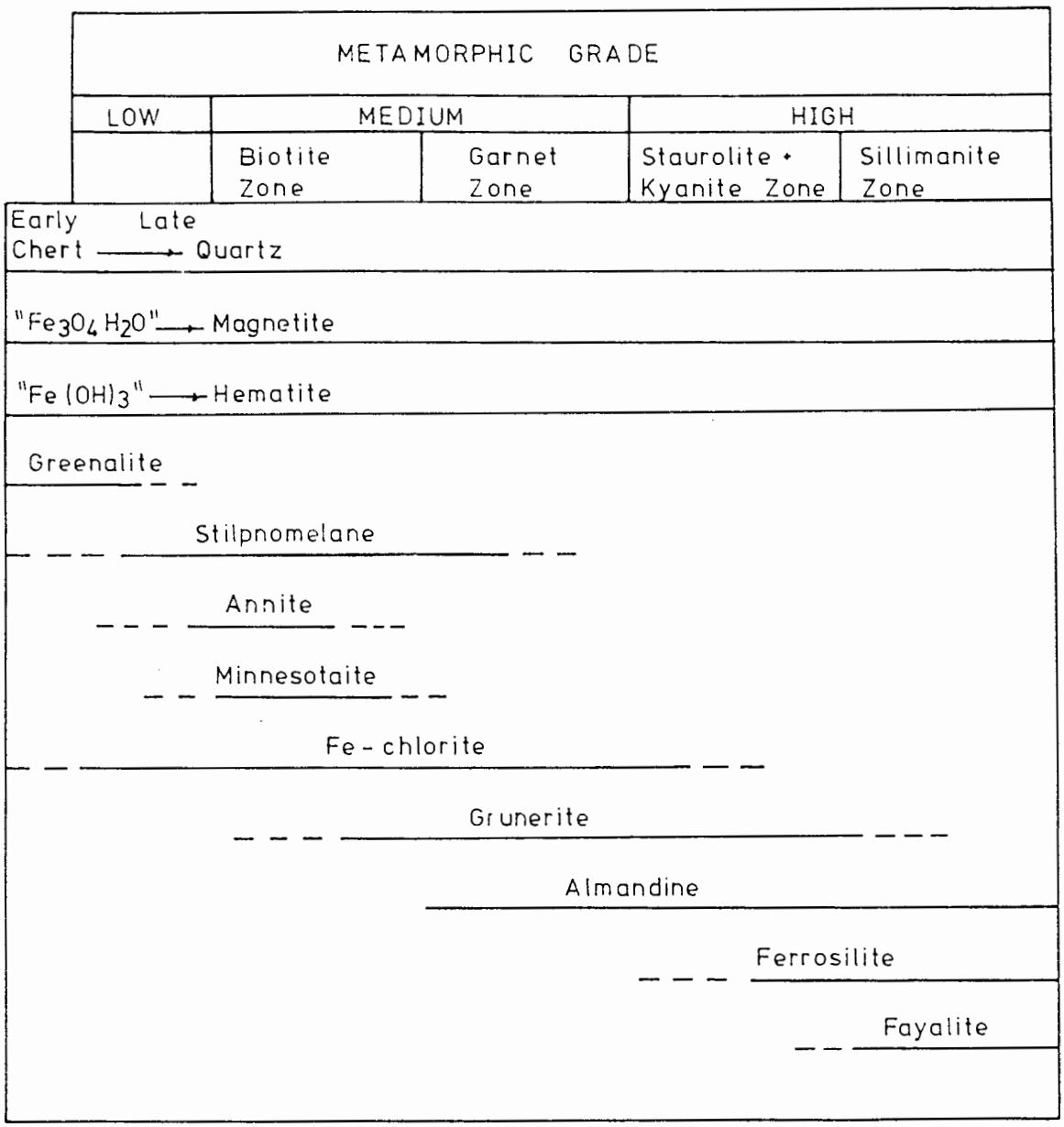

Figure 8.4. Diagram showing stability of minerals in iron formations as a function of metamorphic grade, after Klein (1978).

and pyroxene-bearing assemblages reached peak metamorphic conditions of 840-870 ^{0}C and >2 kb (Floran and Papike, 1978).

By comparison with other regional and contact metamorphosed iron formations, olivine in the LOB silicate bands forms at lower temperatures. The olivine from the Pegmont deposit is also Mn-rich and has experienced similar P-T conditions as the LOB. This is due to the effect of Mn substitution for Fe which expands the temperature field in which Fe-rich olivine is stable. Iron formations associated with higher pressures are characterized by significant proportions of pyroxene. The local occurrence of orthopyroxene and pyroxferroite in the LOB are a function of lower Fe content in the whole rock composition which allowed pyroxene minerals to form at lower pressures.

8.6.OPEN VERSUS CLOSED SYSTEM BEHAVIOUR

The metamorphic parageneses of the LOB iron formation and surrounding metapelitic rocks, together with their associated textures leaves little doubt that the deposit has been affected by prograde metamorphism with peak conditions reaching at least upper amphibolite facies. It has also been shown that the crystallization of silicate minerals in the iron formation involved dehydration reactions during prograde metamorphism. The silicate-rich iron formation assemblages were stabilized at the peak regional P-T conditions established above due to their high Mn contents. The associated fluid composition was essentially H_2O-rich with small but variable amounts of HF.

During metamorphism of the Broken Hill deposit, the infiltration and movement of volatile species and diffusion of ions may have severely affected the original element distribution particularly at the onset where the volatile content was high. Thus, it would be a gross assumption if the present chemical patterns are identical to those that developed during the initial deposition. In light of this, it is necessary to establish with respect to which non-volatile elements and to what extent the iron formation represents either an open or a closed system.

8.6.1.Metasomatism

8.6.1.1.Lithological and compositional contrasts

The general absence of blurring and homogenization across lithological contacts are an indication for limited element diffusion. Sharp boundaries exist between the major lithological units of the LOB. This is well defined for contacts between the massive sulphide rock and the enclosing schist, banded iron formation rock and garnet quartzite rock-types. Thus, the preserved contacts between rock-types indicate that element diffusion was restricted to a great extent.

The marked variation of Mn and Fe-contents in garnet between the iron formation, garnet quartzite and schist confirm the lack of homogenization with respect to these elements between lithological units. There is, however, evidence for local movement of Na, K and Pb where amazonite-rich lenses occur between the LOB massive sulphide rock and the underlying schist. The amazonite-rich lenses are almost monomineralic with only accessory quartz and garnet. The development of coarse-grained low variance mineral assemblages is a strong indication of open system behaviour. A chemical mechanism, for example metamorphic differentiation is thought to be responsible for these lenses. K and Na ions from the schist, and Pb from the massive sulphide rock migrated towards the interface of the two rock-types which acted as a fluid channel-way. The movement of Pb may occur from the desulphurization of galena during metamorphism. This metasomatic front indicates that at the interface there was local open system behaviour with respect to K, Na and Pb over distances of 10-20 cm. At the folded NW edge of the deposit, amazonite-rich 'pegmatite' truncates LOB and UOB rock-types. This discordant rock-type may reach 5-10 metres in thickness. Movement of K, Na, Al, Si and Pb ions over distances of 10 metres form metamorphic differentiates that concentrated in local late stage shear zones of F3 age.

The presence of gahnite in millimetre-thick bands between the massive sulphide rock and schist, and as disseminated grains throughout the LOB rock-types, indicates a decrease in $f(S_2)$. The predominance of gahnite over sphalerite indicates a significant decrease in $f(S_2)$ at the interface of the schist and massive sulphide rock. Accessory proportions of gahnite within the massive sulphide rock and other LOB rock-types indicate that the orebody was

sufficiently large to buffer the fluid's $f(S_2)$ internally.

Gahnite from elsewhere in Namaqualand analysed by Moore and Reid (1989) showed a compositional zonation from one gahnite-rich layer to the next. These were reported with Zn-enriched grains in the outermost layers and Fe-depleted grains for the inner most layers. This feature was interpreted by Moore and Reid (1989) to be the result of changing fluid conditions during prograde metamorphism.

8.6.1.2.Banding contrasts within the iron formation.

Contacts between silicate and magnetite mesobands in the iron formation are remarkably sharp. The contacts between the various silicate bands, in particular the garnet-rich and amphibole-olivine-rich iron formation mesobands are well defined. It is rarely noted that at the contacts between some silicate bands, garnet proportions gradually decrease into amphibole-olivine band over a distance of 2-5 cm.

Garnets show no marked compositional variations with respect to Mn and Fe from one mineral grain to the next across garnet mesobands over distances of 1-30 mm (Chapter 6.1). In addition, garnet compositions are uniform along mesobands layers on the scale of 1-20 mm. Marked changes in Mn contents across garnet bands and uniform Mn contents along garnet bands on the scale of 1-25 mm were, however, found in the iron formation associated with the Broken Hill deposit, Australia (Stanton and Williams, 1978). Their suggestion was that compositional differences in garnet across banding occur on too small a scale to be "attributed to differences in temperature, pressure, or oxygen fugacity". The compositional variability rather reflects primary differences in whole rock composition on a small scale. Nevertheless, it may also be argued that the lack of variation of Mn in garnet on the mesoband scale is a function of a homogeneous precursor composition and constant oxygen fugacity. In the LOB, the uniform Mn distribution in garnet across banding is thought to be the result of the original chemical distribution rather than metamorphic diffusion of cations. This is supported by the well defined contacts between mesobands and microbands.

8.6.1.3.Short range homogenization of individual mineral species.

Garnets in the LOB have experienced P and T conditions of the upper amphibolite facies.

Under such conditions, diffusion rates are sufficiently high to homogenize garnet grains of the size found in the LOB (Florence and Spear, 1991). The difference between core and rim compositions are small compared with garnet in greenschist facies terrains. Furthermore, the slight enrichment and depletion of Fe and Mn in cores and rims, respectively, of garnet reveals no consistent pattern, and precludes prograde growth zonation. The observed zonation is attributed to random retrograde diffusion. A similar pattern is also observed for individual amphibole and olivine. Consequently, individual grains that might have exchanges with their surroundings are limited to the sub-millimetre scale.

8.6.2.Infiltration of fluid

The halogen chemistry of biotite is a useful indicator of metamorphic and hydrothermal fluid-rock interaction (Wood and Walter, 1986; Sisson, 1987). This biotite may be used as an indicator of fluid/rock ratio. Wood and Walter (1986) suggested than since, in metamorphic rocks, the Cl contents in biotite are low whereas the fluids may be Cl-rich, relatively small amounts of fluid are needed to equilibrate an initial varied Cl content of biotite with that of the externally derived fluid. In contrast, F is strongly partitioned into biotite and thus large amounts of fluid are needed to homogenize biotite with respect to its F-content. Estimates of the fluid/rock ratios required to homogenize compositional gradients of halogen contents have been estimated by Wood and Walter (1986). Cl and F in biotite require fluid/rock ratios of 1/40 and 1000/1, respectively, to bring these species into equilibrium with the fluid.

Consequently, it is suggested that there was no major infiltration of external fluids subsequent to the formation of biotite.

9.CONCLUSIONS

Interpretation of the genesis of the LOB iron formation can be considered in terms of processes that are presently operating in geothermal brine systems, e.g. the Red Sea. Minerals associated with these recently forming sulphide deposits assisted in elucidating the ancestral mineralogy of LOB silicate-rich bands.

9.1.PRECURSORS TO METAMORPHIC MINERALS IN THE IRON FORMATION

The interpretation of the precursor minerals requires that no significant chemical redistribution of non-volatile elements has occurred. Evidence used to suggest that movement of non-volatile species were limited to the scale of approximately 1 mm is given in Chapter 8. Consequently, the compositions of the garnet- and amphibole-rich iron formation mesobands reflect to a great extent the original chemical composition.

9.1.1.Magnetite

The formation of magnetite was probably derived from the transformation of amorphous limonite to goethite to hematite to magnetite during diagenesis. In the metalliferous Red Sea sediments, the precipitation of limonite, as suggested by Bischoff (1969), requires oxidation of dissolved ferrous iron and subsequent precipitation of ferric hydroxide. The reactions described by Bischoff (1969) and Hackett and Bischoff (1973) for the formation of magnetite are:

$Fe(OH)_3$ (limonite) = FeO.OH (goethite) + H_2O

FeO.OH (goethite) = Fe_2O_3 (hematite) + H_2O

Fe^{2+} + Fe_2O_3 (hematite) + H_2O = Fe_3O_4 (magnetite) + $2H^+$

For the latter, the transformation of hematite to magnetite was suggested by Hackett and Bischoff (1973) to be favoured by an increase in temperature and the ferrous iron activity.

Magnetite might also have been directly precipitated from the brine solution. Small quantities of precipitated magnetite have been reported from the Red Sea sediments (Hackett and Bischoff, 1973). The extent to which magnetite precipitated directly or from a goethite precursor in the LOB is unknown.

9.1.2.Quartz

Quartz and magnetite are common throughout the LOB iron formation. Quartz might be derived from directly precipitated silica-gels in a silica saturated brine. In the magnetite-rich bands, coexisting quartz might have originated from silica adsorbed onto amorphous limonite, forming colloids, which were subsequently expelled during the formation of goethite (Bischoff, 1969). This association is particularly relevant to the QMIF where quartz and magnetite have co-precipitated.

In the garnet-rich iron formation mesobands, the significant Al_2O_3 and TiO_2 contents suggests a probable clastic protolith. Thus, it is also likely that some quartz has a clastic origin. Quartz was also derived from the desilication of some of the precursor minerals of amphibole, olivine, garnet and biotite (see below).

9.1.3.Amphibole and Olivine

The formation of amphibole might either proceed via metamorphic reaction of chert or quartz and Fe-rich carbonate phases, or from the dehydration of lower grade hydrous iron silicates. Klein (1973) showed that the interpretation of the reaction mechanism using textural evidence is possible only up to metamorphic grades indicated by the biotite isograd. Bearing this in mind, the precursor to LOB amphibole must remain speculative. It was assumed from the absence of relict carbonate minerals in the LOB iron formation and the indications of a CO_2-poor fluid phase from the phase relations of amphibole-olivine-quartz-fluid, that the growth of amphibole and olivine was unlikely to have proceeded via decarbonation reactions. Alternatively, amphibole formed from the dehydration of hydrous iron silicate minerals. The sequence of reactions that form high grade assemblages from hydrous iron silicates have been described by various authors (Klein, 1973; Frost, 1979). The transformation generally involves desilication after the formation of minnesotaite, and dehydration throughout the reaction sequence:

greenalite => minnesotaite => amphibole => olivine

Silicate minerals within the Atlantis II Deep are Si and Fe-rich and are low in Al (Bignell et al., 1976). Hydrous iron silicates found in the Red Sea sediments are Fe-montmorillonite

(Bischoff, 1969) and, Fe- and Mg-rich smectite (e.g. nontronite and Fe-bearing saponite) (Cole, 1988). Average compositions of Fe-montmorillonite facies from the Red Sea reveals that uptake of significant SiO_2 is required to form the LOB amphibole (Fig. 9.1). This precursor is consistent with the uptake of silica required for the formation of minnesotaite from greenalite. The simplified reaction of Klein (1973) showing the transformation is:

$$(Fe,Mg)_6Si_4)O_{10}(OH)_8 + 4SiO_2 = 2(Fe,Mg)_3Si_4O_{10}(OH)_2 + 2H_2O$$

greenalite minnesotaite

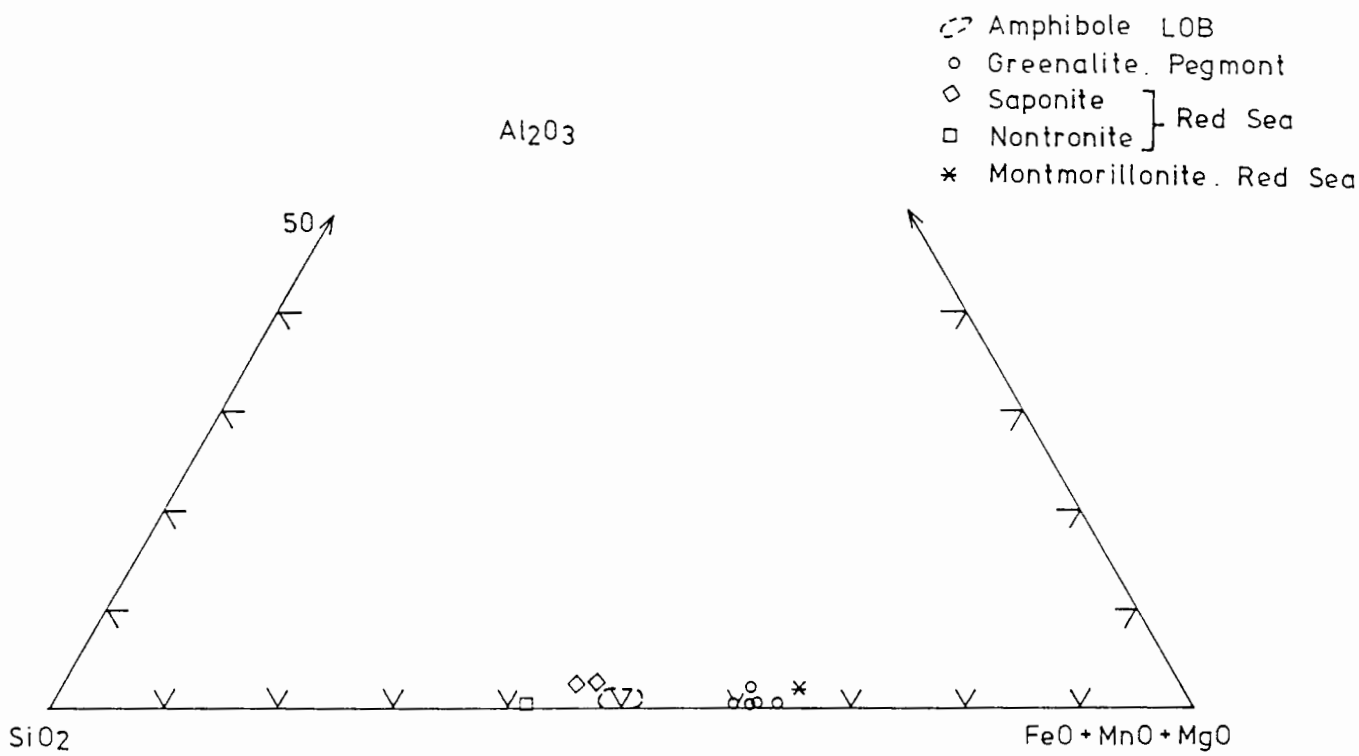

Figure 9.1. Ternary SiO_2-Al_2O_3-(FeO+MnO+MgO) diagram shown the composition of LOB amphibole relative to the compositions of greenalite from the Pegmont deposit (after Vaughan and Stanton, 1986) , saponite and nontronite from the Red Sea (after Cole, 1988) and Fe-montmorillonite from the Red Sea (after Bischoff, 1969).

Desilication and further dehydration of minnesotaite proceeded at higher temperatures. Miyano and Klein (1989) showed that the Fe-endmember of minnesotaite is stable up to approximately 350 ^{0}C with P= 1-2 kb.

Their reaction is:

$$7Fe_3Si_4O_{10}(OH)_2 = 3Fe_7Si_8O_{22}(OH)_2 + 4SiO_2 + 4H_2O$$

minnesotaite grunerite

Alternative precursors, nontronite and Mg-rich saponite which released some silica and underwent copious dehydration, might also be viable precursors to the LOB amphibole.

Vaughan and Stanton (1986) have proposed the formation of amphibole and olivine from the reduction of silicate gel (greenalite) and oxide gel (goethite) with profuse dehydration. Their reactions, given below, account for the absence of quartz in the fayalite-rich "central core zone" of the Pegmont deposit:

$$2(6FeO.4SiO_2.4H_2O) + 10FeO.OH = 7FeO.8SiO_2.H_2O + 5Fe_3O_4 + 12H_2O$$

greenalitic gel gel goethite grunerite magnetite

$$6FeO.4SiO_2.4H_2O + 2FeO.OH = 4(2FeO.SiO_2) + 6H_2O$$

greenalitic gel gel goethite fayalite

The LOB assemblages all contain significant quartz and lesser magnetite, indicating that the transformation above of greenalite to amphibole is not viable.

9.1.4.Garnet

Manganiferous analogues of septechlorites was suggested by Stanton (1976) as the most likely precursor to garnet in the iron formations associated with the Broken Hill deposit, Australia. A similar precursor, chamosite, was proposed by Vaughan and Stanton (1986) for the Pegmont Deposit. The interpretation is founded on the association of high Mn with the Al-bearing phase rather than an oxide, which suggests that the Mn and Al were co-precipitated. Septechlorite is essentially a Fe-rich chlorite which required the uptake of SiO_2, the reduction of Fe_{3+} and the loss of H_2O (Stanton, 1976). Due to the high Mn in the garnet, Stanton (1976) suggested that the septechlorite precursor remained in a low crystalline state until increasing conditions of temperature and pressure were reached. At elevated

temperatures, Mn is accepted from 6-fold into 8-fold coordination sites. This triggered the garnet forming reaction.

This transformation of chamosite to garnet, in which the Mn in the precursor mineral is associated with Al and the presence of a low Ca content, is desirable in a closed metamorphic system. For this reason, chamosite might be considered the likely precursor to LOB garnet. Furthermore, chamosite intermixed with magnetite has been reported to occur in recently deposited metalliferous sediment in the Thetis Deep of the Red Sea (Bignell et al., 1976).

9.1.5.Apatite

Fluoro-apatite is commonly associated with iron formations of the Broken Hill deposit, Australia (Stanton, 1976) and the Pegmont deposit (Vaughan and Stanton, 1986). Plimer (1984) considered fluoro-apatite to have an exhalative origin. Apatite was assumed to form as a chemical precipitate e.g. collophane, which was suggested by Vaughan and Stanton (1986) for the Pegmont deposit.

9.1.6.Sulphide

The sulphide minerals were considered to have been directly precipitated from the original metalliferous brine. The sulphide minerals coarsened due to recrystallization during metamorphism.

9.1.7.Biotite

Glauconitic material was suggested by Stanton (1976) to best satisfy the requirement for the precursor to biotite which involved the adsorption of K^+, release of SiO_2 and the reduction of Fe^{3+} to Fe^{2+}. The conversion is essentially:

glauconite + K^+ e^- = biotite + quartz (Stanton, 1976).

Other likely precursors to biotite are clay minerals e.g. illite.

Glauconite and illite are not known to contain any appreciable amounts of Ba. Ba in the

biotite can be considered either due to sulphur deficiency in the ore forming environment or as a product of post-depositional alteration. In the latter, barite was locally solubilized during metamorphism with Ba substituting for K in the interlayer sites of the biotite.

The solubility of barite depends mainly on the temperature, salinity and possibly on the activity of HF in the metamorphic fluid. At temperatures $>350\ ^0C$, the solubility of barite decreases (Scherp and Strubel, 1974). Consequently, temperature appears not to have been important in solubilizing $BaSO_4$ at the peak P-T conditions of Broken Hill. Furthermore, Scherp and Strubel (1974) showed from their experimental work that at temperatures of 350 ^0C, the solubility of $BaSO_4$ increases by a minimum of 100 times for a 2.0 n NaCl solution compared with a pure H_2O solution. The salinity of the metamorphic fluid was not constrained, but it might have been sufficient to assist in solubilizing barite.

The significant f(HF) in the metamorphic fluid, which is associated Ba-rich biotite (calculated in Chapter 8) might have assisted in locally solubilizing $BaSO_4$ by reducing $f(O_2)$. Where f(HF) is high, barite would be dissociated into Ba^{2+} and SO_4^{2-}, with diffusion of the former into biotite.

The controls on solubilizing barite described above are possible influences and remain subjective. A more simple and plausible explanation of the Ba-rich biotite is the availability of sulphur. The general lack of coexisting barite and Ba-biotite in the iron formation indicates that in a sulphur deficient system, biotite is only other host that will accommodate Ba in its structure.

9.2.GENESIS

Sediment-hosted massive sulphide deposits commonly occur within extensional basins that were formed through crustal attenuation often associated with centres of high geothermal gradient (Large, 1988). Faults which were active at the time of mineralization served as the conduits through which metalliferous fluids were focused and expelled into a third-order size basin or depression. Base metal deposits that formed by this process often have sulphide mineralization conformable with the enclosing sediment in the distal parts of basin. These are modeled as stratiform exhalative-type deposits. Fe-Pb-Zn sulphide mineralization of the

Sullivan deposit is a fine example of this class. The bulk of the mineralization in the ore zone occurs as massive- to poorly-bedded with subordinate inter-bedded siliclastic rock, which is spatially close to the vent (Hamilton et al., 1983). In the distal parts of the Sullivan deposit, Hamilton et al. (1983) describe the ore zone to consist of bedded sulphide rock intercalated with clastic sedimentary rock. The predominance of chemical sediment and the absence of intercalated clastic sedimentary rock in the LOB and UOB successions contrasts significantly with the Sullivan Deposit. The precipitation of chemical sediment of the iron-, sulphide- and silica-rich rocks of the Broken Hill Deposit indicates a virtual cessation of clastic sediment during the ore forming period.

Two sources for the mineralization, and consequently differing ore genesis models have been suggested for the Aggeneys deposits. Moore et al. (1990) proposed that fluids were generated by compaction of the underlying host sediments during basinal compression. These fluids leached significant quantities of Si, Fe, Mn and base metals from a shallow weathered source of underlying leucogneiss. Lipson (1990) has, however, proposed that downward penetrating convection cells of sea water leached base metals from hydrated deep-seated mafic rock. The Pb-Zn enriched leucogneiss (unpublished company data) is a favourable source rock for the Aggeneys deposits. Some obstacles arise from using the model which infers a "deep weathering" source. These include (1) the size of convection cells which are implied to leach the metals might be conjectural (sensu Sawkins, 1984), (2) the model relies on tectonic mechanisms to activate the convection cells on and off for each mineralizing episode, and (3) the limitations of two adjacent deposits may not be less than 18 km apart (sensu Russel et al., 1981).

At Broken Hill, there is no direct evidence to suggest that a growth fault served as the conduit for the metalliferous fluids. Indications for syn-sedimentary faulting in the Aggeneys area are evident from the intraformational conglomerate higher-up in the stratigraphic sequence found in the eastern parts of the Aggeneysberge. Consequently, a feeder fault for exhaling fluids is only inferred at the NW margin of the LOB where the high Cu/(Cu+Pb+Zn) value in the massive sulphide rock indicates a proximal position to a linear zone of fluid discharge. This inferred fault might have served as a plane of weakness, which was probably obliterated by subsequent deformation.

For the Aggeneys deposits, the general consensus is that sulphide mineralization was syngenetic (Rozendaal, 1982; Lipson, 1990; Moore et al., 1990). Support for syngenetic mineralization is exhibited by the fine banding of the constituent Cu-Pb-Zn sulphides which are intimately associated with silicate and oxide facies of the banded iron formation rock. The finely banded sulphide mineralization is considered to have co-precipitated with chemical sediments of banded iron formation rock and precludes a diagenetic ore genesis. Speculation of an early-diagenetic ore genesis might be resolved by examining any variation of $\delta^{34}S$ in the sulphide mineralization. The isotopic variation of $\delta^{34}S$ in pyrite versus that in galena and sphalerite was used by Williams (1991) to interpret the genesis where mineralizing fluids infiltrated unconsolidated sediment in the ore forming environment of the HYC Pb-Zn deposit at McArthur River.

For most parts of the ore forming period, chemical sediments were the major contributors. The transition from garnetiferous quartzite (GQ) to iron formation (QMIF and AMIF) to massive sulphide rock (MSR) reflects abrupt changes in the supply of Si, Fe, Mn, S and base metals, and varying physical-chemical conditions within the brine pool. More specifically, the consideration of the whole rock compositions of the silicate-rich iron formation bands indicates that their development was generated by the interplay of mostly chemical and minor clastic material. In certain regards, amphibole- and garnet-rich iron formation mesobands have compositions comparable to submarine hydrothermally enriched chemical sediments from the Red Sea and the East Pacific Rise (see Chapter 7). Toth (1980) considered the enrichment of Mn in submarine hydrothermal sediments to originate as a result of decreased Fe solubility as both species undergo oxidation. The contrasting Mn and Fe contents in amphibole- and garnet-rich iron formation bands are considered to have resulted from differential precipitation of Fe and Mn species, which was largely controlled by the extent of aerobic conditions within the brine pool.

It would appear from the relative enrichment of Mn, Ca, P, Pb, Ba and REE (La and Ce) in the garnet-mesobands and Fe, Mg, Cu and Co in the amphibole-mesobands, that these bands were precipitated under conditions of distal (more oxidizing) and proximal (less oxidizing) environments, respectively. The garnet and amphibole mesobands are described as "evolved" and "immature" hydrothermal chemical precipitates, respectively. The former precipitated

from metalliferous fluids that were exposed to prolonged periods relative to the latter in the brine pool. This permitted greater fractionation of Fe and Mn, and greater adsorption of trace elements onto colloidal particles that formed the "evolved" chemical sediment.

Consideration of the distribution of the various iron formation types in the LOB would imply the predominance of amphibole-rich bands nearer to the vent at the NW margin and garnet-rich bands further away at the SE margin. Reconstruction of the LOB succession by unfolding the large F2 fold of Ryan et al. (1986) reveals the predominance of garnet mesobands in GMIF at the SE margin, thus supporting the required distribution. Alternatively, if F2 folding is considered to have only modified the LOB at the NW margin, then the distribution of the silicate-rich bands might be considered from the multiple venting of exhaling fluids. It has already been suggested here that Fe- and Mn-rich fluids responded to fluctuations of oxidizing conditions within the brine pool causing fractional precipitation with respect to these elements. The GMIF, being an evolved chemical sediment, at the NW margin might also have precipitated from Fe- and Mn-rich fluids from another vent further towards the west.

Most genetic models for submarine exhalative deposits invoke the transport of metals as chloride complexes, however, hypersaline fluorine brines were considered by Plimer (1984) to have facilitate the mineralizing event of the Broken Hill deposit, Australia. In the LOB, the high F content in biotite within the massive sulphide rock and banded iron formation rock compared to the poorly mineralized garnet quartzite and schist is considered an artifact of the original ore forming fluid composition. The HF-bearing fluids were probably derived from micas in the underlying clastic sediments. Due to the dissociation of HF in water, it is suggested that these fluids were sufficiently acidic to leach significant quantities of Si, Fe, Mn and base metals. Temperature was also an important factor in solubilizing base metals. Fluids with temperatures below 280 ^{0}C are sufficiently heated to carry significant amounts of Pb, Zn and Ag as chloride complexes, and temperatures above 300 ^{0}C are required to transport significant Cu (Large, 1992). Heated basinal waters, required to leach and transport metals from the underlying rhyolite were probably not obtained by the burial of the thin (>1 km) underlying sedimentary pile. Furthermore, the thicker (>2 km) sedimentary sequence considered by Colliston et al. (1989) would also be insufficient to heat basinal waters above

200 ^{0}C. Evidence for high heat flow during the formation of the Broken Hill deposit is lacking. Amphibolites found higher in the sequence have major and trace element contents which are tholeiitic in composition (Reid et al., 1987b). This implies an extensional tectonic regime which in turn allows for a higher heat flow to be generated.

9.3.RECONSTRUCTION OF THE LOB ORE ENVIRONMENT

The unfolded geometry of the Broken Hill deposit reveals that it was likely to have formed within a depression or a third order basin. The preservation of mm-to-cm-thick banding in the iron formation and massive sulphide lens is considered to represent bedding, and is envisaged to have been deposited under quiet conditions in a low energy environment. Lipson (1990) has suggested a shallow water setting such as a lagoon inland from a prograding shoreline, as the most likely ore forming environment of the Broken Hill deposit. This setting as opposed to deep-water setting is preferred because of the thin supracrustal sequence (< 1000 m) considered for the Bushmanland Group. Deep water environments like rift basins in the modern Red Sea accumulate voluminous chemical sediments which are deeply buried by thick sequences of clastic sediment. An obstacle to explain the shallow water depositional environment is the absence of cross-cutting mineralization in stockworks and tourmaline bearing breccias due to boiling of the heated brine waters in contacts with the sea water. A pre-existing footwall breccia might have been obliterated during the subsequent deformational events.

9.4.POST-DEPOSITIONAL ALTERATION

Subsequent to the deposition of the LOB, the metamorphic paragenesis and textural relations of the iron formation and the enclosing schist indicate a single prograde event which reached peak metamorphic conditions of the upper amphibolite facies. Peak P-T conditions for the event were about 4 kb and 670 ^{0}C. In the silicate-rich iron formation mesobands, the predominance of anhydrous assemblages were derived from the release of fluid by dehydration reactions. The fluid released during this process, as indicated by stability relations from the phase equilibria, was essentially H_2O-rich. The HF-chemical gradient within the original ore forming fluid, as indicated from the composition of biotite, has been preserved. This suggests that the peak metamorphic fluid was buffered largely internally by the composition of the various rock types.

REFERENCES

Albat, H. (1984). The Proterozoic granulite facies terrane around Kliprand, Namaqualand Metamorphic Complex. Bull. Precamb. Res. Unit, Univ. Cape Town, 33, 381pp.

Armstrong, R.A., Reid, D.L., Watkeys, M.K., Lipson, R.D. and Compston, W. (1988). Zircon U-Pb ages from the Aggeneys area, Central Bushmanland. Abstr., Geol. Soc. S. Africa, Geocongress 88, Univ. Natal, Durban, 493-496.

Bailey, S.W. (1984). Classification and structures of the micas. Mineralogical Society of America. Reviews in Mineralogy., 13, 61-104.

Barr, J.M. (1988). Isotope character of barite and ore genesis in Central Bushmanland. Unpubl. MSc. Univ. Witwatersrand, 208pp.

Barton, P.B. (1978). Some ore textures involving sphalerite from Furutobe Mine, Akita Prefecture, Japan. Mining Geol., 28, 293-300.

Barton, E.S. (1983). Reconnaissance isotope investigations in the Namaqua mobile belt and implications for Proterozoic crustal evolution- Namaqualand geotraverse. Spec. Publ. Geol. Soc. S. Afr.,10, 45-66.

Beeson, R. (1990). Broken Hill-type lead-zinc deposits- an overview of their occurrence and geological setting. Trans. Instn. Min. Metall. (Sectn. B:), 99, 163-175.

Bence, A.E. and Albee, A.L. (1968). Empirical correction factors for the electron microanalysis of silicates and oxides. Jour. Geol., 76, 382-403.

Bhattacharya, A., Spiering, B., Sen, S.K., Natarjan, R. and Mazumdar, A.C. (1990). Compositional characteristics and phase equilibria in manganiferous iron formations from a high-grade terrain near Satnuru, Karnataka, India. J. Met. Geol., 8, 525-538.

Bignell, R.D., Cronan, D.S. and Tooms, J.S. (1976). Red Sea metalliferous brine precipitates. Spec. Paper Geol. Assos. Can., 14, 147-179.

Bischoff, J.L. (1969). Red Sea geothermal brine deposits: their mineralogy, chemistry and genesis. In: Degens, E.T. and Ross D.A. (Eds.), Hot Brines and Heavy Metal Deposition in the Red Sea, Springer-Verlag, New York, 368-400.

Blignault, H.J., van Aswegen, G., van der Merwe, S.W. and Colliston,W.P. (1983). The Namaqualand geotraverse and environs: part of the Proterozoic Namaqua Mobile Belt. Spec. Publ. Geol. Soc. S. Afr., 10, 1-29.

Bohlen, S.R., Montana, A. and Kerrick, D.M. (1991). Precise determinations of the equilibria kyanite = sillimanite and kyanite = andalusite and a revised triple point for Al2SiO5 polymorphs. Amer. Mineral., 76, 677-680.

Bonatti, E., Fisher, D.E., Joensuu, O., Rydell, H.S. and Beyth, M, (1972). Iron-manganese-barium deposit from the northern Afar Rift (Ethiopia). Econ. Geol., 1967, 717-730.

Bonnichsen, B. (1969). Metamorphic pyroxenes and amphiboles in the Bibwabik Iron Formation, Dunka River area, Minnesota: Mineral. Soc. Am. Spec. Paper 2, 217-239.

Bonnichsen, B. (1975). Geology of the Bibwabik Iron Formation, Dunka River Area, Minnesota. Econ. Geol., 70, 319-340.

Bostrom, K. (1973). The origin and fate of ferromanganoan active ridge sediments. Stockholm Contrib. Geol., 27, 149-243.

Bryndzia, L.T., Scott, S.D. and Spry, P.G. (1990). Sphalerite and hexagonal pyrrhotite geobarometer: correction in calibration and application. Econ. Geol., 85, 408-411.

Carvalho, I.G., Zantop, H and Torquato, J.R.F. (1982). Geologic setting and genetic interpretation of Boquira Pb-Zn deposits, Bahia State, Brazil. Revta bras. Geocien., 12, 414-425.

Clifford, T.N., Gronow, J., Rex, D.C., Burger, A.J. (1975). Geochronological and petrogenetic studies of high-grade metamorphic rocks and intrusives in Namaqualand, South Africa. Jour. Petrol., 16, 154-188.

Cole, T.G. (1988). The nature and origin of smectite in the Atlantis II Deep, Red Sea. Can. Mineral., 26, 755-763.

Colliston, W.P. and Praekelt, H.E. (1988). The recognition of overthrust terranes in the Namaqua mobile belt. Abstr. 22nd Congr. Geol. Soc. S. Africa, Univ. Natal, Durban.

Colliston, W.P., Praekelt, H.E. and Schoch, A.E. (1989). A broad perspective (Haramoep) of geological relations established by sequence mapping in the Proterozoic Aggeneys terrane, Bushmanland, South Africa. S. African Jour. Geol., 92, 42-48.

Colliston, W.P., Praekelt, H.E. and Strydom, D. (1986). Stratigraphic map of Central Bushmanland. Bushmanland Research Group. Univ. Orange Free State.

Crerar, D.A., Namson, J., So Chyi, M., Williams, L and Feigenson, M.D. (1982). General geology, ancient and modern analogues, and implications for hydrothermal convection at oceanic spreading centres. Econ. Geol., 77, 519-540.

De Waal, S.A. (1974). The mineralogy of the Broken Hill orebody, with reference to ore beneficiation. National Institute for Metallurgy (Unpubl. Rep.), 1642, 51pp.

De Waal, S.A. and Johnson, J.A. (1981). Chemical heterogeneity of sphalerite in a base metal sulphide deposit. Econ. Geol., 76, 694-705.

Duncan, A.R., Watkeys, M.K. and Moore, J.M. (1984). Geochemistry of the "Floor" rocks of Namaqualand. Abstr. Confr. Mid-Late Protero. Lithos. Evolut., Precamb. Res. Unit. Cape Town, 75-76.

Ferry, J.M. and Burt, D.M. (1982). Characterization of metamorphic fluid composition through mineral equilibria. In: Ferry, J.M. (Ed.), Characterization of Metamorphism through mineral equilibria. Rev. in Mineralogy, 10, 207-262.

Ferry, J.M. and Spear, F.S. (1978). Experimental calibration of the partitioning of Fe and Mg between biotite and garnet. Contrib. Mineral. Petrol., 66, 113-177.

Floran, R.J. and Papike, J.J. (1978). Mineralogy and petrology of the Gunflint iron formation, Minnesota-Ontario: correlation of compositional and assemblage variations at low to moderate grades. Jour. Petrol., 19, 215-288.

Florence, F.P. and Spear, F.S. (1991). Effects of diffusional modification of garnet growth zoning on P-T path calculations. Contrib. Mineral. Petrol., 107, 4877-500.

Fortey, N.J. and Beddoe-Stephens, B. (1982). Barium silicates in stratabound Ba-Zn mineralization in the Scottish Dalradian. Min. Mag., 46, 63-72.

Forbes, W.C. (1977). Stability relations of grunerite, Fe7Si8O22(OH). Am. Jour. Sci., 277, 735-749.

Froese, E. and Gunter, A.E. (1976). A note on the pyrrhotite-sulphur equilibrium. Econ. Geol., 71, 1589-1595.

Frost, M.J. (1962). Metamorphic grade and iron-magnesium distribution between coexisting garnet-biotite and garnet-hornblende. Geol. Mag., 99, 427-438.

Frost, B.R. (1979). Metamorphism of iron-formations. Paragenesis in the system Fe-Si-C-O-H. Econ. Geol., 74, 775-785.

Ganguly, J and Saxena, S.K. (1984). Mixing properties of aluminosilicate garnets: constraints from natural and experimental data, and applications to geothermo-barometry. Am. Mineral., 69, 88-97.

Geiger, J.A., Newton, R.C. and Kleppa, O.J. (1987). Enthalpy of mixing of synthetic almandine-grossular and almandine-pyrope garnets from high temperature solution calorimetry. Geochem. et Cos. Acta, 51, 1755-1763.

Goldman, D.S. and Albee, A.L. (1977). Correlation of Mg/Fe partitioning between garnet and biotite with $^{18}O/^{16}O$ partitioning between quartz and magnetite. Am. Jour. Sci., 277, 750-767.

Gole M.J. and Klein, C. (1981). High-grade metamorphic Archaean banded iron-formations, Western Australia: assemblages with coexisting pyroxenes +/- fayalite. Am. Mineral., 66, 87-99.

Gross, G.A. (1965). Geology of iron deposits in Canada, 1- general geology and evaluation of iron deposits. Geol. Surv. Can., Econ. Geol. Rep., 22, 181pp.

Gross, G.A. (1980). A classification of iron formations based on depositional environments. Can. Mineral., 18, 215-222.

Gross, G.A. and McLeod, C.R. (1980). A preliminary assessment of the chemical composition of iron formations in Canada. Can. Mineral., 18, 223-229.

Gross, G.A. (1990). Manganese and iron facies in hydrolithic sediments. Spec. Publs. int. Ass. Sediment., 11, 31-38.

Guggenheim, S. (1984). The brittle micas. Mineralogical Society of America. Reviews in Mineralogy., 13, 61-104.

Gunow, A.J., Ludington, S. and Munoz, J.L. (1980) Fluorine in micas from the Henderson molybdenite deposit, Colorado. Econ. Geol, 75, 1127-1137.

Haase, C.S. (1982). Phase equilibria in metamorphosed iron formations: qualitative T-X(CO_2) petrogenetic grids. Am. Jour. Sci., 282, 1623-1654.

Hackett, J.P. and Bischoff, J.L. (1973). New data on the stratigraphy, extent and geological history of the Red Sea geothermal deposits. Econ. Geol., 68, 553-564.

Hackler, R.T. and Wood, B.J. (1989). Experimental determination of Fe and Mg exchange between garnet and olivine and estimation of Fe-Mg mixing properties in garnet. Am. Mineral., 74, 994-999.

Hamilton, J.M., Delaney, G.D., Hauser, R.L. and Ransom, P.W. (1983). Geology of the Sullivan Deposit, Kimberley, B.C., Canada. In: Sangster, D.F. (Ed.), Short course in sediment-hosted stratiform lead-zinc deposits. Mineral. Assoc. of Canada. 31-83.

Hartnady, C.J., Joubert, P. and Stowe, C.W. (1985). Proterozoic crustal evolution in southwestern Africa. Episodes, 8, 236-244.

Hatch, R.A., Humphrey, R.A., Eitel, W. and Comerforo, J.E. (1957). Synthetic mica investigation IX: Review of progress from 1947 to 1955. United States Bureau of Mines Report of Investigations 5337. (not seen, referenced in Solie, D.N. and Su, S., Am. Mineral., 72, 995-999).

Henley, R.W., Truesdell, A.H. and Barton, P.B. (1984). Fluid mineral equilibria in hydrothermal systems. In: Robertson, M., Reviews in Economic Geology, 1, 157.

Hicks, J. (1988). Gahnite and its formation in the context of regional metamorphism and mineralization in the Namaqualand Metamorphic Complex. Unpubl. MSc. thesis, Univ. Cape Town, 158pp.

Hodges, K.V. and Spear, F.S. (1982). Geothermometry, geobarometry and the Al_2SiO_5 triple point at Mt. Moosilauke, New hampshire., 67, 1118-1134.

Holland, R. and Powell, T.J.B. (1988). An internally consistent dataset with uncertainties and correlations: 3. Applications to barometry, worked examples and a computer program. J. Met. Geol., 6, 1988, 173-204.

Hsu, L.C. (1968). Selected phase relationships in the system Al-Mn-Fe-Si-O-H: A model for garnet equilibria. Jour. Petrol., 9, 40-83.

Immega, I.P. and Klein, Jr C. (1976). Mineralogy and petrology of some metamorphic Precambrian iron-formations in southwestern Montana. Am. Mineral., 61, 1117-1144.

Indares, A and Martignole, J. (1985a). Biotite-garnet geothermometry in the granulite facies: the influence of Ti and Al in biotite. Am. Mineral., 70, 272-278.

Indares, A and Martignole, J. (1985b). Biotite-garnet geothermobarometry in granulite-facies rocks: evaluation of equilibrium criteria. Can. Mineral., 23, 187-193.

Jack, A.M. (1980). The geology of western Namaqualand. Bull. Precamb. Res. Unit, Univ. Cape Town, 29, 173pp.

Jacobs, D.C. and Parry, W.T. (1979). Geochemistry of biotite in the Santa Rita porphyry copper deposits, New Mexico. Econ. Geol., 74, 860-887.

James, H.L. (1954). Sedimentary facies of iron formation. Econ. Geol., 49, 235-293.

James, H.L. (1969). Comparison between Red Sea deposits, older iron stones and iron formations. In: Degens, E.T. and Ross D.A. (Eds.), Hot Brines and Heavy Metal Deposition in the Red Sea, Springer-Verlag, New York, 525-532.

Joubert, P. (1971). The regional tectonism of the gneisses of part of Namaqualand. Bull. Precamb. Res. Unit, Univ. Cape Town, 10, 220p.

Joubert, P. (1974). Geological survey of Namaqualand and Bushmanland. Ann. Rep. Precamb. Res. Unit, Univ. Cape Town, 10-11, 24-30.

Joubert, P. (1986). Namaqualand- a model of Proterozoic accretion? Trans. of the Geol. Soc. of S. Africa, 89, 1-79.

Kimberley, M.M. (1978). Palaeoenvironmental classification of iron formations. Econ. Geol., 73, 215-229.

Kimberley, M.M. (1979). Geochemical distinctions between among environment types of iron formations. Chem. Geol., 25, 185-212.

Kimberley, M,M. (1989). Exhalative origins of iron-formations. Ore Geology Reviews, 5, 13-145.

Klein, C. (1966). Mineralogy and petrology of the metamorphosed Wabush iron formation, southwestern Labrador. Jour. Petrol., 7, 246-305.

Klein, C. Jr. (1973). Changes in mineral assemblages with metamorphism of some banded Precambrian iron-formations. Econ. Geol., 68, 1075-1088.

Klein, C. (1978). Regional metamorphism of Proterozoic iron-formation, Labrador Trough, Canada. Am. Mineral., 63, 898-912.

Klein, C. (1983). Diagenesis and metamorphism of Precambrian banded iron formation. In: Trendal, A.F. and Morris, R.C. (Eds.), Iron-formation: Facts and problems, Elsevier, New York, 417-469.

Large, D. (1988). The evaluation of sedimentary basins for massive sulphide mineralization. In Friedrich, G.H. and Herzig, P.M. (Eds.), Base metal sulphide deposits, Berlin Heidleberg, 3-11.

Large, D.E. (1981). Sediment-hosted submarine exhalative lead-zinc deposits- a review of their geological characteristics and genesis. In Wolf, K.H. (Ed.), Handbook of strata bound and stratiform ore deposits. Elsevier, Amsterdam, 9, 469-507.

Large, R.R. (1992). Australian volcanic hosted massive sulphide deposits: Features styles and genetic models. Econ. Geol., 87, 471-510.

Lipson, R.D. (1978). Some aspects of the geology of part of the Aggeneysberge and the surrounding gneisses, Namaqualand. Unpubl. MSc. thesis. Univ. Witwatersrand. 100pp.

Lipson, R.D. (1980). The granitic rocks surrounding the Aggeneysberge: a metamorphosed rapakivi suite?. Trans. of the Geol. Soc. of S. Africa, 83, 179-192.

Lipson, R.D. (1990). Lithogeochemistry and origin of metasediments hosting the Broken Hill Deposit, Aggeneys, South Africa, and implications for ore genesis. Unpubl. Ph.D. thesis, Univ. Cape Town, 250pp.

Lipson, R.D. Martin, G.J. and Hobbs, J.B.M. (1986). Heavy mineral layers: evidence of a clastic origin for Bushmanland quartzite genesis at Aggeneys. Trans. of the Geol. Soc. of S.Africa, 89, 367-372.

Marshall, B. (1990). "Psuedostratigraphy" and thrusting in relation to the structural evolution of the Joma Ore-body, North Trondelag, Norway. Ore. Geol. Rev., 5, 175-210.

Mansker, W.L., Ewing R.C. and Keil, K. (1979). Barian-titanian biotites in nephelinites from Oahu, Hawaii. Am. Mineral., 64. 156-159.

Marchig, V., Grundlach, H., Moller, P and Schley, F. (1982). Some geochemical indicators for discrimination between diagenetic and hydrothermal metalliferous sediments. Marine Geol., 50, 241-256.

Marchig, V. and Grundlach, H. (1982). Iron-rich metalliferous sediments on the East Pacific Rise: prototype of undifferentiated metalliferous sediments on divergent plate boundaries., Erth. and Plan. Sci. Let., 58, 361-382.

Miyano, T. and Klein, C. (1983). Phase relations of orthopyroxene, olivine, and grunerite in high-grade metamorphic iron formation. Am. Mineral., 68, 699-716.

Miyano, T. and Klein, C. (1986). Fluid behaviour and phase relations in the system Fe-Mg-Si-C-O-H: application to high grade metamorphism of iron-formations. Am. Jour. Sci., 286, 540-575.

Miyano, T. and Klein, C. (1989). Phase equilibria in the system K_2O-FeO-MgO-Al_2O_3-SiO_2-H_2O-CO_2 and the stability limit of stilpnomelane in metamorphosed Precambrian iron-formations. Contrib. Miner. Petrol., 102, 478-491.

Moore, J.M. (1977). The geology of Namiesberg, northern Cape. Bull. Precamb. Res. Unit, Univ. Cape Town, 20, 69pp.

Moore, J.M. (1989). A comparative study of metamorphosed supracrustal rocks from the western Namaqualand Metamorphic Complex. Bull. Precamb. Res. Unit, Univ. Cape Town, 37, 370pp.

Moore, J.M. and Reid, A.M. (1988). Implications of sphalerite inclusions in gahnite from Namaqualand Metamorphic Complex, South Africa. Can. Mineral., 26, 293-300.

Moore, J.M. and Reid, A.M. (1989). A Pan-African zincian staurolite imprint on Namaqua quartz-gahnite-sillimanite assemblages. Min. Mag., 53. 63-70.

Moore, J.M., Watkeys, M.K., and Reid, D.L. (1990). The regional setting of the Aggeneys/Gamsberg base metal deposits Namaqualand, South Africa. In: Spry and Bryndzia (Eds.), Regional Metamorphism of Ore Deposits, 77-95.

Mourant, D. and Smith, P. (1986). Addendum to the paper by Ryan et al. (1985) on the Aggeneys base metal sulphide deposits, Namaqualand district. In: Anhaeusser, C.R. and Maske, S. (Eds.), Mineral Deposits of Southern Africa, Geol. Soc. S. Africa., II, 1475.

Munoz, J.W. (1984). F-OH and Cl-OH exchange in micas with applications to hydrothermal deposits. Reviews in Mineralogy, 13, 469-544.

National Geoscience Program. (1987). Abstracts, Progress reports 1987, 197pp.

Neiva, A.M.R. (1974). Geochemistry of tourmaline (schorlite) from granites, aplites and pegmatites from northern Portugal. Geochem. Cos. Acta, 38, 1307-1317.

Nel, C.J., Beukes, N.J. and De Villiers, J.P.R. (1986). The Mamatwan manganese mine of the Kalahari manganese field. In: Anhaeusser, C.R. and Maske, S. (Eds.), Mineral Deposits of Southern Africa, Geol. Soc. S. Africa., II, 963-978.

Norrish, K. and Hutton, J.T. (1969). An accurate X-ray spectrographic method for the analysis of a wide range of geological samples. Geochem. Cos. Acta, 33, 431-453.

Ohmoto, H. and Kerrick, D. (1977). Devolatilization equilibria in graphite schists. Am. Jour. Sci., 277, 1013-1044.

Pattiaratchii, D.B., Soari, E. Sahama, Th. G. (1967). Anandite, a new barium silicate from Wilagedra, North Western Province, Ceylon. Min. Mag., 36, 1-4.

Perkins, B. (1991). Mount Isa Lead-Zinc orebodies. Base metal deposit symposium. Extended Abstract. EGRU, James Cook University, North Queensland, 38, 43-45.

Plimer, I.R. (1983). The association of B- and F-rich rocks with stratiform mineralization. Course notes, Univ. Witwatersrand, Johannesburg, 109pp.

Plimer, I.R. (1984). The role of fluorine in submarine exhalative systems with special reference to Broken Hill, Australia. Mineral. Deposita, 19, 19-25.

Postma, D. (1985). Concentration of Mn and separation from Fe in sediments.: 1. Kinetics and stoitiometry of the reaction between birnessite and dissolved Fe (II) at 10 ^{0}C. Geochem. Cos. Acta, 49, 1023-1033.

Power, G.M. (1968). Chemical variation in tourmalines from south-west England. Min. Mag., 36, 1078-1089.

Praekelt, H.E., Colliston, W.P. and Schoch, A.E. (1983). The stratigraphic interpretation of a highly deformed Proterozoic region in Central Bushmanland, South Africa: First correlation of structurally separated metasediments of the Aggeneys Subgroup. Precamb. Res., 23, 177-185.

Praekelt, H.E., Botha, B.J.V and Malherbe, S.J. (1986). Diskrete korsfragmente in die sentrale gedeelte van die Namakwagordel in die omgewing van Augrabies. Ann. Geol. Surv. S. Africa, 20, 25-40.

Reid, D.L. (1979). Total rock Rb-Sr and U-Th-Pb isotopic study of Precambrian metavolcanic rocks in the lower Orange River Region, Southern Africa. Erth and Plan. Sci Letters, 42, 368-378.

Reid, D.L. (1982). Age relationships within the Vioolsdrif batholith, lower Orange River region. II. A two stage emplacement history and the extent of Kibaren overprinting. Trans. Geol. Soc. S. Afr., 105-110.

Reid, D.L. and Barton, E.S. (1983). Geochemical characterization of granitoids in the Namaqualand geotraverse. Spec. Publ. Geol. Soc. S. Afr., 10, 67-82.

Reid, D.L., Welke, H.J., Erlank, A.J. and Moyes, A. (1987a). The Orange River Group: a major Proterozoic calc-alkaline volcanic belt in the western Namaqua Province, southern Africa. In: Pharoah, T.C., Beckinsale, R.D. and Rickard, D. (Eds.), Geochemistry and Mineralization of Proterozoic Volcanic Suites, Spec. Publ. Geol. Soc., 33, 327-346.

Reid, D.L., Welke, H.J., Erlank, A.J. and Betton, P.J. (1987b). Composition, age and tectonic setting of amphibolites in the central Bushmanland Group, western Namaqua Province, South Africa. Precamb. Res., 36, 99-126.

Ripa, M. (1988). Geochemistry of wall-rock alteration and mixed volcanic-exhalative facies at the Proterozoic Stolberg Fe-Pb-Zn-Mn-(Ag)-deposit, Bergslagen, central Sweden. Geol. Mijnbouw, 67, 443-457.

Robinson, P., Spear, F.S., Schumacher, J.C., Laird, J., Klein, C. Evans, B.W. and Doolan, B.L. (1982). Phase relations of metamorphic amphiboles: natural occurrence and theory. In: Veblen, D.R. and Ribbe, P.H. (Eds.) Amphiboles. Reviews Mineralogy, 9B, 1-65.

Rozendaal, A. (1975). Geological structure of Gamsberg zinc deposit, Namaqualand, South Africa. Ann. Univ. Stell., 2, 1-32.

Rozendaal, A. (1978). The Gamsberg zinc deposit, Namaqualand. In: Verwoed, W.J. (Ed.), Mineralization in metamorphic terranes, Schaik, Pretoria, 235-268.

Rozendaal, A. (1982). The petrology of the Gamsberg zinc deposit and the Bushmanland iron formations with special reference to their relationships and genesis. Unpubl. Ph.D thesis, Univ. Stellenbosch, 349p.

Rozendaal, A. and Stumpfl, E.F. (1984). Mineral chemistry and genesis of Gamsberg zinc deposit, South Africa. Trans. Instn. Min. Metall. (Sect. B:), 93, 161-174.

Russell, M.J., Solomon, M. and Walshe, J.L. (1981). The genesis of sediment- hosted, exhalative zinc + lead deposits. Mineral. Deposita, 16, 118-127.

Ryan, P.J., Lawrence, A.L., Lipson, R.D., Moore, J.M., Paterson, A., Stedman, D.P. and van Zyl, D. (1986). The Aggeneys Base Metal Sulphide Deposits, Namaqualand, South Africa. In: Anhaeusser, C.R. and Maske, S. (Eds.), Mineral Deposits of Southern Africa, Geol. Soc. S. Africa., II, 1447-1473.

SACS (South African Committee for Stratigraphy) (1980). Stratigraphy of South Africa (comp. L.E. Kent). Handb. Geol. Surv. S. Africa, 8, 690pp.

Sawkins, F.J. (1984). Ore genesis by episodic dewatering of sedimentary basins. Application to giant Proterozoic lead-zinc deposits. Geology,

Saxena, S.K. (1969). Silicate solid-solution and geothermobarometry. 3-Distribution of Fe and Mg between coexisting garnet and biotite. Contrib. Mineral. Petrol., 22, 259-267.

Scherp, A. and Strubel, G. (1974). Zur barium-strontium mineralisation. Mineral. Deposit. (Berl.), 9, 155-168.

Scott, S.D. (1973). Experimental calibration of the sphalerite geobarometer. Econ. Geol., 68, 466-474.

Scott, S.D. (1976). Application of the sphalerite geobarometer to regionally metamorphosed terrains. Am. Mineral., 61, 661-670.

Simmons, E.C, Lindsley, D.H. and Papike, J.J. (1974). Phase relations and crystallization sequence in a contact-metamorphosed rock from the Gunflint Iron Formation, Minnesota. J. Petrol., 15, 539-565.

Sisson, V.B. (1987). Halogen chemistry as an indicator of metamorphic fluid interaction with the Ponder pluton, Coast Plutonic Complex, British Columbia, Canada. Contrib. Mineral. Petrol., 95, 123-131.

Smith, P. (1986). The geology of the Broken Hill Pb-Ag-Zn-Cu deposit. Extend. Abstr. Geocongress '86, 881-884.

Smith, P. (1989). Base metal zoning at Broken Hill, Aggeneys. Unpubl. company report.

Solie, D.N. and Su, S. (1987). An occurrence of Ba-rich micas from the Alaska Range. Am. Mineral., 72. 995-999.

Spear, F.S. (1991). On the interpretation of peak metamorphic temperatures in the light of garnet diffusion during cooling. Jour. Met. Geol., 9, 379-388.

Spear, F.S. and Cheney, J.T. (1989). A petrogenetic grid for pelitic schists in the system SiO_2-Al_2O_3-FeO-MgO-K_2O-H_2O. Contrib. Mineral. Petrol., 101, 149-164.

Spry, A. (1976). Metamorphic Textures. Pergamon, Australia, 350pp.

Spry, P.G. (1982). An unusual gahnite-forming reaction, Geco base-metal deposit, Manitowadge, Ontario, Can. Mineral., 20, 549-553.

Spry, P.G. (1987). The chemistry and origin of zincian spinel with the Aggeneys Cu-Pb-Zn-Ag deposits, Namaqualand, South Africa. Mineral. Deposita, 22, 262-268.

Spry, P.G. and Petersen, E.U. (1989). Zincian hogbomite as an exploration guide to metamorphosed massive sulphide deposits. Min. Mag., 53, 263-269.

Spry, P.G. and Scott, S.D. (1986). The stability of zincian spinels in sulphide systems and their potential as exploration guides for metamorphosed massive sulphide deposits. Econ. Geol., 81, 1446-1463.

Spry, P.G. and Wonder, J.D. (1989). Manganese-rich garnet rocks associated with the Broken Hill lead-zinc-silver deposit, New South Wales, Australia. Can. Mineral., 27, 275-292.

Stanton, R.L. (1976). Petrochemical studies of the ore environment at Broken Hill, New South Wales: 2-regional metamorphism of banded iron formations and their immediate associates. Inst. Min. Metall. (Sect. B:), 118-131.

Stanton, R.L. and Williams, K.L. (1978). Garnet compositions at Broken Hill, New South Wales, as indicators of metamorphic processes. Jour. Petrol., 19, 514-529.

Stedman, D.P. (1980). The structural geology and metamorphic petrology of Black Mountain. Unpubl. MSc. thesis. Univ. Witwatersrand. 169pp.

Stevenson, R.K. and Martin, R.F. (1986). Implications of the presence of amazonite in the Broken Hill and Geco metamorphosed sulphide deposits. Can. Mineral., 24, 729-745.

Stowe, C.W. (1983). The Upington Geotraverse and its implications for craton margin tectonics. Spec. Publ. Geol. Soc. S. Afr., 10, 147-171.

Strydom, D. and Visser, J.N.J. (1986). Nappe structures in the Highly deformed Proterozoic metasedimentary Aggeneys-type sequence of western Bushmanland, South Africa. Precamb. Res., 33, 171-187.

Stumm, E. and Morgan, J.J. (1981). Aquatic chemistry. 2nd ed. Wiley-Interscience, New York, 780pp.

Stumpfl, E.F. (1979). Manganese haloes surrounding metamorphic stratabound base metal deposits. Mineral. Deposita, 14, 207-217.

Sugisaki, R., Sugitani, K and Adachi, M. (1991). Manganese carbonate bands as an indicator of hemipelagic sedimentary environments. Jour. Geol., 99, 23-40.

Taylor, B.E. and Slack, J.F. (1984). Tourmalines from Appalachian-Caledonian massive sulphide deposits: textural, chemical and isotope relations. Econ. Geol., 79, 1703-1726.

Theart, H.F.J. (1980). The geology of the Precambrian terrane in parts of Western Namaqualand. Bull. Precamb. Res. Unit, Univ. Cape Town, 30, 103pp.

Thompson, A.B. (1976). Mineral reactions in pelitic rocks II. Calculation of some P-T-X (Fe-Mg) phase relations. Am. Jour. Sci., 276, 425-454.

Toogood, D.J. (1976). Structural and metamorphic evolution of a gneiss terrain in the Namaqua Belt near Onseepkans, South West Africa. Bull. Precamb. Res. Unit, Univ. Cape Town, 19, 189pp.

Toth, J.R. (1980). Deposition of submarine crusts rich in manganese and iron. Bull., Geol. Soc. Am., 91, 44-54.

Valley, J.W. and Essen, E.J. (1980). Calc-silicate reactions in Adirondack marbles: The role of fluids in solid solutions. Geol. Soc. Am. Bull., 91, 114-117, 720-813.

Van Aswegen, G. (1983). The Gladkop Suite - the grey and pink gneisses of Steinkopf. Spec. Publ. Geol. Soc. S. Afr., 10, 31-44.

van Aswegen, G., Strydom, D., Colliston, Praekelt, H.E., W.P., Schoch, A.E., Blignault, H.J., Botha, B.J.V. (1987). The structural-stratigraphic development of part of the Namaqualand Metamorphic Complex- an example of Proterozoic major thrust zones. In: Kroner, A. (Ed.), Proterozoic Lithospheric Evolution. Amer. Geophys. Union Geodynamics Ser., 17, 207-216.

Vaniman, D.T., Papike, J.J. and Labotka, T. (1980). Contact-metamorphic effects of the Stillwater Complex, Montana:the concordant iron formation Am. Mineral., 65, 1087-1102.

Vaughan, J.P. and Stanton, R.L. (1986). Sedimentary and metamorphic factors in the development of the Pegmont stratiform Pb-Zn deposit, Queensland, Australia. Trans. Instn. Min. Metall. (Sect. B:), 95, 94-121.

Von Gehlen, K., Nielsen, H., Chunnet, I. and Rozendaal, A. (1983). Sulphur isotopes in metamorphosed Precambrian Fe-Pb-Zn-Cu sulphides and baryte at Aggeneys and Gamsberg, South Africa. Min. Mag., 47, 481-486.

Waters, D.J. (1986). Metamorphic zonation and thermal history of pelitic gneisses from western Namaqualand, South Africa. Trans. of Geol. Soc. of S. Africa, 89, 80-102.

Waters, D.J. (1987). Open and closed system metamorphism in Bushmanland. Abstr. National Geoscience Programme Progress Reports. NGP Secretariat, Pretoria, 61-70.

Waters, D.J. (1988). Partial melting and the formation of granulite facies assemblages in Namaqualand, South Africa. J. of Met. Petrol., 6, 1-19.

Waters, D.J. (1989). Metamorphic evidence for the heating and cooling of Namaqualand granulites. In: Daly, J.S., Cliff, R.A. and Yardley, B.W.D. (Eds.), Evolution of Metamorphic Belts, Geol. Soc. Spec. Publ., 43, 357-363.

Waters, D.J. and Whales C.J. (1984). Dehydration melting and the granulite transition in metapelites from southern Namaqualand, S. Africa. Contrib. Mineral. Petrol., 88, 269-275.

Watkeys, M.K. (1986). The Achab Gneiss: a "floor" in Bushmanland or a flaw in Namaqualand? Trans. of Geol. Soc. of S. Africa, 89, 98-103.

Watkeys, M.K., Moore, J.M. and Duncan, A.R. (1988). The pink gneiss of Bushmanland: Mid. Proterozoic felsic pyroclastics. Abstr. Geocongress 1987, Univ. Natal, Durban, 717-720.

Welke, H.J., Burger, A.J., Corner, B., Kroner, A. and Blignault, H.J. (1979). U-Pb and Rb-Sr age determinations on middle Proterozoic rocks from the lower Orange River region, south-western Africa. Trans. Geol. Soc. S. Afr., 82, 205-214.

Welke, H.J. and Smith, C.B. (1984). Lead isotope characterization of the Aggeneys-Gamsberg ore bodies in relation to possible source rocks, with implications for Bushmanland metallogenesis. Abs. Conf. on Middle to Late Proterozoic Crustal Evolution, Precamb. Res. Unit. Univ. Cape Town, 8-9.

Williams, M.L. and Grambling, J.A. (1990). Manganese, ferric iron, and the equilibrium between garnet and biotite., Am. Mineral., 75, 889-908.

Williams, N. (1991). Sediment-hosted stratiform Pb-Zn deposits. Base metal deposit symposium. Extended Abstract. EGRU, James Cook University, North Queensland, 38, 46-50.

Wilner, A., Schreyer, W. and Moore, J.M. (1990). Peraluminous metamorphic rocks from the Namaqualand Metamorphic Complex (South Africa): Geochemical evidence for an exhalation-related, sedimentary origin in a Mid-Proterozoic rift system. Chem. Geol., 81, 221-240.

Wood, B.J. and Walter, J.V. (1986). Fluid-rock interactions. Developments in Physical Interactions, 5, 89-108.

Wonder, J.D., Spry, P.G. and Windom, K.E. (1988). Geochemistry and origin of manganese-rich rocks related to iron-formation and sulphide deposits, western Georgia, Econ. Geol., 83, 1070-1081.

Yoshii, M., Maeda, K., Kato, T., Watanabe, T., Yui, S., Kato, A. and Nagashima, K. (1973). Kinoshitalite, a new mineral from the Noda-Tamagwa mine, Iwate Prefecture, Chigaku Kenkyu, 24, 181-190 (not seen; abstracted in Am. Mineral., 60, 486-487, 1975).

Yoshii, M. and Maeda, K. (1975). Relations between barium content and the physical and optical properties in the manganoan phlogopite-kinoshitalite series. Min. Jour. 8, 58-65.

Zaw, U.K. and Clark, A.H. (1978). Fluoride-hydroxyl ratios of skarn silicates. Catung E-zone scheelite ore-body, Tungsten, Northwest territories. Can. Mineral., 16, 207-221.

Zhu, C. and Sverjensky, D.A. (1991). Partitioning of F-Cl-OH between minerals and hydrothermal fluids. Geochem. et Cos. Acta, 55, 1837-1858.

APPENDIX A
ANALYTICAL TECHNIQUES

Whole Rock XRF Analysis

Major and trace element concentrations of whole rock samples were determined by X-ray fluorescence (XRF) spectroscopic technique in use in the Department of Geochemistry at the University of Cape Town. These techniques have been summarized below.

Whole rock samples with masses of 750 to 1000 g were crushed, grinded and sieved to reduced powder samples to less than 300 # grain-size. All samples were fresh and no effects of weathering were observed in those collected.

MAJOR ELEMENTS

Major element concentrations were determined on duplicate Norrish fusion glass discs using the method of Norrish and Hutton (1969). Powder samples (0.28 g) were fused with 1.5 g of a lithium borate flux (Spectroflux 105) and minor $NaNO_3$ (0.02 g). Prior to the preparation of the discs, volatile constituents were estimated by first drying for 12 hours at 110 ^{0}C for H_2O^- and then ashing for the same period at 950 ^{0}C for the Loss on Ignition (LOI). The ashed samples were fused in Pt-Au crucible and the cast in a carbon mold. Major element concentrations were determined using the Siemens SRS-1 XRF spectrometer. Detection limits (LLD) and average absolute error determined by the on-line computer facility for the major elements are given in Table A1. Calculation of matrix correction factors for the major elements were applied using the technique of Norrish and Hutton (1969). Data are reported in Appendix D with total Fe recalculated as FeO.

TRACE ELEMENTS

Two 6 g powder samples were used to prepare powder duplicate briquettes. Trace element concentrations determined for multiple analytical cycles (pellet A and B) were added together and averaged. The difference between element concentrations was small for each analytical cycle indicating sample homogeneity and constancy in the XRF results. Matrix correction factors were applied and spectral interferences between elements were corrected using the techniques of Norrish and Hutton (1969). Average analytical counting errors and lower limits

Table A.1. Average absolute counting errors and detection limits for major element analyses by XRF.

OXIDE	AVERAGE ABSOLUTE ERROR	DETECTION LIMIT
SiO_2	0.316	0.015
TiO_2	0.023	0.006
Al_2O_3	0.193	0.012
FeO	0.101	0.009
MnO	0.010	0.006
MgO	0.095	0.013
CaO	0.053	0.004
Na_2O	0.075	0.020
K_2O	0.029	0.003
P_2O_5	0.009	0.004

of detection are shown in Table A2. Trace element concentrations were determined using the Phillips PW1400 and data are listed in Appendix D.

MINERAL ANALYSES

Mineral chemistries of individual grains in 2 x 4 cm slides were analysed with the Cameca 1100 electron microprobe at the University of Cape Town. Nominal concentrations were corrected for by the on-line reduction facility for Fe-rich samples using the method of Bence and Albee (1968).

Operating conditions

Accelerating Voltage: 15 kV

Beam Current: 40 nA

Beam Focus: Beam focused at 2 microns for all minerals except micas, for which it was defocussed to 5 microns.

Table A.2. Average counting errors (ERR) values and the lower limit of detection (LLD) of trace elements for the XRF analyses.

ELEMENT	LLD	ERR
Co	3.70	1.34
V	3.06	1.15
Cr	2.64	0.99
La	3.37	1.20
Ce	7.33	2.53
Nd	4.11	1.40
Ba	2.44	2.12
Sc	0.72	0.29
Zn	2.10	2.89
Cu	3.00	1.16
Ni	1.72	1.33
Mo	0.85	0.29
Y	1.34	0.47
Rb	1.33	0.47
Nb	1.02	0.35
Sr	1.16	0.41
Th	4.06	1.35
Zr	1.13	0.48
U	2.48	0.83
Pb	4.10	4.30
S	9.28	7.58

Counting Time: 10 seconds

30 seconds for Ba, Zn, F and Cl in some micas

Analysing Crystals: LIF (200) for elements Fe, Mn.

PET for elements Ca, K, Ti, Cr.

TLAP for elements Si, Al, Mg, Na.

Calibration Standards

The calibration standards used for the EMP analyses are shown in Table A.3.

Standards Used

The calibration standards use for the different mineral analyses are given in Table A4.

Lower limits of detection

The LLD for electron microprobe analyses are shown in Table A5.

Table A.3. Table of calibration standards used in the EMP analyses.

Abbreviation	Standard	Type
CHRO	Stillwater chromite	Natural
FLUR	Fluorite	Natural
K-P	Kakunui pyrope	Natural
K-H	Kakunui hornblende	Natural
RHOD	Rhodonite	Synthetic
RUT	Rutile	Synthetic
GAHN	Gahnite	Natural
ILMT	Ilmenite	Natural
CHAL	Chalcopyrite	Natural
SPHA	Sphalerite	Natural
MN	Metal	Natural
NISI	Ni/Si glass	Synthetic
BASI	Ba/Si glass	Synthetic
M-Ol	Marjalahti	Natural
SCAP	Scapolite	Natural
SM-3	Troilite	Natural

Table A.4. Standards used for the elements of the silicate, oxide and sulphide minerals.

MINERAL	ELEMENT	STANDARD
Garnet	Si, Al, Mg, Ca	K-P
	Ti	RUT
	Cr	CHRO
	Mn	RHOD
	Na	K-H
Amphibole	Si, Al, Ca, Mg, Fe,	K-H
	K, Na	K-H
	Ti	RUT
	Mn	RHOD
	Cr	CHRO
Olivine	Si, Fe, Mg	M-OL
Pyroferroite	Al, Ca	K-P
	Ti	RUT
	Cr	CHRO
	Ni	NISI
Micas	Si, Al, Fe, Mg, Ca,	K-H
Tourmaline	Na, K	K-H
	Ti	RUT
	Mn	RHOD
	Cr	CHRO
	Ba	BASI
	F	FLUR
	Cl	SCAP
Spinels	Si	K-P
Magnetite	Al, Zn	GAHN
	Mg, Cr	CHRO
	Fe	ILMT
	Mn	RHOD
	Ti	RUT
	Ni	NISI
Sphalerite	S, Cu	CHAL
	Zn	SPHA
	Fe	SM-3
	Mn	MN

The types of standards are given in Table A.3.

Table A.5. Typical lower detection limits of elements for the various mineral analyses.

	GARNET	OLIV.	AMPH.	MICA	TOURM.	SPINEL	SPHAL.
Si	.041	.048	.042	.049	.045	.045	
Ti	.039	.043	.039	.044	.039	.044	
Al	.036	.038	.033	.041	.041	.047	
Cr	.043	.000	.044	.000	.000	.049	
Fe	.079	.092	.073	.087	.075	.076	.07
Mn	.067	.073	.067	.083	.050	.073	.06
Mg	.025	.038	.027	.031	.029	.033	
Ca	.026	.031	.028	.030	.030	.031	
Na	.031		.035	.035	.038		
K			.023	.026	.023		
Ba				.167			
F				.160	1.190		
Cl				.025			
Ni		.104				.098	
Zn						.168	.16
Cu							.12
S							.04

APPENDIX B

Calculations for sphalerite geobarometry

For the pyrite-pyrrhotite equilibrium, it is possible to calculate a(FeS), provided $f(S_2)$ and ΔG^0 are known, using the expression of Froese and Gunter (1976):

$\Delta G^0 = -RT\ln K = RT[\ln a(FeS) + 1/2 \ln f(S_2)]$ .....Equ. (1)

where $\Delta G^0 = -36774 + 36.006T(^0K)$

for 670 ^0C then $\Delta G^0 = -2820$

For the equilibrium of pyrrhotite and sulphur vapour, Froese and Gunter (1976) use the following expression:

$\square S$ (pyrrhotite) = 1/2 S (in vapour)

$\ln K = 1/2 \ln f(S_2) - \ln (1-X_{FeS}) - \ln \gamma_{\square S}$

where X_{FeS} is the mole fraction of FeS in pyrrhotite

$RT\ln K = -\Delta G^0(2) = 1/2RT\ln f(S_2) - RT\ln(1-X_{FeS}) - RT\ln \gamma_{\square S}$ .....Equ.(2)

where $\Delta G^0(2) = -57966 + 34.824T = -25127$

and $RT\ln \gamma_{\square S} = (2 G^{\infty}_{Fes} - G^{\infty}_{\square S}) X^2_{FeS} + 2(G^{\infty}_{\square S} - G^{\infty}_{Fes}) X^3_{FeS}$

where $G^{\infty}_{Fes} = -141563 + 126.825 = -21967$

and $G^{\infty}_{\square S} = -93911 + 59.250 = -38038$

using $X_{FeS} = 0.847$ for pyrrhotite after DeWaal and Johnson (1981)

$RT\ln \gamma_{\square S} = -23761$

substituting $RT\ln \gamma_{\square S}$ and $\Delta G^0(2)$ into Equ. (2)

$\ln f(S_2) = -2.297$

therefore a(FeS) for pyrite-pyrrhotite equilibrium = 0.700 from Equ. (1)

APPENDIX C

SAMPLE LOCATIONS

Table C.1. Table showing sample locations.

SAMPLE	ROCK TYPE	LOCATION/ BORE HOLE	X-COORD	Y-COORD	Z-COORD
BHG1	IF	15-600-04E	35935	20510	406
BHG2	IF	13-700-01	36005	20642	470
BHF3	P	13-700-10	35955	20783	502
BHA5	IF	6-1185-06E	36267	21135	715
BHG6	IF	6-1185-06E	36267	21135	715
BHA7	IF	15-600-04E	35950	20500	406
BHA8	IF	15-600-04E	35950	20500	406
BHA9	IF	15-600-04E	36005	20642	470
BHA10	IF	15-600-O4E	35985	20455	406
BHA11	IF	15-600-04E	35985	20459	406
BHA12	IF	6-1100-06W	36290	21113	719
BHG13	IF	6-1100-06W	36290	21113	53
BHF14	P	11-700-03W	36020	20840	719
BHMM15	IF	13-700-10W	36047	20708	506
BHG15	IF	13-700-11	35960	20769	502
BHG16	IF	13-700-11	36088	20695	506
BHG17	IF	5-1200-09	36326	21145	763
BHA18	IF	15-600-04	35950	20405	406
BHA19	IF	15-600-06	35910	20385	406
BHS22	S	BHU2590-N13	35897	20125	289
BHGQ23	GQ	13-700-11	36077	20710	506
BHA25	IF	13-700-11	36050	20710	506
TS1	IF	13-700-10W	36000	20780	502
TS2	IF	13-600-10E	36140	20600	502
TS3	IF	11-700-02W	35985	20828	531
TS4	IF	15-600-03	35942	20425	402
TS5	MSR	5-1200-09	36345	21105	759
TS6	IF	6-1185-05W	36118	21245	715
TS7	IF	BHU2609-13	35839	19985	230
TS8	IF	13-600-10W	36125	20625	502
TS9	MSR	13-600-10E	36140	20600	502
TS10	IF	15-600-03	35955	20425	402

TS11	MSR	8-1100-06	36145	21080	655
TS12	MSR	BHU2609-11	35835	19985	233
TS13	GQ	BHU2609-03	35824	19985	247
TS14	FQ	BHU2609-N9	35817	19985	255
TS15	IF	BHU2609-06	35828	19985	241
BH1	MS	13-700-10W	36000	20790	502
BH2	IF	8-1100-08W	36142	21085	665
BH3	S	8-1100-08W	36149	21069	665
BH4	MSR	6-1185-07W	36195	21230	725
BH5	IF	6-1185-07W	36195	21230	725
1782-25	IF	BHU1782-25	35840	20445	320
1782-26	GQ	BHU1782-26	35842	20445	316
1917-8	IF	BHU1917-8	36109	20825	549
1917-N5	Q	BHU1917-N5	36121	20825	542
1917-N6	S	BHU1917-N6	36122	20825	541
1917-10	IF	BHU1917-10	36112	20825	547
1917-13	MSR	BHU1917-13	36117	20825	545
1917-N2	GQ	BHU1917-N2	36100	20825	554
2609-N7	S	BHU2609-N7	35793	19985	281
2609-8	IF	BHU2609-8	35832	19985	235
1891-8	IF	BHU1891-8	36014	20565	660
1891-13	IF	BHU1891-13	36018	20565	671
1891-11	IF	BHU1891-11	36018	20565	665
1891-6	IF	BHU1891-6	36013	20565	657

IF - iron formation (undifferentiated)
MSR - massive sulphide rock
GQ - garnet quartzite
FQ - ferruginous quartzite
S - schist (undifferentiated)
P - pegmatite
Q - quartzite

APPENDIX D

ELECTRON MICROPROBE ANAYLSES

GARNET

Cations calculated on the basis of 24 oxygens.
c-core composition
r-rim composition

	BHG1 1C	BHG1 2C	BHG1 3C	BHG1 4C	BHG1 5C	BHG13 1C	BHG13 1R	BHG13 2C	BHG13 3C	BHG1 4C
SiO_2	36.66	36.89	36.80	36.87	36.56	36.47	36.31	36.64	36.59	35.91
Al_2O_3	20.86	20.66	20.73	20.44	20.99	20.02	20.11	20.14	20.02	19.82
FeO	23.00	23.49	23.06	23.37	23.08	16.92	17.27	17.05	16.88	18.07
MnO	18.66	18.84	18.67	18.68	19.08	26.41	26.49	26.53	26.72	26.95
MgO	0.72	0.74	0.73	0.75	0.75	0.28	0.27	0.28	0.27	0.27
CaO	0.89	0.79	0.77	0.75	0.76	0.39	0.42	0.42	0.45	0.46
Total	100.79	101.40	100.76	100.86	101.21	100.48	100.85	101.07	100.93	101.47
Si IV	5.97	5.98	5.99	6.01	5.94	6.00	5.96	5.99	5.99	5.89
Al IV	0.03	0.02	0.01	-	0.06	0.00	0.04	0.01	0.01	0.11
T site	6.00	6.00	6.00	6.01	6.00	6.00	6.00	6.00	6.00	6.00
Al VI	3.98	3.93	3.97	3.92	3.96	3.88	3.85	3.87	3.86	3.71
Fe^{+3}	0.03	0.08	0.03	0.08	0.06	0.13	0.16	0.13	0.14	0.31
O site	4.01	4.00	4.00	4.00	4.01	4.00	4.01	4.00	4.00	4.03
Fe^{+2}	3.10	3.10	3.11	3.09	3.07	2.19	2.19	2.18	2.15	2.13
Mn	2.57	2.59	2.58	2.58	2.62	3.68	3.68	3.67	3.71	3.74
Mg	0.17	0.18	0.18	0.18	0.18	0.07	0.07	0.07	0.06	0.07
Ca	0.16	0.14	0.13	0.13	0.13	0.07	0.07	0.07	0.08	0.08
A site	6.00	6.00	6.00	5.98	6.01	6.00	6.01	6.00	6.00	6.02
Alm	51.35	50.99	51.64	51.01	50.64	35.70	35.43	35.62	35.00	33.62
Sps	42.66	42.57	42.75	42.48	43.27	60.02	59.66	59.90	60.31	59.12
Prp	2.90	2.94	2.95	3.02	2.99	1.11	1.05	1.12	1.06	1.05
Grs	2.59	2.25	2.23	2.16	2.17	1.12	1.19	1.21	1.28	1.26
Andr	0.50	1.26	0.44	1.33	0.94	2.05	2.67	2.14	2.35	4.95

	BHG13 4R	BHG13 5C	BHG13 5R	BHG2 1C	BHG2 2C	BHG2 2R	BHG2 3C	BHG4 1C	BHG4 2C	BHG4 3C
SiO_2	35.96	35.58	35.97	36.75	36.75	36.60	36.56	36.90	37.00	37.19
Al_2O_3	20.58	19.30	20.65	20.43	20.48	20.20	20.56	20.45	20.72	20.83
FeO	17.30	17.91	16.84	25.02	24.92	24.92	24.82	29.06	28.34	28.66
MnO	27.01	26.36	26.21	17.64	17.80	17.69	17.68	13.97	13.91	13.59
MgO	0.27	0.26	0.28	0.30	0.33	0.35	0.33	1.13	1.12	1.05
CaO	0.44	0.43	0.37	0.66	0.79	0.66	0.68	0.40	0.36	0.36
Total	101.58	99.85	100.32	100.79	101.07	100.42	100.62	101.91	101.46	101.66
Si IV	5.87	5.92	5.92	6.01	6.00	6.01	5.99	5.96	5.99	6.00
Al IV	0.13	0.08	0.08	-	0.00	-	0.01	0.04	0.01	-
T site	6.00	6.00	6.00	6.01	6.00	6.01	6.00	6.00	6.00	6.00
Al VI	3.83	3.71	3.93	3.94	3.93	3.91	3.96	3.85	3.94	3.96
Fe^{+3}	0.20	0.31	0.09	0.07	0.07	0.10	0.05	0.16	0.06	0.04
O site	4.03	4.02	4.02	4.01	4.00	4.01	4.00	4.01	4.00	4.00
Fe^{+2}	2.14	2.15	2.22	3.34	3.32	3.31	3.35	3.75	3.76	3.82
Mn	3.73	3.72	3.66	2.44	2.46	2.46	2.45	1.91	1.91	1.86
Mg	0.07	0.07	0.07	0.07	0.08	0.08	0.08	0.27	0.27	0.25
Ca	0.08	0.08	0.07	0.12	0.14	0.12	0.12	0.07	0.06	0.06
A site	6.02	6.01	6.01	5.98	6.00	5.98	6.00	6.01	6.00	6.00
Alm	34.40	34.06	36.44	55.32	54.76	54.59	55.36	60.90	62.03	63.37
Sps	60.06	58.83	59.94	40.42	40.53	40.53	40.55	31.01	31.42	30.78
Prp	1.07	1.03	1.11	1.20	1.32	1.39	1.34	4.42	4.46	4.18
Grs	1.25	1.21	1.07	1.92	2.26	1.91	1.98	1.13	1.03	1.03
Andr	3.22	4.87	1.44	1.14	1.13	1.58	0.77	2.53	1.07	0.65

	BHG1 1C	BHG1 2C	BHG1 3C	BHG1 4C	BHG1 5C	BHG13 1C	BHG13 1R	BHG13 2C	BHG13 3C	BHG1 4C
SiO_2	36.66	36.89	36.80	36.87	36.56	36.47	36.31	36.64	36.59	35.91
Al_2O_3	20.86	20.66	20.73	20.44	20.99	20.02	20.11	20.14	20.02	19.82
FeO	23.00	23.49	23.06	23.37	23.08	16.92	17.27	17.05	16.88	18.07
MnO	18.66	18.84	18.67	18.68	19.08	26.41	26.49	26.53	26.72	26.95
MgO	0.72	0.74	0.73	0.75	0.75	0.28	0.27	0.28	0.27	0.27
CaO	0.89	0.79	0.77	0.75	0.76	0.39	0.42	0.42	0.45	0.46
Total	100.79	101.40	100.76	100.86	101.21	100.48	100.85	101.07	100.93	101.47
Si IV	5.97	5.98	5.99	6.01	5.94	6.00	5.96	5.99	5.99	5.89
Al IV	0.03	0.02	0.01	-	0.06	0.00	0.04	0.01	0.01	0.11
T site	6.00	6.00	6.00	6.01	6.00	6.00	6.00	6.00	6.00	6.00
Al VI	3.98	3.93	3.97	3.92	3.96	3.88	3.85	3.87	3.86	3.71
Fe^{+3}	0.03	0.08	0.03	0.08	0.06	0.13	0.16	0.13	0.14	0.31
O site	4.01	4.00	4.00	4.00	4.01	4.00	4.01	4.00	4.00	4.03
Fe^{+2}	3.10	3.10	3.11	3.09	3.07	2.19	2.19	2.18	2.15	2.13
Mn	2.57	2.59	2.58	2.58	2.62	3.68	3.68	3.67	3.71	3.74
Mg	0.17	0.18	0.18	0.18	0.18	0.07	0.07	0.07	0.06	0.07
Ca	0.16	0.14	0.13	0.13	0.13	0.07	0.07	0.07	0.08	0.08
A site	6.00	6.00	6.00	5.98	6.01	6.00	6.01	6.00	6.00	6.02
Alm	51.35	50.99	51.64	51.01	50.64	35.70	35.43	35.62	35.00	33.62
Sps	42.66	42.57	42.75	42.48	43.27	60.02	59.66	59.90	60.31	59.12
Prp	2.90	2.94	2.95	3.02	2.99	1.11	1.05	1.12	1.06	1.05
Grs	2.59	2.25	2.23	2.16	2.17	1.12	1.19	1.21	1.28	1.26
Andr	0.50	1.26	0.44	1.33	0.94	2.05	2.67	2.14	2.35	4.95

	BHG13 4R	BHG13 5C	BHG13 5R	BHG2 1C	BHG2 2C	BHG2 2R	BHG2 3C	BHG4 1C	BHG4 2C	BHG4 3C
SiO_2	35.96	35.58	35.97	36.75	36.75	36.60	36.56	36.90	37.00	37.19
Al_2O_3	20.58	19.30	20.65	20.43	20.48	20.20	20.56	20.45	20.72	20.83
FeO	17.30	17.91	16.84	25.02	24.92	24.92	24.82	29.06	28.34	28.66
MnO	27.01	26.36	26.21	17.64	17.80	17.69	17.68	13.97	13.91	13.59
MgO	0.27	0.26	0.28	0.30	0.33	0.35	0.33	1.13	1.12	1.05
CaO	0.44	0.43	0.37	0.66	0.79	0.66	0.68	0.40	0.36	0.36
Total	101.58	99.85	100.32	100.79	101.07	100.42	100.62	101.91	101.46	101.66
Si IV	5.87	5.92	5.92	6.01	6.00	6.01	5.99	5.96	5.99	6.00
Al IV	0.13	0.08	0.08	-	0.00	-	0.01	0.04	0.01	-
T site	6.00	6.00	6.00	6.01	6.00	6.01	6.00	6.00	6.00	6.00
Al VI	3.83	3.71	3.93	3.94	3.93	3.91	3.96	3.85	3.94	3.96
Fe^{+3}	0.20	0.31	0.09	0.07	0.07	0.10	0.05	0.16	0.06	0.04
O site	4.03	4.02	4.02	4.01	4.00	4.01	4.00	4.01	4.00	4.00
Fe^{+2}	2.14	2.15	2.22	3.34	3.32	3.31	3.35	3.75	3.76	3.82
Mn	3.73	3.72	3.66	2.44	2.46	2.46	2.45	1.91	1.91	1.86
Mg	0.07	0.07	0.07	0.07	0.08	0.08	0.08	0.27	0.27	0.25
Ca	0.08	0.08	0.07	0.12	0.14	0.12	0.12	0.07	0.06	0.06
A site	6.02	6.01	6.01	5.98	6.00	5.98	6.00	6.01	6.00	6.00
Alm	34.40	34.06	36.44	55.32	54.76	54.59	55.36	60.90	62.03	63.37
Sps	60.06	58.83	59.94	40.42	40.53	40.53	40.55	31.01	31.42	30.78
Prp	1.07	1.03	1.11	1.20	1.32	1.39	1.34	4.42	4.46	4.18
Grs	1.25	1.21	1.07	1.92	2.26	1.91	1.98	1.13	1.03	1.03
Andr	3.22	4.87	1.44	1.14	1.13	1.58	0.77	2.53	1.07	0.65

	BHG4 4C	BHG6 1C	BHG6 1C	BHG6 1R	BHG6 1R	BHG6 2C	BHG6 2C	BHG6 2R	BHG6 3C	BHG6 3C
SiO_2	37.28	36.69	36.74	36.74	36.80	36.65	36.74	36.81	36.63	36.64
Al_2O_3	20.83	20.47	20.58	20.28	20.44	20.48	20.51	20.14	20.48	20.32
FeO	28.59	21.57	21.78	21.84	22.16	21.26	22.05	21.79	21.61	21.90
MnO	13.55	21.28	21.05	20.88	20.87	21.37	21.13	21.16	21.26	21.05
MgO	1.04	0.26	0.26	0.27	0.26	0.27	0.26	0.26	0.28	0.27
CaO	0.35	-	0.55	-	0.48	-	0.61	-	-	0.51
Total	101.64	100.28	100.97	100.01	101.00	100.03	101.30	100.16	100.27	100.68
Si IV	6.01	6.03	6.00	6.04	6.01	6.03	5.99	6.05	6.02	6.00
Al IV	-	-	0.00	-	-	-	0.01	-	-	0.00
T site	6.01	6.03	6.00	6.04	6.01	6.03	6.00	6.05	6.02	6.00
Al VI	3.96	3.96	3.96	3.93	3.93	3.97	3.92	3.90	3.97	3.92
Fe^{+3}	0.05	0.06	0.04	0.10	0.07	0.05	0.08	0.13	0.05	0.08
O site	4.01	4.02	4.00	4.03	4.00	4.02	4.00	4.03	4.01	4.00
Fe^{+2}	3.80	2.90	2.93	2.89	2.95	2.87	2.92	2.85	2.92	2.91
Mn	1.85	2.96	2.91	2.91	2.89	2.98	2.92	2.94	2.96	2.92
Mg	0.25	0.06	0.06	0.07	0.06	0.07	0.06	0.06	0.07	0.07
Ca	0.06	-	0.10	-	0.08	-	0.11	-	-	0.09
A site	5.96	5.92	6.00	5.87	5.98	5.92	6.00	5.85	5.94	5.99
Alm	63.25	48.51	48.47	48.50	48.68	48.16	47.98	47.55	48.70	48.02
Sps	30.78	49.51	48.18	48.73	47.69	49.93	47.94	49.18	49.39	48.14
Prp	4.17	1.06	1.06	1.12	1.03	1.11	1.03	1.06	1.14	1.07
Grs	0.99	-	1.60	-	1.40	-	1.75	-	-	1.49
Andr	0.80	0.92	0.69	1.65	1.20	0.80	1.29	2.21	0.77	1.29

	BHG6 4C	TS10 1C	TS10 2C	TS10 3C	TS10 4C	TS10 5C	TS10 6C	TS10 7C	TS10 8C	TS10 9C
SiO_2	36.43	35.91	36.66	36.46	36.55	36.54	36.80	37.25	36.47	36.59
Al_2O_3	20.41	20.93	20.79	20.80	20.45	20.30	20.63	20.78	20.39	20.89
FeO	21.30	34.35	34.59	34.65	34.88	35.09	34.94	34.76	34.59	34.97
MnO	21.26	7.63	7.96	7.86	7.77	7.74	7.75	7.73	7.82	7.74
MgO	0.27	0.71	0.60	0.60	0.70	0.70	0.71	0.65	0.57	0.71
CaO	-	0.39	0.41	0.33	0.40	0.39	0.39	0.41	0.38	0.37
Total	99.68	99.92	101.01	100.71	100.76	100.77	101.22	101.57	100.21	101.27
Si IV	6.02	5.92	5.98	5.97	5.98	5.98	5.99	6.02	6.00	5.95
Al IV	-	0.08	0.02	0.03	0.02	0.02	0.01	-	0.00	0.05
T site	6.02	6.00	6.00	6.00	6.00	6.00	6.00	6.02	6.00	6.00
Al VI	3.97	3.99	3.97	3.98	3.92	3.90	3.95	3.96	3.95	3.96
Fe^{+3}	0.04	0.03	0.03	0.03	0.08	0.10	0.06	0.05	0.05	0.05
O site	4.01	4.02	4.01	4.01	4.00	4.00	4.00	4.02	4.00	4.01
Fe^{+2}	2.90	4.70	4.68	4.71	4.68	4.69	4.69	4.64	4.70	4.70
Mn	2.98	1.07	1.10	1.09	1.08	1.07	1.07	1.06	1.09	1.07
Mg	0.07	0.17	0.15	0.15	0.17	0.17	0.17	0.16	0.14	0.17
Ca	-	0.07	0.07	0.06	0.07	0.07	0.07	0.07	0.07	0.06
A site	5.94	6.01	6.00	6.00	6.00	6.00	6.00	5.93	6.00	6.01
Alm	48.51	77.84	77.63	78.10	77.01	76.78	77.46	77.60	77.78	77.67
Sps	49.75	17.65	18.23	18.06	17.71	17.59	17.63	17.70	18.00	17.62
Prp	1.11	2.88	2.43	2.41	2.81	2.80	2.86	2.61	2.29	2.84
Grs	-	1.13	1.20	0.96	1.16	1.12	1.11	1.18	1.12	1.05
Andr	0.63	0.51	0.50	0.47	1.31	1.71	0.94	0.91	0.80	0.82

	TS10 10C	TS10 11C	TS10 12C	TS10 13C	TS12 1C	TS12 2C	TS12 3C	TS12 4C	TS12 4R	TS12 5C
SiO_2	36.38	35.77	35.63	33.77	35.39	36.13	36.57	37.90	36.53	37.19
Al_2O_3	20.15	20.98	20.78	19.84	21.20	20.64	20.54	21.52	20.93	20.60
FeO	35.04	34.98	35.47	33.79	18.56	18.77	18.67	18.28	18.83	19.20
MnO	7.76	7.80	7.53	7.47	21.62	21.76	21.25	21.03	22.02	21.47
MgO	0.65	0.64	0.63	0.57	0.77	0.73	0.94	1.01	0.88	0.96
CaO	0.39	0.40	0.42	3.66	1.99	2.10	2.17	2.69	2.21	2.29
Total	100.36	100.57	100.45	99.11	99.54	100.13	100.15	102.43	101.40	101.70
Si IV	5.98	5.88	5.87	5.66	5.83	5.92	5.97	6.01	5.91	5.98
Al IV	0.02	0.12	0.13	0.34	0.17	0.08	0.03	0.01	0.09	0.02
T site	6.00	6.00	6.00	6.00	6.00	6.00	6.00	6.01	6.00	6.00
Al VI	3.89	3.94	3.90	3.58	3.95	3.90	3.92	4.02	3.89	3.89
Fe^{+3}	0.11	0.09	0.13	0.50	0.09	0.11	0.08	0.00	0.13	0.12
O site	4.00	4.03	4.03	4.08	4.04	4.02	4.01	4.02	4.02	4.00
Fe^{+2}	4.69	4.70	4.74	4.19	2.46	2.44	2.46	2.43	2.40	2.45
Mn	1.08	1.08	1.05	1.06	3.02	3.02	2.94	2.83	3.02	2.92
Mg	0.16	0.16	0.15	0.14	0.19	0.18	0.23	0.24	0.21	0.23
Ca	0.07	0.07	0.07	0.66	0.35	0.37	0.38	0.46	0.38	0.39
A site	6.00	6.02	6.02	6.05	6.02	6.01	6.00	5.95	6.01	6.00
Alm	76.73	77.03	77.12	63.94	40.33	39.91	40.35	40.78	39.14	40.10
Sps	17.67	17.76	17.08	16.21	49.42	49.30	48.26	47.51	49.10	47.80
Prp	2.60	2.58	2.51	2.19	3.10	2.91	3.78	4.03	3.43	3.75
Grs	1.13	1.15	1.19	10.05	5.75	6.02	6.24	7.68	6.25	6.45
Andr	1.86	1.48	2.10	7.60	1.41	1.87	1.37	0.00	2.08	1.90

	TS12 5R	TS12 6C	TS13 1C	TS13 2C	TS13 3C	TS13 4C	TS13 5C	TS14 1C	TS14 2C	TS14 3C
SiO_2	37.04	37.17	36.56	37.18	37.14	36.64	36.54	37.04	37.33	37.26
Al_2O_3	20.86	21.08	21.21	21.25	21.19	21.30	20.88	21.33	20.88	21.12
FeO	18.48	18.38	36.20	36.27	36.43	36.68	36.58	35.86	37.09	36.75
MnO	23.45	23.27	5.04	5.06	4.87	4.99	5.17	4.88	4.56	4.73
MgO	0.65	0.64	1.55	1.42	1.54	1.55	1.42	1.87	1.75	1.62
CaO	0.87	1.03	0.53	0.61	0.52	0.52	0.60	0.70	0.71	0.63
Total	101.35	101.56	101.09	101.79	101.70	101.68	101.19	101.67	102.32	102.11
Si IV	6.00	6.00	5.92	5.98	5.97	5.91	5.93	5.95	5.97	5.97
Al IV	0.00	0.00	0.08	0.02	0.03	0.09	0.07	0.05	0.03	0.03
T site	6.00	6.00	6.00	6.00	6.00	6.00	6.00	6.00	6.00	6.00
Al VI	3.98	4.01	3.97	4.00	3.99	3.95	3.92	3.98	3.90	3.96
Fe^{+3}	0.02	-	0.05	0.01	0.02	0.07	0.10	0.03	0.10	0.05
O site	4.00	4.01	4.02	4.01	4.01	4.02	4.02	4.01	4.01	4.01
Fe^{+2}	2.48	2.48	4.85	4.87	4.88	4.87	4.85	4.78	4.85	4.87
Mn	3.22	3.18	0.69	0.69	0.66	0.68	0.71	0.66	0.62	0.64
Mg	0.16	0.15	0.37	0.34	0.37	0.37	0.34	0.45	0.42	0.39
Ca	0.15	0.18	0.09	0.10	0.09	0.09	0.10	0.12	0.12	0.11
A site	6.00	5.99	6.01	6.00	6.00	6.01	6.01	6.01	6.00	6.00
Alm	41.12	41.38	80.13	81.05	81.08	80.06	79.46	79.08	79.38	80.38
Sps	53.38	53.07	11.42	11.47	11.03	11.21	11.62	10.98	10.11	10.61
Prp	2.60	2.57	6.18	5.65	6.13	6.13	5.62	7.41	6.83	6.38
Grs	2.52	2.97	1.51	1.74	1.49	1.47	1.70	1.99	2.00	1.79
Andr	0.39	-	0.76	0.08	0.27	1.13	1.60	0.54	1.67	0.84

	TS15 1C	TS15 2C	TS15 3C	TS15 4C	TS15 5C	TS2 1C	TS2 2C	TS4 1C	TS4 2C	TS4 3C
SiO_2	36.25	36.54	35.85	35.99	35.95	36.93	36.91	36.38	36.37	36.06
Al_2O_3	20.48	20.66	20.08	20.39	20.35	21.27	21.35	20.35	20.61	20.56
FeO	24.31	24.28	24.40	23.87	24.40	31.45	32.14	34.08	34.12	34.03
MnO	18.80	19.03	18.81	18.69	18.73	9.99	9.92	8.32	8.35	8.53
MgO	0.35	0.38	0.40	0.38	0.37	0.66	0.71	0.58	0.49	0.59
CaO	0.40	0.29	0.43	0.35	0.39	1.13	0.98	0.35	0.37	0.34
Total	100.59	101.18	99.98	99.66	100.18	101.43	102.02	100.07	100.31	100.11
Si IV	5.95	5.96	5.93	5.96	5.93	5.97	5.95	5.99	5.98	5.94
Al IV	0.05	0.04	0.07	0.04	0.07	0.03	0.05	0.01	0.02	0.06
T site	6.00	6.00	6.00	6.00	6.00	6.00	6.00	6.00	6.00	6.00
Al VI	3.92	3.94	3.85	3.94	3.89	4.03	4.00	3.95	3.97	3.94
Fe^{+3}	0.09	0.07	0.16	0.07	0.12	0.00	0.01	0.06	0.03	0.07
O site	4.01	4.01	4.02	4.01	4.02	4.03	4.01	4.00	4.01	4.01
Fe^{+2}	3.23	3.23	3.20	3.23	3.23	4.25	4.31	4.63	4.65	4.61
Mn	2.62	2.63	2.64	2.62	2.62	1.37	1.35	1.16	1.16	1.19
Mg	0.09	0.09	0.10	0.09	0.09	0.16	0.17	0.14	0.12	0.15
Ca	0.07	0.05	0.08	0.06	0.07	0.19	0.17	0.06	0.07	0.06
A site	6.01	6.01	6.01	6.01	6.01	5.97	6.01	6.00	6.00	6.01
Alm	53.03	53.18	51.78	53.14	52.67	71.18	71.65	76.50	77.11	75.85
Sps	42.87	43.27	42.73	43.17	42.69	22.91	22.48	19.18	19.27	19.60
Prp	1.41	1.51	1.61	1.53	1.49	2.65	2.83	2.37	1.99	2.39
Grs	1.15	0.84	1.24	1.02	1.13	3.26	2.81	1.03	1.09	0.98
Andr	1.54	1.20	2.65	1.15	2.01	0.00	0.22	0.93	0.55	1.19

	TS4 4C	TS4 5C	TS4 6C	TS4 6R	TS4 7C	TS4 7R	TS8 1C	TS8 2C	TS8 3C	TS8 4C
SiO_2	36.59	36.46	36.16	35.99	36.63	35.75	36.89	37.05	37.09	36.34
Al_2O_3	20.75	20.25	20.87	20.42	20.39	20.01	20.57	20.68	20.71	20.44
FeO	33.40	34.35	34.91	33.45	34.31	34.13	27.31	26.98	26.54	26.63
MnO	8.34	8.41	8.34	8.34	8.56	8.51	15.76	15.66	16.07	16.26
MgO	0.54	0.51	0.55	0.51	0.51	0.44	0.70	0.70	0.75	0.74
CaO	0.32	0.40	0.36	1.17	0.42	0.34	0.34	0.35	0.31	0.35
Total	99.95	100.37	101.20	99.87	100.83	99.18	101.58	101.42	101.46	100.75
Si IV	6.01	6.00	5.91	5.94	6.00	5.96	5.98	6.01	6.01	5.95
Al IV	0.01	0.00	0.09	0.06	0.00	0.04	0.02	-	-	0.05
T site	6.01	6.00	6.00	6.00	6.00	6.00	6.00	6.01	6.01	6.00
Al VI	4.02	3.92	3.93	3.92	3.93	3.90	3.92	3.95	3.95	3.89
Fe^{+3}	-	0.08	0.10	0.10	0.07	0.11	0.09	0.05	0.05	0.12
O site	4.02	4.00	4.02	4.01	4.00	4.01	4.00	4.00	4.01	4.01
Fe^{+2}	4.59	4.63	4.66	4.51	4.61	4.63	3.61	3.60	3.54	3.51
Mn	1.16	1.17	1.15	1.17	1.19	1.20	2.17	2.15	2.21	2.25
Mg	0.13	0.13	0.13	0.13	0.13	0.11	0.17	0.17	0.18	0.18
Ca	0.06	0.07	0.06	0.21	0.07	0.06	0.06	0.06	0.05	0.06
A site	5.94	6.00	6.01	6.01	6.00	6.01	6.00	5.98	5.98	6.01
Alm	77.28	76.19	76.29	73.84	75.97	75.74	59.21	59.69	58.69	57.30
Sps	19.54	19.27	18.88	19.09	19.54	19.65	35.56	35.64	36.59	36.79
Prp	2.23	2.06	2.20	2.07	2.07	1.77	2.80	2.81	3.00	2.93
Grs	0.95	1.15	1.04	3.39	1.21	0.98	0.98	1.00	0.88	1.01
Andr	-	1.33	1.58	1.61	1.20	1.85	1.45	0.86	0.85	1.97

	TS8 5C	BHG23 1C	BHG23 2C	BHG23 2R	BHG23 3C	BHG16 1C	BHG16 1R	BHG16 2C	BHG16 3C	BHG17 1C
SiO_2	36.90	36.65	36.51	36.42	36.17	36.06	36.13	35.86	36.04	35.88
Al_2O_3	20.61	20.78	20.65	20.53	19.63	20.45	20.41	20.15	20.34	20.44
FeO	26.61	21.21	21.38	21.32	21.65	26.18	25.84	26.35	26.33	19.03
MnO	15.92	20.24	19.50	19.59	19.66	16.08	16.18	16.26	16.28	23.97
MgO	0.72	1.04	1.03	1.04	1.08	0.49	0.48	0.47	0.48	0.34
CaO	0.41	0.83	0.80	0.83	0.98	0.60	0.52	0.70	0.70	0.47
Total	101.18	100.74	99.87	99.73	99.16	99.85	99.54	99.79	100.19	100.14
Si IV	6.00	5.96	5.99	5.98	5.98	5.95	5.98	5.94	5.94	5.92
Al IV	0.00	0.04	0.01	0.02	0.02	0.05	0.02	0.06	0.06	0.08
T site	6.00	6.00	6.00	6.00	6.00	6.00	6.00	6.00	6.00	6.00
Al VI	3.95	3.95	3.98	3.96	3.81	3.93	3.96	3.87	3.89	3.90
Fe^{+3}	0.05	0.06	0.03	0.05	0.17	0.08	0.05	0.14	0.12	0.12
O site	4.00	4.01	4.00	4.00	4.00	4.01	4.00	4.01	4.01	4.02
Fe^{+2}	3.56	2.82	2.90	2.88	2.81	3.53	3.53	3.49	3.49	2.49
Mn	2.19	2.79	2.71	2.73	2.75	2.25	2.27	2.28	2.27	3.35
Mg	0.18	0.25	0.25	0.25	0.27	0.12	0.12	0.12	0.12	0.08
Ca	0.07	0.14	0.14	0.15	0.17	0.11	0.09	0.12	0.12	0.08
A site	6.00	6.01	6.00	6.00	6.00	6.01	6.00	6.01	6.01	6.01
Alm	58.83	46.47	48.14	47.56	45.50	58.03	58.29	56.70	56.97	40.68
Sps	36.22	45.98	44.91	45.05	44.65	36.96	37.50	37.06	37.07	54.65
Prp	2.90	4.17	4.19	4.19	4.32	1.99	1.95	1.87	1.94	1.35
Grs	1.19	2.37	2.32	2.42	2.80	1.76	1.51	2.02	2.02	1.37
Andr	0.86	1.00	0.44	0.77	2.73	1.27	0.75	2.35	2.00	1.95

	BHG17 2C	BHG17 3C	178226 1C	178226 2C	178226 3C	191713 1C	191713 2C	5-1200 1C	5-1200 2C	5-1200 3C
SiO_2	35.97	36.02	36.21	36.87	36.36	36.44	36.41	36.21	36.32	35.96
Al_2O_3	20.38	20.69	20.83	20.66	21.05	20.92	20.85	20.83	20.77	20.66
FeO	19.39	19.67	21.44	23.22	22.54	26.25	24.09	25.89	25.75	26.33
MnO	23.14	23.50	20.77	19.28	19.45	15.27	17.50	16.32	17.14	16.49
MgO	0.38	0.30	1.32	1.40	1.49	1.18	1.15	0.50	0.50	0.59
CaO	0.49	0.42	0.45	0.51	0.50	0.82	0.86	0.40	0.55	0.61
Total	99.75	100.61	101.02	101.94	101.39	100.88	100.86	100.15	101.03	100.64
Si IV	5.95	5.92	5.89	5.94	5.88	5.93	5.92	5.95	5.93	5.90
Al IV	0.05	0.08	0.11	0.06	0.12	0.07	0.08	0.05	0.07	0.10
T site	6.00	6.00	6.00	6.00	6.00	6.00	6.00	6.00	6.00	6.00
Al VI	3.92	3.92	3.88	3.86	3.90	3.93	3.92	3.99	3.93	3.90
Fe^{+3}	0.09	0.10	0.14	0.15	0.13	0.08	0.10	0.02	0.09	0.13
O site	4.01	4.02	4.03	4.01	4.03	4.02	4.02	4.01	4.02	4.02
Fe^{+2}	2.59	2.59	2.76	2.96	2.90	3.48	3.17	3.54	3.42	3.47
Mn	3.24	3.27	2.86	2.63	2.67	2.10	2.41	2.27	2.37	2.29
Mg	0.09	0.07	0.32	0.34	0.36	0.29	0.28	0.12	0.12	0.14
Ca	0.09	0.07	0.08	0.09	0.09	0.14	0.15	0.07	0.10	0.11
A site	6.01	6.01	6.02	6.01	6.02	6.01	6.01	6.01	6.01	6.01
Alm	42.41	42.48	44.72	47.96	47.25	57.07	51.91	58.75	56.13	56.52
Sps	53.19	53.53	46.45	42.67	43.36	34.52	39.49	37.73	38.91	37.32
Prp	1.53	1.20	5.21	5.45	5.84	4.69	4.57	2.03	1.98	2.34
Grs	1.42	1.20	1.27	1.42	1.42	2.36	2.45	1.18	1.57	1.74
Andr	1.45	1.59	2.35	2.50	2.13	1.37	1.58	0.31	1.41	2.08

	5-1200 4C	189113 1C	189113 2C	189113 3C	189113 4C	1917N5 1C	1917N5 2C	18916 1C	18916 2C	18918 1C
SiO_2	36.43	36.30	35.70	35.12	36.32	36.77	36.34	36.17	36.00	36.53
Al_2O_3	20.97	20.38	20.33	20.77	20.17	21.52	21.65	19.83	20.14	20.00
FeO	24.51	21.37	21.48	21.90	21.80	26.10	26.68	20.40	21.12	22.68
MnO	17.80	21.71	21.85	21.61	21.76	13.44	12.66	23.25	22.92	21.15
MgO	0.45	0.37	0.38	0.50	0.39	1.30	1.31	0.30	0.32	0.24
CaO	0.48	0.61	0.68	0.48	0.71	2.25	2.35	0.48	0.50	0.57
Total	100.64	100.74	100.44	100.37	101.14	101.38	100.98	100.43	101.01	101.17
Si IV	5.96	5.95	5.89	5.80	5.94	5.91	5.87	5.96	5.91	5.98
Al IV	0.04	0.05	0.11	0.20	0.06	0.09	0.13	0.04	0.09	0.02
T site	6.00	6.00	6.00	6.00	6.00	6.00	6.00	6.00	6.00	6.00
Al VI	4.00	3.89	3.84	3.84	3.83	3.99	3.99	3.82	3.81	3.84
Fe^{+3}	0.01	0.12	0.19	0.20	0.19	0.03	0.04	0.19	0.22	0.17
O site	4.01	4.01	4.03	4.05	4.01	4.02	4.03	4.01	4.02	4.01
Fe^{+2}	3.35	2.79	2.75	2.80	2.78	3.48	3.57	2.60	2.66	2.91
Mn	2.47	3.02	3.05	3.02	3.01	1.83	1.73	3.25	3.19	2.93
Mg	0.11	0.09	0.09	0.12	0.10	0.31	0.31	0.07	0.08	0.06
Ca	0.08	0.11	0.12	0.08	0.12	0.39	0.41	0.08	0.09	0.10
A site	6.01	6.01	6.02	6.03	6.01	6.01	6.02	6.01	6.01	6.00
Alm	55.64	45.58	44.32	44.91	44.80	57.67	58.88	41.93	42.67	47.22
Sps	41.02	49.20	49.16	48.51	48.66	30.33	28.62	52.40	51.15	47.48
Prp	1.81	1.48	1.50	1.96	1.54	5.16	5.20	1.20	1.28	0.94
Grs	1.40	1.75	1.95	1.35	2.00	6.41	6.71	1.37	1.43	1.61
Andr	0.12	2.00	3.07	3.27	3.00	0.43	0.60	3.11	3.47	2.76

	18918 2C	2609N7 1C	2609N7 2C	1917N2 1C	1917N2 2C	BHS22A 1C	BHS22 2C	26098 1C	26098 2C	191710 1C
SiO_2	36.42	36.67	36.39	36.88	36.97	36.54	36.61	36.59	36.01	36.15
Al_2O_3	19.87	20.80	20.65	21.03	21.10	21.84	21.25	20.27	20.61	19.51
FeO	22.54	35.90	35.45	36.49	36.78	32.36	31.49	21.81	22.48	18.62
MnO	20.81	6.43	6.61	4.30	4.19	7.98	8.10	21.72	21.35	24.92
MgO	0.28	0.96	0.89	2.07	2.10	1.37	1.33	0.43	0.43	0.51
CaO	0.45	1.18	1.27	0.64	0.69	2.49	2.42	0.44	0.44	0.62
Total	100.37	101.94	101.26	101.43	101.84	102.58	101.21	101.25	101.32	100.33
Si IV	6.00	5.92	5.92	5.94	5.93	5.83	5.91	5.97	5.88	5.96
Al IV	-	0.08	0.08	0.06	0.07	0.17	0.09	0.03	0.12	0.04
T site	6.00	6.00	6.00	6.00	6.00	6.00	6.00	6.00	6.00	6.00
Al VI	3.86	3.88	3.88	3.93	3.92	3.93	3.95	3.87	3.85	3.76
Fe^{+3}	0.14	0.14	0.14	0.09	0.10	0.11	0.07	0.14	0.17	0.25
O site	4.00	4.02	4.02	4.01	4.02	4.04	4.02	4.01	4.03	4.01
Fe^{+2}	2.95	4.70	4.66	4.81	4.82	4.20	4.17	2.82	2.88	2.29
Mn	2.90	0.88	0.91	0.59	0.57	1.08	1.11	3.00	2.96	3.48
Mg	0.07	0.23	0.21	0.50	0.50	0.33	0.32	0.10	0.10	0.13
Ca	0.08	0.20	0.22	0.11	0.12	0.43	0.42	0.08	0.08	0.11
A site	6.00	6.01	6.01	6.01	6.01	6.02	6.01	6.00	6.02	6.01
Alm	47.98	76.40	75.81	78.97	78.87	68.41	68.45	45.94	46.52	36.56
Sps	47.28	14.30	14.81	9.62	9.31	17.58	18.18	48.88	47.75	55.64
Prp	1.13	3.75	3.49	8.15	8.21	5.31	5.27	1.69	1.67	2.02
Grs	1.29	3.32	3.60	1.82	1.95	6.93	6.89	1.24	1.26	1.75
Andr	2.32	2.23	2.30	1.44	1.66	1.76	1.22	2.25	2.80	4.03

	191710 2C	BH3 1C	BH3 2C	19178 1C	1917N6 1C	BHA11 AVE	BHA10 AVE	BHA7 AVE	BHA8 AVE	BHA9 AVE
SiO_2	35.90	36.42	34.83	35.50	36.47	36.09	36.24	36.62	36.72	36.72
Al_2O_3	20.04	20.56	21.29	19.61	20.68	20.38	19.95	20.43	20.80	20.46
FeO	17.99	38.36	37.65	17.35	34.48	24.16	24.84	25.37	25.69	25.11
MnO	25.71	4.05	4.71	26.57	7.20	18.63	18.72	18.04	18.13	18.00
MgO	0.48	1.12	1.26	0.35	1.18	0.30	0.31	0.24	0.32	0.25
CaO	0.62	1.25	0.84	0.93	1.77	0.64	0.58	0.50	0.58	0.60
Total	100.73	101.76	100.58	100.32	101.78	100.22	100.64	101.21	102.24	101.13
Si IV	5.90	5.90	5.72	5.88	5.89	5.95	5.96	5.98	5.94	5.99
Al IV	0.10	0.10	0.28	0.12	0.11	0.05	0.04	0.03	0.06	0.01
T site	6.00	6.00	6.00	6.00	6.00	6.00	6.00	6.01	6.00	6.00
Al VI	3.78	3.82	3.85	3.70	3.83	3.91	3.83	3.90	3.90	3.93
Fe^{+3}	0.24	0.20	0.22	0.33	0.20	0.10	0.18	0.11	0.11	0.08
O site	4.02	4.02	4.07	4.03	4.03	4.01	4.01	4.01	4.01	4.00
Fe^{+2}	2.21	4.97	4.93	2.04	4.44	3.22	3.22	3.35	3.35	3.34
Mn	3.58	0.56	0.66	3.73	0.99	2.60	2.61	2.49	2.48	2.49
Mg	0.12	0.27	0.31	0.09	0.28	0.07	0.08	0.06	0.08	0.06
Ca	0.11	0.22	0.15	0.17	0.31	0.11	0.10	0.09	0.10	0.10
A site	6.01	6.01	6.04	6.02	6.02	6.01	6.01	5.99	6.01	5.99
Alm	35.30	80.00	78.72	32.15	71.49	52.67	52.04	54.91	54.68	55.00
Sps	57.26	8.94	10.47	58.73	15.87	42.59	42.18	40.94	40.56	40.98
Prp	1.87	4.34	4.92	1.37	4.56	1.22	1.22	0.97	1.26	1.00
Grs	1.75	3.48	2.37	2.61	4.92	1.86	1.66	1.43	1.65	1.73
Andr	3.83	3.24	3.52	5.15	3.16	1.67	2.90	1.75	1.85	1.29

	BHG1 AVE	BHG13 AVE	BHG16 AVE	BHG2 AVE	BHG4 AVE	BHG6 AVE	TS10 AVE	TS12 AVE	TS13 AVE	TS14 AVE
SiO_2	36.76	36.24	35.96	36.68	37.09	36.63	36.56	36.72	36.81	37.21
Al_2O_3	20.73	19.86	20.30	20.49	20.71	20.46	20.61	20.93	21.17	21.11
FeO	23.20	17.37	26.27	24.92	28.66	21.57	34.79	18.64	36.43	36.57
MnO	18.79	26.59	16.17	17.71	13.75	21.21	7.78	21.73	5.03	4.72
MgO	0.74	0.27	0.48	0.32	1.09	0.27	0.66	0.84	1.50	1.75
CaO	0.79	0.43	0.65	0.71	0.37	0.18	0.39	2.04	0.55	0.68
Total	101.00	100.76	99.82	100.83	101.67	100.32	100.78	100.92	101.49	102.03
Si IV	5.98	5.96	5.95	6.00	5.99	6.02	5.98	5.95	5.94	5.96
Al IV	0.02	0.04	0.05	0.01	0.01	0.00	0.02	0.05	0.06	0.04
T site	6.00	6.00	6.00	6.00	6.00	6.02	6.00	6.00	6.00	6.00
Al VI	3.95	3.81	3.90	3.94	3.93	3.96	3.95	3.95	3.97	3.95
Fe^{+3}	0.05	0.20	0.11	0.06	0.08	0.05	0.06	0.07	0.05	0.06
O site	4.01	4.01	4.01	4.00	4.01	4.01	4.01	4.02	4.01	4.01
Fe^{+2}	3.10	2.16	3.51	3.34	3.79	2.91	4.69	2.45	4.87	4.83
Mn	2.59	3.70	2.26	2.45	1.88	2.95	1.08	2.98	0.69	0.64
Mg	0.18	0.07	0.12	0.08	0.26	0.07	0.16	0.20	0.36	0.42
Ca	0.14	0.08	0.12	0.12	0.06	0.03	0.07	0.35	0.10	0.12
A site	6.00	6.01	6.01	5.99	5.99	5.95	6.00	6.00	6.01	6.01
Alm	51.13	34.79	57.36	55.15	62.38	48.39	77.46	40.47	80.35	79.61
Sps	42.75	59.63	37.01	40.50	31.00	49.14	17.79	49.22	11.35	10.56
Prp	2.96	1.07	1.93	1.28	4.31	1.10	2.65	3.36	5.94	6.87
Grs	2.28	1.22	1.89	2.05	1.04	0.52	1.12	5.85	1.58	1.93
Andr	0.89	3.29	1.81	1.01	1.27	0.85	0.99	1.10	0.77	1.02

	TS15 AVE	TS2 AVE	TS4 AVE	TS8 AVE	BHG17 AVE	BH3 AVE	BHG23 AVE	BH4 AVE	178226 AVE	5-2000 AVE
SiO_2	36.11	36.92	36.38	36.85	35.96	35.63	36.44	36.06	36.48	36.23
Al_2O_3	20.39	21.31	20.54	20.60	20.50	20.92	20.35	20.11	20.85	20.81
FeO	24.25	31.79	34.17	26.81	19.37	38.01	21.41	29.18	22.40	25.62
MnO	18.81	9.96	8.41	15.93	23.54	4.38	19.80	13.25	19.83	16.94
MgO	0.38	0.68	0.54	0.72	0.34	1.19	1.05	0.54	1.40	0.51
CaO	0.37	1.05	0.37	0.35	0.46	1.04	0.87	0.97	0.49	0.51
Total	100.32	101.72	100.41	101.28	100.17	101.17	99.92	100.11	101.45	100.61
Si IV	5.95	5.96	5.98	5.99	5.93	5.81	5.98	5.95	5.90	5.94
Al IV	0.05	0.04	0.03	0.01	0.07	0.19	0.02	0.05	0.10	0.06
T site	6.00	6.00	6.00	6.00	6.00	6.00	6.00	6.00	6.00	6.00
Al VI	3.91	4.01	3.95	3.93	3.92	3.83	3.91	3.86	3.88	3.96
Fe^{+3}	0.10	0.01	0.06	0.07	0.10	0.21	0.09	0.16	0.14	0.06
O site	4.01	4.02	4.01	4.01	4.02	4.05	4.00	4.01	4.02	4.02
Fe^{+2}	3.22	4.28	4.63	3.56	2.56	4.95	2.84	3.85	2.87	3.44
Mn	2.62	1.36	1.17	2.19	3.29	0.61	2.75	1.85	2.72	2.35
Mg	0.09	0.16	0.13	0.18	0.08	0.29	0.26	0.13	0.34	0.12
Ca	0.07	0.18	0.06	0.06	0.08	0.18	0.15	0.17	0.08	0.09
A site	6.01	5.99	6.00	5.99	6.01	6.03	6.00	6.01	6.01	6.01
Alm	52.76	71.41	76.45	58.74	41.85	79.36	46.69	62.50	46.64	56.76
Sps	42.94	22.70	19.32	36.16	53.79	9.71	45.18	30.04	44.16	38.74
Prp	1.51	2.74	2.19	2.89	1.36	4.63	4.23	2.15	5.50	2.04
Grs	1.08	3.04	1.06	1.01	1.33	2.92	2.50	2.78	1.37	1.47
Andr	1.71	0.11	0.97	1.20	1.66	3.38	1.40	2.52	2.33	0.99

	191713 AVE	1917N2 AVE	191710 AVE	1917N5 AVE	26098 AVE	2609N7 AVE	18916 AVE	18918 AVE	189111 AVE
SiO_2	36.43	36.93	36.02	36.55	36.30	36.53	36.09	36.48	35.79
Al_2O_3	20.88	21.07	19.77	21.59	20.44	20.72	19.98	19.94	20.55
FeO	25.17	36.64	18.30	26.39	22.14	35.68	20.76	22.61	31.83
MnO	16.39	4.25	25.32	13.05	21.54	6.52	23.09	20.98	12.43
MgO	1.16	2.09	0.50	1.30	0.43	0.92	0.31	0.26	0.35
CaO	0.84	0.67	0.62	2.30	0.44	1.22	0.49	0.51	0.37
Total	100.87	101.63	100.53	101.18	101.29	101.60	100.72	100.77	101.32
Si IV	5.93	5.93	5.93	5.89	5.93	5.92	5.94	5.99	5.87
Al IV	0.07	0.07	0.07	0.11	0.07	0.08	0.06	0.01	0.13
T site	6.00	6.00	6.00	6.00	6.00	6.00	6.00	6.00	6.00
Al VI	3.93	3.92	3.77	3.99	3.86	3.88	3.81	3.85	3.83
Fe^{+3}	0.09	0.09	0.25	0.03	0.16	0.14	0.20	0.16	0.20
O site	4.02	4.02	4.02	4.03	4.02	4.02	4.02	4.00	4.03
Fe^{+2}	3.32	4.82	2.25	3.52	2.85	4.68	2.63	2.93	4.14
Mn	2.26	0.58	3.53	1.78	2.98	0.90	3.22	2.92	1.73
Mg	0.28	0.50	0.12	0.31	0.10	0.22	0.08	0.06	0.09
Ca	0.15	0.11	0.11	0.40	0.08	0.21	0.09	0.09	0.07
A site	6.01	6.01	6.01	6.02	6.01	6.01	6.01	6.00	6.02
Alm	54.49	78.92	35.93	58.28	46.23	76.11	42.30	47.60	66.65
Sps	37.01	9.47	56.45	29.47	48.31	14.55	51.77	47.38	27.76
Prp	4.63	8.18	1.94	5.18	1.68	3.62	1.24	1.03	1.37
Grs	2.40	1.88	1.75	6.56	1.25	3.46	1.40	1.45	1.05
Andr	1.47	1.55	3.93	0.52	2.53	2.26	3.29	2.54	3.17

AMPHIBOLE

Cations calculated on the basis of 23 oxygens.

	18916 2C	189111 1C	189113 1C	189113 2C	18916 1C	18918 1C	18918 2C	191710 1C	26098 1C	BHA10 1C
SiO_2	49.23	48.59	49.73	50.01	48.91	48.73	48.61	49.36	49.50	47.73
Al_2O_3	0.60	1.20	0.39	0.16	0.57	0.10	0.48	0.10	0.92	0.64
FeO	34.19	40.52	33.68	33.50	33.75	37.86	37.12	30.90	31.96	39.63
MnO	8.75	3.69	6.76	6.68	7.74	9.64	7.42	11.50	7.02	5.63
MgO	5.20	3.92	6.91	7.27	5.55	2.58	3.72	5.50	8.18	4.05
CaO	nd	0.07	0.11	nd	nd	nd	nd	0.09	0.06	0.08
Na_2O	0.23	0.41	0.11	nd	0.23	nd	0.21	nd	0.43	0.23
Total	98.21	98.30	97.69	97.62	96.75	98.99	97.56	97.45	98.07	97.99
Si IV	7.88	7.84	7.89	7.92	7.92	7.91	7.92	7.93	7.77	7.74
Al IV	0.11	0.16	0.07	0.03	0.08	0.02	0.08	0.02	0.17	0.12
Fe^{+3}	0.01	-	0.03	0.05	-	0.07	-	0.05	0.06	0.14
T site	8.00	8.00	8.00	8.00	8.00	8.00	8.00	8.00	8.00	8.00
Al VI	-	0.07	-	-	0.03	-	0.01	-	-	-
Fe^{+3}	0.05	-	0.07	0.08	-	0.09	-	0.07	0.10	0.19
Mg	1.24	0.94	1.64	1.72	1.34	0.62	0.90	1.32	1.92	0.98
Fe^{+2}	3.71	3.99	3.29	3.20	3.63	4.29	4.08	3.61	2.99	3.83
M1,2,3	5.00	5.00	5.00	5.00	5.00	5.00	5.00	5.00	5.00	5.00
Fe^{+2}	0.81	1.48	1.07	1.10	0.94	0.67	0.98	0.42	1.06	1.21
Mn	1.19	0.50	0.91	0.90	1.06	1.33	1.02	1.57	0.93	0.77
Ca	-	0.01	0.02	-	-	-	-	0.02	0.01	0.01
M4 site	2.00	2.00	2.00	2.00	2.00	2.00	2.00	2.00	2.00	2.00
Na	0.07	0.13	0.03	-	0.07	-	0.07	-	0.13	0.07
A site	0.07	0.13	0.03	-	0.07	-	0.07	0.00	0.13	0.07

	BHA10 2C	BHA10 2R	BHA10 3C	BHA11 1C	BHA11 2C	BHA12 1C	BHA12 1R	BHA12 2C	BHA12 3C	BHA5 1C
SiO_2	47.88	48.15	48.36	47.72	48.34	48.93	48.92	50.40	50.11	47.87
Al_2O_3	0.66	0.60	0.66	0.65	0.71	0.81	0.71	0.68	0.67	1.06
FeO	38.53	38.64	39.04	38.94	38.37	28.77	28.84	26.57	26.44	39.46
MnO	5.44	5.40	5.57	5.50	5.42	10.77	10.71	11.66	11.16	6.00
MgO	4.29	4.48	4.29	4.03	4.58	7.28	6.76	8.36	8.78	3.00
CaO	0.09	0.07	0.09	0.07	0.07	0.11	0.09	0.08	0.09	nd
Na_2O	0.24	0.18	0.22	0.20	0.23	0.37	0.31	0.32	0.36	0.40
Total	97.13	97.52	98.23	97.11	97.72	97.04	96.35	98.07	97.62	97.79
Si IV	7.81	7.81	7.80	7.80	7.82	7.81	7.88	7.89	7.86	7.83
Al IV	0.13	0.11	0.12	0.13	0.14	0.15	0.12	0.11	0.12	0.17
Fe^{+3}	0.06	0.08	0.07	0.08	0.05	0.04	-	-	0.02	-
T site	8.00	8.00	8.00	8.00	8.00	8.00	8.00	8.00	8.00	8.00
Al VI	-	-	-	-	-	-	0.02	0.01	-	0.04
Fe^{+3}	0.11	0.13	0.13	0.14	0.11	0.08	0.01	0.00	0.03	0.00
Mg	1.04	1.08	1.03	0.98	1.10	1.73	1.62	1.95	2.05	0.73
Fe^{+2}	3.84	3.78	3.84	3.88	3.79	3.19	3.35	3.04	2.92	4.23
M1,2,3	5.00	5.00	5.00	5.00	5.00	5.00	5.00	5.00	5.00	5.00
Fe^{+2}	1.23	1.25	1.22	1.23	1.25	0.53	0.52	0.44	0.50	1.17
Mn	0.75	0.74	0.76	0.76	0.74	1.46	1.46	1.55	1.48	0.83
Ca	0.01	0.01	0.02	0.01	0.01	0.02	0.02	0.01	0.02	-
M4 site	2.00	2.00	2.00	2.00	2.00	2.00	2.00	2.00	2.00	2.00
Na	0.08	0.06	0.07	0.06	0.07	0.11	0.10	0.10	0.11	0.13
A site	0.08	0.06	0.07	0.06	0.07	0.11	0.10	0.10	0.11	0.13

	BHA5 2C	BHA5 2R	BHA5 2R	BHA5 3C	BHA5 4C	BHA5 4R	BHA7 1C	BHA7 2C	BHA7 2R	BHA8 1C
SiO_2	47.58	47.67	47.89	47.75	47.82	47.70	48.08	48.20	48.06	48.18
Al_2O_3	1.04	1.03	1.00	1.08	1.05	1.06	0.86	0.85	0.85	0.84
FeO	39.32	39.80	39.63	40.31	40.04	39.44	40.32	40.22	40.46	38.74
MnO	6.07	5.93	6.20	5.82	5.91	5.93	5.64	5.50	5.61	6.36
MgO	3.00	2.95	2.83	2.87	2.97	3.07	3.06	3.32	3.08	3.36
CaO	0.05	nd	0.06	nd	nd	nd	0.06	0.06	0.07	0.07
Na_2O	0.42	0.37	0.40	0.42	0.43	0.39	0.31	0.31	0.26	0.27
Total	97.47	97.74	98.01	98.25	98.21	97.59	98.33	98.46	98.51	97.82
Si IV	7.81	7.81	7.83	7.79	7.80	7.82	7.82	7.82	7.80	7.85
Al IV	0.19	0.19	0.17	0.21	0.20	0.18	0.17	0.16	0.16	0.15
Fe^{+3}	-	-	-	0.00	-	-	0.01	0.02	0.04	-
T site	8.00	8.00	8.00	8.00	8.00	8.00	8.00	8.00	8.00	8.00
Al VI	0.01	0.01	0.02	-	0.00	0.02	-	-	-	0.01
Fe^{+3}	0.04	0.07	0.02	0.08	0.06	0.04	0.08	0.09	0.12	0.05
Mg	0.73	0.72	0.69	0.70	0.72	0.75	0.74	0.80	0.74	0.82
Fe^{+2}	4.21	4.21	4.27	4.22	4.21	4.19	4.17	4.11	4.14	4.12
M1,2,3	5.00	5.00	5.00	5.00	5.00	5.00	5.00	5.00	5.00	5.00
Fe^{+2}	1.15	1.18	1.13	1.20	1.18	1.18	1.21	1.23	1.22	1.11
Mn	0.84	0.82	0.86	0.80	0.82	0.82	0.78	0.76	0.77	0.88
Ca	0.01	-	0.01	-	-	-	0.01	0.01	0.01	0.01
M4 site	2.00	2.00	2.00	2.00	2.00	2.00	2.00	2.00	2.00	2.00
Na	0.13	0.12	0.13	0.13	0.14	0.12	0.10	0.10	0.08	0.08
A site	0.13	0.12	0.13	0.13	0.14	0.12	0.10	0.10	0.08	0.08

	BHA8 2C	BHA8 3C	BHA9 1C	BHA9 2C	BHA9 3C	BHA9 4C	BH11 1C	BH11 2C	BHA18 1C	BHA18 2C
SiO_2	48.42	48.19	48.14	47.97	48.12	47.72	47.99	48.28	49.14	48.89
Al_2O_3	0.77	0.85	0.84	0.84	0.87	0.77	0.84	0.77	0.64	0.50
FeO	39.19	38.56	39.40	39.26	39.72	39.32	37.67	37.74	38.22	37.96
MnO	6.26	6.07	5.47	5.47	5.51	5.19	7.36	7.46	5.03	4.72
MgO	3.27	3.35	3.90	3.59	3.45	4.33	3.63	3.78	4.71	4.90
CaO	0.06	0.07	0.08	0.09	0.10	nd	nd	nd	0.06	0.07
Na_2O	0.27	0.32	0.25	0.32	0.27	0.29	0.24	0.32	0.14	nd
Total	98.23	97.42	98.08	97.54	98.04	97.62	97.73	98.35	97.94	97.04
Si IV	7.87	7.89	7.80	7.83	7.82	7.75	7.81	7.81	7.91	7.92
Al IV	0.13	0.11	0.16	0.16	0.17	0.15	0.16	0.15	0.09	0.08
Fe^{+3}	-	-	0.04	0.00	0.01	0.10	0.03	0.04	-	-
T site	8.00	8.00	8.00	8.00	8.00	8.00	8.00	8.00	8.00	8.00
Al VI	0.01	0.05	-	-	-	-	-	-	0.03	0.02
Fe^{+3}	0.04	-	0.12	0.06	0.09	0.16	0.11	0.09	0.02	0.07
Mg	0.79	0.82	0.94	0.87	0.84	1.05	0.88	0.91	1.13	1.18
Fe^{+2}	4.16	4.13	3.93	4.06	4.07	3.79	4.01	4.00	3.82	3.74
M1,2,3	5.00	5.00	5.00	5.00	5.00	5.00	5.00	5.00	5.00	5.00
Fe^{+2}	1.13	1.15	1.24	1.23	1.22	1.29	0.99	0.98	1.30	1.34
Mn	0.86	0.84	0.75	0.76	0.76	0.71	1.01	1.02	0.69	0.65
Ca	0.01	0.01	0.01	0.01	0.02	-	-	-	0.01	0.01
M4 site	2.00	2.00	2.00	2.00	2.00	2.00	2.00	2.00	2.00	2.00
Na	0.09	0.10	0.08	0.10	0.08	0.09	0.08	0.10	0.04	-
A site	0.09	0.10	0.08	0.10	0.08	0.09	0.08	0.10	0.04	-

	BHG13 1C	BHG13 2C	BHG13 3C	BHG13 4C	TS10 1C	TS10 2C	TS10 3C	TS10 4C	TS10 5C	TS10 6C
SiO_2	48.50	49.09	49.35	48.60	48.95	48.45	48.86	48.63	48.62	48.26
Al_2O_3	0.77	0.76	0.55	0.86	0.85	0.77	0.86	0.89	0.80	0.73
FeO	32.26	30.83	31.50	32.52	42.77	42.23	41.66	40.26	40.20	40.04
MnO	8.63	8.97	8.99	9.19	1.80	1.67	1.96	1.82	1.76	1.62
MgO	6.17	6.90	6.72	6.76	5.01	5.01	5.21	5.27	4.94	4.78
CaO	0.05	0.06	nd	0.07	nd	nd	nd	nd	nd	nd
Na_2O	0.37	0.32	0.23	0.41	0.30	0.26	0.25	0.26	0.20	0.21
Total	96.75	96.95	97.34	98.39	99.68	98.43	98.79	97.93	96.52	95.62
Si IV	7.83	7.86	7.88	7.69	7.75	7.77	7.79	7.81	7.88	7.89
Al IV	0.15	0.14	0.10	0.16	0.16	0.15	0.16	0.17	0.12	0.11
Fe^{+3}	0.03	-	0.02	0.15	0.09	0.09	0.05	0.02	-	-
T site	8.00	8.00	8.00	8.00	8.00	8.00	8.00	8.00	8.00	8.00
Al VI	-	0.00	-	-	-	-	-	-	0.03	0.03
Fe^{+3}	0.06	0.04	0.05	0.18	0.16	0.15	0.14	0.10	0.03	0.01
Mg	1.48	1.65	1.60	1.59	1.18	1.20	1.24	1.26	1.19	1.17
Fe^{+2}	3.46	3.31	3.35	3.22	3.66	3.65	3.63	3.63	3.75	3.79
M1,2,3	5.00	5.00	5.00	5.00	5.00	5.00	5.00	5.00	5.00	5.00
Fe^{+2}	0.81	0.77	0.78	0.76	1.76	1.77	1.74	1.66	1.67	1.67
Mn	1.18	1.22	1.22	1.23	0.24	0.23	0.26	0.25	0.24	0.22
Ca	0.01	0.01	-	0.01	-	-	-	-	-	-
M4 site	2.00	2.00	2.00	2.00	2.00	2.00	2.00	2.00	2.00	2.00
Na	0.12	0.10	0.07	0.12	0.09	0.08	0.08	0.08	0.06	0.07
A site	0.12	0.10	0.07	0.12	0.09	0.08	0.08	0.08	0.06	0.07

	TS10 7C	TS10 8C	TS10 9C	TS10 10C	TS10 11C	TS10 12C	TS15 1C	TS15 2C	TS15 3C	TS15 4C
SiO_2	48.54	48.75	48.85	48.52	48.20	48.16	47.76	48.65	48.08	48.35
Al_2O_3	0.82	0.80	0.82	0.69	0.63	0.82	1.02	1.17	1.18	1.15
FeO	40.03	40.02	39.77	39.71	39.24	39.20	36.77	37.09	36.77	36.98
MnO	1.80	1.76	1.81	1.99	1.82	1.86	5.88	5.70	6.38	6.05
MgO	4.90	4.96	5.31	5.07	5.18	5.35	5.07	5.70	5.56	5.68
CaO	nd	nd	nd	nd	nd	nd	nd	0.07	nd	0.05
Na_2O	0.24	0.25	0.27	0.19	0.15	0.25	0.48	0.56	0.56	0.63
Total	96.33	96.54	96.83	97.17	95.22	95.64	96.99	98.94	98.54	98.89
Si IV	7.89	7.89	7.86	7.86	7.90	7.86	7.77	7.73	7.68	7.69
Al IV	0.11	0.11	0.14	0.13	0.10	0.14	0.20	0.22	0.22	0.21
Fe^{+3}	-	-	-	0.00	-	-	0.04	0.05	0.10	0.09
T site	8.00	8.00	8.00	8.00	8.00	8.00	8.00	8.00	8.00	8.00
Al VI	0.05	0.05	0.02	-	0.02	0.02	-	-	-	-
Fe^{+3}	-	-	0.03	0.08	0.03	0.04	0.08	0.10	0.15	0.11
Mg	1.19	1.20	1.27	1.23	1.26	1.30	1.23	1.35	1.32	1.35
Fe^{+2}	3.77	3.76	3.67	3.70	3.68	3.64	3.69	3.55	3.53	3.54
M1,2,3	5.00	5.00	5.00	5.00	5.00	5.00	5.00	5.00	5.00	5.00
Fe^{+2}	1.67	1.66	1.65	1.61	1.66	1.67	1.19	1.22	1.14	1.18
Mn	0.25	0.24	0.25	0.27	0.25	0.26	0.81	0.77	0.86	0.81
M4 site	2.00	2.00	2.00	2.00	2.00	2.00	2.00	2.00	2.00	2.00
Na	0.08	0.08	0.09	0.06	0.05	0.08	0.15	0.17	0.17	0.19
A site	0.08	0.08	0.09	0.06	0.05	0.08	0.15	0.17	0.17	0.19

	TS15 5C	TS15 6C	TS15 7C	TS15 8C	TS15 9C	TS15 10C	18916 AVE	189113 AVE	18918 AVE	BHA10 AVE
SiO_2	47.44	48.19	47.41	48.64	48.36	47.55	49.07	49.87	48.67	48.03
Al_2O_3	1.13	1.06	1.10	1.20	1.08	1.11	0.58	0.28	0.29	0.64
FeO	35.48	34.73	35.69	33.14	35.06	34.50	33.97	33.59	37.43	38.96
MnO	5.80	5.84	5.94	5.42	5.80	5.96	8.24	6.72	8.53	5.51
MgO	5.76	5.89	4.85	7.88	6.24	6.27	5.38	7.09	3.15	4.27
CaO	0.07	0.07	0.06	nd	nd	0.06	nd	0.05	nd	0.08
Na_2O	0.54	0.54	0.55	0.58	0.50	0.57	0.23	0.05	0.10	0.22
Total	96.86	96.56	96.57	97.40	97.45	96.45	97.47	97.65	98.17	97.49
Si IV	7.69	7.82	7.76	7.72	7.76	7.71	7.90	7.91	7.92	7.79
Al IV	0.22	0.18	0.21	0.22	0.20	0.21	0.10	0.05	0.05	0.12
Fe^{+3}	0.09	-	0.02	0.06	0.03	0.08	0.00	0.04	0.04	0.09
T site	8.00	8.00	8.00	8.00	8.00	8.00	8.00	8.00	8.00	8.00
Al VI	-	0.02	-	-	-	-	0.01	-	0.01	-
Fe^{+3}	0.14	-	0.06	0.10	0.08	0.11	0.02	0.08	0.05	0.14
Mg	1.39	1.43	1.18	1.86	1.49	1.52	1.29	1.68	0.76	1.03
Fe^{+2}	3.47	3.55	3.75	3.04	3.42	3.38	3.67	3.25	4.18	3.82
M1,2,3	5.00	5.00	5.00	5.00	5.00	5.00	5.00	5.00	5.00	5.00
Fe^{+2}	1.11	1.16	1.05	1.21	1.16	1.12	0.88	1.09	0.83	1.23
Mn	0.80	0.80	0.82	0.73	0.79	0.82	1.12	0.90	1.17	0.76
Ca	0.01	0.01	0.01	-	-	0.01	-	0.01	-	0.01
M4 site	2.00	2.00	2.00	2.00	2.00	2.00	2.00	2.00	2.00	2.00
Na	0.17	0.17	0.17	0.18	0.16	0.18	0.07	0.02	0.03	0.07
A site	0.17	0.17	0.17	0.18	0.16	0.18	0.07	0.02	0.03	0.07

	BHA11 AVE	BHA12 AVE	BHA5 AVE	BHA7 AVE	BHA8 AVE	BHA9 AVE	BH11 AVE	BHA18 AVE	BHG13 AVE	TS10 AVE
SiO_2	48.03	49.59	47.75	48.11	48.26	47.99	48.13	49.01	48.88	48.56
Al_2O_3	0.68	0.72	1.04	0.85	0.82	0.83	0.80	0.57	0.74	0.79
FeO	38.66	27.65	39.71	40.38	38.83	39.42	37.71	38.09	31.78	40.43
MnO	5.46	11.08	5.98	5.58	6.23	5.41	7.41	4.87	8.94	1.81
MgO	4.30	7.80	2.95	3.15	3.33	3.82	3.70	4.80	6.64	5.08
CaO	0.07	0.09	0.02	0.06	0.07	0.07	nd	0.07	0.05	nd
Na_2O	0.22	0.34	0.40	0.29	0.29	0.28	0.28	0.07	0.33	0.24
Total	97.42	97.27	97.85	98.42	97.83	97.82	98.03	97.48	97.36	96.99
Si IV	7.81	7.86	7.81	7.81	7.87	7.80	7.81	7.91	7.81	7.85
Al IV	0.13	0.13	0.19	0.16	0.13	0.16	0.15	0.09	0.14	0.13
Fe^{+3}	0.06	0.01	0.00	0.02	-	0.04	0.03	-	0.05	0.02
T site	8.00	8.00	8.00	8.00	8.00	8.00	8.00	8.00	8.00	8.00
Al VI	-	0.01	0.01	-	0.03	-	-	0.02	0.00	0.02
Fe^{+3}	0.13	0.03	0.05	0.10	0.03	0.11	0.10	0.04	0.08	0.07
Mg	1.04	1.84	0.72	0.76	0.81	0.92	0.90	1.16	1.58	1.22
Fe^{+2}	3.83	3.12	4.22	4.14	4.14	3.96	4.00	3.78	3.33	3.69
M1,2,3	5.00	5.00	5.00	5.00	5.00	5.00	5.00	5.00	5.00	5.00
Fe^{+2}	1.24	0.50	1.17	1.22	1.13	1.24	0.98	1.32	0.78	1.68
Mn	0.75	1.49	0.83	0.77	0.86	0.75	1.02	0.67	1.21	0.25
Ca	0.01	0.02	0.00	0.01	0.01	0.01	-	0.01	0.01	-
M4 site	2.00	2.00	2.00	2.00	2.00	2.00	2.00	2.00	2.00	2.00
Na	0.07	0.10	0.13	0.09	0.09	0.09	0.09	0.02	0.10	0.07
A site	0.07	0.10	0.13	0.09	0.09	0.09	0.09	0.02	0.10	0.07

	TS15 AVE
SiO_2	48.04
Al_2O_3	1.12
FeO	35.62
MnO	5.88
MgO	5.89
CaO	0.04
Na_2O	0.55
Total	97.14
Si IV	7.73
Al IV	0.21
Fe^{+3}	0.06
T site	8.00
Al VI	0.00
Fe^{+3}	0.09
Mg	1.41
Fe^{+2}	3.49
M1,2,3	5.00
Fe^{+2}	1.15
Mn	0.80
Ca	0.01
Na	0.00
M4 site	2.00
Ca	0.00
Na	0.17
A site	0.17

Muscovite

Cations calculated on the basis of 20 oxygens.

	TS5 1C	TS5 2C	TS5 3C	1917N6 1C	BH1 1C	2609N7 1C	BHS22 1C	TS5 AVE
SiO2	44.96	43.30	44.73	46.64	46.13	46.10	47.78	44.33
TiO2	1.61	1.65	1.44	0.90	1.00	0.60	1.46	1.57
Al2O3	33.90	34.80	34.19	36.57	31.63	36.39	37.09	34.30
FeO	1.70	1.65	1.84	1.76	4.50	1.98	1.36	1.73
MgO	1.52	1.53	1.51	0.71	1.79	0.54	0.81	1.52
BaO	1.98	nd	nd	0.31	nd	nd	nd	0.66
Na2O	0.40	0.60	0.62	0.30	0.30	0.19	0.20	0.54
K2O	8.01	9.84	9.71	8.79	9.11	9.54	7.86	9.19
F	-	0.88	1.03	0.65	2.29	0.56	0.74	0.64
Total	94.08	94.25	95.07	96.63	96.75	95.90	97.30	94.47
Si IV	6.10	5.91	6.05	6.11	6.26	6.10	6.15	6.02
Al IV	1.90	2.09	1.95	1.89	1.74	1.90	1.85	1.98
T site	8.00	8.00	8.00	8.00	8.00	8.00	8.00	8.00
Al VI	3.51	3.51	3.50	3.76	3.31	3.78	3.78	3.51
Ti VI	0.16	0.17	0.15	0.09	0.10	0.06	0.14	0.16
Fe +2	0.19	0.19	0.21	0.19	0.51	0.22	0.15	0.20
Mg	0.31	0.31	0.30	0.14	0.36	0.11	0.16	0.31
O site	4.18	4.18	4.16	4.18	4.29	4.17	4.22	4.17
Ba	0.11	-	-	0.02	-	-	-	0.04
Na	0.11	0.16	0.16	0.08	0.08	0.05	0.05	0.14
K	1.39	1.71	1.68	1.47	1.58	1.61	1.29	1.59
A site	1.60	1.87	1.84	1.56	1.66	1.66	1.34	1.77
OH	4.00	3.62	3.56	3.73	3.02	3.77	3.70	3.73
F	-	0.38	0.44	0.27	0.98	0.23	0.30	0.27

OLIVINE

Cations caluculated on the basis of 4 oxygens.

	TS15 1C	TS15 2C	TS15 3C	TS15 4C	TS15 5C	TS15 6C	TS15 7C	TS15 8C	TS15 9C	TS15 10C
SiO_2	29.72	29.53	29.14	30.01	29.49	29.64	29.25	29.93	29.90	29.67
FeO	57.98	57.66	57.23	57.27	56.63	56.66	57.72	58.61	57.93	58.33
MnO	10.95	11.55	10.89	11.00	11.89	11.47	10.85	11.46	12.06	11.84
MgO	1.09	1.13	1.06	1.27	1.24	1.28	1.01	1.20	1.14	1.05
ZnO	0.33	0.29	ND	0.37	ND	ND	0.28	ND	ND	ND
TOTAL	100.06	100.16	98.31	99.92	99.26	99.05	99.10	101.21	101.02	100.89
Si^{+4}	1.00	0.99	1.00	1.01	1.00	1.00	0.99	0.99	1.00	0.99
Fe^{+2}	1.63	1.62	1.64	1.60	1.60	1.60	1.64	1.63	1.61	1.63
Mn^{+2}	0.31	0.33	0.32	0.31	0.34	0.33	0.31	0.32	0.34	0.34
Mg^{+2}	0.05	0.06	0.05	0.06	0.06	0.06	0.05	0.06	0.06	0.05
Zn^{+2}	0.01	0.01	-	0.01	-	-	0.01	-	-	-
TOTAL	3.00	3.01	3.00	2.99	3.00	3.00	3.01	3.01	3.00	3.01
Fa	81.65	80.80	81.58	81.04	79.88	80.30	81.86	81.00	80.26	80.80
Kn	15.62	16.39	15.72	15.76	16.99	16.46	15.59	16.05	16.93	16.61
Fo	2.73	2.82	2.70	3.20	3.13	3.24	2.55	2.96	2.81	2.59

	TS15 11C	TS4 1C	TS4 2C	TS4 3C	BHA10 1C	BHA10 2C	BHA10 2R	BHA7 1C	BHA7 1R	BHA7 2C
SiO_2	29.50	29.74	29.37	29.62	29.74	29.87	29.62	29.73	29.89	30.07
FeO	56.44	64.43	65.30	64.67	58.52	58.65	58.26	59.93	59.63	60.28
MnO	11.60	3.50	3.46	3.64	11.47	11.23	11.61	10.67	11.10	10.85
MgO	1.20	1.06	0.99	0.94	0.88	1.02	1.01	0.48	0.35	0.59
ZnO	0.21	0.61	ND	ND	ND	ND	ND	ND	ND	ND
TOTAL	98.96	99.34	99.12	98.87	100.60	100.77	100.51	100.82	100.98	101.79
Si^{+4}	1.00	1.00	1.00	1.01	1.00	1.00	0.99	1.00	1.00	1.00
Fe^{+2}	1.60	1.82	1.85	1.84	1.64	1.64	1.63	1.68	1.67	1.67
Mn^{+2}	0.33	0.10	0.10	0.10	0.33	0.32	0.33	0.30	0.31	0.30
Mg^{+2}	0.06	0.05	0.05	0.05	0.04	0.05	0.05	0.02	0.02	0.03
Zn^{+2}	0.01	0.02	-	-	-	-	-	-	-	-
TOTAL	3.00	3.00	3.00	2.99	3.00	3.00	3.01	3.00	3.00	3.00
Fa	80.25	92.22	92.53	92.36	81.62	81.64	81.12	83.70	83.40	83.35
Kn	16.71	5.07	4.96	5.26	16.20	15.84	16.38	15.10	15.72	15.20
Fo	3.04	2.71	2.50	2.38	2.18	2.52	2.50	1.21	0.88	1.45

	BHA7 3C	BHA9 1C	BHA9 2C	BHA9 3C	BHA5 1C	BHA5 1R	BHA5 2C	BHA5 3C	BHA5 2R	BHA5 3R
SiO_2	29.71	29.72	29.95	29.86	29.58	29.94	29.70	29.78	29.42	29.83
FeO	59.56	58.85	58.99	59.85	58.26	57.93	57.19	58.19	57.70	59.18
MnO	11.02	10.85	10.81	10.38	11.93	11.67	12.35	11.91	12.06	11.27
MgO	0.60	0.65	0.59	0.65	0.44	0.46	0.45	0.46	0.41	0.43
ZnO	ND	ND	ND	ND	ND	ND	ND	ND	ND	ND
TOTAL	100.89	100.06	100.35	100.74	100.21	100.00	99.70	100.35	99.59	100.71
Si^{+4}	0.99	1.00	1.00	1.00	1.00	1.01	1.00	1.00	1.00	1.00
Fe^{+2}	1.67	1.66	1.65	1.67	1.64	1.63	1.62	1.64	1.64	1.66
Mn^{+2}	0.31	0.31	0.31	0.29	0.34	0.33	0.35	0.34	0.35	0.32
Mg^{+2}	0.03	0.03	0.03	0.03	0.02	0.02	0.02	0.02	0.02	0.02
Zn^{+2}	-	-	-	-	-	-	-	-	-	-
TOTAL	3.01	3.00	3.00	3.00	3.00	2.99	3.00	3.00	3.00	3.00
Fa	82.96	82.90	83.09	83.68	81.91	82.09	81.12	81.87	81.68	82.93
Kn	15.55	15.48	15.42	14.70	16.99	16.75	17.74	16.98	17.29	15.99
Fo	1.49	1.62	1.49	1.61	1.10	1.16	1.14	1.15	1.03	1.08

	BHA5 4C	BHA5 4R	BHA11 1C	BHA11 2C	BHA11 3C	BHA11 3R	BHA11 4C	BHA11 5C	BHA11 6C	BHA9 4C
SiO_2	29.82	29.68	29.76	29.77	29.75	29.68	29.93	29.70	29.73	28.93
FeO	58.35	58.62	59.17	58.54	58.68	59.06	59.07	58.73	58.56	58.28
MnO	11.61	11.59	11.40	11.43	10.82	10.75	10.98	11.21	11.17	10.73
MgO	0.48	0.48	0.82	0.81	0.83	0.83	0.89	0.91	0.89	0.69
ZnO	ND	ND	ND	ND	ND	ND	ND	ND	ND	ND
TOTAL	100.25	100.37	101.14	100.55	100.07	100.33	100.87	100.54	100.36	98.63
Si^{+4}	1.00	1.00	0.99	1.00	1.00	1.00	1.00	1.00	1.00	0.99
Fe^{+2}	1.64	1.65	1.65	1.64	1.65	1.66	1.65	1.65	1.64	1.67
Mn^{+2}	0.33	0.33	0.32	0.32	0.31	0.31	0.31	0.32	0.32	0.31
Mg^{+2}	0.02	0.02	0.04	0.04	0.04	0.04	0.04	0.05	0.04	0.04
Zn^{+2}	-	-	-	-	-	-	-	-	-	-
TOTAL	3.00	3.00	3.01	3.00	3.00	3.00	3.00	3.00	3.00	3.01
Fa	82.23	82.32	81.98	81.81	82.52	82.68	82.30	81.91	81.94	82.81
Kn	16.57	16.49	16.00	16.17	15.41	15.24	15.49	15.83	15.83	15.44
Fo	1.20	1.19	2.03	2.02	2.07	2.08	2.20	2.26	2.23	1.76

	BHA10 2C	BHA10 1C	BH11 1C	BH11 2C	BHA10 2C	BHA19 1C	BHA19 2C	BHA19 3C	BH11 1C	BH11 2C
SiO_2	30.06	29.90	29.77	30.01	29.62	28.89	29.62	28.88	29.77	30.01
FeO	59.02	59.46	55.31	55.76	58.14	58.18	58.14	58.18	55.31	55.76
MnO	9.95	10.07	14.60	14.80	12.15	12.21	12.15	12.21	14.60	14.80
MgO	1.18	0.94	0.65	0.52	0.29	0.27	0.29	0.27	0.65	0.52
ZnO	ND	ND	ND	ND	ND	ND	ND	ND	ND	ND
TOTAL	100.21	100.37	100.33	101.08	100.19	99.54	100.19	99.54	100.33	101.09
Si^{+4}	1.00	1.00	1.00	1.00	1.00	0.99	1.00	0.99	1.00	1.00
Fe^{+2}	1.65	1.67	1.55	1.55	1.64	1.66	1.64	1.66	1.55	1.55
Mn^{+2}	0.28	0.29	0.42	0.42	0.35	0.35	0.35	0.35	0.42	0.42
Mg^{+2}	0.06	0.05	0.03	0.03	0.01	0.01	0.01	0.01	0.03	0.03
Zn^{+2}	-	-	-	-	-	-	-	-	-	-
TOTAL	3.00	3.00	3.00	3.00	3.00	3.01	3.00	3.01	3.00	3.00
Fa	82.88	83.34	77.62	77.81	81.94	81.91	81.94	81.91	77.62	77.79
Kn	14.16	14.30	20.75	20.91	17.34	17.42	17.34	17.41	20.75	20.91
Fo	2.96	2.35	1.62	1.28	0.72	0.68	0.72	0.68	1.63	1.29

	BHA18 1C	BHA18 2C	TS15 AVE	TS14 AVE	BHA10 AVE	BHA7 AVE	BHA9 AVE	BHHA5 AVE	BHA11 AVE	BH11 AVE
SiO_2	30.06	29.90	29.62	29.58	29.80	29.84	29.84	29.72	29.77	29.89
FeO	59.03	59.46	57.50	64.80	58.58	59.92	59.23	58.00	58.79	55.53
MnO	9.95	10.07	11.41	3.53	11.35	10.85	10.68	11.95	11.17	14.70
MgO	1.18	0.94	1.15	1.00	0.95	0.56	0.63	0.46	0.86	0.58
ZnO	ND	ND	0.13	0.20	ND	ND	ND	ND	ND	ND
TOTAL	100.22	100.37	99.81	99.11	100.68	101.17	100.38	100.13	100.59	100.71
	-	-	-	-	-	-	-	-	-	-
Si^{+4}	1.00	1.00	1.00	1.00	1.00	1.00	1.00	1.00	1.00	1.00
Fe^{+2}	1.65	1.67	1.62	1.84	1.64	1.67	1.66	1.63	1.65	1.55
Mn^{+2}	0.28	0.29	0.33	0.10	0.32	0.31	0.30	0.34	0.32	0.42
Mg^{+2}	0.06	0.05	0.06	0.05	0.05	0.03	0.03	0.02	0.04	0.03
Zn^{+2}	-	-	0.00	0.01	-	-	-	-	-	-
TOTAL	3.00	3.00	3.00	3.00	3.00	3.00	3.00	3.00	3.00	3.00
Fa	82.88	83.34	80.86	92.37	81.63	83.34	83.23	81.78	82.08	77.71
Kn	14.16	14.30	16.26	5.10	16.02	15.28	15.20	17.07	15.79	20.83
Fo	2.96	2.35	2.89	2.53	2.35	1.38	1.57	1.15	2.13	1.46

	BHA19 AVE	BHA18 AVE
SiO_2	29.13	29.98
FeO	58.17	59.24
MnO	12.19	10.01
MgO	0.28	1.06
ZnO	ND	ND
TOTAL	99.76	100.30
Si^{+4}	0.99	1.00
Fe^{+2}	1.65	1.66
Mn^{+2}	0.35	0.28
Mg^{+2}	0.01	0.05
Zn^{+2}	-	-
TOTAL	3.01	3.00
Fa	81.92	83.11
Kn	17.39	14.23
Fo	0.69	2.66

ORTHOPYROXENE AND PYROXFERROITE

Cations calculated on the basis of 6 oxygens.

	51200 1C	191710 1C	191710 2C	191710 3C	191710 4C	178225 1C	178225 2C	178225 3C	178225 4C	19178 1C
SiO_2	46.59	45.60	45.74	45.52	44.87	46.45	46.71	46.72	46.31	45.09
Al_2O_3	0.20	nd	nd	nd	nd	nd	nd	nd	nd	0.14
FeO	40.85	25.57	26.70	26.55	24.37	25.92	26.13	26.24	26.78	27.68
MnO	7.78	27.23	25.01	25.42	28.19	25.23	24.99	25.43	24.15	23.27
MgO	4.13	1.39	1.78	1.75	1.17	1.90	1.92	1.85	1.86	2.18
CaO	nd	0.29	0.35	0.33	0.35	0.27	0.26	0.25	0.26	0.40
Total	99.54	100.08	99.58	99.57	98.95	99.77	100.01	100.49	99.36	98.76
Si^{+4}	1.99	1.98	1.99	1.98	1.98	2.00	2.01	2.00	2.01	1.98
AlIV	0.01	-	-	-	-	-	-	-	-	0.01
T site	2.00	1.98	1.99	1.98	1.98	2.00	2.01	2.00	2.01	1.98
Fe^{+2}	1.46	0.93	0.97	0.97	0.90	0.94	0.94	0.94	0.97	1.01
Mn^{+2}	0.28	1.00	0.92	0.94	1.05	0.92	0.91	0.92	0.89	0.86
Mg	0.26	0.09	0.12	0.11	0.08	0.12	0.12	0.12	0.12	0.14
Ca	-	0.01	0.02	0.02	0.02	0.01	0.01	0.01	0.01	0.02
M1,M2	2.00	2.04	2.02	2.03	2.04	1.99	1.98	1.99	1.99	2.04

	19178 2C	191710 AVE	17828 AVE	19178 AVE
SiO_2	45.32	45.43	46.55	45.21
Al_2O_3	nd	nd	nd	0.07
FeO	25.81	25.80	26.27	26.75
MnO	25.84	26.46	24.95	24.56
MgO	1.64	1.52	1.88	1.91
CaO	0.37	0.33	0.26	0.38
Total	98.98	99.55	99.91	98.87
Si^{+4}	1.99	1.98	2.01	1.98
AlIV	-	-	-	0.00
T site	1.99	1.98	2.01	1.98
Fe^{+2}	0.95	0.94	0.95	0.98
Mn^{+2}	0.96	0.98	0.91	0.91
Mg	0.11	0.10	0.12	0.12
Ca	0.02	0.02	0.01	0.02
M1,M2	2.03	2.03	1.99	2.03

BIOTITE

Cations calculated on the basis of 22 oxygens.

	TS8 1C	TS8 2C	TS8 3C	TS8 3R	TS8 4C	TS8 5C	TS13 1C	TS13 2C	TS13 3C	TS14 1C
SiO_2	30.38	31.21	29.59	31.69	30.04	29.91	36.52	36.76	36.92	35.76
TiO_2	1.74	1.62	2.23	1.80	1.70	1.58	1.11	1.24	1.29	0.45
Al_2O_3	15.53	15.50	15.77	15.56	16.33	16.19	19.29	19.19	19.33	20.14
FeO	23.99	24.17	24.64	23.80	24.36	24.70	21.65	21.26	20.12	24.02
MnO	0.42	0.53	0.35	0.41	0.38	0.42	nd	nd	nd	nd
MgO	8.30	9.07	7.97	8.95	8.44	8.12	10.09	10.01	10.80	8.87
BaO	12.41	11.56	13.94	11.61	13.68	13.52	1.10	1.06	1.03	nd
Na_2O	0.33	0.24	0.27	0.33	0.28	0.35	0.14	0.26	0.17	0.16
K_2O	3.38	3.68	2.91	3.59	3.00	3.00	6.86	6.48	6.44	7.52
F	3.33	3.22	3.11	3.41	3.65	3.39	2.02	3.07	2.63	1.56
Cl	nd	nd	nd	nd	nd	nd	nd	nd	nd	nd
Total	99.81	100.80	100.79	101.16	101.86	101.17	98.77	99.33	98.72	98.48
SiIV	5.10	5.14	4.98	5.19	4.99	5.00	5.47	5.51	5.50	5.39
AlIV	2.90	2.86	3.02	2.81	3.01	3.00	2.53	2.49	2.50	2.61
T site	8.00	8.00	8.00	8.00	8.00	8.00	8.00	8.00	8.00	8.00
Al VI	0.18	0.15	0.10	0.19	0.19	0.20	0.87	0.90	0.90	0.96
Ti VI	0.22	0.20	0.28	0.22	0.21	0.20	0.13	0.14	0.14	0.05
Fe^{+2}	3.37	3.33	3.47	3.26	3.39	3.46	2.71	2.66	2.51	3.03
Mn^{+2}	0.06	0.07	0.05	0.06	0.05	0.06	-	-	-	-
Mg	2.08	2.23	2.00	2.19	2.09	2.03	2.25	2.23	2.40	1.99
O site	5.91	5.98	5.90	5.92	5.94	5.94	5.96	5.94	5.96	6.03
Ba	0.82	0.75	0.92	0.74	0.89	0.89	0.06	0.06	0.06	-
Na	0.11	0.08	0.09	0.10	0.09	0.11	0.04	0.07	0.05	0.05
K	0.72	0.77	0.63	0.75	0.64	0.64	1.31	1.24	1.22	1.44
A site	1.65	1.60	1.63	1.60	1.62	1.64	1.42	1.38	1.33	1.49

	TS14 2C	TS8 6C	TS8 7C	TS13 4C	TS13 5C	TS1 1C	TS3 1C	TS3 2C	TS3 3C	TS3 4C
SiO_2	36.03	29.92	30.66	37.03	37.07	37.83	40.28	39.74	40.23	39.82
TiO_2	0.59	1.50	2.14	1.12	1.17	nd	nd	nd	nd	nd
Al_2O_3	19.46	16.25	16.30	19.00	19.58	16.73	14.98	14.27	15.12	14.67
FeO	24.16	23.49	24.60	17.32	17.77	18.55	11.62	14.02	14.20	14.04
MnO	nd	0.37	0.43	nd	nd	0.85	0.56	0.69	0.71	nd
MgO	8.55	8.38	7.74	11.31	10.60	12.73	17.87	16.37	15.94	16.66
BaO	nd	13.88	13.29	nd	nd	nd	nd	nd	nd	0.44
Na_2O	0.19	0.29	0.27	0.28	0.34	0.18	0.40	0.36	0.28	0.17
K_2O	7.97	2.89	3.11	8.48	8.63	9.23	8.19	8.44	8.00	7.33
F	1.41	3.72	3.24	2.21	2.97	4.60	4.40	4.83	4.90	4.79
Cl	nd	nd	nd	nd	nd	nd	nd	nd	nd	nd
Total	98.37	100.69	101.78	96.74	98.13	100.70	98.29	98.73	99.38	97.92
SiIV	5.45	5.03	5.06	5.57	5.55	5.68	5.93	5.94	5.95	5.95
AlIV	2.55	2.97	2.94	2.43	2.45	2.32	2.07	2.06	2.05	2.05
T site	8.00	8.00	8.00	8.00	8.00	8.00	8.00	8.00	8.00	8.00
Al VI	0.91	0.25	0.23	0.93	1.00	0.64	0.53	0.46	0.58	0.54
Ti VI	0.07	0.19	0.27	0.13	0.13	-	-	-	-	-
Fe^{+2}	3.05	3.30	3.40	2.18	2.22	2.33	1.43	1.75	1.76	1.76
Mn^{+2}	-	0.05	0.06	-	-	0.11	0.07	0.09	0.09	-
Mg	1.93	2.10	1.91	2.54	2.36	2.85	3.92	3.65	3.51	3.71
O site	5.96	5.90	5.86	5.77	5.72	5.93	5.95	5.94	5.94	6.01
Ba	-	0.91	0.86	-	-	-	-	-	-	0.03
Na	0.06	0.09	0.09	0.08	0.10	0.05	0.11	0.10	0.08	0.05
K	1.54	0.62	0.66	1.63	1.65	1.77	1.54	1.61	1.51	1.40
A site	1.59	1.63	1.60	1.71	1.75	1.82	1.65	1.72	1.59	1.47

	TS3 5C	TS3 6C	TS3 7C	TS12 1C	TS12 2C	TS12 3C	TS12 4C	TS11 1C	TS11 2C	TS11 3C
SiO_2	40.25	40.58	40.00	40.74	40.30	40.50	40.29	36.12	35.93	36.53
TiO_2	nd	nd	nd	0.17	0.14	0.19	0.22	2.50	3.09	2.15
Al_2O_3	14.29	13.99	14.87	12.66	12.31	12.59	12.57	18.15	18.14	18.23
FeO	15.07	13.29	14.96	11.67	11.59	11.55	11.48	21.99	22.70	22.01
MnO	nd	nd	nd	0.48	0.49	0.53	0.64	0.49	nd	0.46
MgO	17.07	18.36	16.17	19.25	19.07	18.82	18.74	8.94	8.53	9.27
BaO	0.42	0.80	0.42	nd	nd	nd	nd	nd	nd	nd
Na_2O	0.25	0.28	0.17	0.29	0.32	0.32	0.25	0.13	0.20	0.18
K_2O	7.34	7.70	7.28	8.92	9.00	8.78	9.13	9.04	8.81	8.78
F	4.96	5.14	4.76	5.92	5.59	6.04	5.46	1.46	1.40	1.59
Cl	nd	nd	nd	nd	nd	nd	nd	nd	nd	nd
Total	99.65	100.13	98.62	100.11	98.82	99.31	98.79	98.83	98.80	99.20
SiIV	5.95	5.96	5.95	6.02	6.02	6.04	6.02	5.44	5.41	5.47
AlIV	2.05	2.04	2.05	1.98	1.98	1.96	1.98	2.56	2.59	2.53
T site	8.00	8.00	8.00	8.00	8.00	8.00	8.00	8.00	8.00	8.00
Al VI	0.44	0.38	0.56	0.22	0.19	0.25	0.23	0.66	0.63	0.69
Ti VI	-	-	-	0.02	0.02	0.02	0.02	0.28	0.35	0.24
Fe^{+2}	1.86	1.63	1.86	1.44	1.45	1.44	1.43	2.77	2.86	2.76
Mn^{+2}	-	-	-	0.06	0.06	0.07	0.08	0.06	-	0.06
Mg	3.76	4.02	3.59	4.24	4.25	4.18	4.17	2.01	1.91	2.07
O site	6.06	6.03	6.01	5.98	5.97	5.96	5.94	5.78	5.75	5.81
Ba	0.02	0.05	0.02	-	-	-	-	-	-	-
Na	0.07	0.08	0.05	0.08	0.09	0.09	0.07	0.04	0.06	0.05
K	1.38	1.44	1.38	1.68	1.72	1.67	1.74	1.74	1.69	1.68
A site	1.48	1.57	1.46	1.76	1.81	1.76	1.81	1.77	1.75	1.73

	TS11 4C	TS11 5C	TS11 6C	BHG4 1C	BHG4 2C	BHG4 2R	BHG4 3C	BHG4 3R	BHG2 1C	BHG2 2C
SiO_2	35.93	36.22	36.01	28.65	28.85	28.61	28.85	28.43	28.46	28.10
TiO_2	2.29	2.10	2.82	2.88	2.62	2.60	2.67	2.76	1.54	1.58
Al_2O_3	17.54	18.36	17.93	17.93	17.69	17.93	18.38	18.07	15.45	15.09
FeO	22.53	21.92	21.49	19.67	18.95	18.99	20.07	20.07	27.29	27.57
MnO	-	0.45	0.46	0.22	0.28	0.25	0.26	0.27	0.90	0.97
MgO	9.32	9.48	8.84	9.19	9.80	9.66	8.95	8.96	5.95	5.60
BaO	-	-	-	12.19	11.98	11.89	11.94	11.98	12.60	12.00
Na_2O	0.16	0.13	0.22	0.37	0.38	0.38	0.33	0.34	0.19	0.22
K_2O	8.93	9.00	8.94	2.36	2.45	2.43	2.32	2.32	2.27	2.20
F	1.38	1.48	1.33	3.76	3.85	3.27	3.83	3.84	4.54	4.37
Cl	nd	nd	nd	nd	nd	nd	0.05	nd	nd	nd
Total	98.09	99.14	98.04	97.22	96.84	96.00	97.64	97.03	99.19	97.70
SiIV	5.46	5.43	5.45	4.84	4.87	4.85	4.84	4.82	4.99	4.99
AlIV	2.54	2.57	2.55	3.16	3.13	3.15	3.16	3.18	3.01	3.01
T site	8.00	8.00	8.00	8.00	8.00	8.00	8.00	8.00	8.00	8.00
Al VI	0.59	0.67	0.65	0.40	0.40	0.43	0.48	0.43	0.18	0.15
Ti VI	0.26	0.24	0.32	0.37	0.33	0.33	0.34	0.35	0.20	0.21
Fe^{+2}	2.86	2.75	2.72	2.78	2.68	2.69	2.82	2.84	4.00	4.10
Mn^{+2}	-	0.06	0.06	0.03	0.04	0.04	0.04	0.04	0.13	0.15
Mg	2.11	2.12	1.99	2.31	2.47	2.44	2.24	2.26	1.55	1.48
O site	5.83	5.83	5.74	5.89	5.91	5.92	5.91	5.92	6.07	6.09
Ba	-	-	-	0.81	0.79	0.79	0.79	0.80	0.87	0.84
Na	0.05	0.04	0.06	0.12	0.13	0.12	0.11	0.11	0.06	0.08
K	1.73	1.72	1.73	0.51	0.53	0.52	0.50	0.50	0.51	0.50
A site	1.78	1.76	1.79	1.43	1.45	1.44	1.39	1.41	1.44	1.41

	178226 1C	178226 2C	178226 3C	191713 1C	1917N6 1C	1917N6 2C	1917N6 3C	189113 1C	189113 2C	1917N5 1C
SiO_2	32.40	32.23	40.39	34.87	31.29	34.47	36.65	28.58	28.39	35.52
TiO_2	2.55	3.26	4.75	3.21	1.63	2.91	2.41	1.54	1.26	3.67
Al_2O_3	16.75	16.47	15.15	19.74	23.41	19.41	22.69	15.52	15.89	18.83
FeO	17.76	17.91	10.71	20.45	28.61	25.60	22.21	23.54	24.23	22.59
MnO	0.39	0.39	nd	0.50	0.30	0.24	0.24	1.35	1.30	0.69
MgO	12.53	12.39	12.94	7.23	4.29	5.73	4.56	8.03	7.59	6.96
BaO	11.57	11.78	nd	4.10	nd	nd	nd	16.84	17.06	0.68
Na_2O	0.29	0.25	2.74	0.20	nd	0.10	0.09	nd	0.11	0.11
K_2O	4.10	4.08	1.97	7.19	3.72	8.57	7.82	1.94	1.93	9.18
F	2.49	2.38	nd	2.26	nd	nd	0.51	4.07	3.97	0.87
Cl	nd	nd	nd	nd	nd	nd	nd	nd	nd	nd
Total	100.83	101.14	88.65	99.74	93.25	97.03	97.18	101.41	101.73	99.10
SiIV	5.11	5.08	6.05	5.32	4.94	5.29	5.45	4.93	4.90	5.35
AlIV	2.89	2.92	1.95	2.68	3.06	2.71	2.55	3.07	3.10	2.65
T site	8.00	8.00	8.00	8.00	8.00	8.00	8.00	8.00	8.00	8.00
Al VI	0.22	0.13	0.72	0.87	1.29	0.80	1.43	0.08	0.13	0.70
Ti VI	0.30	0.39	0.53	0.37	0.19	0.34	0.27	0.20	0.16	0.42
Fe^{+2}	2.34	2.36	1.34	2.61	3.78	3.29	2.76	3.40	3.50	2.85
Mn^{+2}	0.05	0.05	-	0.07	0.04	0.03	0.03	0.20	0.19	0.09
Mg	2.95	2.91	2.89	1.65	1.01	1.31	1.01	2.06	1.95	1.56
O site	5.86	5.84	5.49	5.56	6.31	5.76	5.51	5.94	5.94	5.62
Ba	0.72	0.73	-	0.25	-	-	-	1.14	1.15	0.04
Na	0.09	0.08	0.80	0.06	-	0.03	0.03	-	0.04	0.03
K	0.82	0.82	0.38	1.40	0.75	1.68	1.48	0.43	0.42	1.77
A site	1.63	1.62	1.17	1.70	0.75	1.71	1.53	1.57	1.62	1.84

	2609N7 1C	2609N7 2C	TS6 AVE	BH1 AVE	1917N2 AVE	BHS22 AVE	BH4 AVE	BH3 AVE	TS8 AVE	TS13 AVE
SiO_2	34.83	34.47	36.77	35.99	36.20	34.30	36.22	34.70	30.22	36.73
TiO_2	2.94	2.79	nd	2.19	1.85	5.05	1.25	1.69	1.77	1.21
Al_2O_3	20.09	19.66	18.73	18.58	19.53	21.06	18.20	20.30	15.86	19.27
FeO	26.89	26.94	22.63	24.41	22.42	23.37	25.40	26.26	24.37	21.01
MnO	0.31	0.35	1.31	0.51	nd	0.23	0.74	nd	0.42	nd
MgO	4.53	4.32	9.15	5.81	9.22	5.55	6.03	6.12	8.38	10.30
BaO	nd	nd	nd	nd	nd	nd	0.67	nd	13.02	1.06
Na_2O	nd	nd	0.35	0.23	0.24	nd	0.58	0.42	0.29	0.19
K_2O	9.49	9.44	8.98	9.19	8.72	7.73	8.14	8.49	3.19	6.59
F	1.00	1.01	2.54	3.16	0.83	0.84	3.11	1.89	3.34	2.57
Cl	nd	nd	nd	nd	nd	nd	nd	nd	nd	nd
Total	100.08	98.98	100.46	100.07	99.01	98.13	100.34	99.87	100.89	98.94
SiIV	5.28	5.30	5.53	5.51	5.38	5.16	5.56	5.27	5.04	5.49
AlIV	2.72	2.70	2.47	2.49	2.62	2.84	2.44	2.73	2.96	2.51
T site	8.00	8.00	8.00	8.00	8.00	8.00	8.00	8.00	8.00	8.00
Al VI	0.87	0.86	0.84	0.86	0.80	0.89	0.85	0.91	0.16	0.89
Ti VI	0.34	0.32	-	0.25	0.21	0.57	0.14	0.19	0.22	0.14
Fe^{+2}	3.41	3.46	2.84	3.13	2.79	2.94	3.26	3.34	3.40	2.63
Mn^{+2}	0.04	0.05	0.17	0.07	-	0.03	0.10	-	0.06	-
Mg	1.02	0.99	2.05	1.33	2.04	1.24	1.38	1.39	2.08	2.30
O site	5.67	5.68	5.90	5.63	5.84	5.67	5.73	5.83	5.93	5.95
Ba	-	-	-	-	-	-	0.04	-	0.85	0.06
Na	-	-	0.10	0.07	0.07	-	0.17	0.12	0.09	0.06
K	1.83	1.85	1.72	1.79	1.65	1.48	1.59	1.65	0.68	1.26
A site	1.83	1.85	1.82	1.86	1.72	1.48	1.81	1.77	1.63	1.38

	TS14 AVE	TS3 AVE	TS12 AVE	TS11 AVE	BHG4 AVE	BHG2 AVE	BHG6 AVE	BHA5 AVE	BHA8 AVE	178226 AVE
SiO_2	35.90	40.12	40.46	36.12	28.78	28.38	28.13	28.70	28.83	35.01
TiO_2	0.52	nd	0.18	2.49	2.72	1.52	1.96	0.67	0.76	3.52
Al_2O_3	19.80	14.63	12.53	18.06	18.00	15.16	15.14	14.75	15.01	16.12
FeO	24.09	13.99	11.57	22.11	19.56	27.52	27.04	29.27	28.09	15.46
MnO	nd	0.24	0.54	0.31	0.25	0.95	1.60	1.59	1.97	0.26
MgO	8.71	16.89	18.97	9.06	9.31	5.70	5.31	4.70	4.80	12.62
BaO	nd	0.32	nd	nd	12.04	12.36	11.11	10.88	11.28	7.79
Na_2O	0.17	0.26	0.30	0.17	0.36	0.17	0.25	0.22	0.17	1.09
K_2O	7.74	7.61	8.96	8.92	2.37	2.23	2.66	3.04	2.84	3.38
F	1.49	4.88	5.75	1.44	3.81	4.54	3.70	4.98	4.51	1.62
Cl	nd	nd	nd	nd	0.02	nd	nd	nd	nd	nd
Total	98.42	98.96	99.25	98.68	97.23	98.52	96.89	98.80	98.27	96.87
SiIV	5.42	5.95	6.02	5.44	4.85	5.01	4.98	5.10	5.11	5.41
AlIV	2.58	2.05	1.98	2.56	3.15	2.99	3.02	2.90	2.89	2.59
T site	8.00	8.00	8.00	8.00	8.00	8.00	8.00	8.00	8.00	8.00
Al VI	0.94	0.50	0.22	0.65	0.43	0.17	0.15	0.19	0.25	0.36
Ti VI	0.06	-	0.02	0.28	0.35	0.20	0.26	0.09	0.10	0.41
Fe^{+2}	3.04	1.74	1.44	2.79	2.76	4.06	4.01	4.35	4.17	2.01
Mn^{+2}	-	0.03	0.07	0.04	0.04	0.14	0.24	0.24	0.30	0.03
Mg	1.96	3.73	4.21	2.04	2.34	1.50	1.40	1.25	1.27	2.91
O site	5.99	6.00	5.96	5.79	5.91	6.07	6.06	6.12	6.08	5.73
Ba	-	0.02	-	-	0.80	0.86	0.77	0.76	0.78	0.48
Na	0.05	0.08	0.09	0.05	0.12	0.06	0.09	0.08	0.06	0.32
K	1.49	1.44	1.70	1.71	0.51	0.50	0.60	0.69	0.64	0.67
A site	1.54	1.53	1.79	1.76	1.42	1.41	1.46	1.52	1.49	1.47

	1917N6 AVE	191713 AVE	2609N7 AVE	BHMM15 AVE
SiO_2	34.14	28.49	34.65	39.42
TiO_2	2.32	1.40	2.87	nd
Al_2O_3	21.84	15.70	19.88	15.05
FeO	25.47	23.88	26.92	10.92
MnO	0.26	1.33	0.33	0.70
MgO	4.86	7.81	4.43	19.20
BaO	nd	16.95	nd	0.13
Na_2O	0.06	0.05	nd	0.35
K_2O	6.70	1.93	9.47	9.42
F	0.17	4.02	1.00	4.36
Cl	nd	nd	nd	nd
Total	95.82	101.57	99.53	99.54
SiIV	5.23	4.91	5.29	5.77
AlIV	2.77	3.09	2.71	2.23
T site	8.00	8.00	8.00	8.00
Al VI	1.18	0.11	0.86	0.37
Ti VI	0.27	0.18	0.33	-
Fe^{+2}	3.28	3.45	3.44	1.34
Mn^{+2}	0.03	0.19	0.04	0.09
Mg	1.11	2.01	1.01	4.19
O site	5.86	5.94	5.68	5.99
Ba	-	1.15	-	0.01
Na	0.02	0.02	-	0.10
K	1.30	0.43	1.84	1.76
A site	1.33	1.59	1.84	1.87

SPHALERITE

	TS2 1C	TS2 2C	TS2 3C	TS2 4C	TS2 5C	TS5 1C	TS5 2C	TS5 3C	TS5 4C	TS5 5C
S	34.32	34.14	33.97	34.41	33.97	34.07	34.08	33.84	34.38	33.97
Zn	57.42	56.90	56.66	57.15	56.32	57.45	56.75	57.15	56.71	56.60
Fe	8.50	8.28	9.03	8.73	9.35	8.24	9.24	8.46	8.62	8.25
Mn	0.07	0.06	0.05	0.08	0.11	0.52	0.52	0.59	nd	0.55
Cu	-	0.09	0.08	0.10	0.02	nd	nd	nd	nd	0.02
TOTAL	100.32	99.47	99.79	100.48	99.78	100.29	100.60	100.04	99.70	99.39

	TS5 6C	TS1 1C	TS1 2C	TS1 3C	TS1 4C	TS1 5C	TS1 6C	TS1 7C	TS12 1C	TS12 2C
S	34.08	33.88	33.57	34.06	34.15	33.89	33.55	34.04	33.72	33.55
Zn	57.18	56.28	57.13	57.19	56.28	56.84	56.90	56.67	57.63	57.40
Fe	7.75	8.74	8.38	8.81	8.98	9.01	8.40	9.12	8.18	8.19
Mn	0.63	0.31	0.24	0.29	0.30	0.31	0.24	0.34	0.37	0.26
Cu	nd	nd	0.01	nd	0.07	0.02	0.00	0.01	nd	0.03
TOTAL	99.64	99.20	99.33	100.34	99.78	100.07	99.09	100.18	99.89	99.43

	TS12 3C	TS12 4C	TS12 5C	TS12 6C	TS12 7C	TS12 8C	TS15 1C	TS15 2C	TS15 3C	TS15 4C
S	33.80	33.78	34.24	33.96	34.04	33.88	34.15	34.01	33.82	34.62
Zn	56.58	56.26	57.86	57.12	56.57	57.14	60.30	59.97	60.00	62.09
Fe	8.28	8.99	8.30	8.60	8.59	8.68	5.24	5.20	5.01	3.17
Mn	0.28	0.25	0.22	0.26	0.29	0.23	0.09	0.12	0.11	0.08
Cu	nd	nd	0.16	0.03	0.07	0.00	0.10	0.08	0.04	nd
TOTAL	98.93	99.29	100.78	99.97	99.56	99.94	99.87	99.37	98.99	99.95

	TS15 5C	TS15 6C	TS15 7C	TS15 8C	TS15 9C	TS15 10C	TS15 11C	TS3 1C	TS3 2C	TS3 3C
S	34.10	34.17	33.96	34.01	34.02	34.19	34.37	34.21	34.22	34.50
Zn	58.90	57.81	59.61	61.31	59.47	57.15	59.34	56.88	57.56	56.28
Fe	5.80	7.36	5.76	4.30	5.66	7.44	6.23	8.42	8.40	8.61
Mn	0.24	0.16	0.23	0.12	0.16	0.20	0.26	0.25	0.41	0.43
Cu	0.12	nd	nd	0.09	0.01	0.05	nd	nd	nd	0.03
TOTAL	99.16	99.50	99.57	99.83	99.32	99.03	100.20	99.76	100.58	99.85

	TS3 4C	TS3 5C	TS3 6C	TS3 7C	TS4 1C	TS4 2C	TS2 AVE	TS14 AVE	TS1 AVE	TS12 AVE
S	34.21	33.72	34.17	34.51	33.84	33.70	33.97	34.07	33.85	33.87
Zn	57.38	57.26	56.68	58.19	56.90	57.41	56.44	56.88	56.77	57.07
Fe	8.12	8.31	8.64	8.05	8.26	8.39	8.45	8.46	8.72	8.48
Mn	0.25	0.20	0.37	0.31	0.04	0.04	0.08	0.46	0.28	0.27
Cu	nd	0.02	0.08	nd	0.05	nd	0.04	0.00	0.02	0.04
TOTAL	99.96	99.51	99.95	101.05	99.09	99.54	98.98	99.87	99.64	99.72

	TS15 AVE	TS3 AVE	TS4 AVE
S	34.13	34.27	33.77
Zn	59.63	57.12	57.15
Fe	5.56	8.35	8.32
Mn	0.16	0.31	0.04
Cu	0.04	0.02	0.03
TOTAL	99.52	100.06	99.31

GAHNITE

Cations calculated on the basis of 4 oxygens.

	TS11 1C	TS11 2C	TS11 3C	TS11 4C	TS11 5C	TS11 6C	TS11 7C	TS11 8C	TS11 9C	TS11 10C
TiO_2	nd	nd	nd	nd	nd	nd	nd	nd	nd	nd
Al_2O_3	54.89	54.76	55.35	55.59	55.20	55.20	55.06	54.27	54.70	55.54
Cr_2O_3	nd	nd	0.09	0.16	0.17	nd	nd	0.20	0.23	0.15
Fe_2O_3	1.88	1.64	1.76	1.11	1.35	1.57	1.62	2.04	2.08	1.36
FeO	7.80	7.60	7.91	8.25	8.07	8.21	8.21	7.81	7.80	7.99
MnO	0.34	0.30	0.33	0.24	0.29	0.32	0.31	0.34	0.32	0.27
MgO	1.01	0.91	1.01	1.02	0.94	1.10	1.06	0.91	0.97	0.85
ZnO	33.51	33.76	33.74	33.35	33.47	32.97	32.98	33.38	33.68	34.02
TOTAL	99.42	98.97	100.19	99.71	99.49	99.36	99.24	98.96	99.79	100.18
Ti	-	-	-	-	-	-	-	-	-	-
Al	1.96	1.96	1.96	1.97	1.97	1.96	1.96	1.95	1.95	1.97
Cr	-	-	0.00	0.00	0.00	-	-	0.00	0.01	0.00
Fe^{+3}	0.04	0.04	0.04	0.03	0.03	0.04	0.04	0.05	0.05	0.03
Fe^{+2}	0.20	0.19	0.20	0.21	0.20	0.21	0.21	0.20	0.20	0.20
Mn	0.01	0.01	0.01	0.01	0.01	0.01	0.01	0.01	0.01	0.01
Mg	0.05	0.04	0.05	0.05	0.04	0.05	0.05	0.04	0.04	0.04
Zn	0.75	0.76	0.75	0.74	0.75	0.73	0.74	0.75	0.75	0.75
Cations	3.00	3.00	3.00	3.00	3.00	3.00	3.00	3.00	3.00	3.00
Hc	19.74	19.32	19.87	20.76	20.39	20.73	20.76	19.89	19.70	20.06
Spl	4.54	4.11	4.51	4.56	4.22	4.96	4.78	4.15	4.37	3.82
Ghn	74.87	75.79	74.79	74.07	74.65	73.50	73.66	75.08	75.10	75.43
Gal	0.86	0.78	0.83	0.60	0.74	0.81	0.79	0.89	0.83	0.69

	TS11 11C	TS11 12C	TS13 1C	TS13 2C	TS13 3C	TS13 4C	TS13 5C	TS13 6C	TS3 1C	TS3 2C
TiO_2	nd	nd	nd	nd	0.12	nd	nd	nd	nd	nd
Al_2O_3	55.22	54.98	55.74	53.74	54.99	54.71	54.50	52.76	54.62	55.26
Cr_2O_3	nd	nd	0.46	0.46	0.32	0.29	0.23	0.26	nd	nd
Fe_2O_3	1.71	1.63	1.20	4.17	3.41	3.63	3.20	5.36	2.00	1.80
FeO	7.65	8.21	16.59	23.12	19.35	19.41	18.84	19.48	7.38	7.45
MnO	0.33	0.30	0.12	0.21	0.18	0.15	0.15	nd	0.34	0.34
MgO	0.94	1.03	1.13	1.12	1.04	1.30	1.18	1.26	0.67	0.71
ZnO	34.00	32.98	24.12	16.58	21.81	20.88	21.36	20.38	34.52	34.75
TOTAL	99.85	99.13	99.38	99.39	101.22	100.37	99.46	99.51	99.52	100.31
Ti	-	-	-	-	0.00	-	-	-	-	-
Al	1.96	1.96	1.96	1.90	1.91	1.91	1.92	1.87	1.95	1.96
Cr	-	-	0.01	0.01	0.01	0.01	0.01	0.01	-	-
Fe^{+3}	0.04	0.04	0.03	0.09	0.08	0.08	0.07	0.12	0.05	0.04
Fe^{+2}	0.19	0.21	0.41	0.58	0.48	0.48	0.47	0.49	0.19	0.19
Mn	0.01	0.01	0.00	0.01	0.00	0.00	0.00	-	0.01	0.01
Mg	0.04	0.05	0.05	0.05	0.05	0.06	0.05	0.06	0.03	0.03
Zn	0.76	0.74	0.53	0.37	0.47	0.46	0.47	0.45	0.77	0.77
Cations	3.00	3.00	3.00	3.00	3.00	3.00	3.00	3.00	3.00	3.00
Hc	19.29	20.81	41.45	57.85	47.62	48.15	47.16	49.05	18.73	18.75
Spl	4.21	4.66	5.05	4.98	4.57	5.76	5.26	5.64	3.03	3.18
Ghn	75.65	73.76	53.19	36.62	47.37	45.73	47.20	45.31	77.38	77.20
Gal	0.85	0.76	0.31	0.54	0.44	0.37	0.38	-	0.86	0.87

	TS3 3C	TS3 4C	TS6 1C	TS6 2C	TS6 3C	TS6 4C	TS6 5C	TS7 1C	TS7 2C	TS7 3C
TiO_2	nd	nd	nd	nd	nd	nd	nd	nd	nd	nd
Al_2O_3	54.71	56.91	54.48	54.43	53.81	55.28	54.01	54.47	53.72	54.76
Cr_2O_3	nd	nd	nd	nd	nd	nd	nd	nd	0.12	nd
Fe_2O_3	1.85	0.42	2.90	3.01	3.12	2.28	2.91	3.24	3.54	3.61
FeO	7.08	8.67	9.46	9.70	9.19	12.32	9.18	11.68	12.21	12.01
MnO	0.30	0.44	0.37	0.46	0.43	1.26	0.41	0.25	0.25	0.31
MgO	0.70	0.74	0.62	0.62	0.59	0.65	0.63	0.83	0.91	0.91
ZnO	34.84	33.82	32.58	32.23	32.46	28.58	32.44	29.94	28.81	29.75
TOTAL	99.48	100.99	100.40	100.43	99.59	100.37	99.58	100.41	99.55	101.34
Ti	-	-	-	-	-	-	-	-	-	-
Al	1.96	1.99	1.93	1.93	1.93	1.95	1.93	1.93	1.92	1.92
Cr	-	-	-	-	-	-	-	-	0.00	-
Fe^{+3}	0.04	0.01	0.07	0.07	0.07	0.05	0.07	0.07	0.08	0.08
Fe^{+2}	0.18	0.22	0.24	0.24	0.23	0.31	0.23	0.29	0.31	0.30
Mn	0.01	0.01	0.01	0.01	0.01	0.03	0.01	0.01	0.01	0.01
Mg	0.03	0.03	0.03	0.03	0.03	0.03	0.03	0.04	0.04	0.04
Zn	0.78	0.74	0.72	0.72	0.73	0.63	0.73	0.66	0.64	0.65
Cations	3.00	3.00	3.00	3.00	3.00	3.00	3.00	3.00	3.00	3.00
Hc	17.97	21.51	23.82	24.42	23.38	30.81	23.33	29.31	30.90	29.87
Spl	3.16	3.27	2.77	2.76	2.66	2.90	2.87	3.71	4.09	4.03
Ghn	78.10	74.11	72.48	71.65	72.87	63.11	72.75	66.34	64.37	65.32
Gal	0.77	1.10	0.93	1.16	1.10	3.18	1.05	0.64	0.64	0.78

	TS7 4C	TS7 5C	TS7 6C	TS7 7C	BH5 1C	BH5 2C	191713 1C	BH1 1C	BH1 2C	1817N2 1C
TiO_2	nd	nd	nd	nd	nd	nd	nd	nd	nd	nd
Al_2O_3	54.77	54.57	54.62	54.61	55.25	55.03	55.33	55.34	54.46	53.99
Cr_2O_3	nd	nd	nd	nd	nd	nd	nd	nd	nd	nd
Fe_2O_3	2.72	2.79	2.91	3.13	2.71	2.98	0.80	1.61	1.86	2.96
FeO	12.19	11.83	11.36	11.40	8.33	8.45	9.62	9.30	8.69	8.78
MnO	0.32	0.26	0.29	0.29	0.26	0.23	0.37	0.23	0.24	nd
MgO	0.79	0.77	0.77	0.78	0.62	0.65	0.90	0.38	0.29	0.89
ZnO	29.33	29.72	30.33	30.36	34.49	34.30	31.42	33.42	33.71	32.86
TOTAL	100.12	99.94	100.27	100.57	101.67	101.63	98.45	100.28	99.25	99.48
Ti	-	-	-	-	-	-	-	-	-	-
Al	1.94	1.94	1.93	1.93	1.94	1.93	1.98	1.96	1.96	1.93
Cr	-	-	-	-	-	-	-	-	-	-
Fe^{+3}	0.06	0.06	0.07	0.07	0.06	0.07	0.02	0.04	0.04	0.07
Fe^{+2}	0.31	0.30	0.29	0.29	0.21	0.21	0.24	0.23	0.22	0.22
Mn	0.01	0.01	0.01	0.01	0.01	0.01	0.01	0.01	0.01	-
Mg	0.04	0.03	0.03	0.03	0.03	0.03	0.04	0.02	0.01	0.04
Zn	0.65	0.66	0.67	0.67	0.76	0.75	0.71	0.74	0.76	0.74
Cations	3.00	3.00	3.00	3.00	3.00	3.00	3.00	3.00	3.00	3.00
Hc	30.61	29.79	28.55	28.57	20.76	21.07	24.45	23.42	22.16	22.29
Spl	3.55	3.47	3.43	3.47	2.75	2.88	4.08	1.71	1.32	4.03
Ghn	65.03	66.07	67.29	67.21	75.84	75.48	70.51	74.29	75.90	73.68
Gal	0.80	0.67	0.73	0.74	0.66	0.57	0.96	0.59	0.62	-

	BH4 1C	TS11 AVE	TS13 AVE	TS3 AVE	TS6 AVE	TS7 AVE	BH5 AVE	BH1 AVE
TiO_2	nd	nd	0.02	nd	nd	nd	nd	nd
Al_2O_3	51.56	55.06	54.41	55.38	54.40	54.50	55.14	54.90
Cr_2O_3	-	0.08	0.34	-	-	0.02	-	-
Fe_2O_3	6.65	1.65	3.50	1.52	2.84	3.13	2.85	1.73
FeO	9.94	7.96	19.47	7.64	9.97	11.81	8.39	9.00
MnO	0.30	0.31	0.13	0.35	0.58	0.28	0.24	0.23
MgO	0.30	0.98	1.17	0.70	0.62	0.82	0.63	0.34
ZnO	32.24	33.49	20.86	34.48	31.66	29.75	34.39	33.56
TOTAL	101.08	99.52	99.89	100.08	100.08	100.31	101.65	99.76
Ti	-	-	0.00	-	-	-	-	-
Al	1.85	1.96	1.91	1.97	1.94	1.93	1.94	1.96
Cr	-	0.00	0.01	-	-	0.00	-	-
Fe^{+3}	0.15	0.04	0.08	0.03	0.06	0.07	0.06	0.04
Fe^{+2}	0.25	0.20	0.49	0.19	0.25	0.30	0.21	0.23
Mn	0.01	0.01	0.00	0.01	0.01	0.01	0.01	0.01
Mg	0.01	0.04	0.05	0.03	0.03	0.04	0.03	0.02
Zn	0.72	0.75	0.46	0.77	0.71	0.66	0.76	0.75
Cations	3.00	3.00	3.00	3.00	3.00	3.00	3.00	3.00
Hc	26.89	20.11	48.54	19.24	25.15	29.66	20.91	22.79
Spl	3.77	4.41	5.21	3.16	2.79	3.68	2.81	1.51
Ghn	68.56	74.70	45.91	76.70	70.57	65.95	75.66	75.09
Gal	0.78	0.79	0.34	0.90	1.49	0.71	0.61	0.60

TOURMALINE

	TS5 1C	TS5 2C	TS5 3C	BH2 1C	BH2 2C	BH2 3C	BH2 4C
SiO_2	35.50	35.21	35.89	35.15	35.00	35.07	34.26
TiO_2	0.65	0.66	0.55	0.23	0.15	0.17	0.10
Al_2O_3	34.16	35.36	35.56	32.33	31.80	31.80	32.76
FeO	5.12	5.69	5.00	11.81	11.42	11.72	11.82
MnO	0.21	0.16	0.15	nd	0.18	nd	0.19
MgO	7.49	6.97	7.64	5.37	5.23	4.81	4.96
CaO	1.06	1.09	0.82	0.55	0.39	0.40	0.90
K_2O	0.09	0.11	0.06	nd	nd	nd	0.06
Na_2O	1.72	1.92	2.18	2.42	2.59	2.50	2.22
ZnO	0.29	nd	nd	nd	nd	nd	nd
F	nd	0.61	0.82	1.16	1.00	1.11	1.18
TOTAL	86.29	87.78	88.67	89.02	87.76	87.58	88.46

OXIDES

	TS13 1C	TS13 2C	TS13 3C	TS11 1C	TS11 1C	TS11 2C	TS13 3C	TS13 5C
SiO_2	nd	nd	nd	nd	nd	nd	nd	0.13
TiO_2	51.84	51.69	52.53	49.92	99.49	50.54	52.90	52.13
Al_2O_3	nd	0.08	nd	nd	nd	nd	nd	0.09
Cr_2O_3	nd	nd	nd	nd	nd	nd	nd	nd
FeO	47.06	46.31	45.59	44.45	0.23	43.55	44.24	30.53
MnO	2.20	2.26	2.30	4.31	-	4.72	2.77	16.47
TOTAL	101.10	100.34	100.42	98.68	99.72	98.82	99.91	99.35
Si	-	-	-	-	-	-	-	0.00
Ti	0.97	0.98	0.99	0.96	1.99	0.97	1.01	0.99
Al	-	0.00	-	-	-	-	-	0.00
Cr	-	-	-	-	-	-	-	-
Fe^{+2}	0.93	0.93	0.94	0.87	1.99	0.87	0.95	0.64
Mn	0.05	0.05	0.05	0.09	-	0.10	0.06	0.35
Cations	2.00	2.00	2.00	2.00	2.00	2.00	2.00	2.00

	TS4 1C	TS4 2C	TS4 3C	TS4 4C	TS4 5C	TS1 1C	TS15 1C	TS15 2C	TS3 1C	TS3 2C
SiO_2	nd	0.10	nd	0.13	0.15	nd	0.13	0.13	nd	nd
TiO_2	0.49	0.44	0.71	0.58	0.50	0.22	0.32	0.22	nd	nd
Al_2O_3	0.15	0.19	0.09	0.10	0.22	0.12	0.38	0.48	0.36	0.30
Fe_2O_3	67.21	66.62	66.48	65.77	65.89	67.16	67.17	67.08	67.72	68.18
FeO	31.22	31.13	31.25	31.02	31.04	30.69	31.08	31.01	30.47	30.68
MnO	nd	nd	nd	nd	nd	nd	0.28	0.21	0.25	0.20
TOTAL	99.06	98.48	98.52	97.61	97.79	98.19	99.37	99.13	98.80	99.36
Si	-	0.00	-	0.01	0.01	-	0.00	0.01	-	-
Ti	0.01	0.01	0.02	0.02	0.01	0.01	0.01	0.01	-	-
Al	0.01	0.01	0.00	0.00	0.01	0.01	0.02	0.02	0.02	0.01
Fe^{+3}	1.96	1.96	1.95	1.95	1.95	1.98	1.95	1.96	1.98	1.99
Fe^{+2}	1.01	1.02	1.02	1.02	1.02	1.01	1.00	1.00	0.99	0.99
Mn	-	-	-	-	-	-	0.01	0.01	0.01	0.01
Cations	3.00	3.00	3.00	3.00	3.00	3.00	3.00	3.00	3.00	3.00

	TS6 1C	BHA8 1C
SiO_2	0.09	0.10
TiO_2	nd	0.48
Al_2O_3	0.48	0.16
Fe_2O_3	68.29	67.24
FeO	30.87	31.26
MnO	0.40	0.21
TOTAL	100.13	99.45
Si	0.00	0.00
Ti	-	0.01
Al	0.02	0.01
Fe^{+3}	1.97	1.96
Fe^{+2}	0.99	1.01
Mn	0.01	0.01
Cations	3.00	3.00

	TS3 3C	TS3 4C	TS3 5C	TS14 1C	TS14 2C	TS14 3C	TS12 1C	BHG13 1C	BHA9 1C	BHA9 2C
SiO_2	nd	nd	nd	nd	nd	nd	nd	nd	0.12	0.12
TiO_2	nd	nd	nd	0.12	0.11	0.13	0.09	0.42	0.75	0.38
Al_2O_3	0.43	0.36	0.37	0.67	0.29	0.41	0.17	0.32	0.25	0.23
Fe_2O_3	68.33	67.58	67.82	67.94	68.13	67.60	68.59	66.93	65.92	66.28
FeO	30.73	30.43	30.43	31.25	31.05	30.94	30.65	30.65	31.46	30.67
MnO	0.31	0.22	0.34	nd	nd	nd	0.48	0.44	nd	0.28
TOTAL	99.80	98.60	98.95	99.97	99.59	99.08	99.98	98.77	98.50	97.97
Si	-	-	-	-	-	-	-	-	0.00	0.00
Ti	-	-	-	0.00	0.00	0.00	0.00	0.01	0.02	0.01
Al	0.02	0.02	0.02	0.03	0.01	0.02	0.01	0.01	0.01	0.01
Fe^{+3}	1.98	1.98	1.98	1.96	1.98	1.97	1.99	1.96	1.94	1.96
Fe^{+2}	0.99	0.99	0.99	1.00	1.00	1.00	0.99	1.00	1.03	1.01
Mn	0.01	0.01	0.01	-	-	-	0.02	0.01	-	0.01
Cations	3.00	3.00	3.00	3.00	3.00	3.00	3.00	3.00	3.00	3.00
O	4.00	4.00	4.00	4.00	4.00	4.00	4.00	4.00	4.00	4.00

STAUROLITE

Cations calculated on the basis of 46 oxygens.

	TS13 1C
SiO_2	29.90
TiO_2	-
Al_2O_3	56.04
FeO	4.65
MnO	-
MgO	0.20
ZnO	6.67
TOTAL	97.46
	-
SiIV	8.19
TiIV	-
Al+3	18.09
Fe^{+2}	1.07
Mn^{+2}	-
Mg^{+2}	0.08
Zn^{+2}	1.35
CATIONS	28.77

XRF ANAYSES

nd = not detected

Sample	BHG1	BHG2	BHG4	BHG6	BHG13	BHG15	BHG16	BHG17
SiO_2	54.43	54.36	57.96	50.09	39.00	50.60	47.19	58.44
TiO_2	0.60	0.40	0.58	0.55	0.56	0.37	0.46	0.32
Al_2O_3	11.51	10.23	9.46	11.12	11.53	11.51	11.03	5.86
FeO	18.37	21.32	20.56	22.00	30.09	21.46	24.98	22.52
MnO	11.39	9.09	6.73	12.40	15.89	12.09	9.25	8.92
MgO	0.40	0.24	0.65	0.27	0.60	0.35	0.38	0.94
CaO	0.88	0.63	0.55	0.89	0.67	0.58	0.91	0.42
Na_2O	0.02	0.03	0.53	0.19	0.07	0.17	0.04	0.04
K_2O	0.02	0.04	0.03	0.08	0.00	0.09	0.01	0.05
P_2O_5	0.38	0.29	0.37	0.35	0.18	0.24	0.48	0.23
H_2O-	0.02	0.09	0.05	0.05	0.04	0.01	0.01	0.02
LOI	0.93	1.05	1.10	1.26	1.89	1.16	1.09	1.31
TOTAL	98.93	97.77	98.56	99.26	100.52	98.63	95.83	99.07
Mo	2	2	3	1	1	1	3	2
Nb	13	6	11	7	6	5	8	18
Zr	255	206	215	237	179	210	208	184
Y	41	36	33	27	30	36	37	22
Sr	69	58	53	58	20	45	44	26
Rb	0	0	13	30	0	19	0	24
Th	nd	nd	nd	nd	8	14	nd	14
U	nd	nd	nd	nd	nd	3	6	3
La	48	34	34	52	45	59	27	50
Ce	78	64	66	84	67	75	58	71
Nd	27	25	32	32	18	21	22	24
Co	4	0	36	13	13	6	14	22
Cr	67	64	64	67	53	59	51	57
V	38	31	52	47	57	47	57	30
Pb	19589	26466	4353	6087	299	2873	34308	410
S	2670	3520	14516	4092	7769	10242	3897	11759
Ni	11	0	71	33	39	5	8	20
Sc	7	7	8	8	6	8	9	6
Ba	12	3595	6624	6106	13	2316	43	3240
Cu	5	11	165	5	58	50	4	76
Zn	786	709	12086	4410	1028	3958	794	634

Sample	BHA5	BHA7	BHA9	BHA10	BHA11	BHA12	BHA18	BHA19
SiO_2	49.21	35.14	35.33	36.51	36.92	56.60	48.94	48.43
TiO_2	0.04	0.17	0.14	0.26	0.24	0.20	0.02	0.01
Al_2O_3	0.63	1.57	0.85	1.37	1.99	1.20	0.42	0.48
FeO	39.43	52.21	53.20	50.39	49.21	26.94	38.71	39.32
MnO	6.28	6.37	5.77	7.03	7.49	10.15	6.09	6.12
MgO	1.42	1.14	0.96	1.13	1.06	1.63	2.65	1.50
CaO	0.20	0.33	0.33	0.35	0.46	0.18	0.07	0.09
Na_2O	0.25	0.10	0.16	0.07	0.07	0.10	0.12	0.21
K_2O	0.02	0.02	0.01	0.00	0.00	0.01	0.02	0.01
P_2O_5	0.08	0.23	0.23	0.25	0.33	0.04	0.01	0.01
H_2O-	0.13	0.07	0.04	0.04	0.02	0.03	0.02	0.03
LOI	0.68	1.32	1.37	1.05	1.13	2.36	0.37	0.94
TOTAL	98.36	98.66	98.38	98.43	98.90	99.43	97.44	97.15

(continued)

Sample	BHA5	BHA7	BHA9	BHA10	BHA11	BHA12	BHA18	BHA19
Mo	0	2	2	2	3	1	1	1
Nb	0	4	3	5	5	2	1	1
Zr	5	45	41	69	78	43	0	1
Y	2	9	7	9	14	5	0	0
Sr	14	46	29	34	43	5	3	6
Rb	3	nd	nd	nd	nd	nd	nd	nd
Th	nd	nd	nd	5	nd	nd	nd	nd
U	nd	nd	nd	4	nd	nd	nd	nd
La	8	17	15	20	20	13	10	9
Ce	0	31	16	26	29	10	12	0
Nd	0	7	0	6	10	0	0	0
Co	26	20	29	25	22	15	38	29
Cr	16	25	24	27	29	22	8	4
V	6	42	38	56	52	25	0	0
Pb	2545	418	1015	586	586	454	8763	358
S	3387	9936	12500	19314	22008	50443	1695	2555
Ni	14	6	0	14	13	5	11	7
Sc	4	2	2	3	3	3	1	3
Ba	671	15	56	13	12	15	6	8
Cu	20	222	191	645	674	581	104	52
Zn	6286	1600	3778	1581	1502	1876	3914	6339

Sample	BHA25	BHA8	BHGQ23	BHS22	BHF3	BHF14	BHMM15
SiO_2	37.86	44.03	71.34	61.10	67.20	66.96	9.60
TiO_2	0.11	0.39	0.75	0.89	0.01	0.00	0.15
Al_2O_3	2.07	2.55	5.76	19.02	16.14	18.21	4.25
FeO	48.05	37.27	12.01	7.09	1.36	0.71	74.91
MnO	5.21	2.04	5.77	0.33	0.06	0.05	0.72
MgO	0.74	1.08	0.54	1.58	0.00	0.00	0.86
CaO	0.27	0.48	0.34	0.23	0.41	0.08	1.14
Na_2O	0.45	0.18	0.03	0.09	0.59	1.11	0.06
K_2O	0.02	0.35	0.03	3.85	11.84	8.03	0.59
P_2O_5	0.16	0.37	0.04	0.03	0.26	0.02	0.55
H_2O-	0.01	0.02	0.09	0.53	0.08	0.10	0.13
LOI	1.09	2.20	1.97	4.05	0.60	1.06	4.79
TOTAL	96.02	90.94	98.68	98.79	98.55	96.33	97.75
Mo	5	4	2	3	1	1	2
Nb	3	14	16	21	nd	1	3
Zr	31	133	310	256	2	nd	67
Y	5	5	22	33	11	nd	26
Sr	19	102	12	22	174	403	24
Rb	0	57	6	287	513	527	78
Th	nd	nd	15	24	nd	nd	nd
U	nd	nd	4	2	nd	nd	nd
La	14	11	38	39	18	3	26
Ce	20	39	60	89	44	12	64
Nd	7	24	19	38	20	11	34
Co	96	25	9	17	2	nd	86
Cr	28	40	61	124	12	10	34
V	29	6	42	94	nd	nd	20
Pb	14472	47602	28	61	7254	10708	2598
S	16150	5795	41026	675	317	nd	10553
Ni	0	35	11	37	3	nd	35
Sc	3	2	5	20	1	nd	3
Ba	33	19934	165	542	3141	15621	342
Cu	56	18	369	323	328	nd	2961
Zn	14013	5735	668	143	596	614	5736